Chapter 7
Nitroxide-Mediated Polymerization

7.1 Introduction

Controlled radical polymerization (CRP) under radical initiation conditions belongs to priority areas in the development of the synthetic chemistry of polymers of the last years [1–16]. Nitroxide-mediated polymerization (NMP) was invented by Solomon [1, 13]. Since this discovery, nitroxide-mediated radical polymerization is a powerful method to synthesize well-defined macromolecular architectures with precisely controlled topologies, compositions, microstructures, and functionalities [3–5].

The most common mechanisms for reversible activation in polymerization reactions are schematically illustrated in Scheme 7.1.

Persistent radical effect (PRE) occurs when two radicals are generated at the same time, at the same rate, and one is more persistent than the other, the self-termination reactions are lowered, leading to an unusually high selectivity for the cross-coupling reaction [10]. The effect has been investigated for the preparation of macromolecules with a narrow molar mass distribution through radical polymerization.

Nitroxide-mediated polymerization is widely applied in industrial polymer syntheses as a method for production of large-tonnage polymers and is employed to manufacture new pigments, sealants, emulsion stabilizers, and block copolymers, etc., with a various set of properties. NMP has also paved an avenue for complex macromolecular architectures (statistical, block, graft) in the fields of nanoscience and nanotechnology [5, 9, 12] and references cited therein. A brief summary of NMP developments in both the patent and open literature during the period of the early

Scheme 7.1 Mechanisms for reversible activation in polymerization reactions [6]

G. I. Likhtenshtein, *Nitroxides*, Springer Series in Materials Science 292,
https://doi.org/10.1007/978-3-030-34822-9_7

1980–2000 was presented in [11]. Various important aspects in this area, such as synthesis of nitroxides and alkoxyamines, fundamentals to applications in materials science, kinetic aspects of NMP, recent developments in NMP, nitroxide-mediated polymerization in dispersed media, NMP of methacrylic esters, complex macromolecular architectures prepared by NMP, surface-initiated NMP, from nanoporous materials to microelectronics, NMP under homogenous conditions, and NMP-derived materials for biomedical applications were presented and discussed in separate chapters of the book [12]. In this chapter, fundamentals and recent developments in the NMP area are briefly summarized and illustrated by particular examples.

7.2 Mechanism of the Nitroxide-Mediated Polymerization

The basic idea of the NMP method (Scheme 7.1) is that the initiation of the "living" free polymerization (LEP) process occurs as a result of the dissociation of a special compound (A-S) into two radicals, active ($AR^{\cdot}$) and stable ($SR^{\cdot}$) ones. Persisted radical effect (PRE) can also occur for radicals generated from the decomposition of two different initiators affording the active radical and a persistent radical. The active radical involves into the polymer chain initiation and self-recombination reactions. The recombination of a stable radical is thermodynamically forbidden, and, in this case, it can only participate in reversible cross-recombinations with the partner radical ($AR^{\cdot}$) and with a polymer radical $Rn^{\cdot}$.

The perfect candidates for the role of initiator of LFP were found to be alkoxyamines. These compounds cleave into transient alkyl and persistent aminoxyl radicals which then combine and regenerate the parent compounds. Simultaneously, the alkyl species self-terminate, and this causes a continuous buildup of excess aminoxyl. Hence, the back-reaction to the alkoxyamine (e.g., R_1R_2NOR) accelerates, and the self-termination slows down in time. The cross-recombination of macroradical ($Rn^{\cdot}$) with $R_1R_2NO^{\cdot}$ leads to a very low concentration of $AR^{\cdot}$, limiting the self-termination reaction of the alkyl radical, and allowing the controlled growth of the macroradical.

The first work on alkoxyamines R_1R_2NOR was reported by Jones and Major in 1927 [17]. The radical reactivity of these compounds was discovered by Kovtun et al. in 1974 [18]. The formation of R_1R_2NOR in recombination of corresponding radicals was also demonstrated.

In NMP, the principle stages are [9]: (1) Initiation can be either performed in a bicomponent system or in a unimolecular initiation process. (2) The nitroxide can then cross-recombine with the propagating active chain to give a nitroxide-terminated radical as dormant species. (3) This macroalkoxyamine can undergo reversible C–ON bond homolysis at elevated reaction temperatures and releases the stable nitroxide radical as well as the active polymer chain. Detail schemes of the reaction mechanism in NMP and initiation mechanism of uni- and bimolecular initiators were presented in review [9]. The development of alkoxyamines as initiators permits controlled homopolymerization of acrylates and acrylamides. Data on

TEMPO derivatives, alkoxyamines including alkoxyamines bearing stereo centers, and light-sensitive alkoxyamines used in DNP were also described in the review.

Steps involved in the TEMPO-mediated nitroxide-mediated polymerization are as follows: (1) The TEMPO/monomer adduct is formed with a source of radicals from a conventional initiator like benzoyl peroxide. (2) With an increase in temperature, the equilibrium is shifted to the addition of monomer, and the radical concentration is controlled by the persistent radical effect. (3) Propagation continues and the growing polymer is capped by TEMPO and the cycle continues. The recent review [5] also provided information on the key components of NMP such as TEMPO derivatives used as nitroxides, alkoxyamines derivatives showing improved bond hydrolysis, alkoxyamines bearing stereo centers, nitroxides and alkoxyamines used for the polymerization (RDRP), of methyl methacrylate (MMA), and functional alkoxyamines.

Spin traps are agents that are commonly used in electron spin resonance spectroscopy (ESR) as a tool to convert transient radicals into a stable form. In polymerizations, spin traps act as radical scavengers, and hence, mostly inhibit chain growth. Nitroxides and nitrons can be radical spin trap scavengers and used in ESR studies to quantify radical initiation [19–22]. A nitrone, for example,

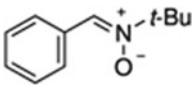

possesses higher affinity toward reacting with oxygen-centered radicals, acrylates, styrenic, and tertiary carbon-centered radicals [20, 21]. In enhanced spin capturing polymerization (ESCP), (macro)radical spin trapping by nitrons is in competition with conventional macroradical chain growth, leading to an effective chain length control of the polymerization, namely trapping macroradicals and shorting the residual polymer chains. The trapped species constitutes a macronitroxide, which by itself is able to trap a further transient radical in a radical recombination event. Thus, the polymer product consists of a coupling product of two polymers, which is bridged by an alkoxyamine functionality in a typical example of the nitroxide-mediated polymerization, the preparation of ABA-type block copolymers

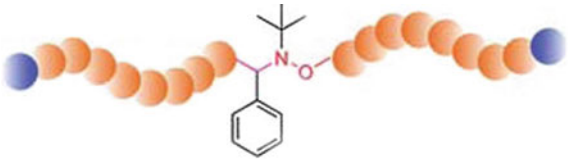

via tandem enhanced spin capturing polymerization (ESCP) [23]. Midchain alkoxyamine functional polystyrenes (M_n = 6200, 12,500, and 19,900 g mol^{-1}) were chain extended with styrene as well as *tert*-butyl acrylate at elevated temperature NMP conditions (T = 110 °C), generating a tandem ESCP-NMP sequence. It

was found that the efficiency of the block copolymer formation process decreases with an increasing chain length of the ESCP precursor macromolecules.

Photopolymerization reactions are recognized as powerful tool for modification of coatings, inks, photoresists, dual-cure systems, and others [24, 25]. Nitroxide-mediated photopolymerization (PNMP) is characterized by important advantages, e.g., thin films can be polymerized very rapidly by UV irradiation, and PNMP is an ecological alternative to thermal processes and is able to modify and pattern surfaces.

During PNMP, the photolysis of an alkoxyamine bearing a chromophore, for example,

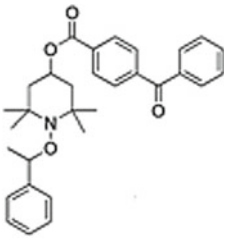

leads to a reversible equilibrium between the alkoxyamine and the generated nitroxide and alkyl radicals, providing a controlled radical photopolymerization [26]. In the alkoxyamines with a closer proximity between the chromophore and the C–O bond, the homolysis of the alkoxyamine is facilitated due to an energy transfer from the chromophore ("antenna") to the weak C–O bond. In work [27], the thermally driven polymerizations were performed via the cleavage of the alkoxyamine functionality; whereas, the photochemically induced polymerizations were carried out either by nitroxide-mediated photopolymerization (NMP2) or by a mechanism, depending on the structure of the light-sensitive alkoxyamine employed. With each alkoxyamine, as initiators of thermally and photoinduced polymerizations, block copolymers were obtained, and the system was applied to the post-modification of polymer coatings for application in patterning and photografting.

The photoradical polymerization of vinyl acetate was performed using 4-methoxy-2,2,6,6-tetramethylpiperidine-1-oxyl as the mediator in the presence of bis(alkylphenyl)iodonium hexafluorophosphate (BAI) [28]. It was found that in this condition: (1) The polymerization proceeds by the living mechanism based on linear increases in the first-order time–conversion and conversion–molecular weight plot. (2) The molecular weight distribution increased with the increasing conversion due to cloudiness of the solution as the polymerization proceeded. (3) The polymerization had a photolatency because the propagation stopped by interruption of the irradiation and was restarted by further irradiation. It was shown [29] that the combination of living radical photopolymerization and lithographic techniques can provide the regiospecificity of graft-polymerized surfaces and precision graft-chain architectures, including their surface graft-chain density, spatio segmental or graded block chains, molecular shape or configuration segmental density. Via such an approach, it

was possible to obtain thickness above 100 nm and a linear growth of the thickness versus irradiation time.

7.3 Nitroxide-Mediated Polymerization Kinetics

The complete kinetic scheme is composed of three stages [6, 7, 30–34].

In Scheme 7.2, k_d and $k_{d,ds}$ are the homolysis rate constants of the initiator R_1R_2NOR and of the dormant species, respectively; k_c and $k_{c,ds}$ are the rate constants for the cross-coupling between the alkyl radicals (the initiating one $R^{\cdot}$ and the propagating one $RMn^{\cdot}$) and the controlling nitroxide $R_1R_2NO^{\cdot}$, respectively; k_{add} is the rate constant of addition of the initiating alkyl radical $R^{\cdot}$ onto monomer M; k_p is the propagation rate constant of the propagating radical $RMn^{\cdot}$; k_t the self-termination rate constants for the C-centered radicals; k_{dD} is the rate constants for the intramolecular proton transfer (Cope-type elimination) between the initiator and the dormant species; and k_{cD} the rate constant for the intermolecular H-transfer between nitroxides and C-centered radicals.

In comprehensive review [7], principle aspects of the NMP kinetics were described and discussed in separate paragraphs including (1) equations for NMP and the phase

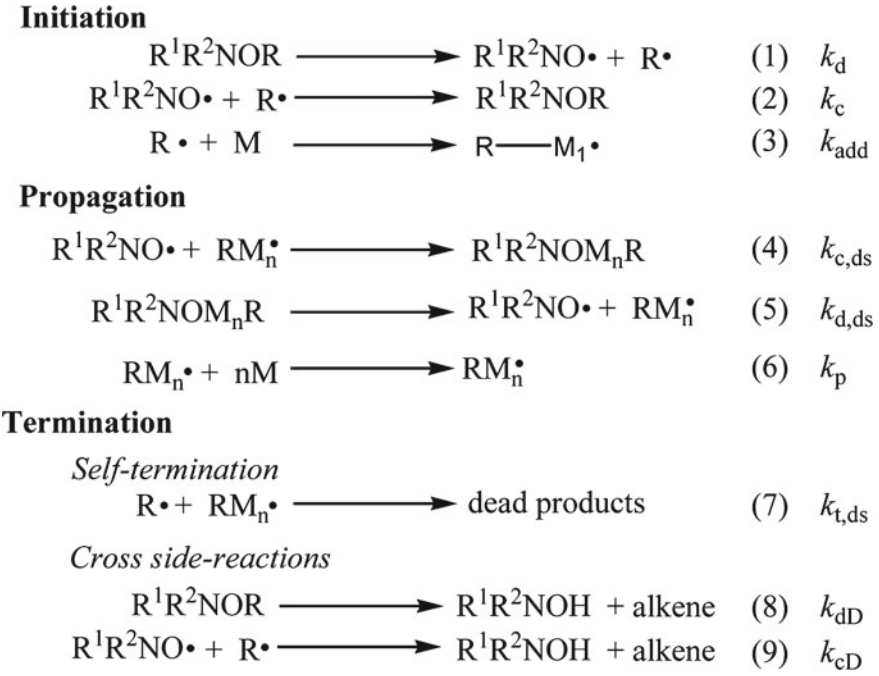

Scheme 7.2 Three-stage scheme for NMP [6]

diagram approach, (2) evidence of the occurrence of PRE in NMP, (3) importance of the k_c, k_d, initiation stage, and side-reactions on the fate of NMP. Data on cross-recombination of nitroxides and alkyl radicals are discussed in Chap. 3. In the review, equations for the PRE dependence on the quasi-equilibrium constant, affording the control, the livingness, and the polymerization time were also presented.

Figure 7.1 illustrates the enthalpic and entropic contributions of the various effects in the NDP homolysis stage.

Effects of the polarity and polarizability on the NDP hemolysis are schematically described in Fig. 7.2.

One of examples of the occurrence of PRE is the decomposition of the TEMPO-based alkoxyamine in monocomponent systems initiated in both bicomponents and

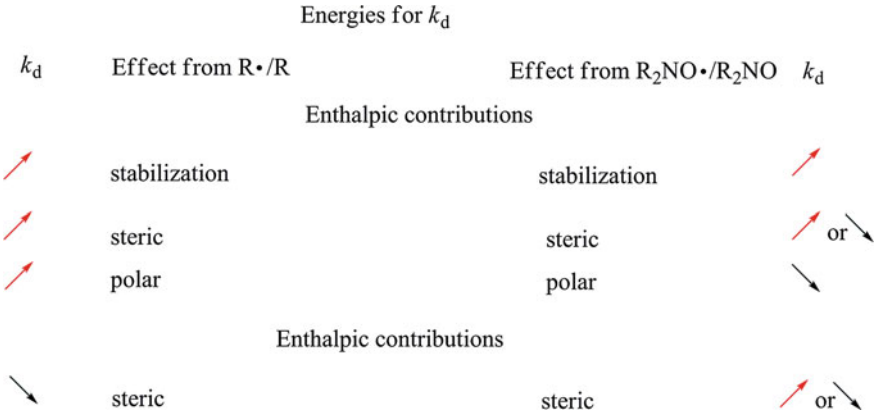

Fig. 7.1 Enthalpic and entropic contributions of the various effects governing k_d values [7]. Private communication from Prof. Elena Bagryanskaya

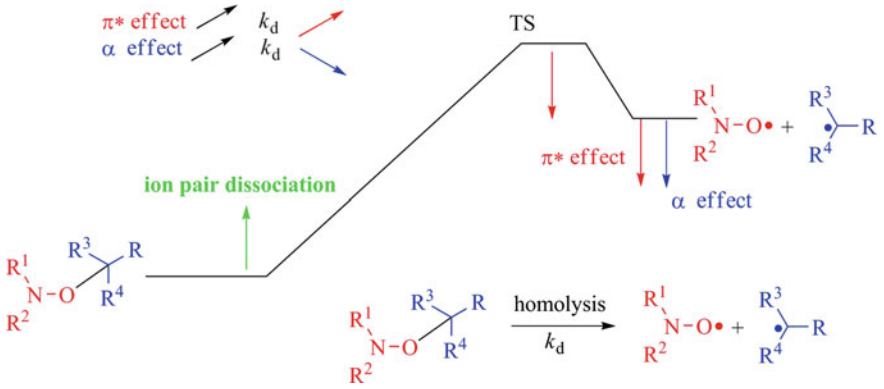

Fig. 7.2 Energy profile for the solvent displaying the effects of the polarity/polarizability of the displaying solvent [7]. Private communication from Prof. Elena Bagryanskaya

monocomponent systems [33]. The following stages are involved in the reaction (1) the C–ON bond hemolysis in the 2-phenyl-2-(2′,2′,6′,6′-tetramethylpiperidine-1′-oxyl)propane (cumyl–TEMPO) 1 afforded an persistent nitroxide and an alkyl radical $PhMe_2C^{\cdot}$ (k_d), (2) the latter either cross-recombined (k_c) in or self-terminated (k_t), and (3) the decay of 1 is accelerated in the presence of a free alkyl radical scavenger galvinoxyl. Solving the kinetic equations predicted the possibility of three different kinetics regimes, that is (1) very short regime I for less than 0.1 s where a transient and a persistent radical are generated at the same rate, (2) regime II lasting around 10^7 s, when the pre-equilibrium is set, and the growth of the nitroxide obeys a $t^{1/3}$ law and the decay of the transient cumyl radical obeys a $t^{-1/3}$ law; and (3) the third regime III which would last 10^7 s with the decays of alkoxyamine 1 and of the cumyl radical 3 obeying a $1/t$ law.

It was shown [34] that in NMP, the concentration of persistent species obeys a $t^{1/3}$ law (7.1) [7]

$$\left[\mathrm{P}^*\right] = [\mathrm{PT}]_0^{2/3} \cdot \left(\frac{3k_\mathrm{d}^2 \cdot 2k_\mathrm{t}}{k_\mathrm{c}^2}\right)^{1/3} \cdot t^{1/3} \tag{7.1}$$

where $[\mathrm{PT}]_0$ is the initial concentration of alkoxyamine, k_d is the rate constant of alkoxyamine homolysis, k_t is the recombination rate constant of transient radicals T*, and k_c is the recombination rate constant for radical T* and persistent radical P*. In reversible-deactivation radical polymerization (RDRP), the self-termination stage can be quantified by determining the dead chain fraction (DCF) as given in (7.2) [35].

$$\mathrm{DCF} = \frac{[\mathrm{T}]}{[\mathrm{R}-\mathrm{X}]} = \frac{2DP_\mathrm{r}k_\mathrm{t}[\ln(1-p)]^2}{[\mathrm{M}]_0 k_\mathrm{p}^2 t} \tag{7.2}$$

where [T] is the number of dead chains, [R X] is the number of all initiated chains [R X], DP_T is the decreasing degree of polymerization, p is the conversion (p), and k_t and k_p rate coefficients of termination and propagation (k_p). $[M]_0$ is the monomer concentration, and t is the reaction time (t).

Review [35] describes the methods influencing C–ON bond homolysis without alteration of temperature are protonation of functional groups in an alkoxyamine, formation of metal–alkoxyamine complexes, and chemical transformation of alkoxyamines. These approaches can have a significant effect on the homolysis rate constant, by a factor of up to 30, and can shorten the half-lifetime from days to seconds. Importance of the side-reactions on the fate of NMP such as the dimerization and disproportionation of alkyl and polymeric radicals, self-termination reactions of alkyl radicals, the nitroxide self-decomposition, the intramolecular proton transfer reaction, the thermal decomposition of the alkoxyamine and nitroxides, and the presence of an additive was also emphasized in [7]. More details on the development of the kinetic equations and the subsequent consequences are available in papers [2–7, 34, 36].

7.4 Surface and Dispersed Systems

Surface-initiated nitroxyl-mediated polymerization (SI-NMP) on either flat or curved (e.g., nanoparticles) structures has been applied to a diverse range of substrates and applications including the formation of polymer brushes, and the graft modification of nanoparticles (organic and inorganic) and renewable polymers to make new hybrid materials for electronics, optoelectronics, biomedicine, etc. [37–56]. The most significant peculiarity of the surface-initiated nitroxyl-mediated polymerization (SI-NMP) is that the local chain concentrations can be much higher than in solution or bulk [5–9, 12]. In such systems, the initiating and propagating sites are in close proximity, possibly several nanometers apart, and the polymer chain ends remain constrained in closer proximity to each other than occurs in homogeneous NMP. Therefore, the presence of a surface can have a profound impact on the course of polymerization, including kinetics, chain length distribution, and chain end livingness.

Among the numerous inorganic–organic hybrid materials, silica–polymer hybrid materials are the most commonly investigated. Grafting of polymer brushes by SI-NMP has been widely dedicated to surface modification of spherical silica particles exhibiting cylindrical organized mesopores of 2.5–10 nm [37]. Using three alkoxyamine chemical structures on the silicon wafers based on TEMPO, SG1 and TIPNO

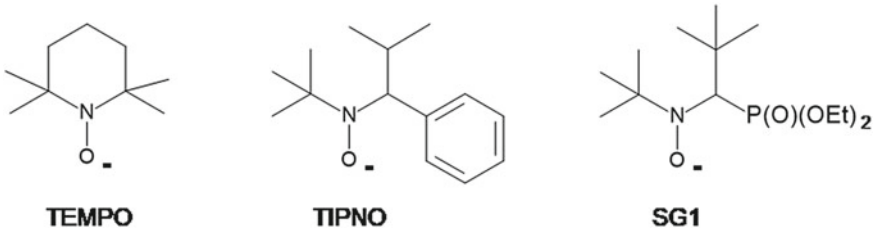

TEMPO TIPNO SG1

and the surface pressure during Langmuir–Blodgett (LB) deposition, polystyrene brushes with grafting densities of 0.3–1.0 chains nm 2 and stretching values of 40–70% were obtained [38]. Other inorganic surfaces subjected to NMP are clays, Fe_3O_4 (Magnetite), c-Fe_2O_3 (Maghemite), TiO_2 (titanium dioxide), zinc oxide ZnO nanoparticles, CuO (cupric oxide), quantum dots cadmium selenide (CdSe) nanoparticles, polystyrene surfaces, multiwalled carbon nanotubes, graphene oxide, and chitosan. A newly designed diazonium-based isoindoline nitroxide was grafted to a number of carbon allotropes including single and multiwalled carbon nanotubes, graphene, glassy carbon, and carbon fiber [39]. Synthetic pathway for grafting of various carbon allotropes with isoindoline nitroxide-free radicals was descried. Spin-labeled compound

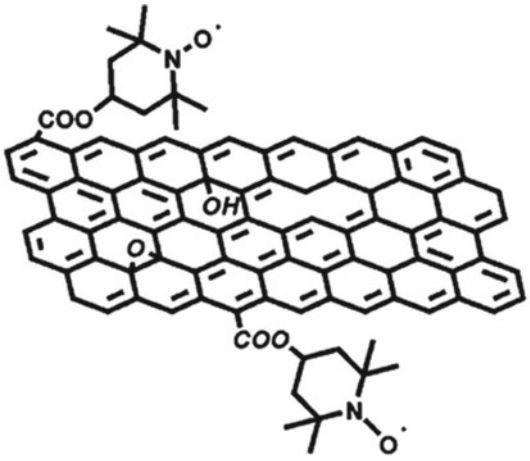

was also synthesized.

To design higher capacity next generation lithium ion batteries, graphene was grafted with 4-hydroxy-TEMPO via conventional esterification of its carboxylic acid groups [40]. The hybrid nitroxide–graphene anode conjugate material possesses superior lithium storage capacity as a result of its dual reservoir of graphene and the reversible redox cycling nitroxide.

Though the majority of polymers produced via a radical mechanism in the industry originates from bulk processes, emulsion and miniemulsion polymerizations together with dispersion polymerization have been also widely studied techniques in reversible-deactivation radical polymerization protocols (RDRP). Implementation of polymerization in a dispersible environment is characterized as the row of features that is especially important at an industrial production. In this process, kinetics is usually faster, and final conversion and degree of polymerization are higher [41–58]. The concentration of radicals in the entire organic phase of a latex is largely superior to that of the corresponding homogeneous system. The final product of such a polymerization in aqueous dispersed media is a latex, suspension of stable nano- or microparticles that found applications as elastomers, adhesives, paints, and in biotechnology.

As an example, using oleic acid/potassium hydroxide and alkoxyamine, particles with diameters less than 20 nm were obtained by conventional radical polymerization and nitroxide-mediated radical polymerization of styrene conducted in miniemulsion SG1 [41]. The method was based on miniemulsion polymerization exploiting combination of the in situ surfactant generation approach whereby the surfactant is formed at the oil–water interface by reaction between an organic acid and a base and by ultrasonication. Microemulsions are formed spontaneously upon TEMPO mixing of oil in water with a very high concentration of surfactant. In emulsions, the initiation can occur in the aqueous phase and leads to the rapid formation of oligomers reaching a critical length for exclusion from the aqueous phase, in combination with appropriate concentrations of nitroxide in both aqueous and organic phases [42].

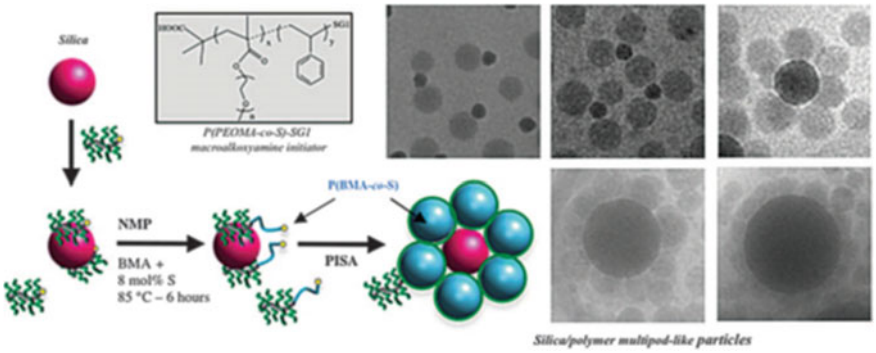

Fig. 7.3 Strategy for the synthesis of hybrid polymer latex/silica particle supracolloidal assemblies and typical examples of obtained morphologies [44]. Reprinted from [44], Copyright 2012 American Chemical Society

Ab initio emulsion polymerizations, in which monomer droplets are present during polymerization, droplet polymerization can be responsible for the formation of large (>1 μm) particles that can lead to coagulum formation. Coagulum-free latexes can be produced using a TEMPO-mediated ab initio emulsion polymerization by suppressing droplet polymerization [42].

Overall strategy for the synthesis of hybrid polymer latex/silica particle supracolloidal assemblies is schematically illustrated in Fig. 7.3 [43].

Dispersion polymerization operated in an organic solvent and yielded large particles (200 nm to 10 μm) was accomplished in the presence of a stabilizer [45]. Diblock copolymers consisting of a poly(acrylic acid) (PAA) segment and a LCST-type poly(*N*,*N*-diethylacrylamide) (PDEAAm) block were obtained by nitroxide-mediated polymerization in aqueous dispersion using a water-soluble macroalkoxyamine. Polymeric nanoparticles, prepared via atom transfer radical polymerization (ATRP BEFOR) and reversible addition–fragmentation chain transfer (RAFT BEFOR), have gained importance as carrier systems for drugs [46, 47]. About 70 imaging scaffolds, micellar systems as nanostructures for biomedical applications, and as component in polymer mixtures to change the rheology of materials were prepared [46]. Polymeric nanoparticles for biomedical delivery applications were also designed in work [47]. The synthesis of micelles from diblock copolymers consisting of a poly(acrylic acid) (PAA) segment and an LCST-type poly(*N*,*N*-diethylacrylamide) (PDEAAm) block, utilized the water soluble of the SG1-capped poly(sodium acrylate) macroalkoxyamine, was performed by nitroxide-mediated aqueous dispersion polymerization. The polymer characterization, physical core cross-linking of pH- and thermoresponsive dynamic diblock copolymer micelles, and proposed mechanism for *PAA-SG1*-initiated DEAAm dispersion polymerization were reported [45].

The generation of block copolymers micelles from biohybrid polymers of poly(n-butyl acrylate) (PnBA) and polystyrene using a TIPNO and SG1-based bifunctional initiator in combination with a controlled polypeptide synthetic technique,

such as N-carboxyanhydride (NCA) ring-opening polymerization was achieved [48]. The peptide block, poly(L-glutamate) was used as the hydrophilic component and the formed vesicles and micelles for the transportation of thermolysin and elastase. Gemcitabine, a hydrophilic anticancer drug, was linked to an SG1-based alkoxyamine and served as an initiator for the NMP of isoprene which led to stable nanoparticles of 130–160 nm in diameter with narrow particle size distribution and great colloidal stability [49]. A perfluorinated SG1-capped macroalkoxyamine at 90% conversion was synthesized in supercritical carbon dioxide ($scCO_2$) by MAMA-initiated homogeneous polymerization of heptadecafluorodecyl acrylate and used to initiate the polymerization and simultaneously stabilize the particles. Polymerization of styrene at 110 °C in the presence of a large excess of nitroxide was carried out [51]. TIPNO (2,2,5-trimethyl-4-phenyl-3-azahexane-3-nitroxide)-alkoxyamine was used for nitroxide-mediated precipitation polymerizations of styrene in supercritical carbon dioxide ($scCO_2$) [52]. Under the same conditions, the analogous SG1 (N-tert-butyl-N-(1-diethylphosphono-2,2-dimethylpropyl)nitroxide)-alkoxyamine gave higher rates of polymerization and inferior controlled/living character. All polymerizations proceeded at a similar rate and level of control to the TIPNO system in solution toluene. Suspension polymerization was proved as a route to the synthesis of poly(methacrylic) resins with controlled molecular weight and complex macromolecular architectures [53]. Using 3-(((2-cyanopropan-2-yl)oxy)(cyclohexyl)amino)-2,2-dimethyl-3-phenylpropanenitrile, the synthesis of methacrylic homopolymers by nitroxide-mediated suspension polymerization was carried out. Both methyl methacrylate and *n*-butyl methacrylate were successfully polymerized and showed the narrow molecular weight up to 100,000 g/mol. Dialkoxyamine bearing two carboxylic acid groups was synthesized and used as an initiator for the bulk polymerizations of *n*-butyl acrylate and styrene [54]. Very stable latexes were obtained with small particles and narrow particle size distributions employing the sodium salt counterpart as a water-soluble initiator in the emulsion polymerizations of n-butyl acrylate and styrene via a multistep process. As a result, well-defined poly(n-butyl acrylate) and polystyrene-b-poly(n-butyl acrylate)-b-polystyrene triblock copolymer were synthesized.

In review [55], progress by 2012 in living radical polymerization (LRP) dispersions was presented with a discussion of outstanding issues and challenges as well as the outlook for adoption of LRP dispersions by industry. It was stressed that conducting LRP within nanoparticles enables faster reaction times and will provide better control over the polymer livingness; it also has the potential in the control of the particle mesostructure and microstructure.

Statistical NMP copolymerizations of α-gamma butyrolactone methacrylate, 3-hydroxy-1-adamantyl methacrylate, and 2-methyl 2-adamantyl methacrylate with 5–10 mol% of controlling comonomers (i.e., styrene, p-acetoxystyrene, 2-vinyl naphthalene, acrylonitrile, and pentafluorostyrene) were accomplished [56]. All of the resulting copolymers have relatively low dispersities and show relatively low absorbance at 193 nm. Reported in [57], emulsifier-free emulsion iodine transfer polymerization of styrene with self-assembly nucleation was comprised with the

following stages: (1) poly(methacrylic acid) (PMAA) was synthesized in dioxane at 40 °C, (2) dioxane solution of PMAA37-I and styrene were added stepwisely under stirring into an aqueous solution(pH ∼ 9), and (3) emulsion was initiated by adding 4,4′-azobis(4-cyanopentanoic acid) at 60 °C. Stable polystyrene emulsion was obtained without coagulation.

The first nitroxide-mediated synthesis of multipod-like silica/polymer latexes by polymerization-induced self-assembly of amphiphilic block copolymers in aqueous emulsion was reported [58]. A water-soluble brush-type PEO-based macroalkoxyamine initiator composed of poly(ethylene oxide) methacrylate and a small amount of styrene was synthesized and adsorbed on the surface of silica particles through hydrogen-bonding interactions and employed to initiate the emulsion polymerization of *n*-butyl methacrylate with a small amount of styrene under mild conditions (85 °C).

7.5 NMP in Creation of Complex Macromolecular Architectures

Data on controlled radical polymerization (CRP) of inimers or transmers (compounds chain transfer group and vinyl group in one molecule) for the synthesis of hyperbranched polymers were published [59–63]. Inimers and transmers carry numerous functional groups could be homopolymerized, or copolymerized with monovinyl monomers, using nitroxide-mediated polymerization producing hyperbranched polymers and hyperstar polymers with tunable molecular weights, compositions, and degree of branching. CRP-produced hyperbranched can be applied for encapsulation of guest molecules, nanomedicine, diagnostic imaging, and catalysis.

A typical example of production of CRP-produced hyperbranched dendric polystyrene polymers is the first bulk chain transfer polymerization of styrene with 4-vinylbenzyl dithiobenzoate [60]. Starting from diblock copolymer [poly(vinyl acetate)-b-poly(acetonitrile)] that was endcapped by a labile cobalt complex, general structures of transmers to produce hyperbranched polymers were obtained. One way to construct complex macromolecular architectures was based on employing functional nitrones, for example, (α-4-(3-(trimethylsilyl)prop-2-ynyloxy)-*N*-*tert*-butyl nitrone (Fig. 7.4) [59]. This nitron was used to introduce a secondary functionality in the midchain position of a chain, which can be an alkyne for by copper-assisted azide alkyne cycloaddition or an N-hydroxysuccinimide ester for bioconjugation.

Using nitrone spin capturing with PBN derivative, the diblock copolymer [poly(vinyl acetate)-b-poly(acetonitrile)], endcapped by a labile cobalt complex, was obtained from cobalt-mediated radical polymerization (CMRC) [61]. CMRC-derived polymers were efficiently trapped by the nitrone, leading to symmetrical alkyne-functionalized triblock copolymers. By reaction with a homotelechelic poly(ethylene glycol) azide, the synthesis of H-shaped polymers via a combination of CMRP and NMRC followed by CuAAC conjugation was performed. An approach to grow dense

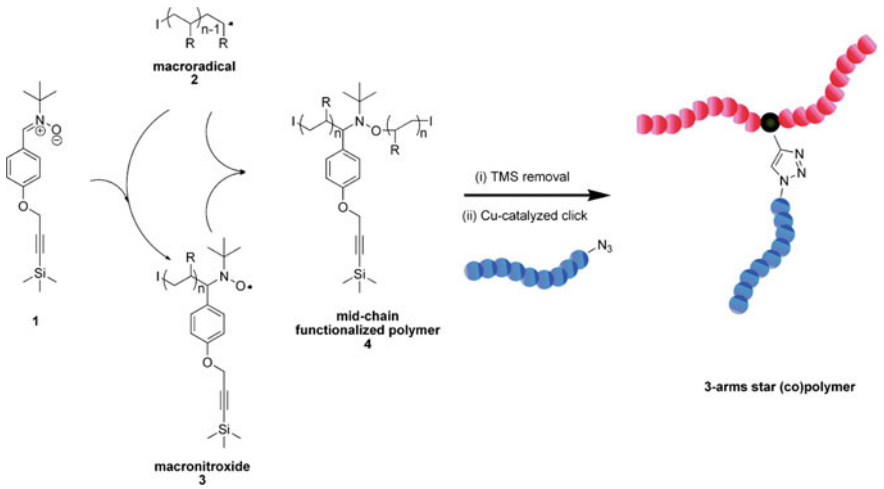

Fig. 7.4 Spin capturing of macroradicals with an alkyne derivative of PBN and the subsequent Cu-catalyzed click reaction form in three-armed star (co)polymers. I denotes the polymer end group resulting from the employed initiator, and R represents the monomer side group (COOR for iBoA or phenyl for styrene) [60]. Reprinted from [60], Copyright 2010 American Chemical Society

polymer brushes via SI-NMP from an ultrathin polymer coating was introduced (Fig. 7.5) [62]. The synthesis of NMP inimer M1 comprised three consecutive synthetic steps was described. A new NMP inimer of ethylbenzene-TEMPO derivative to grow polymer brushes via SI-NMP was designed and employed to afford polymer brushes with controlled molecular weights and low dispersity. Surface-initiated nitroxide-mediated polymerization (SI-NMP) was conducted to grow polystyrene (PS) brushes on the coating with a sacrificial layer designed to cleave the brushes

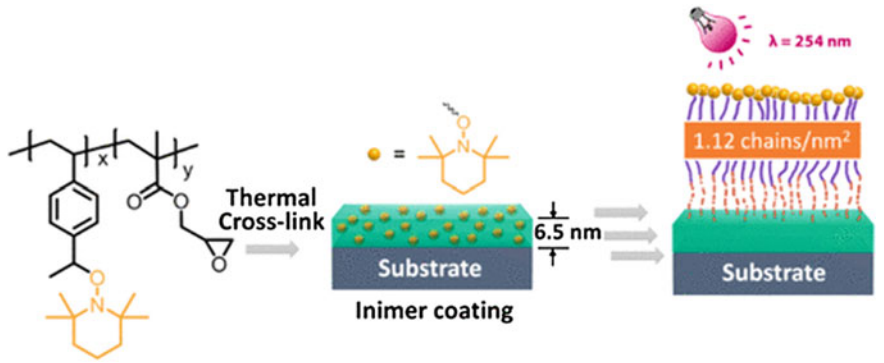

Fig. 7.5 Substrate-independent approach to dense cleavable polymer [63]. Reprinted from [63], Copyright 2018 American Chemical Society

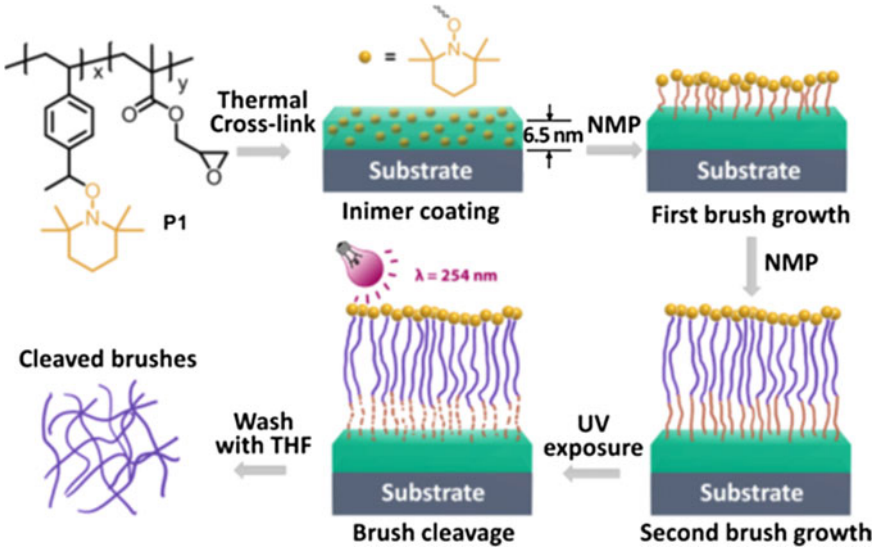

Fig. 7.6 Schematic illustration for the SI-NMP of polystyrene (PS)PS. Surface modification with polymer brushes is an attractive method for tuning of physical and chemical properties of interfaces such as wetting, adhesion, electronic, catalytic, or biological activity [64]. Reprinted from [64], Copyright 2017 American Chemical Society

The brushes are grown on an inimer coating cross-linking and bearing nitroxide-mediated polymerization (inimers and glycidyl methacrylate (Fig. 7.5). The cleaved brushes have larger molecular weights than the corresponding free polymers.

Figure 7.6 shows an overview of the SI-NMP strategy including the following steps to create bilayer polymer brushes: (1) P1 was thermally cross-linked to form an inimer coating which provided high-density NMP initiators on the substrate. (2) Then, a layer was designed to be a sacrificial layer. (3) The second brush layer is released [63].

Therefore, the regiospecificity of graft-polymerized surfaces and precision graft-chain architectures, including their surface graft-chain density, spatio segmental density, segmental or graded block chains, molecular shape or configuration, can be accomplished.

7.6 NMP and Polymer Materials

Over the past two decades, NMP is widely used for designing numerous organic electronic devices, nanoporous membranes, and other technologies [8, 64–73]. The use of NMP can result in homopolymers and copolymers that are characterized by having a narrow molecular weight distribution providing a high quality of produced materials. Chromatography, pharmaceutical purification and filtration, high surface area

catalysis, microelectronics, imprint lithography, and others are fields of application of nanoporous membranes and nanoporous surfaces.

In work [64], a facile reaction method for incorporation of (TEMPO group into poly(2,6-dimethyl-1,4-phenylene oxide) (PPO) chains through the atom transfer radical coupling reaction has been elaborated. The TEMPO-functionalized PPO (PPO-TEMPO) was used as a macroinitiator for NMP of styrene to result in the corresponding PPO-g-PS graft copolymers and to carry out a thermally induced self-crosslinking reaction through radical coupling. The cross-linked PPO enhanced mechanical properties, reduced oxygen permeability coefficient, and provided low dielectric constant and low dissipation factor. Reaction route for incorporation of TEMPO groups to poly(2,6-dimethyl-1,4-phenylene oxide) chains through an atom transfer nitroxide radical coupling reaction was indicated in a scheme. The authors suggested that the obtained materials have high potential for application in dielectric layers of microelectronic. TEMPO was also used to synthesize poly(4-hydroxystyrene) homopolymers possessing preferred absorption characteristics in the UV range (220–260 nm) [66]. Using NMP, well-defined narrowly disperse glycidyl methacrylate (GMA) and pentafluorostyrene (PFS) random copolymers for application in photoresists were synthesized employing NMP. The polymer was proved to be amenable to aqueous base microlithographic fabrication technologies. Poly(styrene)-block-poly(ethylene oxide) [poly(S)-block-poly(EO)] and other block copolymers were demonstrated to be suitable materials for nanoporous membranes and templates, what is the basis for the next generation of photonics including polymer waveguides, materials for lithography, etc. [67]. Role of NMP in polymer templating was reviewed.

Poly(S) nanoporous membrane, coated with terpyridine groups, was prepared [68]. The preparation was carried out by the following stages: (1) the synthesis of functional terpyridine poly(S) homopolymers by NMP and coupling them to other terpyridine functional poly(EO) homopolymers by forming nickel–terpyridine complexes, (2) the resulting block copolymers self-assembled into a thin film with hexagonal morphology and were treated with a competing ligand, and (3) these ligands reacted with the poly(S) blocks resulting in the dissolution of free poly(EO) blocks. A formation of microporous thin films that made self-assembled poly(ethylene oxide)-block-poly(styrene) was schematically illustrated. Obtained materials can be utilized for further heterogeneous surface reactions.

Employing NMP, microporous thin films were made from acid cleaving and washing of a thin film of self-assembled poly(ethylene oxide)-block-poly(styrene) [poly(EO)-block-poly(S) [69]. The used breath figure technique is based on the principle of a solution evaporating in the presence of wet air, which results in the polymers self-assembling around the drying water droplets. A mixture of styrene and a styrenic p-conjugated oligo(fluorene) side chain was polymerized in the presence of fluoromicasilicate layers [70]. A cation exchange between the silicate layers and amine functional TEMPO molecules followed by a polymerization of the styrenic monomers in the presence of this hybrid TEMPO-containing surface was investigated. The obtained polymer exhibits in the solids a blue photoluminescence.

7.7 Nitroxide on Inorganic Templates

For high temperature and electronic applications, block copolymers can be used as a template for the nanofeatured design of inorganic materials, to make silicon oxide hierarchical nanostructures, for example, utilizing self-assembly of silicon-containing block copolymer. On this way, a series of silicon-containing styrenic polymers and block copolymers by narrow molecular weight distribution (Mw/Mno1.2) was synthesized and exposed the final materials to an oxygen plasma [71]. Poly(styrene-ran-acrylonitrile)-block-poly(EO)-block-poly(styrene-ran-acrylonitrile) [poly(S-ran-AN)-block-poly(EO)-block-poly(S-ran-AN)] block copolymers were prepared [72]. It was found that when spin coating the resulting polymers from different solvent mixtures occurred free-standing nanoparticle films were obtained.

Proton exchange membranes or polymer electrolyte membranes (PEMs) allow the transfer of protons while preventing the passage of reactive gases such as hydrogen and oxygen. These materials are an integral part of the modern fuel cell. Star polymers of sodium styrenesulfonate with regulated, molecular weight, arm length, narrow polydispersity, and with variable amounts of SO_3OH groups were prepared in a one-pot TEMPO-controlled polymerization [73]. Poly(sodium styrenesulfonate) was terminated with divinyl benzene, and star polymers were produced via stable-free radical coupling of vinylic terminal groups. The polymers based on arms of 20 and 32 repeat units possessed ~33 and ~41 arms per star, respectively. Micrographs of copolymer membranes: (poly(styrene)-graft-poly(styrene sulfonate) (poly(S)-graft-poly(S)SA) and poly(styrene)-ran-poly(styrene sulfonate) (poly(S)-ran-SSA) were obtained.

Ionic liquids are thermally stable, with negligible vapor pressure. Polymerizing an ionic liquid-containing monomer allows for the combination of the ionic liquid properties with the desirable polymer mechanical properties. These polymers are potential candidates for next generation ion conducting membranes, polymer electrolytes, and other electrochemical applications. NMP has been utilized to incorporate ionic liquid-containing monomers into a copolymer [74]. As an example, using Bloc-Builder-MA as the initiator, the controlled homopolymerization of N-vinylimidazole as well as a styrenic derivative, 1-(4-vinylbenzyl)-imidazole (ionic liquid-containing monomers), was accomplished [75]. A difunctional alkoxyamine NMP initiator based on SG173

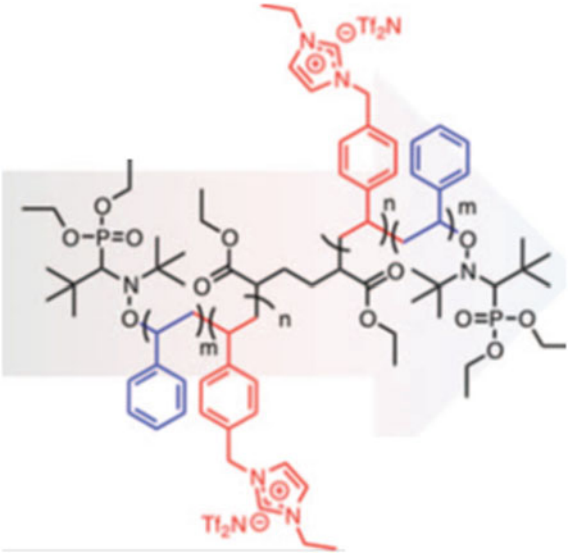

was employed for the synthesis of an imidazole-based ABA triblock copolymer.

7.8 NMP for Organic Electronics and Other Devices

Over the past two decades, significant progress has been made in the performance of relatively more complex organic optoelectronic devices, such as organic light-emitting diodes (OLEDs), thin film transistors (OTFT), and organic photovoltaic (OPV) devices [40, 76–84]. Morphology, photophysical properties, electrochemical behavior and BHJ organic photovoltaic device performance of poly(vTPA)-block-poly(PerAcr), coil–coil block copolymer synthesized by NMP, and poly(vTPA) and poly(PerAcr) homopolymers have been evaluated [76].

Donor–acceptor rod–coil block copolymers–acceptor block copolymers, composed of poly(3-hexylthiophene) homopolymers were synthesized by NMP, utilizing the poly (3-hexylthiophene) macroinitiator to homopolymerize a perylene diimide acrylate [77]. The resulting donor–acceptor block copolymers were characterized by having a narrow molecular weight distribution of 1.2–1.4. Obtained copolymers showed efficient photoluminescence quenching in the solid state, indicative of charge separation, and were employed to produce a solar cell with power conversion efficiency of 0.49%. The viability of three different synthetic pathways to achieve poly[1-(4-vinylbenzyl)-3-butylimidazolium bis(trifluoromethylsulphonyl)-imide-*co*-methyl methacrylate] (poly(VBBI$^+$TFSI$^-$-*co*-MMA)) was explored including direct NMP polymerization of the ionic liquid monomer (VBBI$^+$TFSI$^-$) and post-functionalization of precursor polymer poly(4-vinylbenzyl imidazole-*co*-methyl methacrylate) [78]. A full synthetic, kinetic, and

compositional comparison between methods was described. In the first example of plasmon-assisted NMP of stimuli-responsive block copolymers poly(*N*-isopropylacrylamide)-*co*-4-vinylboronic acid, the growth of a polymer film at room temperature was achieved via plasmon-induced homolysis of alkoxyamines covalently attached to the surface of plasmon-active gold gratings at room temperature [79]. EPR and other assays provided strong support for the plasmon-initiated mechanism of NMP. The resulting polymers are of interest as potential materials for electronics. NMP has also been employed to synthesize well-defined poly(2-(N-carbazolyl)ethyl acrylate) [poly(VAK)] homopolymers, which were subsequently used as effective polymer hosts for blue and blue–green-emitting phosphor-based device [80].

Electrical memory is inherently fast compared to other memory storage devices, such as hard drives, floppy disks, DVDs, or CDs. The memory cell is an electronic circuit that stores one bit of binary information, and it must be set to store a logic 1 (high-voltage level) and reset to store a logic 0 (low-voltage level). Polymer-based memory devices comprising with memory cells can provide fast digital electrical memory. NMP can be used to synthesize polymers for applications in memory devices. An oxadiazole-containing brush polymer, poly-((5-phenyl-1,3,4-oxadiazol-2-yl-[1,10-biphenyl]carboxyloxy-(n-nonyl acrylate) was synthesized using st-TIPNO [81]. The material exhibits volatile or non-volatile memory behavior based on the packing of the oxadiazole molecules within the polymer film, which could be controlled with subsequent annealing steps. Authors of work [82] employed NMP for the synthesis of a series of random copolymers containing pendant electron-donating 9-(4-vinylphenyl)carbazole and electron-accepting 2-phenyl-5-(4-vinylphenyl)-1,3,4-oxadiazole or 2-(4-vinylbiphenyl)-5-(4-phenyl)-1,3,4-oxadiazole with various copolymer ratios. It was found that when building simple anode/polymer/cathode devices, the electrical switching behavior could be tuned through the donor–acceptor ratio. Thus, these copolymers exhibit memory behavior.

Over a decade ago, it was estimated that controlled radical polymerization would be a $20 billion market [83]. Based on the use of the Bloc-Builder alkoxyamine, the range of polymeric products was developed by the chemicals and advanced materials company (ARKEMA). Various all-acrylic poly(methyl methacrylate)-poly(n-butyl acrylate)-b-poly(methyl methacrylate) (MAM), triblock copolymers were produced at industrial scale.

To design higher capacity next generation lithium ion batteries, graphene was grafted with 4-hydroxy-2,2,6,6-tetramethylpiperidin-1-oxyl (4-hydroxy-TEMPO) via conventional esterification of its carboxylic acid groups [40]. When applied as the anode material for lithium ion batteries (LIBs), TEMPO-G exhibited a high reversible capacity with cycling stability for lithium storage in terms of 1080 mA h g^{-1} at a current density of 100 mA g^{-1} after 400 cycles. Thus, the resultant 4-hydroxy-TEMPO-functionalized graphene (TEMPO-G) was revealed to consist of an electrically conducting network of graphene sheets with abundant electrochemically active

nitroxide radical functionalities. The grafting reagents and conditions were described in details, and unwanted dissolution of nitroxide radicals in the electrolyte was also discussed.

7.9 NMP and Materials for Biomedical Applications

Polymer derived from the nitroxide-mediated polymerization, glycopolymers, bioconjugates, nanoparticulate, systems, and polymer nanocomposites have been recognized as biomaterials [22, 85–91]. The main requirement for these materials is compatibility with biological and medical objects. Another avenue to use these polymers is their biologic activity.

In work [86], poly(2-(b-D-galactosyloxy)ethyl methacrylate-costyrene)-β-polystyrene (P(GalEMA-co-S)-b-PS) amphiphilic block copolymers were obtained from SG1-mediated polymerization of glycomonomer G10, using either P(AcGalEMA-co-S)-SG1 or PS-SG1 macroinitiators, followed by deacetylation of AcGalEMA moieties. The polymer was used to prepare honeycomb-structured porous films with bioactivity (Fig. 7.7). A fluorophore was conjugated with the sugar moieties on the porous film, and proteins were conjugated to glycopolymer inside the pore.

The combination of synthetic polymers with polypeptides has paved a way toward innovative materials with unprecedented properties [22, 87–90]. For example, the covalent linkage of poly(ethylene glycol) (PEG), a hydrophilic and flexible polymer, to poly(peptide)-based therapeutics resulted in the synthesis of bioconjugates

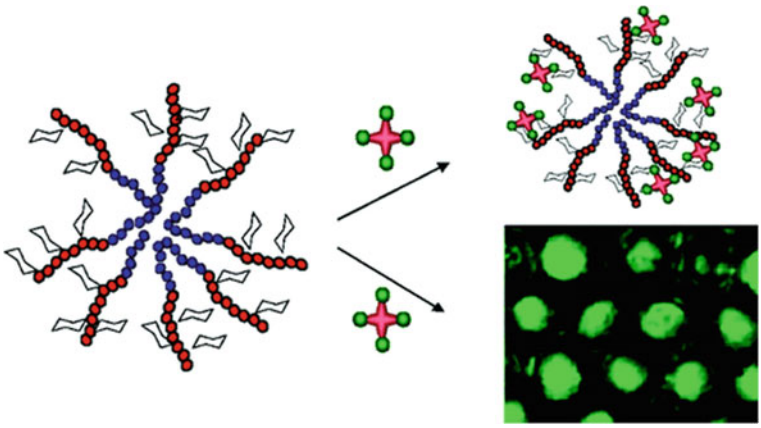

Fig. 7.7 Schematic presentation formation of porous films with a fluorophore conjugated with the sugar moieties on the porous film and proteins conjugated to glycopolymer inside the pore [86]. Reprinted from [86], Copyright 2009 American Chemical Society

exhibited improved biodistribution and pharmacokinetics, high stability and solubility, reduced immunogenicity and longer plasma half-lives due to both reduced renal filtration and proteolysis [87]. An SG1-functionalized peptide (SG1-GGGWIKVAV) was also constructed by solid-phase peptide synthesis SPPS followed by the direct attachment of the Bloc-Builder alkoxyamine to the terminal amine group of the peptide in the presence of PyBOP as the coupling agent [22].

The conjugation of preformed polymer to free peptides and proteins relied on the design of a-functional comb-shaped polymethacrylates with PEG side chains from NMP of OEGMA with a few percent of acrylonitrile initiated by SG1-based alkoxyamines bearing an N-hydroxysuccinimidyl moiety was achieved [88]. The polymers exhibited tunable reactivities toward nucleophiles. Copolymers derived from the SG1-based alkoxyamine can be quantitatively coupled with small molecules and a neuroprotective peptide; whereas, partial conjugation was obtained with lysozyme. α-functional, fluorescent comb-shaped polymethacrylates with PEG side chains for bioconjugation purposes were designed. Reversible switching of the activity in the conjugates was demonstrated. The preparation of block copolymers of PNVP and polypeptides (PNVP-b-PBLG, PNVP-b-PBLL and PNVP-b-PBLG-b-PBLL), with PBLL for poly(tert-butyloxycarbonyl-L-lysine) in a sequential fashion was performed using 4-Amino-TEMPO [89].

Carboxybetaine monomers differing in intercharge separating spacer groups were synthesized, and nitroxide-mediated free radical polymerization was conducted using alkoxyamine initiators with hydrophobic (TEMPO) and hydrophilic (β-phosphonate) terminal groups (Fig. 7.8) [90]. The effect of the charge, hydration, and end groups for corresponding films attached to silica surfaces on absorbed protein conformation was studied with three plasma proteins, lysozyme, bovine a-lactalbumin, and human serum albumin.

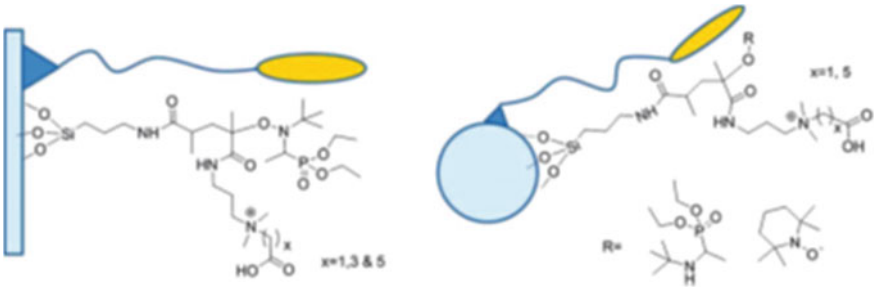

Fig. 7.8 Combination of non-fouling properties with integrated biomimetic cell adhesive end groups on silica surfaces and silica particles SiNP [91]. Reprinted from [91], Copyright 2011 American Chemical Society

7.10 NMP Miscellaneous Applications

Well-defined PMMA-rich P(MMA-*co*-AN) copolymers using the nitroxide-mediated controlled/living free radical polymerization of methyl methacrylate initiated by the SG1-based alkoxyamine Bloc-Builder were prepared [91]. It was found that a minimal amount of acrylonitrile turns the nitroxide-mediated polymerization of methyl methacrylate into the controlled/living system. The polymer structure was characterized by ^{1}H, ^{13}C, and ^{31}P NMR technics. Detrembleur et al. [92] made nitroxide-mediated polymerization of methacrylates at moderate temperature straightforward by preparing and isolating the methyl 2-methyl-3-nitro-2-nitrosopropionate (NMMA). Nitrone (a-phenyl-N-tert-butylnitrone PBN) was involved in the homopolymerization of a variety of methacrylates by an NMP process at moderate temperature (40–50 °C). The combination of a low-temperature azo-initiator with a hindered nitroso-compound produces a mixture of hindered nitroxides in the polymerization medium that act as efficient polymerization control agents. Results of ESR spectroscopy experiments combined with mass spectrometric studies support the proposed in situ NMP mechanism.

Water-soluble nitroxides based on 1,1,3,3-tetramethylisoindolin-2-oxyl and 1,1,3,3-tetraethylisoindolin-2-oxyl with an ionic group on the aromatic ring (either a quaternary ammonium or a sulfonate substituent) and TEMPO were tested as mediators in the controlled free radical polymerization of sodium 4-styrenesulfonate carried out in water at 130 °C [93]. It was found that the steric hindrance at the nitroxide site (ethyl or methyl substituent) had a much larger influence on the activation–deactivation equilibrium than the type of ionic group. For nitroxides bearing four ethyl substituents, the equilibrium constant was one order of magnitude larger than that obtained for nitroxides with four methyl substituents. Controlled radical polymerization (CRP) of inimers or transmers for the synthesis of hyperbranched polymers was summarized in review [94]. Data on nitroxide-mediated polymerization (or reversible addition–fragmentation chain-transfer (RAFT) polymerization techniques, producing hyperbranched polymers and hyperstar polymers with tunable molecular weights, compositions, and degree of branching were also reviewed.

The ability of NMP to reduce the dispersity, to increase chain end homogeneity, to synthesize block copolymers that could self-assemble, to tether the polymers to surfaces, and to incorporate novel functional monomers has been well documented. Aforementioned data showed that the use of NMP was explored in numerous applications, such as organic electronics nanoporous templating, photoresists, and membranes for fuel cells. Thus, nitroxide-mediated polymerization (NMP) is a robust and industrially relevant technique.

References

1. D.H. Solomon, Polymer group and the discovery and significance of nitroxide-mediated living radical polymerization. J. Polym. Part A: Polym. Chem. **43**(23), 5748 (2005)

2. H. Fischer, M. Souaille, The persistent radical effect in living radical polymerization – border cases and side-reactions. Macromol. Symp. **174**, 231–240 (2001)
3. D. Bertin, D. Gigmes, S.R.A. Marque, P. Tordo, Kinetic subtleties of nitroxide mediated polymerization. Chem. Soc. Rev. **40**, 2189 (2011)
4. J. Nicolas, G. Yohann, C. Lefay, D. Bertin, D. Gigmes, B. Charleux, Nitroxide-mediated polymerization. Prog. Polym. Sci. **38**(1), 63–235 (2013)
5. J. Kreutzer, Yu. Yagci, Metal free reversible-deactivation radical polymerizations: advances, challenges, and opportunities. Polymers **10**, 35 (2018)
6. D.F. Grishin, I.D. Grishin, Controlled radical polymerization: prospects for application for industrial synthesis of polymers (review). Russ. J. Appl. Chem. **84**(12), 2021 (2011)
7. E.G. Bagryanskaya, S.R.A. Marque, Kinetic aspects of nitroxide mediated polymerization. RSC Polym. Chem. Ser. **19**(Nitroxide Mediated Polymerization), 45–113 (2016)
8. K. Matyjaszewski, Macromolecular engineering: from rational design through precise macromolecular Matyjaszewski synthesis and processing to targeted macroscopic material properties. Prog. Polym. Sci. **30**, 858–875 (2005)
9. M. Maric, Application of nitroxide mediated polymerization in different monomer. Curr. Org. Chem. **22**, 1264–1284 (2018)
10. W.E. Bachmann, F.Y. Wiselogle, The relative stability of pentaarylethanes. III.[1] The reversible dissociation of pentaarylethanes. J. Org. Chem. **1**, 354 (1936)
11. G. Moad, E. Rizzard, The history of nitroxide-mediated polymerization, in *RSC Polymer Chemistry Series No. 19. Nitroxide Mediated Polymerization: From Fundamentals to Applications in Materials Science*, ed. by D. Gigmes (The Royal Society of Chemistry, 2016), pp. 1–44
12. D. Gigmes (ed.), *RSC Polymer Chemistry Series No. 19. Nitroxide Mediated Polymerization: From Fundamentals to Applications in Materials Science* (The Royal Society of Chemistry, 2016)
13. D.H. Solomon, J. Macromol. Sci. Chem. **17**, 337 (1982)
14. G. Moad, D.H. Solomon, *The Chemistry of Radical Polymerization* (Elsevier, 2006)
15. R.B. Grubbs, Nitroxide-mediated radical polymerization: limitations and versatility. Polym. Rev. **51**, 104 (2011)
16. L. Marx, P. Hemery, Synthesis and evaluation of a new polar, TIPNO type nitroxide for "living" free radical polymerization. Polymer **50**, 2752–2761 (2009)
17. L.W. Jones, R.T. Major, Substituted O-alkyl hydroxylamines chemically related to medicinally valuable amines. J. Am. Chem. Soc. **49**, 1527 (1927)
18. G.A. Kovtun, A.L. Aleksandrov, V.A. Golubev, Interaction of peroxide radicals with esters of hydroxylamines. Bull. Akad. Sci. USSR: Div. Ser. 2115 (1974); Izv. Akad. Nauk SSSR: Ser. Khim. 2197 (1974)
19. E.M. Pliss, I.V. Tikhonov, A.I. Rusakov, Kinetics and mechanism of reactions of aliphatic stable nitroxide radicals in chemical and biological chain processes, in *Nitroxides—Theory, Experiment and Applications*, ed. by A.I. Kokorin (IntechOpen). https://doi.org/10.5772/39115
20. A. Debuigne, M. Hurtgen, C. Detrembleur, C. Jerome, C. Barner-Kowollik, T. Junkers, Spin capturing with nitrones: radical coupling reactions with concurrent introduction of mid-chain functionality. Prog. Polym. Sci. **37**, 1004–1030 (2012)
21. G. Wang, J. Huang, Versatility of radical coupling in construction of topological polymers. Polym. Chem. **5**, 277–308 (2014)
22. J. Nicolas, Y. Guillaneuf, C. Lefay, D. Bertin, D. Gigmes, B. Charleu, Nitroxide-mediated polymerization. Prog. Polym. Sci. **38**, 63–235 (2013)
23. T. Junkers, L. Zang, E. H.H. Wong, N. Dingenouts, C. Barner-Kowollik, Formation of triblock copolymers via a tandem enhanced spin capturing nitroxide-mediated polymerization reaction sequence. J. Polym. Sci. Polym. Chem. **49**(22), 4841–4850 (2011)
24. J.P. Fouassier, J. Lalevée, *Photoinitiators for Polymer Synthesis—Scope, Reactivity, and Efficiency* (Wiley, Weinheim, 2012)
25. Y. Guillaneuf, D.L. Versace, D. Bertin, J. Lalevee, D. Gigmes, J.P. Fouassier, Importance of the position of the chromophore group on the dissociation process of light sensitive alkoxyamines. Macromol. Rapid Commun. **31**, 1909 (2010)

26. Y. Guillaneuf, D. Bertin, D. Gigmes, D.L. Versace, J. Lalevee, J.P. Fouassier, Toward nitroxide-mediated photopolymerization. Macromolecules **43**(5), 2204–2212 (2010)
27. J. Morris, S. Telitel, K.E. Fairfull-Smith, S.E. Bottle, J. Lalevée, J.L. Clément, Y. Guillaneuf, D. Gigmes, Novel polymer synthesis methodologies using combinations of thermally- and photochemically-induced nitroxide mediated polymerization. Polym. Chem. **6**, 754–763 (2015)
28. E. Yoshida, Nitroxide-mediated photo-living radical polymerization of vinyl acetate. Colloids Polym. Sci. **288**, 73 (2010)
29. K.T. Haraldsson, J.B. Hutchison, R.P. Sebra, B.T. Good, K.S. Anseth, C.N. Bowman, 3D polymeric microfluidic device fabrication via contact liquid photolithographic polymerization (CLiPP). Sens. Actuators B **113**, 454 (2006)
30. J. Johnson, G. Moad, D.H. Solomon, T.H. Spurling, D.J. Vearing, The application of supercomputers in modeling chemical reaction kinetics: kinetic simulation of 'quasi-living' radical polymerization. Aust. J. Chem. **43**, 1215 (1990)
31. H. Fischer, The persistent radical effect: a principle for selective radical reactions and living radical polymerizations. Chem. Rev. **101**, 3581 (2001)
32. D. Greszta, K. Matyjaszewski, Mechanism of controlled/"living" radical polymerization of styrene in the presence of nitroxyl radicals, kinetics and simulations. Macromolecules **29**, 7661 (1996)
33. T. Kothe, S. Marque, R. Martschke, M. Popov, H. Fischer, Radical reaction kinetics during homolysis of *N*-alkoxyamines: verification of the persistent radical effect. J. Chem. Soc. Perkin Trans. **2**, 155 (1998)
34. D. Gigmes, S.R.A. Marque, Nitroxide mediated polymerization and its applications, in *Encyclopedia of Radicals in Chemistry, Biology, and Materials*, ed. by C. Chatgilialoglu, A. Studer (Wiley, 2012)
35. M. Edeleva, G. Audran, S. Marque, E. Bagryanskaya, Smart control of nitroxide-mediated polymerization initiators' reactivity by pH, complexation with metals, and chemical transformations. Materials (Basel) **12**(5), 688 (2019)
36. M. Asteasuain, Deterministic approaches for simulation of nitroxide-mediated radical polymerization. Int. J. Poly. Sci. Article ID 7803702, 16 pages (2018). https://doi.org/10.1155/2018/7803702
37. H. Blas, M. Save, C. Boissière, C. Sanchez, B. Charleux, Surface-initiated nitroxide-mediated polymerization from ordered mesoporous silica. Macromolecules **44**, 2577 (2011)
38. R.-V. Ostaci, C. Celle, G. Seytre, E. Beyou, J.-P. Chapel, E. Drockenmull, J. Polym. Sci. Part A: Polym. Chem. **46**, 3367 (2008)
39. J.P. Blinco, B.A. Chalmers, A. Chou, K.E. Fairfull-Smith, S.E. Bottle, Spin-coated carbon. Chem. Sci. **4**, 3411 (2013)
40. Z. Du, W. Ai, L. Xie, W. Huang, Organic radical functionalized graphene as a superior anode material for lithium-ion batteries. J. Mater. Chem. A **2**, 9164 (2014)
41. Y. Guo, P.B. Zetterlund, Synthesis of nanosized (<20 nm) polymer particles by radical polymerization in miniemulsion employing in situ surfactant formation. Macromol. Rapid Commun. **32**, 1669–1675 (2011)
42. R. González-Blanco, E. Saldívar-Guerra, J. Herrera-Ordonez, P.B. Zetterlund, A. Cano-Valdez, TEMPO-mediated emulsion polymerization. Macromol. Symp. **325–326**, 89–95 (2013)
43. X.G. Qiao, P.Y. Dugas, B. Charleux, M. Lansalot, E. Bourgeat-Lami, Synthesis of multipod-like silica/polymer latex particles via nitroxide-mediated polymerization-induced self-assembly of amphiphilic block copolymers. Macromolecules **48**, 545–556 (2015)
44. M.E. Thomson, J.S. Ness, S.C. Schmidt, M.F. Cunningham, Nitroxide mediated polymerization: from fundamentals to applications. Macromolecules **44**, 1460–1470 (2011)
45. G. Delaittre, M. Save, M. Gaborieau, P. Castignolles, J. Rieger, B. Charleux, Synthesis by nitroxide-mediated aqueous dispersion polymerization, characterization, and physical core-crosslinking of pH- and thermoresponsive dynamic diblock copolymer micelles. Polym. Chem. **3**, 1526–1538 (2012)
46. J. Nicolas, S. Mura, D. Brambilla, N. Mackiewicz, P. Couvreur, Design, functionalization strategies and biomedical applications of targeted biodegradable/biocompatible polymer-based nanocarriers for drug delivery. Chem. Soc. Rev. **42**, 1147–1235 (2013)

47. M. Elsabahy, K.L. Wooley, Design of polymeric nanoparticles for biomedical delivery applications. Chem. Soc. Rev. **41**, 2545–2561 (2012)
48. G.J.M. Habraken, M. Peeters, P.D. Thornton, C.E. Koning, A. Heise, Selective enzymatic degradation of self-assembled particles from amphiphilic block copolymers obtained by the combination of *N*-carboxyanhydride and nitroxide-mediated polymerization. Biomacromolecules **12**, 3761–3769 (2011)
49. S. Harrisson, J. Nicolas, A. Maksimenko, D.T. Bui, J. Mougin, P. Couvreur, Nanoparticles with in vivo anticancer activity from polymer prodrug amphiphiles prepared by living radical polymerization. Angew. Chem. Int. Ed. **52**, 1678–1682 (2013)
50. B. Grignard, T. Phan, D. Bertin, D. Gigmes, C. Jerome, C. Detrembleur, Dispersion nitroxide mediated polymerization of methyl methacrylate in supercritical carbon dioxide using *in situ* formed stabilizers. Polym. Chem. **1**, 837–840 (2010)
51. R. McHale, F. Aldabbagh, P.B. Zetterlun, M. Okubo, Nitroxide SG1-mediated and conventional radical precipitation polymerizations of styrene. Macromol. Chem. Phys. **208**, 1813–1822 (2007)
52. Ch. Magee, A. Earla, J. Petraitis, J. Petraitis, Ch. Higa, R. Braslau, P. Zetterlund, F. Aldabbagh, Synthesis of fluorinated alkoxyamines and alkoxyamine-initiated nitroxide-mediated precipitation polymerizations of styrene in supercritical carbon dioxide. Polym. Chem. **5**, 5725 (2014)
53. M. Aguirre, A. Simula, J.R. Leiza, S. van Es, J.M. Asua, Nitroxide mediated suspension polymerization of methacrylic monomers. Chem. Eng. J. **316**, 655–662 (2017)
54. J. Nicolas, B. Charleux, O. Guerret, S. Magnet, Nitroxide-mediated controlled free-radical emulsion polymerization using a difunctional water-soluble alkoxyamine initiator. Toward the control of particle size, particle size distribution, and the synthesis of triblock copolymers. Macromolecules **38**, 9963–9973 (2005)
55. M.J. Monteiro, M.F. Cunningham, Polymer nanoparticles via living radical polymerization in aqueous dispersions: design and applications. Macromolecules **45**(12), 4939–4957 (2012)
56. Z.J. Wang, K. Wylie, M. Marić, Synthesis of narrow molecular weight distribution copolymers for ArF photoresist materials by nitroxide mediated polymerization. Macromol. React. Eng. **11**(3), 1600029 (2017)
57. S. Sueeng, T. Boonchuwong, P. Chaiyasat, M. Okubo, A. Chaiyasat, Preparation of stable poly(methacrylic acid)-b-polystyrene emulsion by emulsifier-free emulsion iodine transfer polymerization (emulsion ITP) with self-assembly nucleation. Polymer **110**, 124–130 (2017)
58. X.G. Qiao, P.-Y. Dugas, B. Charleux, M. Lansalot, E. Bourgeat-Lami, Synthesis of multipod-like silica/polymer latex particles via nitroxide-mediated polymerization-induced self-assembly of amphiphilic block copolymers. Macromolecules **48**, 545–556 (2015)
59. E.H.H. Wong, M.H. Stenzel, T. Junkers, C. Barner-Kowollik, Spin capturing with "clickable" nitrones: generation of miktoarmed star polymers. Macromolecules **43**, 3785–3793 (2010)
60. A.J. Heidenreich, J.E. Puskas, Synthesis of arborescent (dendritic) polystyrenes via controlled inimer-type reversible addition-fragmentation chain transfer polymerization. J. Polym. Sci. A **46**, 7621–7627 (2008)
61. C. Detrembleur, A. Debuigne, O. Altintas, M. Conradi, E.H.H. Wong, C. Jerome, C. Barner-Kowollik, T. Junkers, Synthesis of star and H-shape polymers via a combination of cobalt-mediated radical polymerization and nitrone-mediated radical coupling reactions. Polym. Chem. **3**, 135–147 (2012)
62. W. Wei, A. Balamurugan, J.H. Dwyer, P. Gopalan, Substrate-independent approach to dense cleavable polymer brushes. ACS Macro Lett. **7**(1), 100–104 (2018)
63. W.-L. Chen, R. Cordero, H. Tran, C.K. Ober, 50th anniversary perspective: polymer brushes: novel surfaces for future materials. Macromolecules **50**, 4089–4113 (2017)
64. C.-Y. Lin, C.-H. Huang, C.-C. Hu, Y.-L. Liu, Self-crosslinkable nitroxide-functionalized poly(2,6-dimethyl-1,4-phenylene oxide) through atom transfer radical coupling reaction. Polymer **154–161**, 135 (2018)
65. G.G. Barclay, C.J. Hawker, H. Ito, A. Orellana, P.R.L. Malenfant, R.F. Sinta, Macromolecules **31**, 1024–1031 (1998)

66. Z.J. Wang, M. Maric, Nitroxide mediated synthesis of low dispersity random copolymers for low-loss optical waveguides. J. Polym. Sci. Polym. Chem. **51**, 2970–2978 (2013)
67. C.G. Gamys, J.-M. Schumers, C. Mugemana, C.-A. Fustin, J.-F. Gohy, Pore-functionalized nanoporous materials derived from block copolymers. Macromol. Rapid Commun. **34**, 962–982 (2013)
68. C. Mugemana, J.-F. Gohy, C.-A. Fustin, Functionalized nanoporous thin films from metallo-supramolecular diblock copolymers. Langmuir **28**, 3018–3023 (2012)
69. K. Satoh, J.E. Poelma, L.M. Campos, B. Stahl, C.J. Hawker, A facile synthesis of clickable and acid-cleavable PEO for acid-degradable block copolymers. Polym. Chem. **3**, 1890 (2012)
70. G. Leone, U. Giovanella, F. Bertini, S. Hoseinkhani, W. Porzio, G. Ricci, C. Botta, F. Galeotti, Hierarchically structured, blue-emitting polymer hybrids through surface-initiated nitroxide-mediated polymerization and water templated assembly. J. Mater. Chem. C **1**, 6585–659 (2013)
71. K.-I. Fukukawa, L. Zhu, P. Gopalan, M. Ueda, S. Yang, Synthesis and characterization of silicon-containing block copolymers from nitroxide-mediated living free radical polymerization. Macromolecules **38**, 263–270 (2005)
72. D. Quemener, G. Bonniol, T.N.T. Phan, D. Gigmes, D. Bertin, A. Deratani, Free-standing nanomaterials from block copolymer self-assembly. Macromolecules **43**, 5060–5065 (2010)
73. J. Ding, S. Holdcroft, Polymers of sodium styrenesulfonate prepared by one-pot TEMPO-controlled. J. Chem. **65**, 1117–1123 (2012)
74. B.H. Lessard, Novel materials: from nanoporous materials to micro-electronics. Polym. Chem. Ser. **19**(Nitroxide Mediated Polymerization), 441–493 (2016)
75. M.D. Green, D. Wang, S.T. Hemp, J.-H. Choi, K.I. Winey, J.R. Heflin, T.E. Long, Synthesis of imidazolium ABA triblock copolymers for electromechanical transducers. Polymer **53**, 3677–3686 (2012)
76. S.M. Lindner, S. Huttner, A. Chiche, M. Thelakkat, G. Krausch, Charge separation at self-assembled nanostructured bulk interface in block copolymers. Angew. Chem. Int. Ed. **45**, 3364–3368 (2006)
77. Q. Zhang, A. Cirpan, T.P. Russell, T. Emrick, Donor–acceptor poly(thiophene-block-perylene diimide) copolymers: synthesis and solar cell fabrication. Macromolecules **42**, 1079–1082 (2009)
78. A.J. Peltekoff, I. Therrien, B.H. Lessard, Nitroxide mediated polymerization of 1-(4-vinylbenzyl)-3-butylimidazolium ionic liquid containing homopolymers and methyl methacrylate copolymers. Can. J. Chem. Eng. **97**(1), 5–16 (2019)
79. O. Guselnikova, S.R.A. Marque, E.V. Tretyakov, D. Mares, V. Jerabek, G. Audran, J.-P. Joly, M. Trusova, V. Svorcik, O. Lyutakov, P. Postnikov, Unprecedented plasmon-induced nitroxide-mediated polymerization (PI-NMP): a method for preparation of functional surfaces. J. Mater. Chem. A **7**, 12414–12419 (2019)
80. X. Savelyeva, B. Lessard, Amphiphilic poly(4-acryloylmorpholine)/poly[2-(N-carbazolyl)ethyl acrylate] random and block copolymers synthesized by NMP. Macromol. React. Eng. **6**, 200–212 (2012)
81. W. Kwon, B. Ahn, D.M. Kim, Y.-G. Ko, S.G. Hahm, Y. Kim, H. Kim, M. Ree, Morphology-dependent electrical memory characteristics of a well-defined brush polymer bearing oxadiazole-based mesogens. J. Phys. Chem. C **115**, 19355–19363 (2011)
82. Y.-K. Fang, C.-L. Liu, G.-Y. Yang, P.-C. Chen, W.-C. Chen, New donor–Acceptor random copolymers with pendent triphenylamine and 1,3,4-oxadiazole for high-performance memory device applications. Macromolecules **44**, 2604–2612 (2011)
83. Gerard, L. Couvreur, S. Magnet, J. Ness, S. Schmidt, in *Controlled/Living Radical Polymerization: Progress in Raft, DT, NMP & OMRP*, vol. 1024, ed. by K. Matyjaszewsik (2009), pp. 361–373
84. C. Auschra, E. Eckstein, R. Knischka, Synthetic glycopolymers: an overview. Eur. Coat. J. **156**, 162–163 (2005)
85. V. Ladmiral, E. Melia, D.M. Haddleton, Synthetic glycopolymers: an overview. Eur. Polym. J. **40**, 431 (2004)

86. S.R.S. Ting, E.-H. Min, P. Escale, M. Save, L. Billon, M.H. Stenzel, Lectin recognizable biomaterials synthesized via nitroxide-mediated polymerization of a methacryloyl galactose monomer. Macromolecules **42**, 9422–9434 (2009)
87. F.M. Veronese, Peptide and protein PEGylation. A review of problems and solutions. Biomaterials **22**, 405–417 (2001)
88. M. Chenal, C. Boursier, Y. Guillaneuf, M. Taverna, P. Couvreur, J. Nicolas, First peptide/protein PEGylation with functional polymers designed by nitroxide-mediated polymerization. Polym. Chem. **2**, 1523–1530 (2011)
89. A. Karatzas, P. Bilalis, H. Iatrou, M. Pitsikalis, N. Hadjichristidis, Synthesis of well-defined functional macromolecular *chimeras* based on poly(ethylene oxide) or poly(N-vinyl pyrrolidone). React. Funct. Polym. **69**, 435–440 (2009)
90. S. Abraham, A. So, L.D. Unsworth, Poly(carboxybetaine methacrylamide)-modified nanoparticles: a model system for studying the effect of chain chemistry on film properties, adsorbed protein conformation, and clot formation kinetics. Biomacromolecules **12**, 3567–3580 (2011)
91. J. Nicolas, S. Brusseau, B. Charleux, A minimal amount of acrylonitrile turns the nitroxide-mediated polymerization of methyl methacrylate into an almost ideal controlled/living system. J. Polym. Sci. Part A: Polym. Chem. **48**, 34–47 (2010)
92. C. Detrembleur, C. Jerome, J. De Winter, P. Gerbaux, J.L. Clement, Y. Guillaneuf, D. Gigmes, Nitroxide mediated polymerization of methacrylates at moderate temperature. Polym. Chem. **5**, 335–340 (2014)
93. W. Huang, B. Charleux, R. Chiarelli, L. Marx, A. Rassat, J.-P. Vairon, Synthesis of water-soluble nitroxides and their use as mediators in aqueous-phase controlled radical polymerization Macromol. Chem. Phys. **203**, 1715 (2002)
94. X. Wang, H. Gao, X. Wang, H. Gao, Recent progress on hyperbranched polymers synthesized via radical-based self-condensing vinyl polymerization. Polymers **9**(6), 188 (2017)

Chapter 8
Nitroxides as Materials

8.1 Introduction

Paramagnetic nitroxides show a fairly robust nature and bidentate character, and therefore, have found various practical applications [1–14]. Metal-free paramagnetic soft materials bearing nitroxides exhibit a unique dynamic, magnetic, and electrical behavior induced by applied magnetic fields at high inhomogeneous intermolecular contacts due to the molecular motion and coherent collective properties of molecules in the soft phases temperatures. Advanced chemistry techniques permit structural modifications in order to fine-tune their physical. The synthesis and development of organometallic-based magnetic materials are of great interest to current research because of their possible technological applications in recording, quantum computing, molecular spintronics, and high-density data storage.

Starting from pioneering work of Gatteschi groups [13], complexes paramagnetic metals with the nitronyl nitroxide-based ligans have received much attention after being successfully implemented as potential building blocks for molecular magnetic materials. The pure organic nitroxide liquid crystals [3–7, 10] have great advantage for directly obtaining microscopic information on dipole–dipole interactions and exchange coupling of paramagnetic centers, p–p interactions, hydrogen bonding, the molecular orientation, relative molecular position, and intermolecular magnetic interactions in the LC phases by the use of electron paramagnetic resonance (EPR) spectroscopy, X-ray diffraction, neutron scattering, and optical techniques. Metal-free paramagnetic soft materials bearing nitroxides exhibit a unique dynamic magnetic and electrical behavior induced by applied magnetic fields at high inhomogeneous intermolecular contacts due to the swift molecular motion and coherent collective properties of molecules in the soft phases temperatures. Advanced chemistry techniques permit structural modifications in order to fine-tune their physical properties.

G. I. Likhtenshtein, *Nitroxides*, Springer Series in Materials Science 292,
https://doi.org/10.1007/978-3-030-34822-9_8

8.2 Nitroxide Bearing Liquid Crystals

4-Nitrophenylnitronyl nitroxide (NPNN) was the **first** pure organic ferromagnet [10]. From the measurements of magnetization of magnetic susceptibility and heat capacity, the γ-phase crystal of 2-(4′-nitrophenyl)-4,4,5,5-tetramethyl-4 5-dihydro-1*H*–imidazol-1-oxy-3-*N*-oxide was shown to become a bulk ferromagnet below about 0.65 K. These organic nitroxide radical crystals lost ferromagnetic behavior above the Curie–Weiss temperature T_c which did not exceeded 1.46 K.

Magneto-electric or magneto-optical properties in the nitroxide liquid crystal **(LC) state** afford the following possibilities [11–14]: (i) formation of magnetic domains in applied magnetic fields, (ii) occurrence of interactions between magnetic dipole and electric dipole moments (magneto-electric effects) in the ferroelectric LC state, (iii) realization of paramagnetic susceptibility anisotropy (Δpara)-controlled molecular orientation by weak magnetic fields, and (iv) providing ferroelectricity. The latter is a characteristic of certain materials that have a spontaneous electric polarization that can be reversed by the application of an external electric field. Liquid crystalline phases combining fluidity and anisotropy are considered to be non-equilibrium dynamic states due to the molecular motion and the coherent collective properties of molecules in the LC state. Accordingly, they are sensitive to external stimuli, such as heat, light, temperature, pressure, electric, or magnetic field, and added chiral dopants, etc.

The various complexes using 3d and rare earth/4f/5f-metal ions such as cobalt(II), nickel(II), manganese(II), copper(II), and so forth and nitronyl nitroxide radicals have been synthesized and extensively studied using inelastic neutron scattering, electron paramagnetic resonance (EPR) spectroscopy, and magnetization measurements [14].

Another area of application of nitroxide as potential materials could be magnetic organic chains containing nitroxide groups. As it was predicted in [15], these polymers may be a basis for a device which acts as effective spin filter and for other spintronic constructions. The organic paramagnetic compounds nitroxides also have a great potential as magnetic resonance imaging (MRI) contrast agents.

Tamura group [11], reported in 2014 the preparation and magnetic properties of the first example of the second generation of paramagnetic all-organic rod-like liquid crystal (LC) compounds. Specifically, the LC contains a chiral cyclic nitroxil (PROXYL) unit in the mesogen core and shows various chiral and achiral phases over a wide temperature range. The molecular orientation of the bulk liquid crystals generated ferroelectric properties induced by weak magnetic fields was confirmed by magnetic susceptibility measurements and EPR spectroscopy.

The next fundamental step in this area was made by the same group in [16] when first observation of an unusual intermolecular magnetic interaction in the liquid crystalline state of an all-organic radical compound at 73 °C on water was demonstrated. The magnetic interaction allows the LC droplet to move freely on water under the influence of an ordinary permanent magnet (Fig. 8.1); whereas, the crystalline phase did not respond to the magnet. Experimental results on the magnetic field dependence of magnetization measured on a SQUID magnetometer, and the temperature

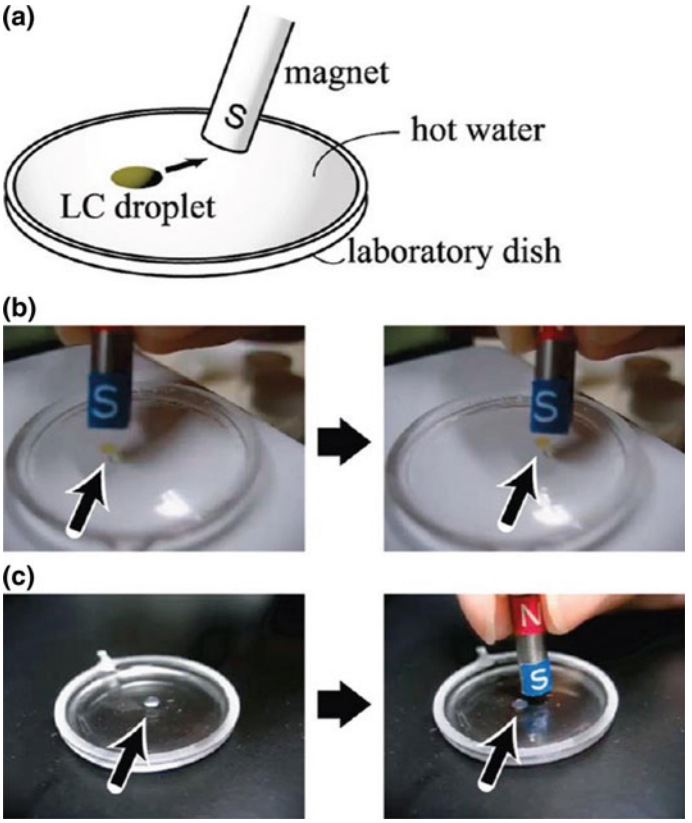

Fig. 8.1 Motion of LC droplets on water under the action of a permanent magnet (maximum 0.5 T). **a** Schematic representation of the experimental setup for observing the attraction by a permanent magnet of a paramagnetic LC droplet on water in a shallow laboratory dish. **b** Photographs showing the attraction of the yellow paramagnetic N droplet of -**1b** on water at 73 °C to the magnet. **c** Photographs showing the repulsion of the white diamagnetic N droplet of ZLI-1132 (Merck) on water at 25 °C from the magnet [16]. Reprinted from [16], Copyright 2012 American Chemical Society

dependence of g-value, and peak-to-peak line width (ΔH_{pp}) obtained by EPR spectroscopy showed the ferromagnetic effect which was discussed in terms of spin–spin dipole and exchange interactions [16].

This material exhibits of spin glass-like inhomogeneous ferromagnetic interactions (average spin–spin-exchange interaction constant $J > 0$) induced by weak magnetic fields in various chiral and achiral LC phases at high temperatures (30–150 1C). The origin of such unique magnetic interactions was referred to as positive 'magneto-LC effects. The synthesized second generation of chiral NR molecules satisfies the following four mandatory requirements having: (1) a nitroxyl group with a large electric dipole moment (ca. 3 Debye) and known principal g-values (g_{xx},

g_{yy}, g_{zz}), (2) high thermal stability, (3) the rigid core of LC molecules, and (4) both enantiomerically enriched and racemic samples.

In work [17], the generation of spin glass-like inhomogeneous magnetic interactions (the average spin–spin interaction constant: $\_J > 0$ or $J < 0$) was referred to as positive or negative magneto-LC effects, respectively. To clarify the relationship between positive or negative magneto-LC effects with spin–spin interaction constant ($J > 0$ or $\_J < 0$, respectively) and magnitude of magneto-LC effects and the types of rod-like LC phase and molecular structure, compounds with a terminal formyl group were synthesized and investigated.

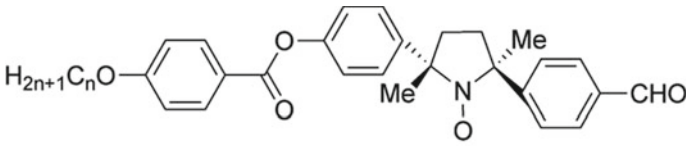

2a (n = 10)
2b (n = 18)

The following measurements were carried out: (i) the temperature dependence of molar magnetic susceptibility (χ_M) measured on a SQUID magnetometer and (ii) the temperature dependence of relative paramagnetic susceptibility (χ_{rel}), g value, and peak-to-peak line width (ΔH_{pp}) of EPR spectra. The origin of observed positive magneto-LC effects ($J > 0$) operating in the SmA* and N* phases was interpreted in terms of the generation of ferromagnetic head-to-tail spin–spin dipole interactions; whereas, antiferromagnetic interactions ($J > 0$) arising from the formation of the RS magnetic dipolar interaction were responsible for the negative magneto-LC effects in the N phase.

To elucidate the relationship between the ferroelectricity which is a characteristic of materials that have a spontaneous electric polarization and positive magneto-LC effects of (2*S*,5*S*)-1 composed of nitroxide, the electric field dependence of EPR spectra of (2*S*,5*S*)-1 confined in a surface-stabilized liquid-crystal cell was measured [18].

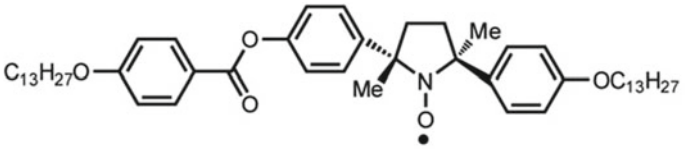

The influence of the electric fields on the positive magneto-LC effects in the FLC phase of nitroxide (2*S*,5*S*)-1 was evaluated by measuring the electric field dependence of *g*-value (*g*), paramagnetic susceptibility (χ_{para}), and the peak-to-peak line width (ΔH_{pp}) of the EPR spectra. By the application of electric field between +25 and −25 V, two magnetic bistable states resulted from the anisotropy in

spin–spin dipole interactions were observed. Spin–spin dipole interactions between localized spins in the FLC phase were illustrated in a scheme.

To investigate the effects of the gelator on the positive magneto-LC effects observed in the nematic phase of (±)-**1** and the molecular alignment of (±)-**1** in the resulting nematic gels, liquid crystalline physical gels which consist of a chiral racemic nitroxide radical compound (±)-**1** indicating a nematic phase and a diamagnetic, chiral organic gelator (*R*,*R*)-**2** were prepared [4]. Experiments showed that (1) the increasing amount of the gelator decreased the domain size, (2) the molecular reorientation by a magnetic field (0.34 T) was considerably restricted in the nematic gel phase, and (3) the intermolecular magnetic interactions (positive magneto-LC effects) increased in the fine and random nematic polydomain structure formed by self-assembled fibers of organic gelator molecules.

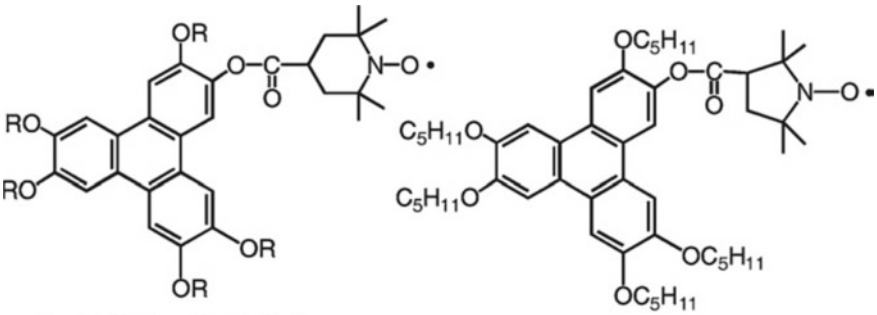

The magneto-responsive discotics formed by covalently linking triphenylene with TEMPO or PROXYL molecular radicals have been evaluated for the first time [19]. The phase transition behavior of the discotics was determined with the help of a polarizing optical microscope (POM), differential scanning calorimeter (DSC), and X-ray diffraction (XRD). The measurements in the fluid columnar, frozen columnar, and solid states using a SQUID susceptometer in the temperature range 2–300 K revealed the antiferromagnetic intermolecular interactions of Curie–Weiss behavior.

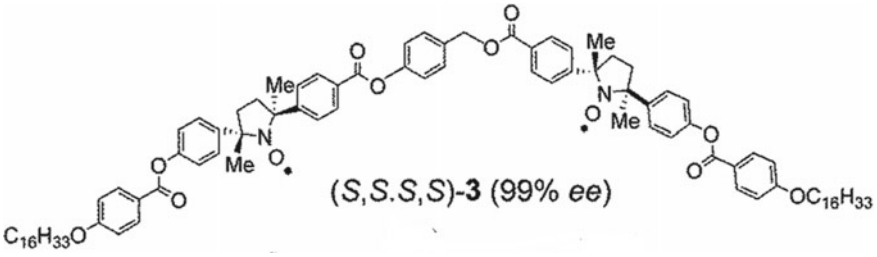

The preparation of liquid crystalline chiral biradical nitroxide (*S*,*S*,*S*,*S*)-3 as the first all-organic biradical LC compound which showed large magneto-LC effects

in the chiral nematic (N*) phase was performed [20]. The (*S*,*S*,*S*,*S*)-3 properties and phase transition behavior of (*S*,*S*,*S*,*S*)-3 were characterized by EPR spectroscopic analysis, χ_M measurement, differential scanning calorimetry, polarized optical microscopy, and X-ray diffraction analysis. It was suggested that the occurrence of large positive magneto-LC effects originates from increased intermolecular spin–spin exchange and dipole interactions due to inhomogeneous intermolecular short contacts in the biradical N* phase. The biradical (*S*,*S*,*S*,*S*)-3 has shown much larger positive magneto-LC effects in the chiral nematic (N*) phase than the monoradical (*S*,*S*)-1. Scheme illustrated molecular structure of (*S*,*S*,*S*,*S*)-3 and LC superstructure in the N* phase.

The observation of a unique superparamagnetic-like behavior and a large positive magneto-LC effect in the nanocrystalline solid phases and the hexagonal columnar (Colh) and smectic (Sm) LC phases, respectively, of non-π-delocalized nitroxide diradical compounds **1** was reported [21]. The SQUID magnetization measurement revealed that (*R*,*S*)-**1** containing a small amount of racemic diastereomers (*R**,*R**)-**1** possessed an unusual and large temperature-independent magnetic susceptibility ($\chi_{TIM} > 0$) component in the original nanocrystalline solid **1** that was responsible for the observed superparamagnetic-like behavior under low magnetic fields.

The mesonitroxide diradical (*R*,*S*)-**1** was prepared by the condensation of the dicarboxylic acid (*R*,*S*)-**2**, which was derived from the bisnitrone, and two equivalents of 2-[3,4,5-tris(hexadecyloxy)phenyl]ethanamine (**5**) using 4-(4,6-dimethoxy-1,3,5-triazin-2-yl)-4-methylmorpholinium chloride (DMT-MM), and a catalytic amount of *N*-methylmorpholine (NMM) in dichloromethane [21]. The following three new important findings that elucidate the origin of the superparamagnetic-like behavior and positive magneto-LC effect under low magnetic fields were observed: (1) The achiral mesoorganic diradical (*R*,*S*)-1 with an intramolecular spin–spin-exchange interaction at low temperatures showed a unique phase transition behavior. (2) By SQUID magnetization measurement, it was revealed that (*R*,*S*)-1 containing small amount of racemic diastereomers (*R**,*R**)-1 possessed a large temperature-independent magnetic susceptibility ($\chi_{TIM} > 0$) component in the original nanocrystalline solid which was responsible for the observed superparamagnetic-like behavior. (3) Such unique magnetic phenomena were substantially induced by thermal processing for (*R*,*S*)-1 or by adding a small amount of racemic diastereomers (*R**,*R**)-1 to (*R*,*S*)-1 as the impurity. The origin of aforementioned magnetic phenomenon in terms of the formation and enlargement of magnetically inhomogeneous domains in the solids and LC phases was discussed.

The aim of work [22] was to obtain the detailed structural information of magnetic LC phases composed of nitroxide from analysis and the shape and angular dependence of EPR spectra of paramagnetic LC materials.

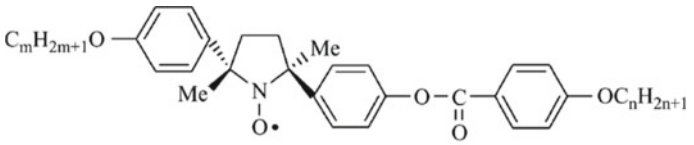

1: m = 7, n = 8 **2**: m = n = 13 **3**: m=n=4

The analysis carried out using the density functional theory calculations of spin density distribution in the interacting molecules based on the crystal structure (Fig. 8.2) and allowed to reveal the origin of the positive magneto-LC effects. The obtained structural data indicated that spin polarization interactions between neighboring molecules rather than the direct through space interactions between paramagnetic centers are responsible for the specific magnetic properties of the studied LC materials. Spin polarization is the degree to which the spin is aligned with a given direction. Figure 8.3 demonstrates the mutual location of LC molecules in layer of SmC phase along C-director neighboring molecules in two orthogonal planes.

The factors that control the orientation of guest molecules in anisotropic LC media such as the nematic 4-*n*-pentyl-4′-cyanobiphenyl (5CB) and smectic 4-*n*-octyl-4′-cyanobiphenyl (8CB) liquid crystals were evaluated [23]. For this purpose, TEMPOL and novel nitroxide spin radicals with different molecular shapes were applied. The orientation distributions of the radicals in the aligned samples in a frozen state were determined in detail by means of EPR spectroscopy. A numerical simulation of the EPR spectra recorded at 105 K was used for the determination of the anisotropic magnetic parameters. The computation of the molecular geometry

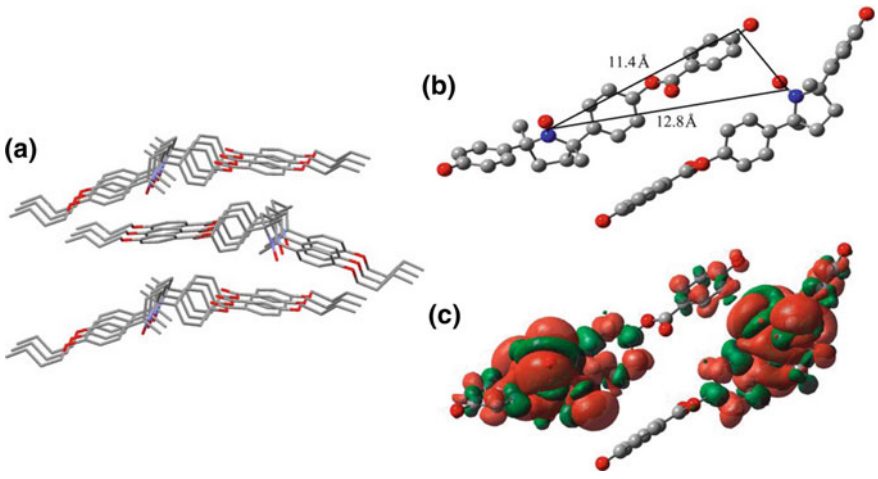

Fig. 8.2 Crystal structure of (*S*,*S*)-3 determined by X-ray crystallographic analysis (**a**), relative position of a pair of molecules in the crystal (**b**), and spin density distribution in the same pair by quantum chemical calculations (**c**). The hydrocarbon chains are omitted for clarity in panels **b** and **c** [22]. Reprinted from [22], Copyright 2014 American Chemical Society

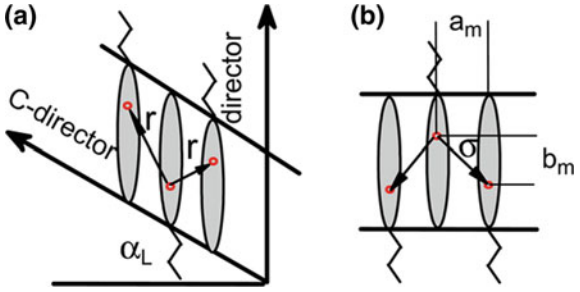

Fig. 8.3 Mutual location of LC molecules in layer of SmC phase along C-director (**a**) and in perpendicular direction (**b**). Circles denote the positions of paramagnetic nitroxide groups [22]. Reprinted from [22], Copyright 2014 American Chemical Society

of the radicals under consideration was performed with help of the ORCA software package and computational model B3LYP/N07D using optimization. Orientation distribution functions of the radicals in aligned liquid crystals were determined by the joint numerical simulation of set of 10–20 EPR spectra recorded at different angles (θ, φ) between the director of the sample and the magnetic field vector. Calculated orientation distribution functions of various radicals are shown in Fig. 8.3.

The rigid fused phenanthrene-based (A5) and 2-azaphenalene (A4) nitroxides as well as the rigid core elongated C11 and 5α-cholestane (CLS) nitroxides were found to be most sensitive to the orientation of the liquid crystal matrixes. The authors concluded that the nitroxide radicals which are the most suitable for characterization of the order of liquid crystals can be the more rigid fused systems with limited degrees of intramolecular motions and with prospects for π-stacking with the LC media (Figs. 8.4 and 8.5).

The synthesis of chiral all-organic NR compounds analogs of showing disordered Colh phases, which have a new type of mesogen core including intermolecular N–O···H–O H-bonds, was performed [3].

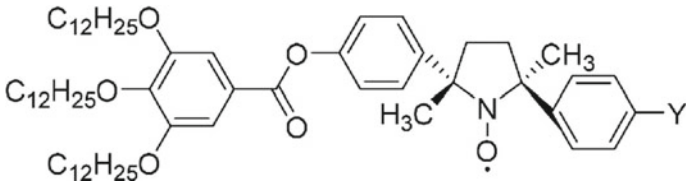

The Colh phases were found to be stable at room temperature for both (±)-1 and (2*R*,5*R*)-1. The LC compounds form hexagonal columnar phases at room temperature, which solidify as LC glasses at low temperature. Data on magnetic susceptibilities suggested that molecular mobility is one of the origins of the magneto-LC effects. The results of SQUID magnetometry and EPR spectroscopy implied that the spin–spin dipolar interactions are one of the origins of the positive magneto-LC effect.

For targeted drug delivery systems visible by magnetic resonance imaging, robust metal-free magnetic nanoemulsions (mean particle size less than 20 nm) consisting of

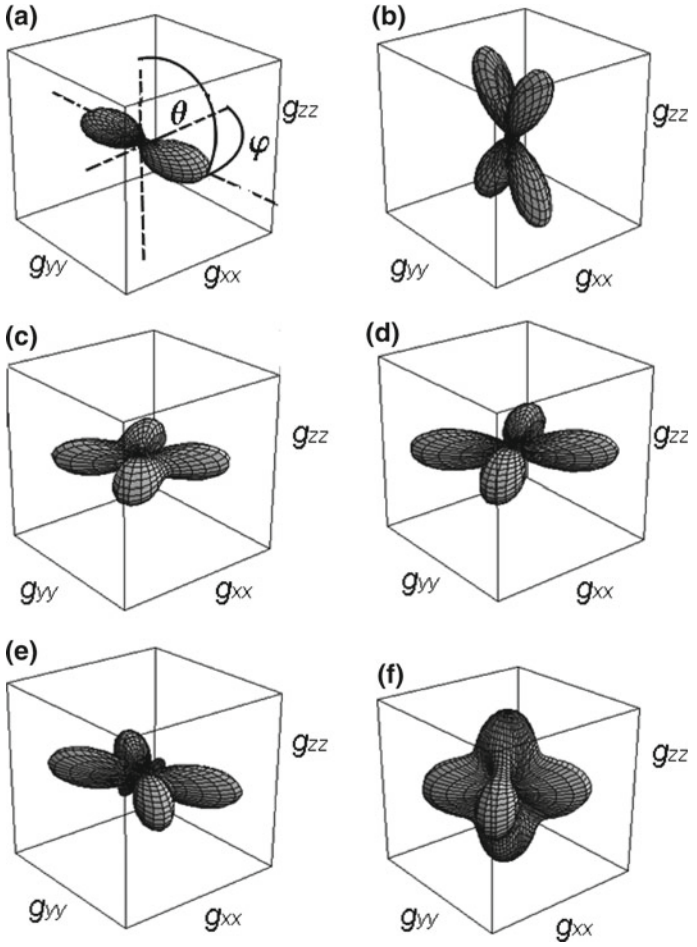

Fig. 8.4 Orientation distribution functions of radicals A4 (**a**) C11 (**b**), A3 (**c**), A6 (**d**), A2 (**e**), and A1 (**f**) in aligned liquid crystal 5CB. The distributions are presented in reference frames of the radicals [23]. Reprinted from [23], Copyright 2014 American Chemical Society

a biocompatible non-ionic surfactant polyethylene glycol hexadecyl and hydrophobic and low molecular weight 2,2,5-trimethyl-5-(4-alkoxy)phenylpyrrolidine-*N*-oxyl radicals were prepared [24]. The structure of the nanoemulsions was characterized by ESR spectroscopy, dynamic scattering, and small-angle neutron-scattering measurements. The obtained nanoemulsions possess: (1) high colloidal stability, (2) low cytotoxicity, (3) reduction resistance to excess ascorbic acid, and (4) sufficient contrast enhancement in the proton longitudinal relaxation time (T_1) in vitro and in vivo. Additional hydrophobic drugs and anticancer drug paclitaxel were incorporated into the nanoemulsions. A preliminary MRI experiment was performed with living mouse

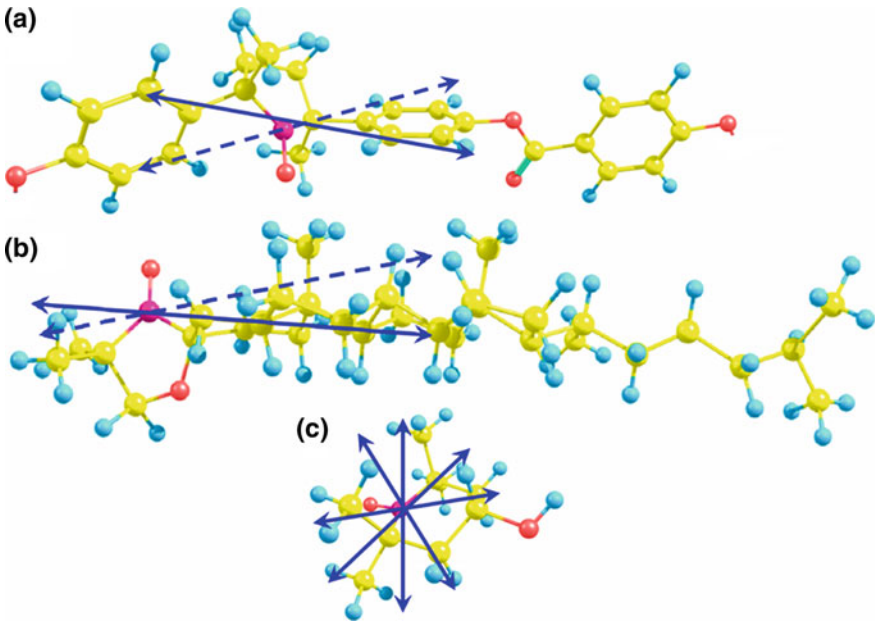

Fig. 8.5 Possible orientation axes for radicals C11 (**a**), CLS (**b**), and TEMPOL (**c**) [23]. Reprinted from [23], Copyright 2014 American Chemical Society

brain tissues. A distinct MRI contrast enhancement with high reproducibility was observed in the pituitary gland after the drugs injection to living mouse brain tissues.

Novel achiral non-p-delocalized nitroxide diradical compounds (*R*,*S*)-1 and racemic diastereomers (*R**,*R**)-1 were prepared, and its magnetic behavior was characterized by EPR, differential scanning calorimetry, polarized optical microscopy, and X-ray diffraction (XRD) and small-angle X-ray scattering analyses [25]. The SQUID magnetization measurement revealed that (*R*,*S*)-1 containing a small amount of racemic diastereomers (*R**,*R**)-1 demonstrated an unusual magnetic property in the original nanocrystalline solid in the nanocrystalline solid phases and the hexagonal columnar Colh LC phase, namely possess a large temperature-independent magnetic susceptibility component ($c_{\mathrm{TIM}} > 0$) in the original solid I before heating. The component is responsible for the observed superparamagnetic-like M-H behavior under low magnetic fields. In addition, the experiment showed a large increase in the molar magnetic susceptibility (cM) (positive magneto-LC effect) at the solid I-to-Colh transition in the first heating run at 0.05 T. The next step of the research was molecular dynamic simulations on the mechanism of a large increase in the magnetic susceptibility in the solid and LC phases. The influence of the coherent collective molecular motion and inhomogeneous intermolecular short contacts on the magnetic susceptibility, together with the in-depth data concerning the spin glass-like properties was taken in consideration. The authors summarized that strong intermolecular

spin–spin dipole as well as exchange interactions should operate in the magnetically inhomogeneous domains formed in the Colh phase to result in the χ_M and χ_{TIM} increase.

8.3 Nitroxide Crystal Structure Materials

Mixtures of new synthesized 2-(4,5,6,7-tetrafluorobenzimidazol-2-yl)-4,4,5,5-tetramethyl-4,5-dihydro-1*H*-imidazole-3-oxide-1-oxyl (F4BImNN) and 2-(benzimidazol-2-yl)-4,4,5,5-tetramethyl-4,5-dihydro-1*H*-imidazole-3-oxide-1-oxyl (BImNN) were crystallized [26]. The following results were reported: (1) Solid solutions (alloys) $(F4BImNN)_x(BImNN)_{(1-x)}$ with $x < 0.8$ gave orthorhombic unit cells, while $x \geq 0.9$ gives monoclinic unit cells. (2) In one-dimensional hydrogen-bonded chains, the dominant intermolecular packing leads to strong ferromagnetic exchange along the chains (J/k = 12–22 K). (3) For the various compositions, interchain exchange was estimated to be 33- to 150-fold weaker. An antiferromagnetic ordered phase formation (Fig. 8.6) Néel temperatures in the 0.4–1.2 K range was evaluated.

An organic biphenyl-4,4′-bis(nitronyl nitroxide) biradical with intermediately strong antiferromagnetic interactions was synthesized as a potential building block for the design of new quantum magnets [27]. In coupled $S = {}^1/_2$ dimer compounds with the antiferromagnetic intradimer coupling constant $J/k_B = -14.0$, short contacts between the oxygen atoms of the nitronyl nitroxide units and the hydrogen atoms of the benzene rings stabilize a planar geometry of the biphenyl spacer. This effect is probably responsible for a small magnetic interdimer coupling. In crystal state, the deviations from the isolated-dimer model are attributed to a small interdimer coupling J'/k_B, in the order of 1 K.

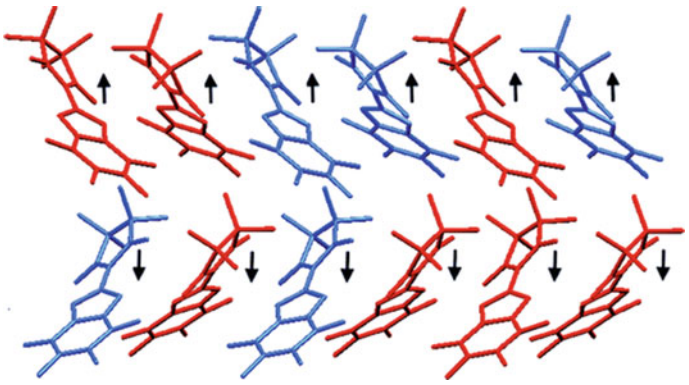

Fig. 8.6 A scheme of suggested an antiferromagnetic ordered phase formation [26]. Reprinted from [26], Copyright 2012 American Chemical Society

The first neutral paramagnetic hexabenzocoronene (HBC) derivative possessing a tert-butyl nitroxide radical moiety was prepared [28] (Fig. 8.7). As was probed by differential scanning calorimetry and ESR spectroscopy, HBC with five alkyl chains exhibits a positive magneto-LC effect in columnar hexagonal liquid crystalline phase. HBC derivative carrying a conjugated tertbutyl nitroxide radical moiety (HBCNO) was found to exist in a helical hexagonal phase at low temperature and a columnar hexagonal phase at higher temperatures. An obtained significant quenching of fluorescence indicated extensive energy or electron transfer on excitation of HBCNO. The electrochemical properties of HBCNO were investigated by cyclic voltammetric

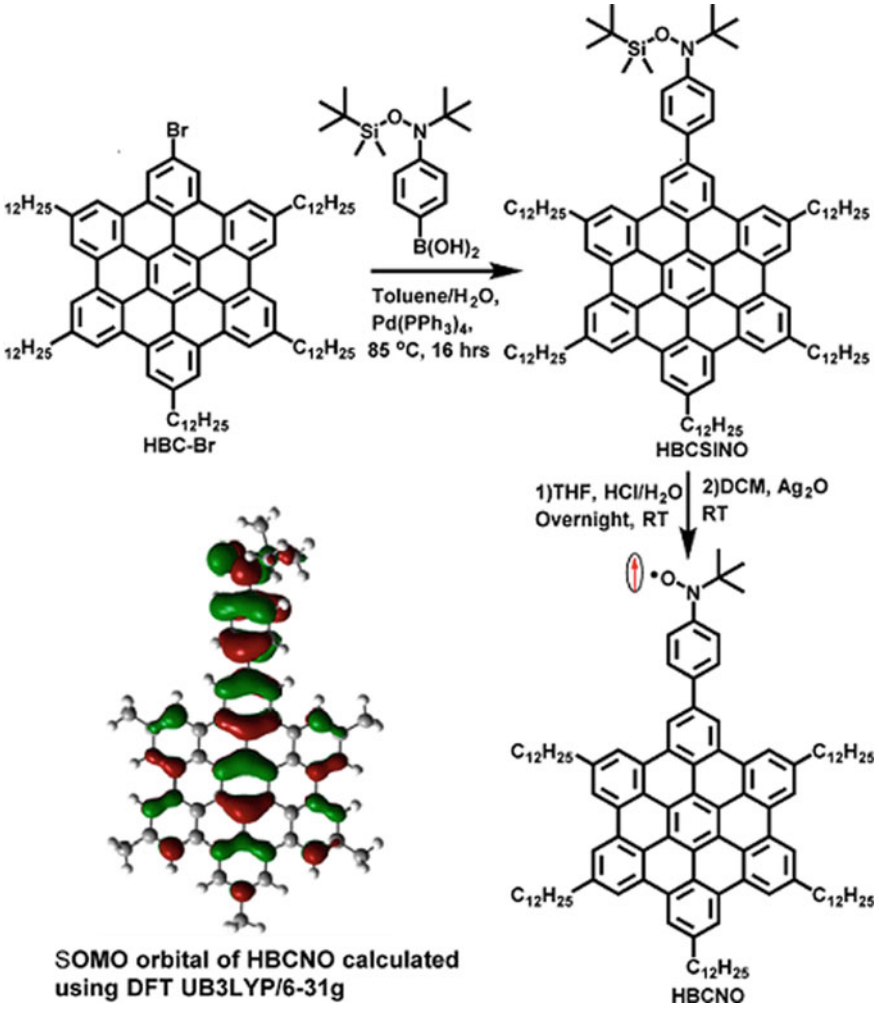

Fig. 8.7 Synthesis of HBCNO from HBC-Br [28]. Reprinted from [28], Copyright 2014 American Chemical Society

(CV) measurements. CV scans of HBCNO displayed a reversible oxidation (0.269 V vs. Fc/Fc^+) and a non-reversible reduction wave. The change in magnetic interaction during phase transition, variable temperature EPR spectra of a powder sample was measured during the cooling process in the temperature range 380 K (Colh phase) to 270 K (Helh phase). Closer π-stacking of disks in the Colh phase can provide stronger intracolumnar magnetic interactions.

The influence of the p-bridges on the intra- and intermolecular exchange interactions in conjugated biradicals was studied [29].

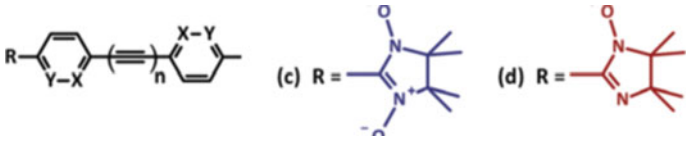

X-ray structural data and performed DFT calculations suggested that the torsion angles have crucial impacts on the overall p-conjugation in the nitroxide biradical systems, which is responsible for the efficient communication between the nitroxide fragments. Magnetic measurements, carried out on single-crystalline samples, showed that for investigated biradicals, weak antiferromagnetic intramolecular interactions are predominant and π-bridged nitroxides possess a moderate intradimer the intramolecular exchange constant J_{intra} in the range −2 to −6 K.

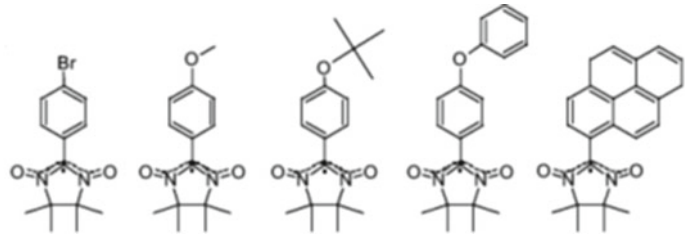

Investigation of the conduction mechanisms of nitronyl nitroxides NIT-R using structural analysis, transport measurements, low-energy, subTHz spectroscopy, and theoretical modeling was carried out [2]. Additional information on the mechanism was obtained in the analysis of data on introducing differently substituted phenyl appendages. Crystal structure of radical NIT-PhOMe, with the cylinders, highlights the presence of overlap between the electronic clouds of aromatic appendages, and the NIT moiety was established. For all substituents NIT-R attached to the NIT-R radical transport parameters, namely minimum mobility μ_{min}, surface thermal carrier density nth, sheet resistance R_S, crossover voltage V_c, Ohmic conductance and fitting exponent (G Ω and η Ω), charge-limited parameters G_{SCL}, η_{SCL}, and low-field mobility μ_0 for the different NIT-R radicals were measured. Below threshold voltage V_c between the Ohmic regime and the nonlinear regime, the generated free carriers inside density of the crystal were dominant with respect to the injected charge carriers. In such condition, the behavior is given by Ohm's law. Obtained findings

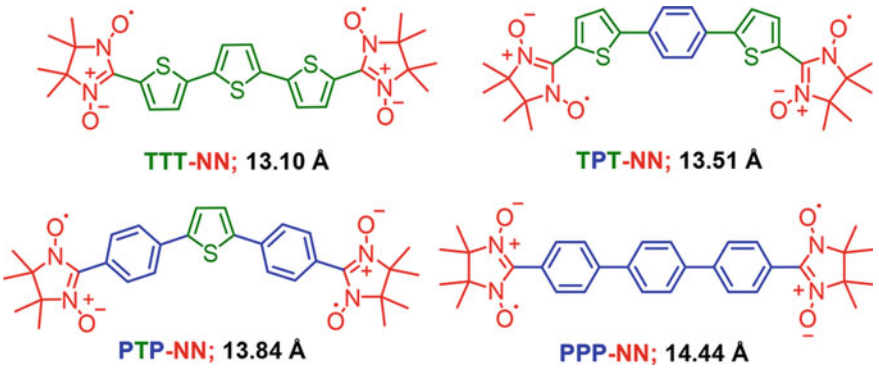

Fig. 8.8 Structures of TTT-NN, TPT-NN, PTP-NN, and PPP-NN; distance between C2–C2 of NN [30]. Reprinted from [30], Copyright 2017 American Chemical Society

show that a non-trivial surface charge-limited regime is present in addition to the standard low-voltage Ohmic conductance. Schematic representation of the different conduction regimes and the different types of traps available for NIT-R systems was presented.

Four nitronyl nitroxide (NN) biradicals (Fig. 8.8) were synthesized, and their structure, molecular packing, magnetic susceptibility, and spin state were investigated using a combined approach involving by X-ray diffraction studies, SQUID measurements, UV–Vis spectroscopy, EPR, and quantum chemical DFT calculations [30].

As it is displayed in Fig. 8.9 in the slipped π-stacked, the π–π distance between two TPT-NNs with the edge-to-edge (between thiophene and thiophene) approach of the molecules is 3.5 Å. The molar magnetic susceptibility (χ_{mol}) of the polycrystalline sample for TTT-NN and TPT-NN recorded using a SQUID magnetometer in the temperature range $K \leq T \leq 300$ K revealed that (1) The intradimer magnetic exchange coupling constant J_{intra} between two $S = 1/2$ spins are $2J/k_B = -6.2$ K for TPT-NN and $J/k_B = -11.9$ K for TTTNN. (2) At room temperature, the magnetic moments are close to the theoretical value 2.45 μB for magnetically uncorrelated spins of biradicals, and for TPT-NN biradical. (3) EPR studies revealed that $\Delta MS = 1$ and $\Delta MS = 2$ transitions at 130 K.

8.4 Nitroxides in Electric Batteries

Recent progress in the chemistry of charge transport by non-conjugated polymers with ultimate density of redox sites has demonstrated that these polymers are promising as electroactive materials for various electronic devices such as rechargeable batteries, hybrid capacitors, solar cells, electrochromic cells, sensors, and memory devices. An organic nitroxide polymers battery being notable for its flexibility, rapid

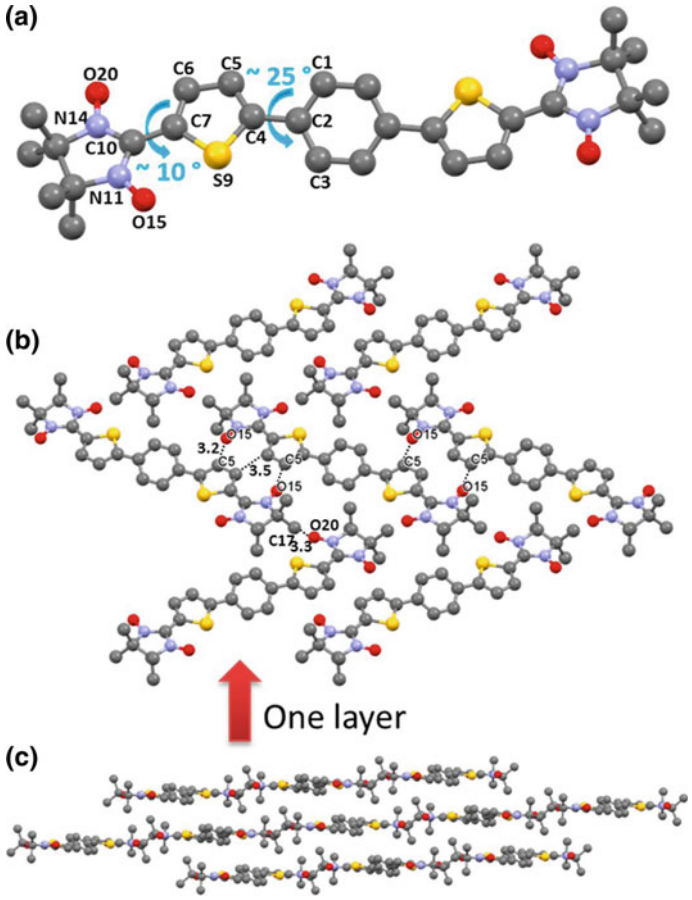

Fig. 8.9 X-ray crystal structure of the TPT-NN, **a** molecule, **b** edge-to-edge packing mode, and **c** face-to-face mode of crystal packing; hydrogen atoms are omitted for clarity [30]. Reprinted from [30], Copyright 2017 American Chemical Society

charging, and small size is candidates for replacing lithium transition metal oxide [2, 31–41]. The p-type reaction of nitroxyl radical polymers is closest to a practical alternative to lithium transition metal oxides [33]. An organic nitroxide radical battery (ORB) was first developed in 2004 [34]. The highlight review describes the performance of organic radical batteries using a nitroxyl radical polymer as the cathode-active material in publications before 2011 [35]. Below are some typical examples in this area.

Employing nitronyl nitroxide pendant, which undergoes both p- and n-type (i.e., negative) charging, potential capability of playing a dual role as cathode- and anode-active material in corresponding batteries was evaluated [35]. As an example, electrode-attached layer of poly(phenylacetylene) bearing a pendant nitronyl nitroxide group per repeating unit, obtained by the Rh-catalyzed polymerization of

2-(4-ethynylphenyl)-4,4,5,5-tetramethylimidazoline-l-oxyl 3-oxide, underwent oxidation and reduction at 0.80 and 0.84 V versus. Ag/AgCl. Galvanostatic coulometry revealed the plateau voltages for both p- and n-type charging. Galvanostatic Coulomb titration confirmed the charge-storage capability of the polymer. This finding supports suggestion that the radical survived during the course of the polymerization to allow both positive and negative charging of the pristine neutral polymer substantially per repeating unit. Electrochemical reversible bipolar charging and discharging processes in **the** dual dopable poly(phenylacetylene) with nitronyl nitroxide pendants were illustrated in a scheme.

Nitroxide polymer brushes with the poly(2,2,6,6-tetramethylpiperidin-4-yl methacrylate) (PTMPM) segment for organic radical batteries were synthesized via surface-initiated atom transfer radical polymerization (SI-ATRP) [36]. The following results were reported: (1) Patterned nitroxide polymer brush thin-film electrodes of the voltammetry and AC impedance and X-ray photoelectron spectroscopy results showed that an increase in the oxidation time could oxidize the PTMPM segment at the bottom of the brush. (2) This results in overoxidation of the brush at the top, which decreases the energy capacity of the polymer brush. (3) The energy capacity of the polymer brush electrode for organic radical batteries was determined to be approximately 94.0 mA h g^{-1} at a discharge rate of 20 C. (4) Its cycle-life performance exhibits 97.3% retention after 100 cycles. (5) Atomic force microscopy results indicated, in this condition, the polymer brush resists dissolution of polymers into electrolytes.

Poly(3-hexylthiophene)/ZnO (P3HT/ZnO) hybrid film was prepared from by in situ hydrolysis of a cross-linked block copolymer poly(3-hexylthiophene)-b-poly(zinc dimethacrylate) (P3HT-b-PZn$(MA)_2$) [37]. The device based on cross-linked P3HT/ZnO hybrid film obtained by in situ hydrolyzing P3HT-b-PZn$(MA)_2$ block copolymer yielded a power conversion efficiency of 0.45% under AM 1.5 G illumination from a calibrated solar simulator with an intensity of 100 mW/cm^2. Current density–voltage characteristics of solar cells under AM 1.5G irradiation with irradiation intensity of 100 mW/cm^2 were also determined. Normalized power conversion efficient of photovoltaic cells based on cross-linked P3HT/ZnO hybrid films obtained by hydrolyzing P3HT-b-PZn(MA)2 block copolymer and non-cross-linked P3HT/ZnO hybrid films obtained by hydrolyzing P3HT-TIPNO/Zn(MA)2 blend film during long-term exposure to air was illustrated in a figure.

Ambipolar redox-active polymers with a reversible charging and discharging capability were synthesized via ring-opening metathesis polymerization of nitronyl nitroxide radical (NN) mono- and disubstituted norbornenes [38]. The NN polymer/carbon composite electrode exhibited both p- and n-type charging/discharging with plateau potentials near the redox potentials of the polymer at 0.78 and −0.80 V versus Ag/AgCl, respectively. The spin-coated layer electrode of the NN polymer immobilized on a current collector demonstrated a fast charging/discharging performance in the range of 10–100 C rates and a cycle stability especially for the p-type reaction.

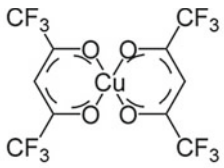

Cu(hfac)$_2$

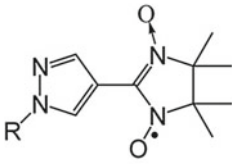

L^R

An affordable, safe, and scalable redox-flow batteries were fabricated [39]. The battery was characterized by using organic polymers as the charge-storage material in combination with dialysis membranes. The membranes separate the anode and the cathode by the retention of the non-metallic, active species, and an aqueous sodium chloride solution as the electrolyte. The water- and polymer-based RFB have an energy density of 10 W hours per liter, current densities of up to 100 milliamperes per square centimeter, and stable long-term cycling capability.

An organic molecule possessing two bipolar redox-active nitronyl nitroxide units connected via a tetraethylene glycol chain was synthesized and used as symmetric redox-flow battery (RFB) soluble in organic solvents [40]. In this battery, NN units are employed as a bipolar redox-active charge-storage material. The battery exhibits the following properties: (1) quasi-reversible redox reactions of the NN^+/NN redox couple at $E_{½} = 0.37$ V and the NN/NN^- redox couple at $E_{½} = -1.25$ V versus $AgNO_3/Ag$, (2) cell voltage of 1.62 V, (3) a stable charge/discharge performance over 75 consecutive cycles with a high-energy efficiency of 82% and an overall energy density of the electrolyte system of 0.67 W h l^{-1}, (4) an overall energy density of the electrolyte system of 4.1 W h l^{-1}, and (5) an energy efficiency of 79%.

A novel approach for the immobilization of polymer poly(2,2,6,6,-tetramethylpiperidinyl-1-oxyl methacrylate (PTMA) on reduced graphene oxide (rGO) via π–π-stacking of pyrene-functionalized PTMA-chains, forming a clayered composite material with well-dispersed PTMA among the carbon layers (Figs. 8.10 and 8.11) was developed [41]. The results in P(TMA-*co*-PyMA) random copolymers with near quantitative amounts of pyrene along the PTMA chain were suitable for greater π–π interaction with graphene oxide (rGO), while the nitroxide radicals on the polymer could simultaneously be used for energy storage. Attaching PTMA to surfaces reduced capacity loss due to dissolution of the organic polymer into the electrolyte. Faradaic reactions and a cooperative effect in the rGO-g-PTMA/rGO electrodes were evaluated.

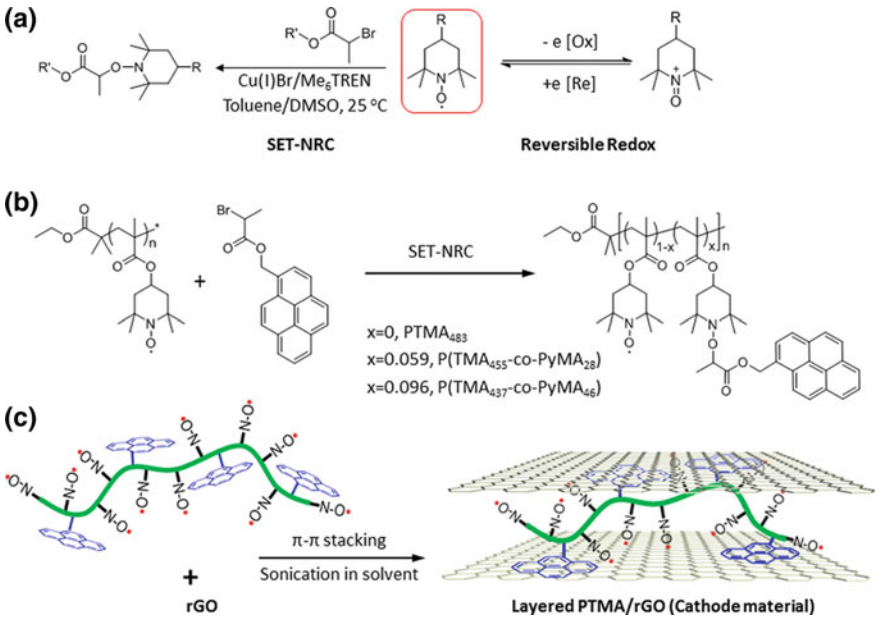

Fig. 8.10 Immobilization strategies of PTMA on rGO preventing restacking of the individual sheets. **a** π–π-Interactions between rGO and pyrenefunctionalized PTMA. **b** Surface-grafted PTMA [41]. Reprinted from [41], Copyright 2017 American Chemical Society

In study [42], ionic liquids (IL) as electrolytes with the view of increasing redox potentials of nitroxide radicals were used. A series of imidazolium, phosphonium, and pyrrolidinium-based ionic liquids (IL) coupled with widely used anions was chosen to predict redox potentials of TEMPO radical using state-of-the-art quantum chemical calculations. Some ILs showed a significant increase in the redox potential of this radical to reach as much as 5.5 eV, compared to the previously measured value of 2.2 eV in aqueous media. In particular, ILs were shown to stabilize the aminoxy anion.

Robust radical-substituted polymers PTGE with effective redox capability were used as surfaces for liquid crystal orientation [43]. The alignment of the smectic liquid crystal electrolytes with low-dimensional ion conduction pathways was reversible and switched in response to the redox states of the polymers enabling both a rapid cell response and long charge retention. PTGE cathode triggers realignment of the self-assembled liquid crystal from planar in the discharged state to homeotropic in the fully charged state (Fig. 8.12).

A novel styrenic nitroxide polymer, poly(5-vinyl-1,1,3,3-tetramethylisoindolin-2-yloxyl) (PVTMIO) was synthesized and employed as an effective organic p-dopable cathode materials [44]. Cyclic voltammetry revealed a high oxidation potential of 3.7 V versus Li. The suitability of PVTMIO for utilization in a high-voltage organic radical battery was confirmed with a discharge capacity of 104.7 mAh g^{-1}, high rate

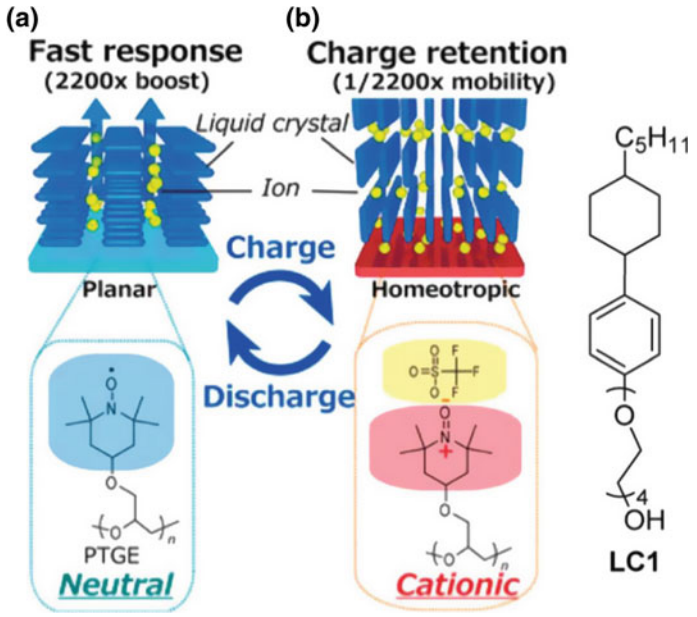

Fig. 8.11 An illustration of the radical "command surface" triggering a redox-responsive switching of the smectic liquid crystal electrolyte [43]. Reprinted from [43], Copyright 2017 American Chemical Society

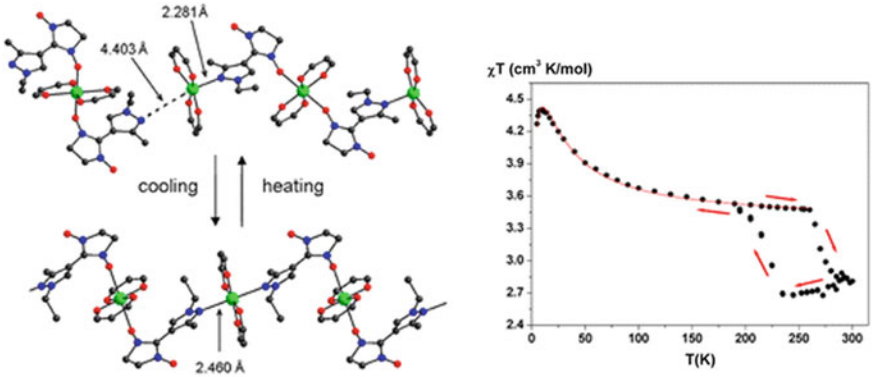

Fig. 8.12 Dependence $\chi T(T)$ for $[[Cu(hfac)_2]_3(\mu\text{-}O,N\text{-}L^a)_2][Cu(hfac)_2(O\text{-}L^a)_2]$ (data points represent experimental values; solid line denote the theoretical curve). The arrows indicate the direction of variation of χT during the cooling and subsequent heating of the sample [46]. Reprinted from [45], Copyright 2012 American Chemical Society

performance, and stability under cycling conditions (90% capacity retention after 100 cycles).

Recent review presented a comprehensive summary of synthetic strategies available for the preparation of nitroxide radical polymer materials for electric batteries [33].

8.5 Nitroxide Single-Crystal Molecular Magnet

Polymer chain complexes $Cu(hfac)_2L^R$ represent a new type of molecular magnets exhibiting thermally induced and light-induced magnetic switching, in many respects similar to a spin crossover [45–53]. In the majority of these compounds, the polymer chain consists of alternating one- and three-spin units composed of copper(II) ions and nitronyl nitroxides. A review [45] highlighted works on the capabilities of EPR in investigating magnetic interactions breathing crystals published before 2017. The "breathing crystals" Cu(hfac)2LR (where hfac is hexafluoroacetylacetonate, and LR is a pyrazolyl-substituted nitroxideligand) represent a new family of switchable molecular magnets based on copper(II) ions bridged by stable nitroxide radicals (Fig. 8.1) [6–14]. In many compounds, crystals also include solvent molecules (Solv) located in the interchain space (Cu(hfac)2LR·0.5Solv).

First example of a reversible single-crystal-to-single-crystal polymerization–depolymerization accompanied by a unique magnetic anomaly was reported by Ovcharenko group [46].

A paired heterospin complex $[[Cu(hfac)_2]_3(\mu\text{-}O,N\text{-La})2][Cu(hfac)_2(O\text{La})_2]$ (Fig. 8.12) was prepared in the reaction of copper(II) hexafluoroacetylacetonate $[Cu(hfac)_2]$ with the stable nitronyl nitroxide 2-(1-ethyl-3-methyl-1H-pyrazol-4-yl)-4,4,5,5-tetramethyl-4,5-dihydro-1H-imidazole-3-oxide-1-oxyl (La). Magnetic measurements were carried out on an SQUID magnetometer in the temperature range of 2–300 K and in a magnetic field of up to 5 kOe. X-ray structural analysis revealed the great shortening of intermolecular distances (from 4.403 Å at 295 K to 2.460 Å at 150 K; $\Delta d = 1.943$ Å) between the terminal Cu atoms of the trinuclear fragments. The crystals of the compound were found to be capable of a reversible single-crystal-to-single-crystal (SC–SC) transformation initiated by the variation of temperature. A reversible topotactic polymerization–depolymerization coordination reaction takes place in the solid during repeated cooling–heating cycles: $[Cu(hfac)_2]3(\mu\text{-}O,N\text{-La})_2][Cu(hfac)2(O\text{-La})_2] \rightleftharpoons Cu(hfac)_2(\mu\text{-}O,N\text{-La})$. The lengthening of distances between the paramagnetic centers on cooling below 225 K resulted in a transition from antiferromagnetic to ferromagnetic exchange. A transition from ferromagnetic exchange to antiferromagnetic exchange occurs during the heating of the heterospin polymer above 270 K (Fig. 8.12), as a result of the shortening of spin–spin distances.

The "breathing crystals" $Cu(hfac)_2LR$ where hfac is hexafluoroacetylacetonate, and LR is a pyrazolyl-substituted nitroxyl ligand also represent a family of switchable molecular magnets based on copper(II) ions bridged by stable nitroxide radicals [47].

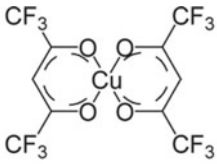

$Cu(hfac)_2$

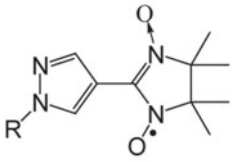

L^R

Diagram of magneto-structural transitions between the weakly coupled (SS) and strongly coupled (WS) states (top) is shown in Fig. 8.13. The energy levels of a spin triad based on spin-Hamiltonian in SS were found to be with $|J| \gg 10\ cm^{-1}$ and $J < 0$, and for WS $|J| \sim 10–20\ cm^{-1}$. A scheme of the energy levels of an exchange-coupled spin triad in SS and WS states was also presented.

Three plausible mechanisms that can cause dynamic mixing processes of mixing of the two doublets $D(S = 1/2)$ and $(S = 1/2)$ and one quartet $Q(S = 3/2)$, namely (1) modulation of exchange interaction, (2) dynamic Jahn–Teller effect, and (3)

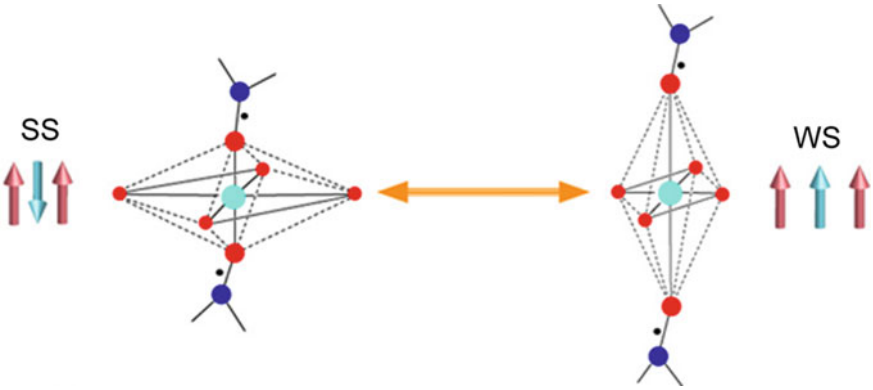

Fig. 8.13 Diagram of magnetostructural transitions between the weakly coupled and strongly coupled states [47]

intercluster exchange couplings between different spin triads were discussed [47]. It was found that for breathing crystals exhibiting abrupt spin transitions, in spin triads the jump-like change of exchange interaction from weak ferromagnetic ($J \sim 1$–$10\,cm^{-1}$) to strong antiferromagnetic ($J \sim -100$ to $-200\,cm^{-1}$) occurs. Experimental data and calculation for the SS state indicated that (1) exchange parameters ($J_{R\text{-}R}$) for the nearest nitronyl nitroxide radicals belonging to different polymer chains, (2) the magnetic chains contain only spin triads (no Cu_2 units) and owe to the nitroxide–nitroxide interchain couplings J_{inter}, (3) the week intercluster exchange interaction between Cu_2 and the spin triad is ~0.1–1.5 cm^{-1}, and (4) breathing crystals exhibits abrupt spin transitions, in spin triads the jump-like change of exchange interaction from weak ferromagnetic ($J \sim 1$–$10\,cm^{-1}$) to strong antiferromagnetic ($J \sim -100$ to $-200\,cm^{-1}$) occurs. The authors stressed on unusual properties of the copper-nitroxide-based molecular magnets in which the magnetic chains can be turned across or along the structural polymer chains by varying the type of nitroxide radicals.

Q-band (EPR) spectroscopy demonstrated that $Cu(hfac)_2L^R$ complexes are one-dimensional in the sense of the topology of their exchange channels, and the magnetic chains spread across the structural polymer chains and consist solely of spin triads of nitroxide–copper(II)–nitroxide [48]. Utilizing four selected examples of complexes $Cu(hfac)_2L^R$, it was found that the exchange coupling values between the spin triads of neighboring polymer chains range from <1 to 10 cm^{-1}. Pair exchange parameters (*JR-R*) for the nearest nitronyl nitroxide radicals belonging to different polymer chains calculated for the SS states of the corresponding breathing crystals using the spin-unrestricted broken-symmetry approach UB3LYP/6-31 were tabulated.

A comparative study of photoluminescence from new synthesized compounds substituted nitroxide derivatives of substituted 2-pyrazolylquinolines indicated that introduction of a nitronyl nitroxide radical group results in the reduction in photoluminescence from the pyrazolylquinoline moiety ($\lambda_{max} = 425$ nm, life time $\tau_1 = 0.055$ ns), and appearing a new red photoluminescence band ($\lambda_{max} = 692$ nm, $\tau_1 = 1.76$ ns) in acetonitrile from the radical fragment [49]. The experiments were performed in acetonitrile with the excitation $\lambda_{max} = 280$.

The first study on the spatial distribution of high- and low-temperature (HT/LT) magneto-structural states (HT/LT) phases of copper(II)–nitroxide-based molecular magnets Cu(hfac)2LR during gradual transitions in these compounds was carried out [50].

To explore the possibility of domain formation at intermediate temperatures, the EPR and X-ray diffraction data were analyzed, and numerical calculations of EPR spectra for different models of exchange-coupled networks were performed. Based on the models of the typical structure of breathing crystals and EPR data, the infinite chain of coupled spin triads by 16- or 32-membered rings was considered, suggesting that each triad has *g*-factor (gSS or gWS) depending on its state. A thorough analysis showed that formation of single-phase domains larger than 4–8 clusters is doubtful.

The synthesis of novel nitroxides, 4-[(3-methoxy-3-oxoprop-1-en-1-yl)oxy]-(1) and 4-[(3-ethoxy-3-oxoprop-1-en-1-yl)oxy]-TEMPO and their application as ligands for assembly of heterospin chain polymers of $[Cu(hfac)2L]_n$ type was reported

[51]. The polymers solid state was characterized by X-ray analysis, FT-IR, UV–Vis, and EPR spectroscopy. The temperature dependences of the effective magnetic moment (χ_{eff}) for heterospin complexes show the χ_{eff} values 2.56–2.67 lB (300 K) for the complexes which corresponded to the spin-only one (2.45 lB) for two non-interacting paramagnetic centers with spins $S = 1/2$ and $g = 2.00$. The χ_{eff} value increases with lowering temperature below 50 K that points to a presence of ferromagnetic exchange interactions, which are typical for Cu(II) complexes with axially coordinated nitroxides.

The electronic absorption spectra of single crystals of three thermoswitchable molecular magnets ($Cu(hfac)_2LMe$, $Cu(hfac)_2LEt$-CP, $Cu(hfac)_2LPr$), and observed thermochromism of the complexes were investigated in the visible and near-IR regions [45]. It was established that the color of the complexes is mainly determined by optical properties of the nitroxide radicals; whereas, the $Cu(hfac)_2$ fragment contributes to the near-IR range with the intensity smaller by an order of magnitude. The following trends in UV–Vis–near-IR spectroscopy of breathing crystals $Cu(hfac)_2LR$ were pointed out: (1) UV/Vis–near-IR spectra are dominated by the absorption bands of nitroxides in both WS (high-temperature) and SS (low-temperature) states. (2) The spectra are changed moderately depending on the magneto-structural state. (3) The nitroxide spectrum shifts to the higher energies upon the transition from the WS to SS state. (4) Three-spin nitroxide–copper(II)–nitroxide clusters manifest a new band centered at ~500 nm in the SS state, tentatively assigned to the charge transfer transition. (5) The d–d transitions of copper(II) are relatively weak in intensity; the band positions and shapes do change upon WS ↔ SS conversion, but cover the same spectral region ~700–2000 nm.

Ferromagnetic coupling in a new bis(3,6-di-tert-butyl-catecholato) manganese complex (Fig. 8.14) was revealed by an approach combined X-ray diffraction, measurement of temperature dependence of effective magnetic moment (μ_{eff}) value in the temperature range of 100–300 K [52]. The following findings were reported:

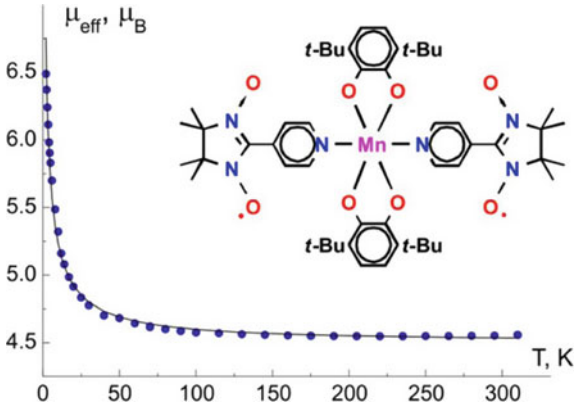

Fig. 8.14 Temperature dependence of for bis(3,6-di-tert-butyl-catecholato)manganese complex [52]. Reprinted from [52], Copyright 2017 American Chemical Society

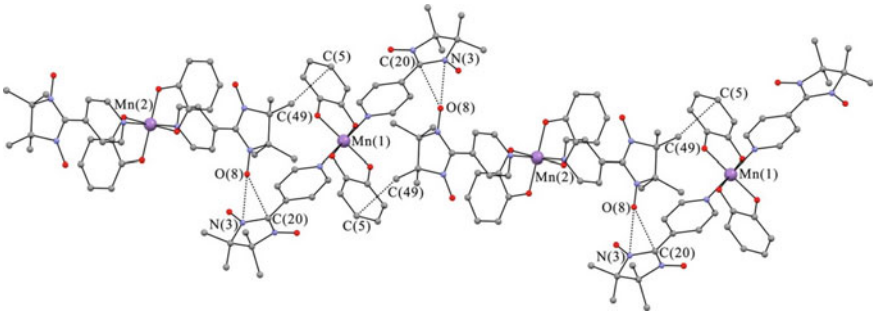

Fig. 8.15 Fragment of crystal packing of 1. The tert-butyl groups and H atoms have been omitted for the sake of clarity [52]. Reprinted from [52], Copyright 2017 American Chemical Society

(1) X-ray diffraction indicated an octahedral environment of the manganese atom with a transarrangement of ligands and the compound specific packing in solid state (Fig. 8.15). (2) Values of the bonds lengths in the inner coordination core of the metal and in the chelate cycles were found to be correspondent to the charge distribution between the metal and ligands displayed a Mn(IV)(Cat_2^{2-}). (3) Intramolecular ferromagnetic coupling between the Mn(IV) $S = 3/2$ spins and spins of nitronyl–nitroxyls and intermolecular ferromagnetic interactions of spins of adjacent nitronyl nitroxide fragments in a chain of molecules at low temperatures were revealed. (4) The μ_{eff} value in the temperature range of 100–300 K is ~4.55 μB that is close to a theoretical spin-only one (4.58 μB) for a NIT-Py ligands and the manganese(IV) ion. (5) In this condition, the Curie constant value is close to the theoretical magnitude of 1.875 K cm^{-3} mol^{-1} for a single paramagnetic center ($S = 3/2$) with ($g = 2.6$) Below 100 K, μ_{eff} increases and reaches 6.5 μB at 2 K, which points to a domination of ferromagnetic exchange interactions between spins of nitroxide ($S = 1/2$) and Mn(IV) ions ($S = 3/2$).

In work [53], a model compound $Cu(hfac)_2$Liso-Pr (Fig. 8.16) residing in the mixed SS/WS state at a room temperature was investigated using femtosecond optical spectroscopy and measurement of the temperature dependence of the effective magnetic moment (μ_{eff}) of the compound. The kinetics of photoswitching was measured in a pump-probe time-resolved experiment by pumping the system at 675 nm and probing with white light. The switching SS to WS occurs within less than 200 fs; whereas, the lifetime of the excited (WS) state is in the order of 100 ps. Suggested energy scheme of photoexcitation, switching, and relaxation processes in $Cu(hfac)_2$Liso-Pr at 300 K showing SS → WS → WS* → WS transitions was **sketched** in Figs. 8.16 and 8.17. Thus, this study is the first time evidence of the feasibility of photoswitching in nitroxide–copper(II)–nitroxide molecular magnets at room temperature.

The structural, electronic, and magnetic properties of two different models of the heterospin polymer chain complexes of Cu^{2+} hexafluoroacetylacetonate with two pyrazole-substituted nitronyl nitroxides $Cu(hfac)_2$LR have been studied by means of multiconfigurational perturbation theory. The calculation revealed an important role of the end-standing NO in the exchange interactions with Cu(II) [54].

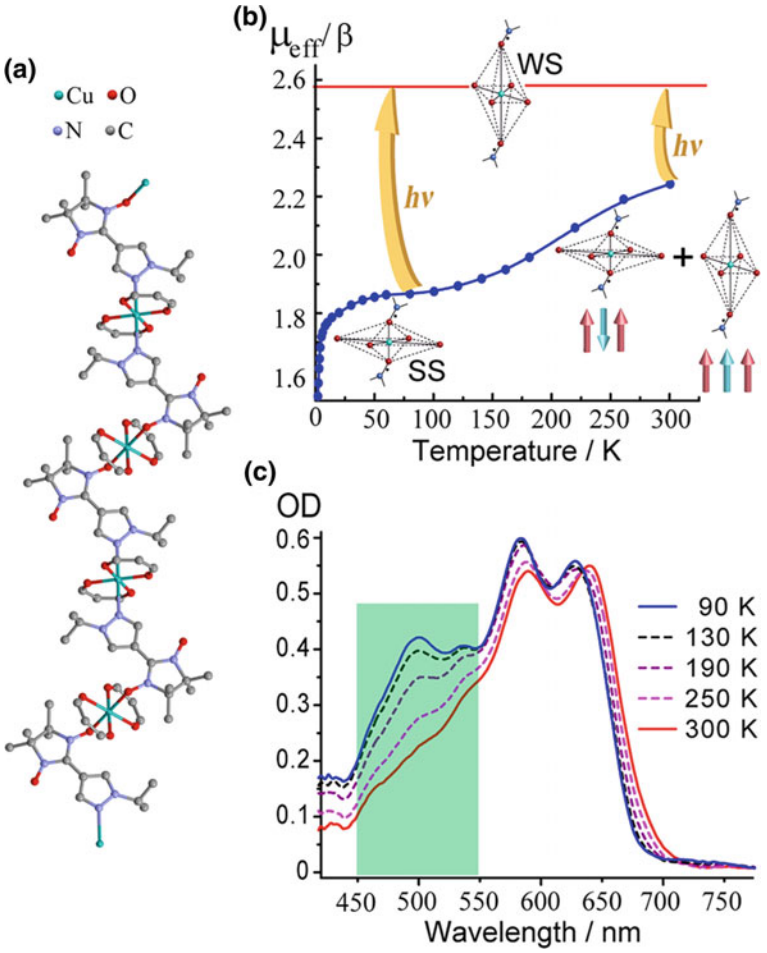

Fig. 8.16 **a** Structure of polymer-chain complex $Cu(hfac)_2L^{iso\text{-}Pr}$. **b** Temperature dependence of the effective magnetic moment (μeff) of $Cu(hfac)_2L^{iso\text{-}Pr}$. Structures of SS and WS states are sketched, and corresponding arrangements of spins are shown using arrows. Yellow arrows illustrate the photoswitching to WS state, and the horizontal red line is the magnetization level characteristic of WS state. **c** Temperature dependence of UV(vis) absorption spectrum of $Cu(hfac)_2L^{iso\text{-}Pr}$. Spectral region of the MLCT band is shaded with green [53]. Reprinted from [53], Copyright 2017 American Chemical Society

The calculations, employing multiconfigurational ab initio theoretical description of the structure and magnetic properties of nitroxide–Cu(II)–nitroxide spin triads *o*, revealed the presence of two minima in the electronic energy curve along the $Cu–O_L$ bond, separated by only 6 kcal/mol, and corresponding to the X-ray structures of the CuO_6 centers in $Cu(hfac)_2L^{Pr}$ at 115 and 293 K, respectively. At low temperatures, the predicted ground state is ^2A_u, well separated from the ^2A_g, ^4A_u states and calculated

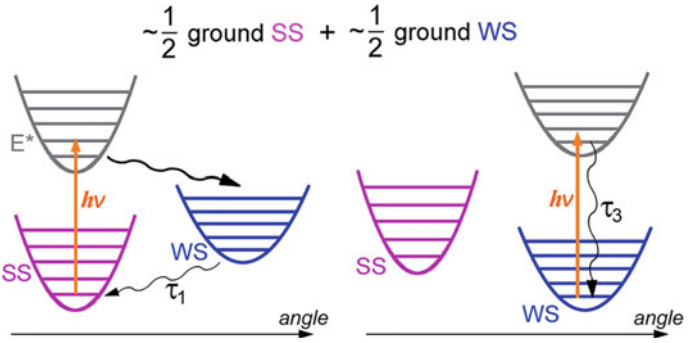

Fig. 8.17 Energy schemes of Cu(hfac)2Liso-Pr at 300 K residing in ~50% of ground SS states (left) and ~50% ground WS states (right). Corresponding photoexcitation, switching, and relaxation processes are shown [53]. Reprinted from [53], Copyright 2017 American Chemical Society

g-factors, $g_{\parallel} = 1.848$, $g_{\perp} = 1.965$, 1.974, qualitatively correspond to the observed $g < 2$ signals in the low-temperature EPR spectra.

References

1. Y. Uchida, S. Oki, R. Tamura, T. Sakaguchi, K. Suzuki, K. Ishibashi, J. Yamauchi, Electric, electrochemical and magnetic properties of novel ionic liquidnitroxides, and their use as an EPR spin probe. J. Mater. Chem. **19**, 6877–6881 (2009)
2. N. Dotti, E. Heintze, M. Slota, R. Hubner, F. Wang, J. Nuss, M. Dressel, L. Bogani, Conduction mechanism of nitronyl-nitroxide molecular magnetic compounds. Phys. Rev. B **93**, 165201 (2016)
3. S. Nakagami, T. Akita, D. Kiyohara, Y. Uchida, R. Tamura, N. Nishiyama, Molecular mobility effect on magnetic interactions in all-organic paramagnetic liquid crystal with nitroxide radical as a hydrogen-bonding acceptor. J. Phys. Chem. B **122**(29), 7409–7415 (2018)
4. Y. Takemoto, Y. Uchida, S. Shimono, J. Yamauchi, R. Tamura, Preparation and magnetic properties of nitroxide radical liquid crystalline physical gels. Mol. Cryst. Liq. Cryst. **647**(1), 279–289 (2017)
5. R. Tamura, K. Suzuki, Y. Uchida, Y. Nodac, EPR characterization of diamagnetic and magnetic organic soft materials using nitroxide spin probe techniques. Electron Paramag. Reson. **23**, 1–21 (2013)
6. Y. Uchida, N. Ikuma, R. Tamura, S. Shimono, Y. Noda, J. Yamauchi, Y. Aoki, H. Nohira, Unusual intermolecular magnetic interaction observed in an all-organic radical liquid crystal. J. Mater. Chem. **18**, 2950 (2008)
7. R. Tamura, Organic functional materials containing chiral nitroxide units, in *Nitroxides: Application in Chemistry, Biomedicine, and Materials Science*, ed. by G.I. Likhtenshtein, J. Yamauchi, S. Nakatsuji, A. Smirnov, R. Tamura (Wiley-VCH, Weinhem, 2008), pp. 303–3030
8. S. Nakatsuji, Preprations, reactions, and properties of functional nitroxide radicals, in *Nitroxides: Application in Chemistry, Biomedicine, and Materials Science*, ed. by G.I. Likhtenshtein, J. Yamauchi, S. Nakatsuji, A. Smirnov, R. Tamura (Wiley-VCH, Weinhem, 2008), pp. 161–238
9. M. Dvolaitzky, J. Billard, F. Poldy, Smectic *E*, *C* and *A* free radicals. Tetrahedron **32**, 1835–1838 (1976)

10. M. Kinoshita, P. Turek, M. Tamura, K. Nozawa, D. Shiomi, Y. Nakazawa, M. Ishikawa, M. Takahashi, K. Awaga, T. Inabe, Y. Maruyama, Chem. Lett. **20**, 1225 (1991)
11. N. Ikuma, R. Tamura, S. Shimono, N. Kawame, O. Tamada, N. Sakai, J. Yamauchi, Y. Yamamoto, Magnetic properties of all-organic liquid crystals containing a chiral five-membered cyclic nitroxide unit within the rigid core. Angew. Chem. Int. Ed. **43**, 3677–3682 (2004)
12. M. Mannini, F. Pineider, C. Danieli, F. Totti, L. Sorace, P. Sainctavit, M.-A. Arrio, E. Otero, L. Joly, J.C. Cezar, A. Cornia, R. Sessoli, Quantum tunnelling of the magnetization in a monolayer of oriented single-molecule magnets. Nature **468**, 417–421 (2010)
13. A. Caneschi, D. Gatteschi, R. Sessoli, P. Rey, Toward molecular magnets: the metal-radical approach. Acc. Chem. Res. **22**, 392–398 (1989)
14. P. Bhatt, K. Kolanji, A. Ivanova, A. Yogi, G. Jakob, M.D. Mukadam, S.M. Yusuf, M. Baumgarten, Soid state magnetic exchange interaction in nitronyl nitroxide radical-based single crystals of 3d metal complexes: a combined experimental and theoretical study. ACS Omega **3**, 2918–2933 (2018)
15. K. Zberecki, R. Swirkowicz, Transport and thermoelectric properties of magnetic organic chains. Phys. Status Solidi B: Basic Solid State Phys. **254**(7) (2017)
16. Y. Uchida, K. Suzuki, R. Tamura, N. Ikuma, S. Shimono, Y. Noda, J. Yamauchi, Anisotropic and inhomogeneous magnetic interactions observed in all-organic nitroxide radical liquid crystals. J. Am. Chem. Soc. **132**, 9746–9752 (2010)
17. K. Suzuki, Y. Uchida, R. Tamura, S. Shimono, J. Yamauchi, Observation of positive and negative magneto-LC effects in all-organic nitroxide radical liquid crystals by EPR spectroscopy. J. Mater. Chem. **22**, 6799 (2012)
18. K. Suzuki, Y. Uchida, R. Tamura, Y. Noda, N. Ikuma, S. Shimono, J. Yamauchi, Influence of applied electric fields on the positive magneto-LC effects observed in the ferroelectric liquid crystalline phase of a chiral nitroxide radical compound. Soft Matter **9**, 4687 (2013)
19. C.V. Yelamaggad, A.S. Achalkumar, D.S. Shankar Rao, M. Nobusawa, H. Akutsu, J.-I. Yamadab, S. Nakatsuji, The first examples of discotic radicals: columnar mesomorphismin spin-carrying triphenylenes. J. Mater. Chem. **18**, 3433–3437 (2008)
20. K. Suzuki, Y. Takemoto, S. Takaoka, K. Taguchi, Y. Uchida, D.G. Mazhukin, I.A. Grigor'evd, R. Tamura, Chiral all-organic nitroxide biradical liquid crystals showing remarkably large positive magneto-LC effects. Chem. Commun. **52**, 3935 (2016)
21. Y. Takemoto, E. Zaytseva, K. Suzuki, N. Yoshioka, Y. Takanishi, M. Funahashi, Y. Uchida, T. Akita, J. Park, S. Sato, S. Clevers, G. Coquerel, D.G. Mazhukin, S. Shimono, M. Sugiyama, H. Takahashi, J. Yamauchi, R. Tamura, Unique superparamagnetic-like behavior observed in non-π-delocalized nitroxide diradical compounds showing discotic liquid crystalline phase. Chem. Eur. J. **24**(65), 17293–17302 (2018)
22. A.K. Vorobiev, N.A. Chumakova, D.A. Pomogailo, Y. Uchida, K. Suzuki, Y. Noda, R. Tamura, Determination of structural characteristics of all-organic radical liquid crystals based on analysis of the dipole–dipole broadened EPR spectra. J. Phys. Chem. B **118**, 1932–1942 (2014)
23. N.A. Chumakova, T.S. Yankova, K.E. Fairfull-Smith, S.E. Bottle, A.K. Vorobiev, Molecular orientational order of nitroxide radicals in liquid crystalline media. J. Phys. Chem. B **118**, 5589–5599 (2014)
24. K. Nagura, Y. Takemoto, S. Moronaga, Y. Uchida, S. Shimono, A. Shiino, K. Tanigaki, T. Amano, F. Yoshino, Y. Noda, S. Koizumi, N. Komatsu, T. Kato, J. Yamauchi, R. Tamura, Preparation of robust metal-free magnetic nanoemulsions encapsulating low-molecular-weight nitroxide radicals and hydrophobic drugs directed toward MRI-visible targeted delivery. Chem. Eur. J. **23**, 15713–15720 (2017)
25. Y. Takemoto, E. Zaytseva, K. Suzuki, N. Yoshioka, Y. Takanishi, M. Funahashi, Y. Uchida, T. Akita, J. Park, S. Sato, C. Simon, D.G. Coquerel, S. Mazhukin, M. Shimono, H. Sugiyama, J. Takahashi, R.Tamura Yamauchi, Unique superparamagnetic-like behavior observed in non-pdelocalized nitroxide diradical compounds showing discotic liquid crystalline phase. Chem. Eur. J. **24**, 17293–17302 (2018)
26. G. Seber, R.S. Fretas, J.T. Mague, A. Paduan-Filho, X. Gratens, V. Bindilatti, N.F. Oliveira Jr., N. Yoshioka, P.M. Lahti, Magnetic tuning of all-organic binary alloys between two stable radicals. J. Am. Chem. Soc. **134**, 3825 (2012)

27. E. Mostovich, Y. Borozdina, V. Enkelmann, K. Remović-Langer, B. Wolf, M. Lang, M. Baumgarten, Planar biphenyl-bridged biradicals as building blocks for the design of quantum magnets. Cryst. Growth Des. **12**, 54 (2012)
28. P. Ravat, T. Marszalek, W. Pisula, K. Müllen, M. Baumgarten, Positive magneto-LC effect in conjugated spin-bearing hexabenzocoronene. J. Am. Chem. Soc. **136**, 12860–12863 (2014)
29. Y.B. Borozdina, E.A. Mostovich, P.T. Cong, L. Postulka, B. Wolf, M. Lang, M. Baumgarten, Spin-dimer networks: engineering tools to adjust the magnetic interactions in biradicals. J. Mater. Chem. C **5**, 9053 (2017)
30. K. Kolanji, P. Ravat, A.S. Bogomyakov, V.I. Ovcharenko, D. Schollmeyer, M. Baumgarten, Mixed phenyl and thiophene oligomers for bridging nitronyl nitroxides. J. Org. Chem. **82**, 7764–7773 (2017)
31. D. Gatteschi, R. Sessoli, J. Villain, *Molecular Nanomagnets* (Oxford University Press, Oxford, 2006)
32. S. Maekawa, *Concepts in Spin Electronics* (Oxford University Press, Oxford, 2006)
33. K.-A. Hansen, J.P. Blinco, Nitroxide radical polymers—a versatile material class for high-tech applications. Polym. Chem. **9**, 1479 (2018)
34. H. Nishide, S. Iwasa, Y.-J. Pu, T. Suga, K. Nakahara, M. Satoh, Organic radical battery: nitroxide polymers as a cathode-active material. Electrochim. Acta **50**(2–3), 827–831 (2004)
35. Kenichi Oyaizu, Takashi Sukegawa, Hiroyuki Nishide, Dual dopable poly(phenylacetylene) with nitronyl nitroxide pendants for reversible ambipolar charging and discharging. Chem. Lett. **40**, 184–185 (2011)
36. M.-K. Hung, Y.-H. Wang, C.-H. Lin, H.-C. Lin, J.-T. Lee, Synthesis and electrochemical behaviour of nitroxide polymerbrush thin-film electrodes for organic radical batteries. J. Mater. Chem. **22**, 1570–1577 (2012)
37. K. Yuan, F. Li, L. Chen, Y. Chen, Approach to a block polymer precursor from poly(3-hexylthiophene) nitroxide-mediated in situ polymerization for stabilization of poly(3-hexylthiophene)/ZnO hybrid solar cells. Thin Solid Films **520**, 6299–6306 (2012)
38. T. Sukegawa, A. Kai, K. Oyaizu, H. Nishide, Synthesis of pendant nitronyl nitroxide radical-containing poly(norbornene)s as ambipolar electrode-active materials. Macromolecules **46**(4), 1361–1367 (2013)
39. T. Janoschka, N. Martin, U. Martin, C. Friebe, S. Morgenstern, H. Hiller, M.D. Hager, U.S. Schubert, An aqueous, polymer-based redox-flow battery using non-corrosive, safe, and low-cost materials. Nature **527**, 78–81 (2015)
40. T. Hagemann, J. Winsberg, B. Häupler, T. Janoschka, J.J. Gruber, A. Wild, U.S. Schubert, A bipolar nitronyl nitroxide small molecule for an all-organic symmetric redox-flow battery. NPG Asia Mater. **9**, e340 (2017)
41. K. Zhang, Y. Hu, L. Wang, M.J. Monteiro, Z. Jia, Pyrene-functionalized PTMA by NRC for greater π–π stacking with rGO and enhanced electrochemical properties. ACS Appl. Mater. Interfaces **9**, 34900–34908 (2017)
42. L. Wylie, K. Oyaizu, A. Karton, M. Yoshizawa-Fujita, E.I. Izgorodina, Toward improved performance of all-organic nitroxide radical batteries with ionic liquids: a theoretical perspective. ACS Sustain. Chem. Eng. **75**, 5367–5375 (2019)
43. K. Sato, T. Mizuma, H. Nishide, K. Oyaizu, Command surface of self-organizing structures by radical polymers with cooperative redox reactivity. J. Am. Chem. Soc. **139**, 13600–13603 (2017)
44. K.-A. Hansen, J. Nerkar, K. Thomas, S.E. Bottle, A.P. O'Mullane, P.C. Talbot, J.P. Blinco, New spin on organic radical batteries—an isoindoline nitroxide-based high-voltage cathode material. ACS Appl. Mater. Interfaces **10**(9), 7982–7988 (2018)
45. IYu. Barskaya, S.L. Veber, E.A. Suturina, P.S. Sherin, KYu. Maryunina, N.A. Artiukhova, E.V. Tretyakov, R.Z. Sagdeev, V.I. Ovcharenko, N.P. Gritsanb, M.V. Fedin, Spin-state-correlated optical properties of copper(II)–nitroxide based molecular magnets. Dalton Trans. **46**, 13108 (2017)

46. V.I. Ovcharenko, S.V. Fokin, E.T. Kostina, G.V. Romanenko, A.S. Bogomyakov, E.V. Tretyakov, First example of a reversible single-crystal-to-single-crystal polymerization-depolymerization accompanied by a magnetic anomaly for a transition-metal complex with an organic radical. Inorg. Chem. **51**(22), 12188–12194 (2012)
47. M.V. Fedin, S.L. Veber, E.G. Bagryanskay, V.I. Ovcharenko, Electron paramagnetic resonance of switchable copper-nitroxide-based molecular magnets: an indispensable tool for intriguing systems. Coord. Chem. Rev. **289–290**, 341–356 (2015)
48. M.V. Fedin, S.L. Veber, K.Y. Maryunina, G.V. Romanenko, E.A. Suturina, N.P. Gritsan, R.Z. Sagdeev, V.I. Ovcharenko, E.G. Bagryanskaya, Intercluster exchange pathways in polymer-chain molecular magnets $Cu(hfac)_2L^R$ unveiled by electron paramagnetic resonance. J. Am. Chem. Soc. **132**(39), 13886–13891 (2010)
49. E.V. Tretyakov, V.F. Plyusnin, A.O. Suvorova, S.V. Larionov, S.A. Popov, O.V. Antonova, E.M. Zueva, D.V. Stass, A.S. Bogomyakov, G.V. Romanenko, V.I. Ovcharenko, Luminescence of the nitronyl nitroxide radical group in a spin-labelled pyrazolylquinoline. J. Lumin. 14833–14838 (2014)
50. M.V. Fedin, S.L. Veber, E.G. Bagryanskaya, G.V. Romanenkoa, V.I. Ovcharenko, Spatial distribution of phases during gradual magnetostructural transitions in copper(II)–nitroxide based molecular magnets. Dalton Trans. **44**, 18823 (2015)
51. A.V. Artemev, O.V. Vysotskaya, L.A. Oparina, A.S. Bogomyakov, S.S. Khutsishvili, I.V. Sterkhova, V.I. Ovcharenko, B.A. Trofimov, New heterospin chain-polymers based on $Cu(hfac)_2$ complex with TEMPO derivatives bearing b-(oxy)acrylate moiety: synthesis, structural and magnetic properties. Polyhedron **119**, 293–299 (2016)
52. M.P. Bubnov, I.A. Teplova, E.A. Kopylova, K.A. Kozhanov, A.S. Bogomyakov, M.V. Petrova, V.A. Morozov, V.I. Ovcharenko, V.K. Cherkasov, Ferromagnetic coupling in the heterospin bis-catecholato–manganese(IV) complex with pyridine substituted by nitronylnitroxide. Inorg. Chem. **56**, 2426–2431 (2017)
53. X. Dong, M. Lorenc, E.V. Tretyakov, V.I. Ovcharenko, M.V. Fedin, Light-induced spin state switching in copper(II)-nitroxide-based molecular magnet at room temperature. J. Phys. Chem. Lett. **8**, 5587–5592 (2017)
54. S. Vancoillie, L. Rulısek, F. Neese, K. Pierloot, Theoretical description of the structure and magnetic properties of nitroxide-Cu(II)-nitroxide spin triads by means of multiconfigurational Ab initio calculations. J. Phys. Chem. A **113**, 6149–6157 (2009)

Chapter 9
Nitroxides in Disease

9.1 Introduction

The mostly used nitroxides in biology and medicine are a group of heterocyclic nitroxide derivatives of piperidine, pyrroline, and pyrrolidine. The nitroxides are served as antioxidants and drugs for cancers, neurodegenerativity (Parkinson, Alzheimer, and others diseases), ischemia, obesity, radiation damage, age-related degeneration, immunomodulatory patology, oxidative stress, inflammation, etc.

Design and application of anticancer drugs of breast, hepatic, lung, ovarian, lymphatic, prostatic, and thyroid cancers still are challenging fundamental problem in modern medicine to be solved. Anticancer effects of nitroxides and their derivatives, involving in synergetic effects with known anticancer drugs in vivo and in vitro experiments in cancer cells and tumor tissue are as follows: (1) reducing the viability of tumor cell lines, (2) slow down ATP production, (3) damage to electron transport chain, (4) mitochondrial mitosis, (5) induction of apoptosis, (6) cell cycle arrest in G1 phase, (7) the induction of oxidative stress, and (8) protection against obesity.

Since the pioneering work of Konovalova, Bogdanov, Miller, Rozantsev, Neiman, and Emanuel in which was demonstrated on model tumor, leukemia, [1] nitroxide radicals and their biologically active derivatives have found increasing application in biomedicine and medicine [2–10].

9.2 Nitroxides in Cancer

9.2.1 Cells

Mito-CP11, a mitochondria-targeted nitroxide formed by conjugating a triphenylphosphonium cation to a five-membered nitroxide, carboxy-proxyl (CP), was used as a superoxide dismutase (SOD) mimetic [4]. The antiproliferative and cytotoxic properties of submicromolar levels of Mito-CP11 alone and in combination

G. I. Likhtenshtein, *Nitroxides*, Springer Series in Materials Science 292,
https://doi.org/10.1007/978-3-030-34822-9_9

with fluvastatin, a cholesterol lowering drug, in breast cancer cells were investigated. The nitroxide inhibited MCF-7 breast cancer cell proliferation, significantly enhanced fluvastatin-mediated cytotoxicity in MCF-7 cells. Mito-CP11 alone, and in combination with fluvastatin also inhibited nuclear factor kappa-B activity mainly in MCF-7 cells. It was concluded that Mito-CP11, being non-toxic to non-tumorigenic cells could enhance the cytostatic and cytotoxic effects of statins in breast cancer cells.

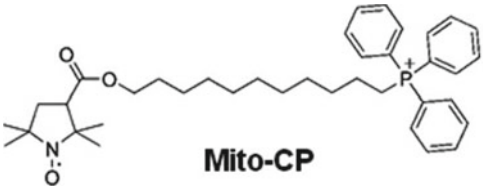

Mito-carboxy-proxyl (Mito-CP), a lipophilic cationic nitroxide, accumulated in the mitochondria HepG2 cell line and primary hepatocytes was coadministered with 2-deoxyglucose (2-DG), a glycolysis disrupting agent. Mito-CP has been shown to act by disrupting the energy-producing mechanism, inducing mitochondrial-mediated apoptosis, and also enhancing the action of other chemotherapeutic agents in cancer cells [5].

Tert-butyl-2(4,5-dihydrogen-4,4,5,5-tetramethyl-3-o-1 h-imidazole-3-cationic-1-oxyl-2)-pyrrolidine-1-carboxylic ester (L-NNP) displayed cytotoxicity on human breast cancer MCF-7 and MDA-MB-231 cell lines [6]. The nitroxide was selective for liver cancer cells, while being non-toxic to normal hepatocytes. It was found that L-NNP reduced cell viability and increased ROS production and lipid peroxidation accompanied by a reduction in mitochondrial potential and GSH level in hepatoma cells. Mitochondria-targeted metabolism-interfering triphenyl-phosphonium-conjugated nitroxide can effectively suppress human B-RafV600E melanoma cell lines and their/PLX4032-resistant progenies using Mito-CP and ubiquinone [7].

Two series of novel spin-labeled combretastatin derivatives were synthesized and evaluated for cytotoxicity against tumor cell lines (K562, SGC-7901, Hela and HepG-2) [8]. The results indicated that some of the compounds showed significant cytotoxicity against four tumor cell lines in vitro with IC(50) values ranging from 0.15 to 1.05 μM, compared with values of 0.014–0.403 μM for 3-amino-deoxycombretastatin A-4.

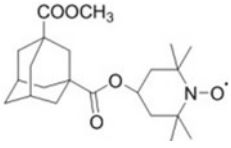

An adamantyl nitroxide derivative displayed a higher anticancer activity against all the tested human hepatoma cells (Bel-7404 cells) with IC50 of 68.1 μM in Bel-7404 cells, compared to the positive control 5-FU (IC50 = 607.7 μM) [9]. This

nitroxide: (1) significantly inhibited tumor growth in a xenograft mouse model with low toxicity, (2) suppressed the cell migration and invasion, (3) induced the G2/M phase arrest, and (4) induced cell death, which was accompanied with damaging mitochondria, increasing the generation of intracellular reactive oxygen species, cleavages of caspase-9 and caspase-3, as well as activations of Bax and Bcl-2. The effect of synthetic antioxidant Pirolin (3-carbamoyl-2,2,5,5-tetramethylpyrroline-1-oxyl) on breast cancer progression in Sprague-Dawley rats was evaluated [10]. The rats were administered with 7,12-dimethylbenz anthracene (DMBA) and then treated with the nitroxide. The median number of tumors and their volume, at the end of the study, was found to be considerably smaller in antioxidant-treated groups.

A novel nitroxide derivative, 4-ferrocenecarboxyl-2,2,6,6-tetramethyl piperidine-1-oxyl (FC-TEMPO), was synthesized for evaluating the effects of spin-label compounds on tumor cells (metastatic lung cancer cell line 95-D) and its biological effects on tumor and normal cells [11]. This compound resulted in: (1) 50% reduction in the viability (390 μM, 48 h), while other nitroxide TEMPOL had no effect at the same concentration, (2) FC-TEMPO inhibiting the viability of cancer cells i, while it was less toxic to a normal human cell line, (3) suppressing the growth of tumor cells by induced apoptosis through activating caspase-3, (4) a significant release of extracellular lactatedehydrogenase (LDH), (5) enhance apoptosis and caspase-3 activity (260 μM, 48 h), and 6) increase of superoxide dismutase and catalase. It was suggested that the cytotoxicity of FC-TEMPOL may result from the presence of ferrocenecarboxyl group at position 4, which interacts with cancer cell DNA or induces genotoxicity resulting from redox reaction.

Three series of novel spin-labeled rotenone derivatives analogs

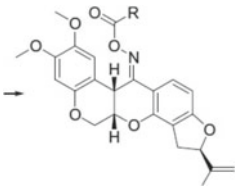

where R are nitroxides were synthesized and evaluated for cytotoxicity against four tumor cell lines, A-549, DU-145, KB and KBvin [12]. All of the derivatives exhibited promising in vitro cytotoxic activity against the tumor cell lines tested, with IC_{50} values ranging from 0.075 to 0.738 μg/mL. A series of spin-labeled fluorouracil derivatives of compound

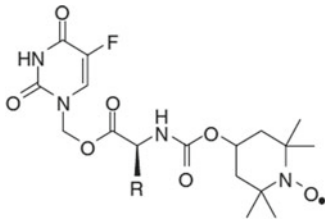

were used as a drug against lung cancer A549 cell line with anticancer activity at IC50 values of 2.76–2.38 μM [13]. These compounds were twofold more cytotoxic than 5-FU and less toxic against other tested cell lines. To evaluate the proof-of-concept anticancer-versus-antioxidant efficacy of the DAPs, a novel class of bifunctional compounds based on diarylidenyl piperidone conjugated to an N-hydroxypyrroline (NOH) and a nitroxide precursor group, HO-3867, for example, were tasted.

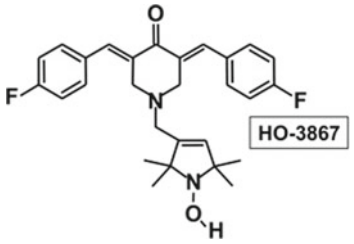

A number of cancerous (breast, colon, head and neck, liver, lung, ovarian, and prostate cancer) and non-cancerous (smooth muscle, aortic endothelial, and ovarian surface epithelial) human cell lines were subjects of interest for work [14]. The study utilized four DAPs, namely H-4073 and H-4318 without NOH and HO-3867 and HO-4200 with NOH substitution. All four compounds induced significant loss of cell viability in cancer cells; whereas, HO-3867 and HO-4200 showed significantly less cytotoxicity in non-cancerous cells. EPR and biochemical measurements indicated (1) a metabolic conversion of the N-hydroxylamine function to nitroxide, (2) significantly higher levels of the metabolite, (3) superoxide radical-scavenging activity in non-cancerous cells compared to cancer cells, (4) arrest and apoptosis in cancer cells growth mediated by inhibition of phosphorylation human protein (STAT3) at the Tyr705 and Ser727 residues, and (5) induction of apoptotic markers of cleaved caspase-3 and PARP were also evaluated.

In work [15], several principle mitochondrial effects of TEMPOL in a human promyelocytic leukemic cell line (HL-60) on 24-h exposure to TEMPOL were evaluated. Experiments revealed the following alterations: (1) decrease in both the intracellular and mitochondrial glutathione pools, (2) impairment of oxidative phosphorylation, and (3) decrease in mitochondrial membrane potential. In addition, TEMPOL specifically targeted complex I of the respiratory chain, with minor effects on complexes II and IV, suggesting that mitochondrial effects might play a role in the nitroxide-induced oxidative stress and apoptosis.

The cytotoxicity and genotoxicity of **TEMPO** in mammalian cells were investigated using the mouse lymphoma assay (MLA) and in vitro micronucleus assay [16]. Specifically, the following effects were described: (1) In the absence of metabolic activation (S9), 3 mM TEMPO produced significant cytotoxicity and marginal mutagenicity in the MLA; (2) In the presence of S9, treatment of mouse lymphoma cells with 1–2 mM TEMPO resulted in decreases of the relative total growth and increases in mutant frequency; (3) treatment of TK6 human lymphoblastoid cells with 0.9–2.3 mM TEMPO increased the frequency of both micronuclei (a marker for clastogenicity) and hypodiploid nuclei (a marker of aneugenicity), (4) TEMPO induced reactive oxygen species and decreased glutathione levels in mouse lymphoma cells; and (5) The majority of TEMPO-induced mutants had loss of heterozygosity at the *Tk*locus, with allele loss of $\leq$34 Mbp. The authors concluded that TEMPO is mutagenic in the MLA and induces micronuclei and hypodiploid nuclei in TK6 cells, and oxidative stress may account for part of the genotoxicity induced by TEMPO in the cell lines.

Eighteen novel spin-labeled analogs of camptothecin exhibited significant in vitro antiproliferative activity against these four tested human tumor cell lines (A-549, MDA-MB-231, KB, and KBvin) [17].

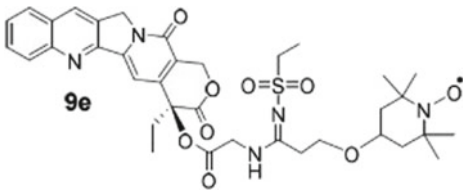

For example, compounds 9e displayed the greatest cytotoxicity against the multidrug-resistant KBvin cell line.

The selective cytotoxicity of Tert-butyl-2(4,5-dihydrogen-4,4,5,5-tetramethyl-3-O-1H-imidazole-3-cationic-1-oxyl-2)-pyrrolidine-1-carboxylic ester (L-NNP on isogenetic human hepatoma HepG2 and normal L-02 cell lines was investigated [6]. Effects of L-NNP on cell growth inhibition, intracellular reactive oxygen species production, the mitochondrial membrane potential loss, malondialdehyde generation, and glutathione levels were analyzed.

Curcumin is a phytochemical agent with diverse molecular targets and well known for its antitumor potential. Curcumin-loaded pH-sensitive redox nanoparticles (RNP(N)) by self-assembling amphiphilic block copolymers conjugated with reactive oxygen species (ROS) scavenging nitroxide radicals were prepared [18]. In conditions mimicking the physiological environment, the entrapment of both curcumin and nitroxide radicals in the hydrophobic core of RNP(N) suppressed curcumin degradation. Curcumin-loaded RNP(N) induced strong cell apoptosis compared to free curcumin. Intravenous injection of curcumin-loaded RNP(N) suppressed tumor growth in vivo, which is probably due to the increased bioavailability and significant ROS scavenging at tumor sites.

The pro-oxidative effect of TEMPOL on the inhibition of cellular proliferation and its role in enhancing the effect of anticancer drug cisplatin (DDP) on the induction of apoptosis in ovarian cancer cells was studied [19]. The experiments revealed that: (1) Cell viabilities of OVCAR3 and SKOV3 cells were decreased by TEMPOL in dose-dependent manner at concentrations of 2–10 mM after 48 h incubation. (2) The cell proliferation rates of OVCAR3 and SKOV3 cells were suppressed by TEMPOL at lower toxic concentrations of 1.5 and 1 mM, respectively, compared with the control group. (3) The combination therapy significantly inhibited the cell proliferation of OVCAR3 cells compared with treatment with DDP alone. (4) The combination treatment increased the proportion of early apoptotic cells in OVCAR3 cells compared with single DDP treatment. (5) The combination treatment markedly decreased the Bcl–2:Bax expression ratio compared with treatment with DDP alone. (6) The combination therapy significantly increased cellular ROS generation compared with the DDP-only therapy.

Nitroxide 1.3. 5-carboxy-1,1,3,3-tetramethylisoindolin-2-yloxyl (CTMIO) has been investigated in the context of *Ataxia Telangiectasia* (A-T), an autosomal recessive disorder including progressive neurodegeneration, immunodeficiency, a strong predisposition to cancer [20]. This nitroxide and its derivative DCTEIO were found to regulate the expression of a collection of genes involved in oxidative stress and antioxidant defense and significantly expressed genes participation also in the inflammatory response or innate immunity. It was suggested that these nitroxides may function as immune-modulating agents. CTMIO and DCTEIO also exhibited a similar pattern of gene regulation to H_2O_2. This finding indicates that the nitroxides may have a pro-oxidant inducing oxidative stress, either by generating reactive oxygen species or by inhibiting antioxidant system rather than antioxidant role in prostate cancer cells. It is important that CTMIO demonstrated minimal toxicity in prostate cancer cells in comparison with TEMPO and TEMPOL.

Rotenone is used as a broad spectrum insecticide, piscicide, and pesticide.

Ability of twelve new derivatives of known antioxidants trolox (TroH), trolox succinate (TroS), α-tocopheryl succinate (α-TOS)-containing nitroxyl radicals to protect bacterial cells from spontaneous and peroxide-induced mutagenesis and their cytotoxicity against six different tumor cells as well as two normal cells was evaluated [21]. In contrast to TroH and TroS, all nitroxide derivatives demonstrated not only antioxidant properties, but also suppressed the growth of human tumor cells: myeloma, mammary adenocarcinoma, hepatocarcinoma, T cells leukemia, histiocytic lymphoma, and T-cellular leucosis. In addition, one group of compounds was capable of inhibiting the growth of normal mouse (LMTK) and hamster (AG17) fibroblast cells, while some nitroxide conjugates showed pronounced selectivity in suppressing the growth of several cancer cells. The authors concluded that the most perspective derivatives as antioxidants and as antitumor agents are the compounds containing pyrrolidine nitroxides.

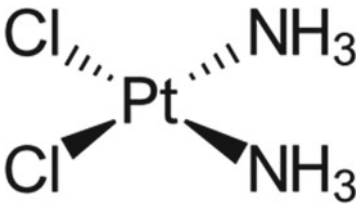

Cisplatin [Cis-Diammine-Dichloroplatinum(II)], CDDP is one of the most widely used anticancer drugs. Nevertheless, the efficacy of the anticancer drug cisplatin is restricted by tumor cell resistance and occurrence of severe side effects. It was reported that platinum (IV)-nitroxyl complexes (PNCs) are able to circumvent CDDP resistance in RT112 bladder cancer cells, thus being hybrid compounds combining platinum and biologically active nitroxyl pharmacophores [2, 22]. For further improving the therapeutic efficacy of the anticancer drug cisplatin, newly synthesized platinum-nitroxyl complexes (PNCs) (Fig. 9.1) were investigated for their potential to circumvent cisplatin resistance [23]. Intracellular platinum accumulation, DNA platination, and cytotoxicity upon treatment with the PNCs in a model system of the bladder cancer cell line RT112 and its cisplatin-resistant subline RT112-CP were evaluated. Induction of DNA strand breaks, and oxidative base modifications were assessed using the PM2 DNA relaxation assay. It was found that platinum accumulation and DNA platination were similar in RT112 and RT112-CP cells for both bivalent and four-valent PNCs. Experiments also indicated a significant decrease in the amount of Pt bound to DNA in cisplatin-treated resistant RT112-CP cells as compared to the parental RT112 line (62 vs. 152.4 nmol Pt/g DNA). A strong correlation was observed between cellular accumulation, DNA platination, and cytotoxicity in RT112 cells. Using a cell-free assay, induction of oxidative DNA damage by cisplatin but not by PNCs was observed. It was suggested that cisplatin exerts its toxic

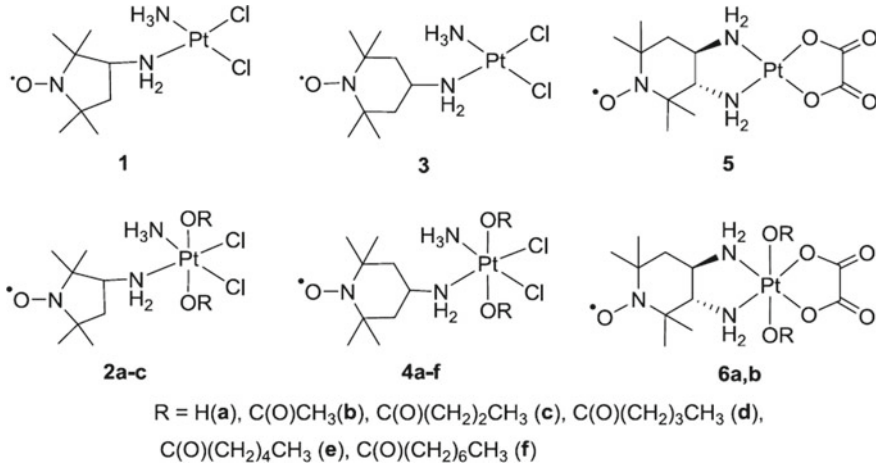

Fig. 9.1 Structure of platinumnitroxyl complexes (PNCs) [23]

action by platination and oxidative DNA damage, while cells treated with PNCs are protected against oxidatively induced lesions. The authors concluded that system PNCs were able to circumvent cisplatin resistance and may be used as improved platinating drugs in cisplatin-resistant cancer.

In work [24], the mode of action of the platinum(IV)-nitroxyl complex PN149

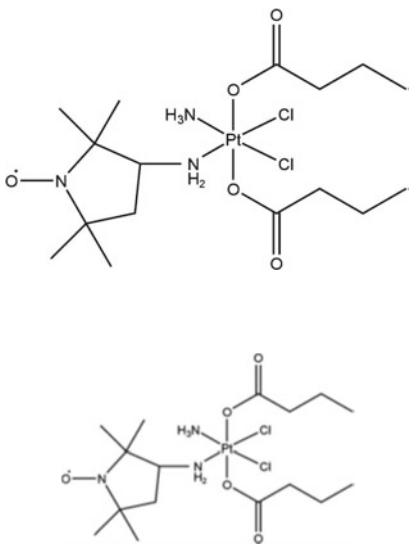

was investigated in the bladder cancer cell line RT112 and the renal cell carcinoma cell line A498 on the molecular and cellular level. For gene expression, analysis high-throughput RT-qPCR was applied. Atomic absorption spectroscopy was used to determine the intracellular platinum content. Apoptosis and cell cycle were analyzed by flow cytometry simultaneously. The p53 protein (a protein encoded by homologous genes in various organisms) level upon treatment with PN149 or CDDP was analyzed using immunoblotting. Cytotoxicity was investigated by relative cell count as well as by colony forming ability. Gene expression analysis was applied to identify the mode of action of PN149 in comparison with CDDP. The following impacts were evaluated: (1) MT gene expression and platinum uptake, (2) genes related to oxidative stress response, (3) genes related to DNA damage response (DDR) and on p53, and (4) progression and control of the cell cycle on the transcriptional and functional level. Gene expression analysis showed that PN149-induced genes related to DNA damage response (RRM2B, GADD45A), cell cycle regulation (CDKN1A, PLK3, PPM1D, and coding for the pro-apoptotic factors PUMA and Noxa.

9.2.2 Animals

The effect of synthetic antioxidant Pirolin (3-carbamoyl-2,2,5,5-tetramethylpyrroline-1-oxyl) on breast cancer progression in Sprague-Dawley rats was evaluated [10]. The rats were administered with 7,12-dimethylbenz(*a*)anthracene (DMBA) and then treated with the nitroxide. The median number of tumors and their volume, at the end of the study, were found to be considerably smaller in antioxidant-treated groups. The role of oxidative stress in carcinogenesis in the investigated animals was emphasized.

The antineoplastic properties of TEMPO in the human hormone-dependent/hormone-independent prostate carcinoma models (LNCaP, DU-145, and PC-3) were examined [25]. TEMPO treatment of LNCaP cells resulted in: (1) enhanced activities of caspase-9 and caspase-3, (2) enhanced number of cells in G_2/M phase of the cell cycle, (3) decreased BrdU incorporation indicating a decline in the number of proliferating cells, (4) a significant inhibition of tumor growth, and (5) in hormone-refractory prostate carcinoma cells, a combination of relatively low doses of TEMPO and doxorubicin or mitoxantrone caused enhanced cytotoxicity as compared with single agents.

The influence of the structure of the nitroxide on the reduction rate in normal tissue, tumor, kidney, and artery regions in mice was investigated by MRI using two cell-permeable nitroxides, 4-hydroxy-2,2,6,6,-tetramethyl-1-piperidynyloxyl (TEMPOL) and 3-carbamoyl-2,2,5,5-tetramethylpyrrolidine-1-oxyl (3CP), and one cell-impermeable nitroxide, 3-carboxy-2,2,5,5,5-tetramethylpyrrolidine-1-oxyl (3CxP) [26]. MRI measurements were done with a 4.7 T scanner. EPRI data acquisition was carried out using a home-built 300 MHz CW EPR imager. The combination of the nitroxide contrast agent and SPGR MRI studies provided pharmacokinetic information for various tissues. The decay of TEMPOL and 3CP in tumor tissue was found to be significantly faster than in normal tissue, while in the case of 3CxP (membrane impermeable), there was no difference in the reduction rates between normal and tumor tissue.

Daunorubicin (Dauno) is commonly used as a drug for acute myeloid leukemia, acute lymphocytic leukemia, chronic myelogenous leukemia, and Kaposi's sarcoma. The activity of ruboxyl (Rbx), a nitroxyl analog of daunorubicin in experimental rat models of hepatic metastases from colorectal carcinoma was compared with its parent compound and with 5-fluorouracil (5FU) [27]. Experiments indicated that in mice treated by intraperitoneal injections, Rbx and 5FU were more effective than Dauno. In addition, Rbx showed only minor and manageable toxic side effect. The regional reduction and pO_2 status in a mouse radiation-induced fibrosarcoma tumor model were evaluated using sequential three-dimensional EPR imaging after intravenous injection of a tissue-permeable nitroxyl probe, HM-PROXYL, and EPR oximetry with lithium phthalocyanine (LiPc) microcrystals implanted within the tumor [28]. The experiments indicated that the regional decay of HM-PROXYL signal obeyed first-order kinetics, and the amplitude of the reduction rate and extent of its heterogeneity in a tumor varied among six mice. The relationship between pO_2 and the

reduction rate at the region of pO_2 measurement were found to be low ($r = 0.357$) in 13 tumor-bearing mice.

9.3 Miscellaneous

Aging causes decrease in the ability to cope with environmental stress resulting in increased susceptibility and vulnerability to diseases. The seminal proposal in the 1950s by Denham Harman that reactive oxygen species are a cause of aging invoked the discussion about free radical theory of aging [29]. It was concluded that certain age- and environmental-related pathophysiological changes, degenerative conditions, and diseases are driven and accelerated by radical—(i.e., $^{\bullet}OH$, H_2O_2, and O_2–) induced oxidative stress and inflammation [30].

Nitroxides mostly used in biology and medicine are a group of heterocyclic nitroxide derivatives of piperidine, pyrroline, and pyrrolidine, which may also be served as antioxidants to delay aging. Nitroxides have been proved to be preventative or therapeutic pharmaceutical drugs for diseases of aging which associated with patient genetics, smoking, diet, oxidative stress, chronic inflammation, and other environmental-induced pathophysiological conditions [31]. In addition to aging, nitroxides can prevent the destructive consequences of smoking, high sugar or high fat diet, or radiation, etc. For example, radical-induced oxidative stress and inflammation can be modulated by TEMPOL (TP)-based nitroxide drugs to prevent or treat vascular, ocular, and other pathological conditions and aging-associated disease. Effects of TP, TEMPOL hydroxylamine (TP-H), and TP-H prodrug (OT-551) on age-related degeneration (Fig. 9.2) were evaluated in groups of patients. It was found that: (1) Non-smokers versus smokers with cutaneous microvascular dysfunction, rapidly reversed by cutaneous TP. (2) Elderly cancer patients at risk for radiation-induced skin burns or hair loss were prevented by topical TP. (3) Elderly smoker or non-smoker AMD patients at risk for vision loss were prevented by daily eye drops of OT-551. (4) Both TP and TP-H topically penetrate and function in skin or mucosa, protecting and treating radiation burns and hair loss or smoking-induced cutaneous vascular dysfunction. (5) OT-551 penetrates and travels to the back of the eye, preserving visual acuity and preserving normal and low light luminance in dry AMD smokers and non-smoker patients. (6) OT-551 can activate nuclear factor E2-related factor (Nrf-2) and the antioxidant response element (ARE) and can inhibit nuclear factor kappa-light-chain-enhancer of activated B cells (NF-κB. Clinical data for TP, TEMPOL hydroxylamine (TP-H), and the more lipophilic TP-H prodrug, OT-551, were reviewed [31].

The antioxidant effects of TEMPOL on ovarian ischemia/reperfusion (I/R) injury in rats were investigated treating forty female Wistar albino rats [32]. TEMPOL (50 mg/kg) was found to be effective in the reducing ovarian I/R injury. A hypothesis that scavenging reactive oxygen species with TEMPOL would protect renal oxygenation and nitric oxide (NO) levels in the acute phase of renal ischemia/reperfusion I/R was tested [33]. Results demonstrated that scavenging ROS using TEMPOL not

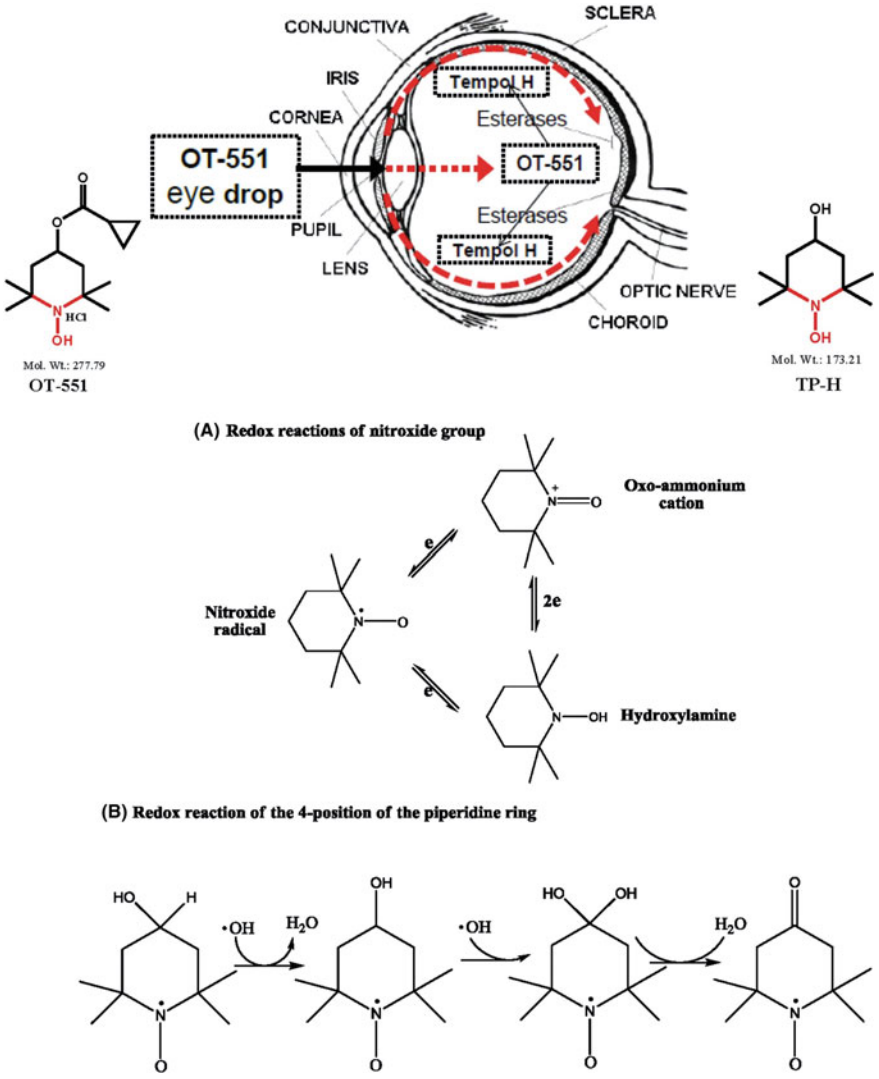

Fig. 9.2 Piperidine nitroxide OT-551 eye drop for preserving visual acuity (VA) in AMD (top), nitroxide group redox cycling (bottom, **a**), and piperidine ring redox reactions (bottom, **b**). (top) [31]. Reprinted from reference [31] with permission of Frontiers in Genetics

only reduced renal oxidative stress following I/R but also normalized renal tissue NO levels and thereby reduced rapid ventricular rate, improved drenal blood flow, renal DO_2, and renal microvascular oxygenation.

Administration of the antioxidant TEMPOL (TP) in the food of mice prevents obesity, causing significant weight loss without toxicity [34]. The results showed that the treatment of 3T3-L1 cells with TEMPOL inhibits the expression of key

adipogenesis factors, adipose differentiation, lipid storage and may underlie some of the in vivo effects of TEMPOL on body weight. In addition, dietary TEMPOL decreased body mass and plasma lipid level, both parameters caused by high fat feeding of apoE$^{-/-}$ mice. ApoE$^{-/-}$ mice were fed a high fat diet without or with the nitroxide TEMPOL. The latter suppressed metabolic changes, increased leptin, plaque collagen, macrophage numbers, and atherosclerotic plaque stability [35]. TP and TP-H inhibit tissue oxidative stress and inflammation, and also have effects on the gut microbiome, food energy utilization, and metabolism. TP has been shown to prevent obesity-induced changes in adipokines in cell and animal systems. Supplementation with TB inhibits inflammation and atherosclerosis in apoE($^{-/-}$) mice fed a high fat diet (HFD). TEMPOL had a significant impact on body mass, atherosclerosis, hyperlipidaemia, and inflammation.

The immunomodulatory effects and therapeutic potential of orally delivered TEMPOL in the mouse experimental autoimmune encephalomyelitis EAE model were examined [36]. Mice receiving TEMPOL for 2 weeks prior to induction of active EAE displayed delayed onset and reduced incidence of disease compared to control-fed animals. Reduced disease severity was suggested to be associated with limited microglial activation and fewer inflammatory infiltrates. After the induction of disease, and the onset of clinical symptoms, TEMPOL reduced the severity of multiple sclerosis (MS).

Ten healthy young male smokers, who had smoked for 6 years with an average daily consumption of nine cigarettes, were tested with TEMPOL [37]. Experiments indicated the nitroxide acutely and rapidly (within 30 min) improves the thermal hyperemia response in young adult smokers, returning the response back to that typically observed in healthy non-smokers and effectively reversing their impaired endothelial function observed. The authors concluded the effect of TEMPOL was due to the removal of oxidative stress. The purpose of work [38] was to investigate the effect of the superoxide dismutase mimetic TEMPOL on decreases in retinal blood flow that are found in diabetic STZ mice. A three-week administration of TEMPOL in the STZ mice led to significantly higher blood flow rates than in the untreated mice.

Novel compound SANR was synthesized by introducing functional moiety of salicylic acid into α-nitronyl nitroxides, and the strong analgesic effects of this newly synthesized compound in a rat low back pain of a rat were examined [39]. Both acute and repeated SANR treatment exerted strong analgesic effect in low back pain mimicked by chronic compression of dorsal root ganglion in rats. Four compounds, apocynin (inhibitor of NADPH oxidase, 4-oxo-tempo, U-83836E), and tirilazad (drug for treating acute ischemic stroke), that reduce reactive oxygen species (ROS) and the downstream lipid peroxidation products, affected on nocioceptive behaviors in chronic SCI animals [40]. Specifically, apocynin and 4-oxo-tempo were found to reduce abnormal mechanical hypersensitivity measured in forelimbs and hindlimbs in a model of chronic SCI-induced neuropathic pain.

TEMPOL-H was administered in increasing doses via an intraperitoneal route to C3H mice and provided protection against the lethality of whole body radiation in the mice with a dose modification factor of 13 [41]. TEMPOL-H was associated

with less hemodynamic toxicity than TEMPOL. The efficacy of TEMPOL in cell culture and animal models of the central and peripheral dysfunction associated with Parkinson's disease was examined [42]. In vivo, intraperitoneal TEMPOL protects mice from intrastriatal 6-hydroxydopamine (6-OHDA)-induced cell and dopamine metabolite loss in the striatum. In addition, TEMPOL protects mice from the ptosis, activity level decrement, and mortality induced by intraperitoneal administration of 6-OHDA, a model of autonomic dysfunction in Parkinson's disease. Adjunctive use of polynitroxylated albumin enhances the in vitro and in vivo effects of TEMPOL.

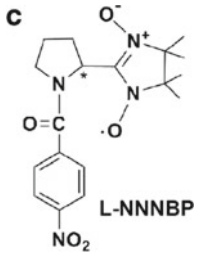

L-NNNBP

Protective effects of L-NNNBP on β-amyloid (Aβ) deposition and memory deficits in an Alzheimer disease (AD) model of APP/PS1 mice were evaluated [42]. Treatment with L-NNNBP for one month led to a marked decrease in brain Aβ deposition and tau phosphorylation in the blinded study on APP/PS1 transgenic mice, as well as decrease of astrocyte activation and improvement of spatial learning and memory compared with the vehicle-treated APP/PS1 mice. Using a rat model of paclitaxel-induced pain (intraperitoneal 2 mg/kg paclitaxel on days 0, 2, 4, 6), the effects of a non-specific ROS scavenger, N-tert-Butyl-α-phenylnitrone (PBN) and a superoxide selective scavenger, 4-hydroxy-2,2,6,6-tetramethylpiperidine-1-oxyl (TEMPOL) were compared [43, 44]. TEMPOL significantly inhibited mechanical hypersensitivity and paclitaxel-induced painful peripheral neuropathy, but in a lesser extent than PBN. Thus, such effects cannot be attributed to superoxide radicals alone.

A nitroxide radical-containing nanoparticle (RNPO) that accumulates specifically in the colon to suppress inflammation and reduce the undesirable side effects of nitroxide radicals was designed [45]. RNP(O) was synthesized by assembly of an amphiphilic block copolymer that contains stable nitroxide radicals in an ether-linked hydrophobic side chain. RNP(O), with a diameter of 40 nm and a shell of poly(ethylene glycol), had a significantly greater level of accumulation in the colonic mucosa than low-molecular-weight TEMPOL or polystyrene latex particles. The effects of RNPO that accumulates specifically in the colons of mice with colitis were determined with dextran sodium sulfate (DSS)-induced colitis and are more effective in reducing inflammation than low-molecular-weight TEMPOL or mesalamine that commonly treats inflammatory bowel disease, including ulcerative colitis.

Intravenous TEMPOL administration to hypertensive rodent models caused rapid and reversible dose-dependent reductions in blood pressure in 22 of 26 studies [46]. The administration is accompanied by vasodilation, increased nitric oxide activity, reduced sympathetic nervous system activity at central and peripheral sites, and

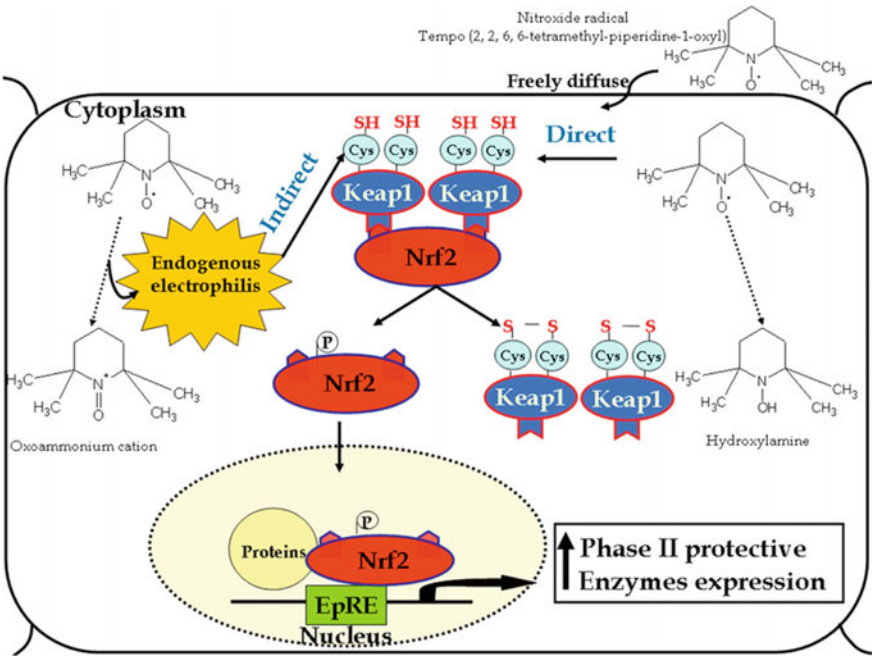

Fig. 9.3 Keap1-Nrf2-ARE pathway in human keratinocytes (HaCaT) [47]. Reprinted from [47], Copyright 2013 Elsevier

enhanced potassium channel conductance in blood vessels and neurons. Oral or by infusion administration over days or weeks to hypertensive rodent models reduced blood pressure in 59 of 68 studies and was accompanied by correction of salt sensitivity and endothelial dysfunction. In addition, the administration reduced agonist-evoked oxidative stress, contractility of blood vessels, renal vascular resistance, and increased renal tissue oxygen tension.

Study [47] showed that nitroxides may act as electrophiles, directly or indirectly, capable of activating the Keap1-Nrf2-ARE pathway in human keratinocytes (HaCaT) and in human skin (human organ culture model) (Fig. 9.3). The high potency of oxoammonium cations versus hydroxylamines in activating the system was demonstrated.

Various aspects of nitroxides as antioxidants and anticancer were recently discussed in a comprehensive review [48].

References

1. N.P. Konovalova, G.N. Bogdanov, V.B. Miller, E.G. Rozantsev, M.B. Neiman, N.M. Emanuel, Antitumor activity of stabile free radicals. Dokl. Akad. Nauk SSSR, **157**(3), 707–709 (1964).

Dokl. Chem. (Engl. Transl.)
2. Sen, A.A. Terentiev, N.P. Konovalova, Platinum complexes with bioactive nitroxyl radicals: synthesis and antitumor properties, in *Nitroxides-Theory, Experiment and Applications*, ed. by A. Kokorin (InTech, London)
3. G. Sosnovsky, S.W. Li, In the search for new anticancer drugs XII. Synthesis and biological evaluation of spin labeled nitrosoureas. Life Sci. **36**, 1479–1483 (1985)
4. G. Cheng, M. Lopez, J. Zielonka, A.D. Hauser, J. Joseph, D. Mcallister, J.J. Rowe, S.L. Sugg, C.L. Williams, B. Kalyanaraman, Mitochondria-targeted nitroxides exacerbate fluvastatin-mediated cytostatic and cytotoxiceffects in breast cancer cells. Cancer Biol. Ther. **12**, 707–717 (2011)
5. A. Dilip, G. Cheng, J. Joseph, S. Kunnimalaiyaan, B. Kalyanaraman, M. Kunnimalaiyaan, T.C. Gamblin, Mitochondria-targeted antioxidant and glycolysis inhibition: synergistic therapy in hepatocellular carcinoma. Anticancer Drugs **24**, 881–888 (2013)
6. J. Guo, Y. Zhang, J. Zhang, J. Liang, L. Zeng, G. Guo, Anticancer effect oftert-butyl-2(4,5-dihydrogen-4,4,5,5-tetramethyl-3-o-1h-imidazole-3-cationic-1-oxyl-2)-pyrrolidine-1-carboxylic ester on human hepatoma HepG2 cell line. Chem. Biol. Interact. **199**, 38–48 (2012)
7. S.K. Hong, D. Starenki, P.K. Wu, J.I. Park, Suppression of B-RafV600E melanoma cell survival by targeting mitochondria using triphenyl-phosphonium-conjugated nitroxide or ubiquinone. Cancer Biol. Ther. **18**, 106–114 (2017)
8. Y.Q. Liu, X.J. Li, C.Y. Zhao, X. Nan, J. Tian, S.L. Morris-Natschke, Z.J. Zhang, X.M. Yang, L. Yang, L.H. Li, X.W. Zhou, K.H. Lee, Synthesis and mechanistic studies of novel spin-labeled combretastatin derivatives as potential antineoplastic agents. Bioorg. Med. Chem. **21**, 1248–1256 (2013)
9. J. Sun, S. Wang, W. Bu, M.Y. Wei, W.W. Li, M.N. Yao, Z.Y. Ma, C.T. Lu, H.H. Li, N.P. Hu et al., Synthesis of a novel adamantyl nitroxide derivative with potent anti-hepatoma activity in vitro and in vivo. Am. J. Cancer Res. **6**, 1271–1286 (2016)
10. S. Tabaczar, K. Domeradzka, J. Czepas, J. Piasecka-Zelga, J. Stetkiewicz, K. Gwozdzinski, A. Koceva-Chyla, Anti-tumor potential of nitroxyl derivative Pirolin in the DMBA-induced rat mammary carcinoma model: A comparison with quercetin. Pharmacol. Rep. **67**, 527–534 (2015)
11. Y. Wu, W. Tang, C.L. Li, J.W. Liu, L.D. Miao, J. Han, M.B. Lan, Cytotoxicity of a newly synthesized nitroxide derivative of 4-ferrocenecarboxyl-2,2,6,6-tetramethylpiperidine-1-oxyl in high metastatic lung tumor cells. Pharmazie **61**, 1028–1033 (2006)
12. Y.Q. Liu, E. Ohkoshi, L.H. Li, L. Yang, K.H. Lee, Design, synthesis and cytotoxic activity of novel spin-labeled rotenone derivative. Bioorg. Med. Chem. Lett. **22**, 920–923 (2012)
13. L. Yang, M.J. Wang, Z.J. Zhang, S.L. Morris-Natschke, M. Goto, J. Tian, Y.Q. Liu, C.Y. Wang, X. Tian, X.M. Yang, K.H. Lee, Synthesis of novel spin-labeled derivatives of 5-FU as potential antineoplastic agents. Med. Chem. Res. **23**(7), 3269–3273 (2014)
14. K. Selvendiran, S. Ahmed, A. Dayton, M.L. Kuppusamy, M. TazI, A. Bratasz, L. Tong, B.K. Rivera, K. Kalai, P.Kuppusamy Hideg, Safe and targeted anticancer efficacy of a novel class of antioxidant-conjugated difluorodiarylidenyl piperidones: Differential cytotoxicity in healthy and cancer cells. Free Radic. Biol. Med. **48**, 1228–1235 (2010)
15. E. Monti, R. Supino, M. Colleoni, B. Costa, R. Ravizza, M.B. Gariboldi, Nitroxide tempol impairs mitochondrial function and induces apoptosis in HL60 cells. J. Cell. Biochem. **82**, 271–276 (2001)
16. X. Guo, R.A. Mittelstaedt, L. Guo, J.G. Shaddock, R.H. Heflich, A.H. Bigger, M.M. Moore, N. Mei, Nitroxide TEMPO: a genotoxic and oxidative stress inducer in cultured cells. Toxicol. Vitro **27**, 1496–1502 (2013)
17. X.B. Zhao, D. Wu, M.J. Wang, M. Goto, S.L. Morris-Natschke, Y.Q. Liu, X.B. Wu, Z.L. Song, G.X. Zhu, K.H. Lee, Design and synthesis of novel spin-labeled camptothecin derivatives as potent cytotoxic agents. Bioorg. Med. Chem. **15**, 6453–6458 (2014)
18. S. Thangavel, T. Yoshitomi, M.K. Sakharkar, Y. Nagasaki, Redox nanoparticles inhibit curcumin oxidative degradation and enhance its therapeutic effect on prostate cancer. J. Controll. Release **209**, 110–119 (2015)

19. M. Wang, K. Li, Z. Zou, L. Li, L. Zhu, Q. Wang, W. Gao, Y. Wang, W. Huang, R. Liu, K. Yao, Q. Liu, Piperidine nitroxide Tempol enhances cisplatin–induced apoptosis in ovarian cancer cells. Oncol. Lett. 4847–4854 (2018)
20. G.T.A. Eng, An investigation of the effect of some stable nitroxide antioxidants in prostate cancer cells. https://eprints.qut.edu.au/82982/4/Grace_Eng_Thesis (2105)
21. O.D. Zakharova, T.S. Frolova, Y.V. Yushkova, E.I. Chernyak, A.G. Pokrovsky, M.A. Pokrovsky, S.V. Morozov, O.I. Sinitsina, I.A. Grigore'v, G.A. Nevinsky, Antioxidant and antitumor activity of trolox, trolox succinate, and α-tocopheryl succinate conjugates with nitroxides. Eur. J. Med. Chem. **122**, 127–137 (2016)
22. V.D. Sen, A. Goluvev, N.Y. Lugovskaya, T.E. Sashenkova, N.P. Konovolova, Synthesis and antitumor properties of new platinum(IV) complexes with aminonitroxyl radicals. Russ. Chem. Bull. **55**(1), 62–65 (2006)
23. M. Cetraz, V. Sen, S. Schoch, K. Streule, V. Golubev, A. Hartwig, B. Köberle, Platinum(IV)-nitroxyl complexes as possible candidates to circumvent cisplatin resistance in RT112 bladder cancer cells. Arch. Toxicol. **91**, 785–797 (2017)
24. S. Schocha, V. Senb, S. Gajewskia, V. Golubevb, B. Straucha, A. Hartwiga, B. Köberlea, Activity profile of the cisplatin analogue PN149 in different tumor cell lines. Biochem. Pharmacol. **156**, 109–119 (2018)
25. S. Suy, J.B. Mitchell, A. Samuni, S. Mueller, U. Kasid, Nitroxide tempo, a small molecule, induces apoptosis in and suppresses tumor growth in athymic mice. Cancer **103**, 1302–1313 (2005)
26. F. Hyodo, K. Matsumoto, A. Matsumoto, J.B. Mitchell, M.C. Krishna, Probing the intracellular redox status of tumors with magnetic resonance imaging and redox-sensitive contrast agents. Can. Res. **66**(20), 9921–9927 (2006)
27. I. Sirovich, N. Konovalova, G. Codacci-Pisanelli, L.M. Volkova, A. Giuliani, F. Cicconetti, P. Seminara, F. Franchi, Activity of ruboxyl, a nitroxyl derivative of daunorubicin, on experimental models of colorectal cancer metastases. Tumor Biol **20**, 270–276 (1999)
28. K. Takeshita, K. Kawaguchi, K. Fujii-Aikawa, M. Ueno, S. Okazaki, M. Ono, M.C. Krishna, P. Kuppusamy, T. Ozawa, N. Ikota, Heterogeneity of regional redox status and relation of the redox status to oxygenation in a tumor model, evaluated using electron paramagnetic resonance imaging. Cancer Res. **70**(10), 4133–4140 (2010 May 15)
29. D. Harman, Aging: a theory based on free radical and radiation chemistry. J. Gerontol. **11**, 298–300 (1956)
30. C.S. Wilcox, Effects of tempol and redox-cycling nitroxides in models of oxidative stress. Pharmacol. Ther. **126**, 119–145 (2010)
31. J.A. Zarling, V.E. Brunt, A.K. Vallerga, W. Li, A. Tao, D.A. Zarling, C.T. Minson, Nitroxide pharmaceutical development for age-related degeneration and disease. Front Genet. **6**, 325 (2015)
32. N. Pınar, K.O. Soylu, O. Özcan, E. Atik Dogan, S. Bayraktar, Protective effects of tempol in an experimental ovarian ischemia-reperfusion injury model in female Wistar albino rats. Can. J. Physiol. Pharmacol. **95**, 861–865 (2017)
33. U. Aksu, B. Ergin, R. Bezemer, A. Kandil, D.M. Milstein, C. Demirci-Tansel, C. Ince, Scavenging reactive oxygen species using tempol in the acute phase of renal ischemia/reperfusion and its effects on kidney oxygenation and nitric oxide levels. Intensive Care Med. Exp. **3**, 57 (2015)
34. Y. Samuni, J.A. Cook, R. Choudhuri, W. Degraff, A.L. Sowers, M.C. Krishna, J.B. Mitchell, Inhibition of adipogenesis by Tempol in 3T3-L1 cells. Free Radic. Biol. Med. **49**, 667–673 (2010)
35. C.H.J. Kim, J.B. Mitchell, C.A. Bursill, A.L. Sowers, A. Thetford, J. Cook, The nitroxide radical TEMPOL prevents obesity. Atherosclerosis **240**, 234–241 (2015)
36. S. Neil, J. Huh, V. Baronas, X. Li, H.F. McFarland, M. Cherukuri, J.B. Mitchell, J.A. Quandt, Oral administration of the nitroxide radical TEMPOL exhibits immunomodulatory and therapeutic properties in multiple sclerosis models. Brain Behav. Immun. **62**, 332–343 (2017)

37. N. Fujii, V. Brunt, C. Minson, Tempol improves cutaneous thermal hyperemia through increasing nitric oxide bioavailability in young smokers. Am. J. Physiol. Heart Circ. Physiol. **306**, H1507–H1511 (2014)
38. A. Yadav, N. Harris, Effect of tempolon diabetes-induced decreases in retinal blood flow in the mouse. Curr. Eye Res. **36**, 456–461 (2011)
39. W.-J. Han, L. Chen, H.-B. Wang, X.-Z. Liu, S.-J. Hu, X.-L. Sun, C. Luo, A novel nitronyl nitroxide with salicylic acid framework attenuates pain hypersensitivity and ectopic neuronal discharges in radicular low back pain. Hindawi Publishing Corporation Neural Plasticity Volume Article ID 752782, 14 pages
40. S.N. Hassler, K.M. Johnson, C.E. Hulsebosch, Reactive oxygen species and lipid peroxidation inhibitors reduce mechanical sensitivity in a chronic neuropathic pain model of spinal cord injury in rats. J. Neurochem. **131**, 413–417 (2014)
41. M. Hahn, M.C. Krishna, A.M. Deluca, D. Coffin, J.B. Mitchell, Evaluation of the hydroxylamine tempol-H as an in vivo radioprotector. Free Radic. Biol. Med. **28**(6), 953–958 (2000)
42. Q. Liang, A.D. Smith, S. Pan, V.A. Tyurin, V.A. Kagan, T.G. Hastings, N.F. Schor, Neuroprotective effects of TEMPOL in central and peripheral nervous system models of Parkinson's disease. Biochem. Pharmacol. **70**(9), 1371–1381 (2005)
43. T.-Y. Shi, D.-Q. Zhao, H.-B. Wang, S. Feng, S.B. Liu, J.H. Xing, Y. Qu, P. Gao, X.L. Sun, M.G. Zhao, A new chiral pyrrolyl-nitronyl nitroxide radical attenuates -amyloid deposition and rescues memory deficits in a mouse model of Alzheimer disease. Neurotherapeutics **10**(2), 340–353 (2013)
44. M. Fidanboylu, L.A. Griffiths, S.J.L. Flatters, Global inhibition of reactive oxygen species (ROS) inhibits paclitaxel induced painful peripheral neuropathy. PLoS ONE **6**(9), Article ID e25212, (2011)
45. L.B. Vong, T. Tomita, T. Yoshitomi, H. Matsui, Y. Nagasaki, An orally administered redox nanoparticle that accumulates in the colonic mucosa and reduces colitis in mice. Gastroenterology **143**, 1027–1036 (2012)
46. C.S. Wilcox, A. Pearlman, Chemistry and antihypertensive effects of tempol and other nitroxides. Pharmacol. Rev. **60**, 418–469 (2008)
47. M. Greenwald, S. Anzi, S. Ben Sasson, H. Bianco-Peled, R. Kohen, Can nitroxides evoke the Keap1–Nrf2–ARE pathway in skin? Free Radic. Biol. Med. **77**, 258–269 (2014)
48. M. Lewandowski, C. Gwozdzinski, Nitroxides as antioxidants and anticancer drugs. Int. J. Mol. Sci. **18**(11), 2490 (2017)

Chapter 10
Spin Labeling

10.1 Introduction

A number of problems concerning the structure and dynamics of complex molecular systems including examples from biology can be solved by a modification of a chosen portion of the object of interest by a physical label such as a stable radical, paramagnetic complex, luminophore, or Moessbauer atom followed by monitoring the label's properties by appropriate physical methods. In this series, a special place is occupied by nitroxide stable radicals and methods of electron paramagnetic resonance (EPR) and nuclear magnetic resonance (NMR), and its combination.

The birth of the spin-labeling method pioneered by McConnell group in 1965 [1] was preceded by the development of synthetic chemistry of nitroxide starting with classical synthesis of Frémy's salt [2] (Chap. 1). The work by Neiman et al. [3], in which the principal possibility of the reaction of stable radicals without affecting the center of free valence, was demonstrated, happened to be of crucial importance. Since then, synthetic chemistry of nitroxides and their use for modification of biological and non-biological molecules have received a powerful development. In the last decade, triarylmethyl (TAM) radicals and labels based on complexes of paramagnetic metal, gadolinium in particular, also found wide application. According to the generally accepted classification, a covalently bound compound is called "a label," while an adsorbing or free-moving compound is considered "a probe."

Numerous applications of labels and probes are based on four types of spin–spin interactions: (1) the dipole–dipole interaction arises from the magnetic dipole field of one paramagnetic center inducing a local magnetic field at the site of another paramagnetic group, (2) the exchange interaction is caused by overlap of the orbitals occupied by unpaired electrons as the particles approach each other, (3) the electron–nuclear dipole hyperfine interaction which can affect the powder pattern and spectra arising from rotational motion, and (4) the contact hyperfine (spin electron–spin nucleus) interaction, which arises from a finite electron spin density at the nucleus.

G. I. Likhtenshtein, *Nitroxides*, Springer Series in Materials Science 292,
https://doi.org/10.1007/978-3-030-34822-9_10

On the basis of these fundamental phenomena, the following methods were invented and developed to determine: (1) the electron spin–electron spin and electron spin–nuclear spin distances (spin ruler), (2) local viscosity and molecular motion (spin viscose meter), (3) local acidity (spin pH meter), (4) oxygen dynamics (spin oximeter), (5) functional group analysis (spin assay), and (6) spatial distribution of labeled molecular objects (spin imaging). This fundamental approach can provide a wealth of information for establishing the system's structural and dynamic properties. Since pioneered McConnell group work, application of spin labeling in chemistry, biology, and physics has received increasing attention. At present, the SciFinder program offers 4100 references with the keywords "nitroxide spin label and spin probe." The progress of the spin-labeling approach is largely associated with the use of modern methods of magnetic resonance, with their pulsed versions in particular (Chap. 4).

10.2 Nitroxide Labeling

10.2.1 Proteins and Peptides

The method of double spin labeling (DSL), pioneered by Likhtenshtein in 1968 [4], is based on specific modification of chosen groups in the object of interest by two or several spin labels, nitroxides or complexes of paramagnetic metal followed by analysis of the effects of the spin–spin interactions on the label ESR spectra or spin relaxation times. The principle feasibility of the method was demonstrated, for example, albumin covalently labeled with copper complexes. Later on, at the beginning of the 1970, a method using spin dipole–dipole interaction between nitroxides was developed on a quantitative level and then widely employed [5–21]. The method for determining the distance between nitroxides based on the phenomenon of spin exchange was first used by Likhtenshtein group [16, 17] on the example of non-heme iron proteins and nitrogenase.

The first applications of dipole–dipole spin–spin interactions for the investigation of protein surface topography were based on changes in the lineshape of nitroxide radical ESR spectra, arising from interactions with a second nitroxide radical or a paramagnetic ion, allowed one to estimate distances between the paramagnetic centers up to 2.5 nm. Later, the higher sensitivity of power saturation curves of a radical to interactions with paramagnetic species and development advance pulse EPR spectroscopy allowed to expand the distance determination maximum in specific cases up to 15 nm [15–21].

As a first example of quantifying the distance between selected groups in proteins, estimation of distances between the heme group of human hemoglobin and the nitroxide fragment of three spin labels attached covalently to the β-93 SH-group was carried out using analysis of CW power saturation curves in solids based on static dipolar interaction [10, 13, 22]. The values of r (in Å with an accuracy 5–6%)

Table 10.1 Comparison of distances (r in Å) between heme iron and spin labels on hemoglobin [22]

Labels	$\Delta(1/T_{1s})$	$\Delta(1/T_{2s})$	$\Delta(1/T_{1s})\Delta(1/T_{2s})$	r
IA-TEMPO[a]	17.0	15.1	15.9	18.6
M-TEMPO[a]	15.2	15.2	15.2	16.3
PCMB-TEMPO[a]	16.5	15.1	15.8	17.3

[a]*TEMPO* 2,2,6,6-tetramethylpiperidine-N-oxyl; *IA* 4-iodoacetamido; *M* 4-maleimido; *PCMB* p-chloromercuribenzoate

between heme and the nitroxide fragment were found to be in reasonable agreement with the X-ray diffraction structure of hemoglobin (Table 10.1).

Two heme-containing proteins, human neuroglobin (NGB) and sperm whale myoglobin (Mb), were used to test a method exploiting wideband excitation techniques based on composite pulses and relaxation properties of low-spin Fe(III) in high magnetic fields [23]. The proteins were both prepared to have low-spin Fe(III) heme centers. Four different samples (NGB-C120R1, Mb-S3R1, Mb-S117R1, and the doubly spin-labeled Mb-S3R1-S117R1) were obtained using mutagenesis to provide free cysteine amino acids for attachment of the (1-oxyl-2,2,5,5-tetramethyl-Δ3-pyrroline-3-methyl) methanethiosulfonate (MTS) spin label. The results on the label—heme distance measurement (3.2 nm) and schematical presentation of the DEER finding—are shown in Fig. 10.1.

To investigate the difference between native and melted global (MG) state in open- and closed-form mutants, maltose-binding protein (MBP) 09-11, continuous-wave

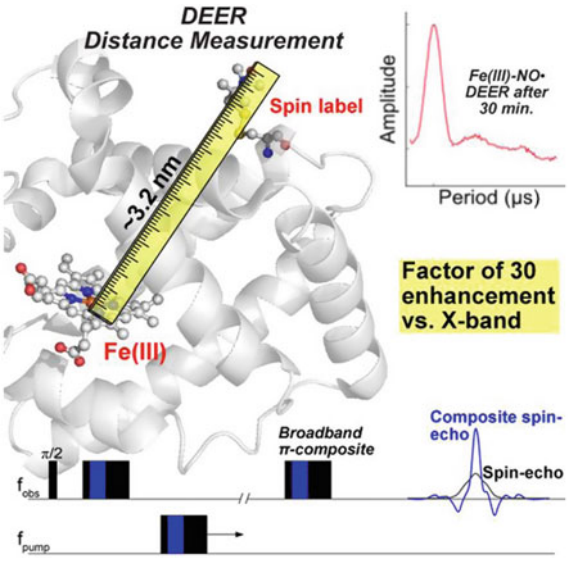

Fig. 10.1 Schematical presentation spin labeled heme protein and DEER traces [23]. Reprinted from [23], Copyright 2016 American Chemistry Society

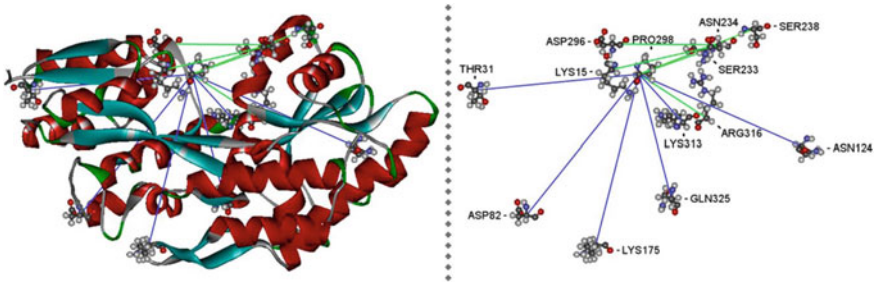

Fig. 10.2 Overview of the complete set of MBP mutants in open-state MBP (Protein Data Bank entry: 1OMP). Blue lines indicate Cα amino acid distances of mutants MBP 01–06. Green lines indicate Cα amino acid distances of mutants MBP 07–11 [24]. Reprinted from [24], Copyright 2018 American Chemical Society

and double electron–electron resonance (DEER) EPR spectroscopy in combination in spin labeling were employed [24]. The spin label (*S*-(1-oxyl-2,2,5,5-tetramethyl-2,5-dihydro-1H-pyrrol-3-yl)methyl methanesulfonothioate, MTSL) positions were placed near the active site (Fig. 10.2). Binding of the protein ligands leads to a conformational change from open to closed state, where the two domains are more closely together. All distances in MBP samples were measured by double-quantum coherence (DQC) EPR using the six-pulse sequence $\pi/2–t_p–\pi–t_p–\pi/2–t_d–\pi–t_d–\pi/2–(t_m–t_p)–\pi–(t_m–t_p)$–echo. The experimental complete set of MBP mutants obtained at pH 3.2 (MG) and pH 7.4 (native state) was in agreement with theoretic predictions of distances between the labels in biradicals constructed by molecular modeling from the crystal structures of MBP in open and closed forms. Measurements showed a defined structure around the binding pocket of MBP in MG, which explains maltose binding. In both states, ligand-free MBP can be found in open and closed forms, while ligand-bound MBP only appears in closed form due to maltose binding. In combination with MD simulation, analysis of MTS distances in mutants MBP 01–11 reveals the changes between open and closed state and ligand binding.

Hsp70s are allosteric molecular chaperones with conformational landscapes that involve large rearrangements of their two domains (viz. the nucleotide-binding domain and substrate-binding domain) in response to adenine nucleotides and substrates. Two complementary methods, ion-mobility mass spectrometry (IMMS) and double electron–electron resonance (DEER), were employed to map the conformational species present under biologically relevant ligand-bound conditions (ATP, ADP/substrate, and ATP/substrate) [25]. Spins are introduced by attaching MTSL to Cys pairs engineered into the protein at strategic and tolerant locations. A DnaK mutant carrying the mutation T199A impairs ATP hydrolysis and thus allows the study of the protein-binding ATP and ATP/substrate. The mobility of the protein ions in the gas phase through a helium-filled tube under a weak electric field was studied using IMMS. The mobility depends on mass and conformation on protein

under investigation. DEER yielded the distance distributions between two spin systems for a frozen sample and is sensitive to distances between 20 and 80 Å. Energetic profile and allosteric conformational rearrangement, the interconversion between the domain-docked and domain-undocked states of DnaK in of DnaK were also established.

The architecture of Aer2, a soluble gas-sensing receptor that has emerged as a model for PAS (Per-Arnt-Sim) and poly-HAMP (histidine kinase-adenylyl cyclase-methyl-accepting chemotaxis protein-phosphatase) domain signaling, was investigated by X-ray analysis and pulsed dipolar ESR measurements [26]. Aer2 was labeled by MTSL at position S183, and the interdomain PAS–PAS distance was assessed by monitoring the magnetic dipolar interactions between spins (Fig. 10.3). PDS distance measurements of MTSSL spin-labeled Aer2 1–402 S183C gave sharp $P(r)$ distribution centered at 26.7 Å and were in good agreement with the expected distance based on the crystal structure. It was found that the helical lid of DnaK is a highly dynamic unit of the structure in all ligand-bound states, and DnaK populates

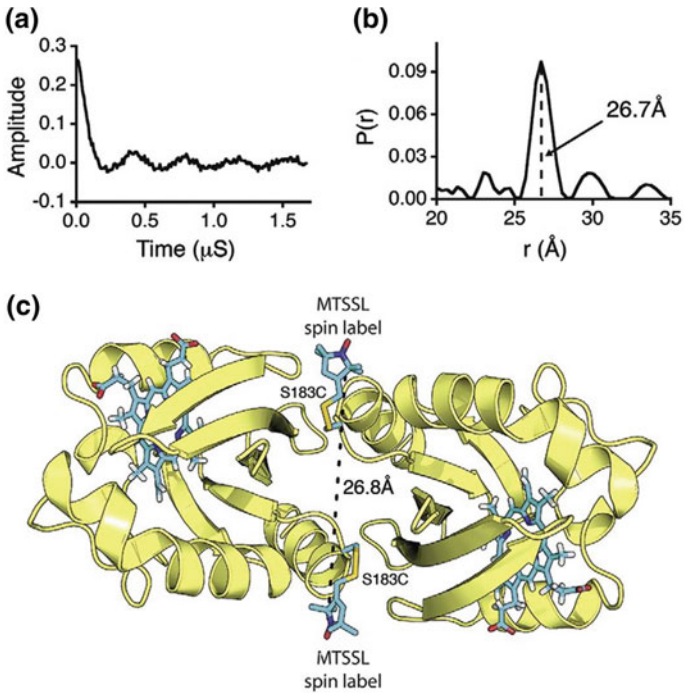

Fig. 10.3 Interdomain distance is only consistent with a PAS dimer. **a** Time-domain signal and **b** corresponding probability distance distribution [$P(r)$] for spin-labeled Aer2 1–402 S183C. A sharp $P(r)$ centered at 26.8 Å is smaller than the diameter of a HAMP domain and fully consistent with the ferric Aer2 PAS dimer. **c** Model of MTSSL spin-labeled Aer2 S183C PAS dimer. The dimer interface directs the two spin labels (blue) away from each other to add approximately 15 Å to the S183 Cα–Cα atom distance [26]. Reprinted from [26], Copyright 2013 Elsevier

a partially docked state in the presence of ATP and substrate. This state represents an energy minimum on the DnaK allosteric landscape.

An overview of available spin labels, the strategies for their introduction into proteins, and the associated potentials for protein structural studies in vitro and in the context of living cells was published.

Figures 10.4 and 10.5 describe commonly employed nitroxide spin labels and protein SDSL strategies.

Site-specific incorporation of Cu^{2+} into non-metalloproteins was accomplished through the use of a genetically encodable non-natural amino acid, 3-pyrazolyltyrosine (PyTyr), in cyan fluorescent protein CFP) (Fig. 10.6) [27]. Then, distances between Cu^{2+}- and nitroxide spin label were measured by the DEER spectroscopy, and the effects of solvent conditions on Cu^{2+} binding and protein aggregation were examined. This method was also applied to characterize the complex formed by the histidine kinase CheA and its target response regulator CheY.

N-terminal-labeled gramicidin A (GALN) and double-labeled gramicidin C (GCDL) modified by 2,2,5,5-tetramethyl-3-pyrrolin-1-oxyl-3-carboxylic acid radicals (Fig. 10.7) were reconstituted into phospholipid bilayers proteoliposomes with consequence investigation by ESR and dynamic nuclear polarization-cryogenic solid-state nuclear magnetic resonance DNP-SSNMR [28]. It was found that the doubly spin-label tagged protein can be used as enhancement agents. Analysis of the labeled GALN and GCDL incorporated into the membrane allowed to establish distances between the labels and the protein mutual disposition (Fig. 10.7). It was also demonstrated that the doubly spin-label tagged protein can be used as enhancement agents. Specifically, ^{1}H–^{13}C cross-polarization ^{1}D ^{13}C NMR spectra of GALN and GCDL showed obtained signal enhancements of sixfold for the dimeric protein and the overall impact of spin label to the sample T_1.

IA new Gd(III)-based spin label, BrPSPy-DO3A-Gd(III), derived from a label, BrPSPy-DO3MA-Gd(III), by removing the methyl group from the methyl acetate pending arms, was prepared [29]. This small chemical modification (Fig. 10.8) led to a reduction in the zero-field splitting and to a significant increase in the phase memory time, which together culminated in a remarkable improvement of in-cell DEER sensitivity, while maintaining the high distance resolution. The performance of BrPSPy-DO3A-Gd(III) in in-cell DEER measurements was demonstrated on doubly labeled ubiquitin and GB1 delivered into HeLa cells by electroporation.

Site-directed spin-labeling (SDSL) and EPR spectroscopy were applied to study oligomerization of the bacterial toxin colicin A (ColA) upon membrane insertion in vitro and in vivo (Fig. 10.9) [30] ColA labeling was carried out with purified proteins in vitro, and the labeled protein was incubated with *Escherichia coli* cells. Labeling ColA with MTSSL at position 192, located on helix H10. DEER interspin distance measurements were performed on proteoliposomes containing ColA-A192R1. Reconstitution of spin-labeled ColA into liposomes for the EPR experiments was carried out with a high-protein lipid ratio of (1:500) to maximize the EPR signal strength. Analysis of the data in terms of a distance distribution yields a mean distance of 2.6 nm, comparable to the results obtained for proteoliposomes. Applying SDSL-EPR led to conclusion that the pore-forming domain of colicin A

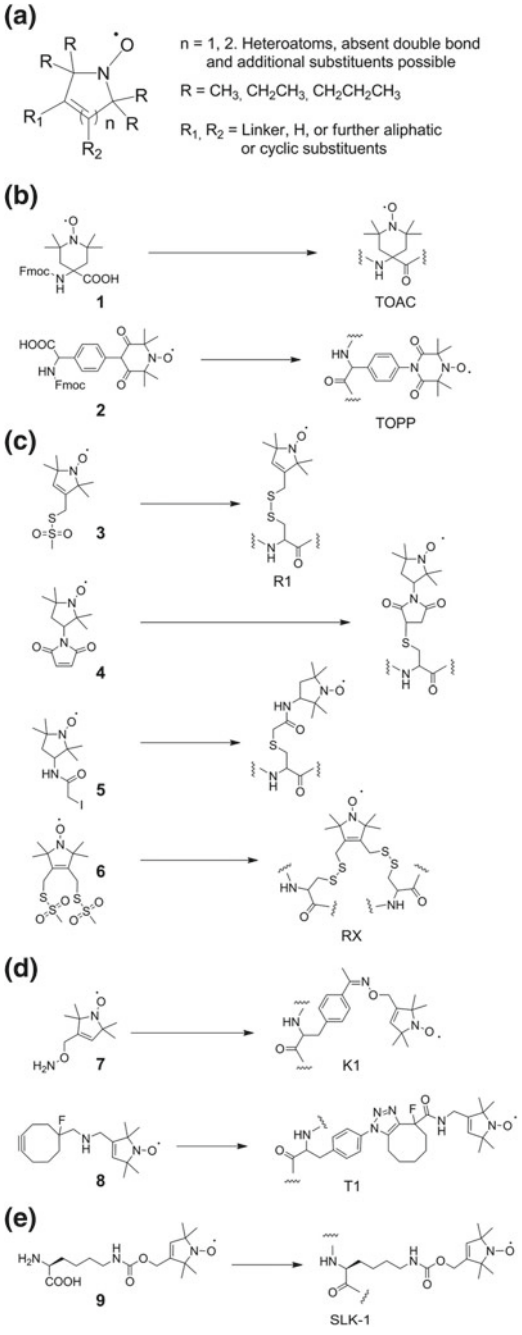

Fig. 10.4 Nitroxide spin labels. **a** General structure of commonly employed nitroxide spin labels. **b** Nitroxides for peptide labeling by solid-phase synthesis. **c** Sulfhydryl-reactive nitroxides for protein labeling by cysteine conjugation reactions. **d** Nitroxides for protein labeling by conjugation with genetically encoded ncAA. **e** Nitroxide ncAA for protein labeling by direct genetic encoding [118]. Reprinted from [118], Copyright 2016 RCSr

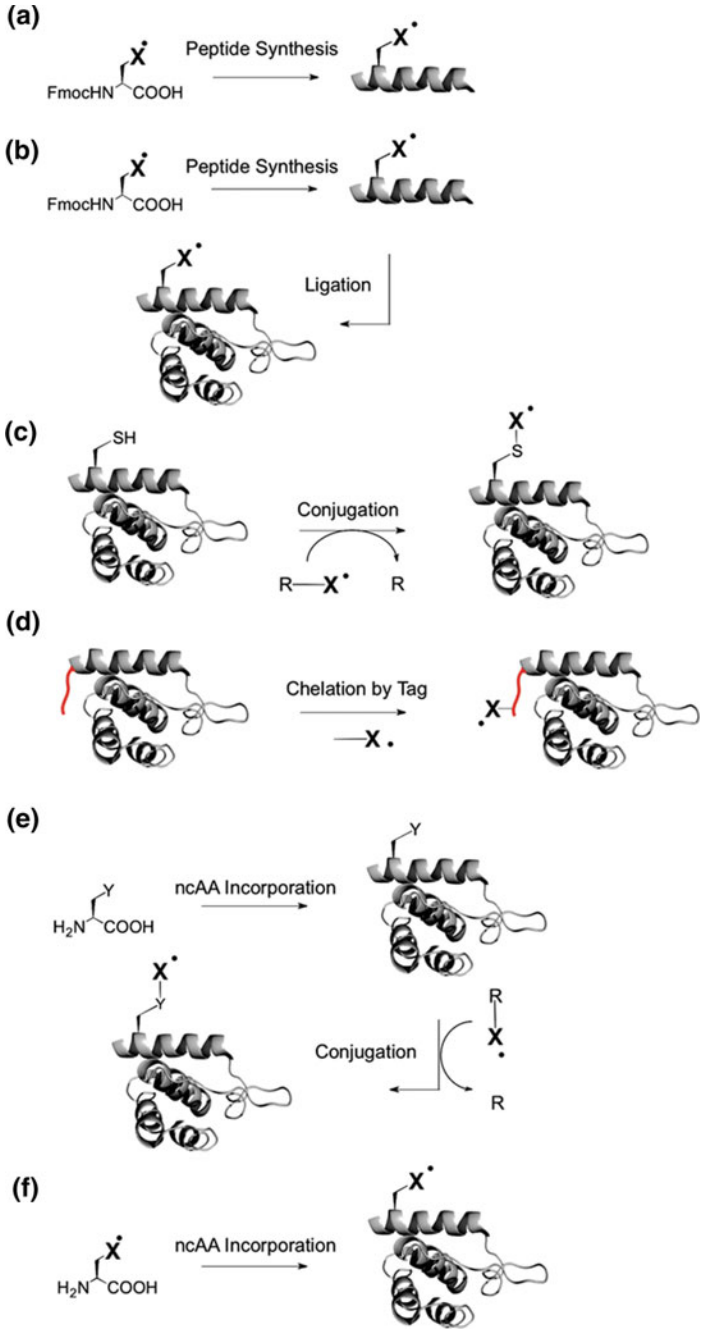

Fig. 10.5 Protein SDSL strategies. **a** Solid-phase peptide synthesis. **b** Peptide–protein ligation. **c** Conjugation reactions with canonical amino acids. **d** Chelation by genetically encoded peptide tags. **e** Conjugation reactions with genetically encoded ncAA. **f** Direct genetic encoding of spin-labeled ncAA [118]. Reprinted from [118], Copyright 2016 RCS

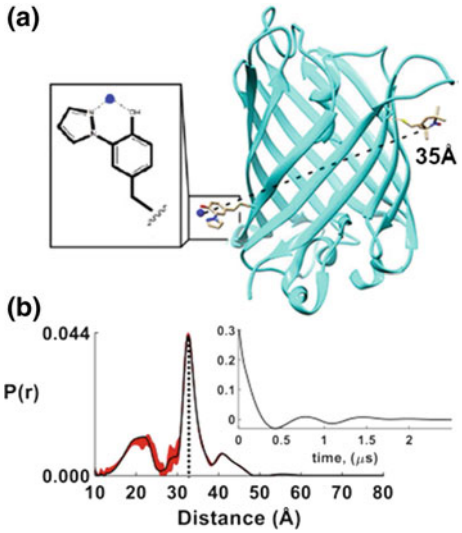

Fig. 10.6 Targeted Cu^{2+} incorporation into CFP. **a** Cu^{2+}-binding amino acid PyTyr shown with Cu^{2+}–NO separation in CFP expected from the crystal structure of CFP (PDB: 3ZTF18) modeled with a nitroxide on residue 208. **b** Distance distribution and denoised time-domain spectrum (inset) obtained by Cu^{2+}–NO DEER spectroscopy in H_2O-based buffer The red regions indicate the small uncertainty arising from the SVD of the denoised signal [27]. Reprinted from [27], Copyright 2018 American Chemical Society

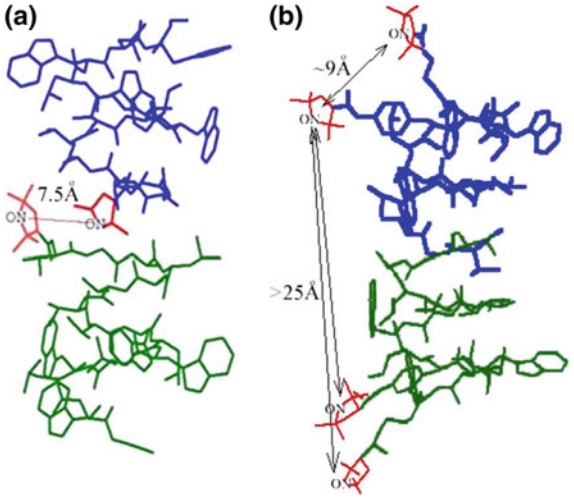

Fig. 10.7 Spin-labeled gramicidin compounds used in this study; **a** N-terminally labeled gramicidin A (GALN). Two spin labels, each from a different monomer, form a membrane embedded spin pair in the dimer, with an experimentally characterized interspin distance of 7.5 Å. **b** Doubly labeled gramicidin C (GCDL) has spin pairs on each gramicidin monomer, located close to the membrane surface and separated by an average interspin distance of 9 Å. The intermolecular interspin distance between spin labels on neighboring GCDL molecules is 25 Å. The right-handed b6.3-helical structure (PDB: 1MAG) is depicted for both compounds, as confirmed by ESR [28]

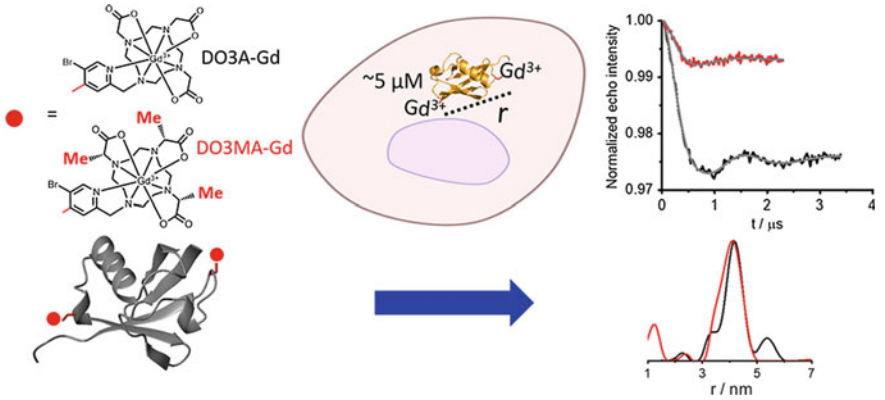

Fig. 10.8 Structure of BrPSPy-DO3A-Gd(III), BrPSPy-DO3MA-Gd(III) label protein and spin the results of DEER measurements [29]. Copyright 2018 American Chemistry Society

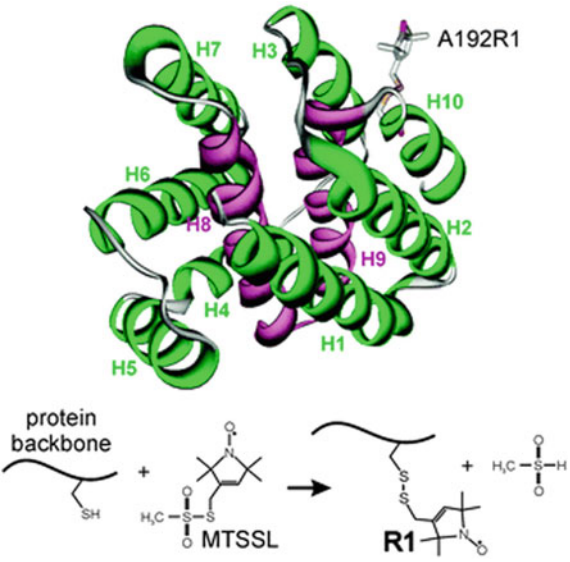

Fig. 10.9 Top panel: crystal structure of the ColA pfd (PDB: 1COL7), with a spin label side chain attached at position A192. Amphipathic helices are colored in green, and the hydrophobic hairpin is shown in magenta. Bottom panel: site-directed spin labeling. After site-directed mutagenesis to replace the residue of interest by cysteine, reaction of the methanethiosulfonate spin label (MTSSL) with the thiol of the cysteine yields the spin-label side R1 [30]. Reprinted from [30], Copyright 2015 RCS

forms oligomers in artificial membranes as well as in the membrane of live *E. coli* cells, most likely in the form of dimers.

ESR was used to investigate the direct interaction between a protein and a particular lipid, illustrating the case of lipid binding into a hydrophobic pocket of chlorocatechol 1,2-dioxygenase, a non-heme iron enzyme responsible for catabolism of aromatic compounds [31]. The effects of GPI-anchored tissue-non-specific alkaline phosphatase, a protein that plays a crucial role in skeletal mineralization, on the ordering and dynamics of lipid acyl chains were revealed. The interaction saturated, or unsaturated fatty acids with model membranes of the brain fatty acid binding

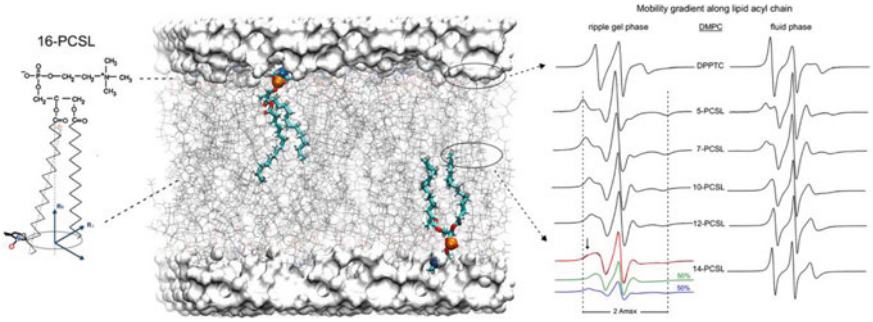

Fig. 10.10 Spin-labeling ESR from the membrane perspective and structural dynamics-line-shape correlations. The lipid bilayer was built with CHARMM-GUI Membrane Builder and rendered with Visual Molecular Dynamics. Reprinted from [31], Copyright 2016 Elsevier

protein, was evaluated. Different *n*-PCSL ($n = 5$, 7, 10, 12, 14, and 16) spin labels reported on specific regions of the lipid bilayer (Fig. 10.10).

An elegant method for determining the position of proteins in membranes was proposed in [32]. The method utilized an oxygen permeability gradient, which is a smooth continuous function of the distance from the center of the membrane. The relaxation gradient of oxygen in zwitterionic and anionic phospholipid membranes was detected by attaching a single nitroxide probe to the transmembrane α-helical polypeptide followed by studies of the oxygen effect on spin relaxation parameters of the spin labels. The peptide was used to determine the depth of penetration of the calcium-binding loops of the C2 domain of cytosolic phospholipase A2. Experiments showed that the relaxation gradient constrains the possible values of the membrane-dependent oxygen concentration and the oxygen diffusion gradients. The average oxygen diffusion coefficient is estimated to be at least twofold smaller in the membrane than that in water.

Complexin is a small soluble presynaptic protein that interacts with neuronal SNARE proteins in order to regulate synaptic vesicle exocytosis. Optical and magnetic resonance spectroscopy were employed to precisely define the boundaries of the two disordered C-terminal domain (CTD) membrane-binding motifs of complexin and to characterize their conformations [33]. The structure of the CTD in the presence of dodecylphosphocholine (DPC) micelles was characterized by standard solution-state NMR experiments. The AH and CT motifs of phospholipid vesicle bound CPX-1 CTD were investigated by electron spin resonance (ESR) spectroscopy with site-directed spin labeling. Together, these experiments provided a model of the structure and boundaries of the membrane-binding motifs of the CPX-1 CTD with MTSL. The crystal structure of full-length glycoprotein B (gB), the fusogen from herpes simplex virus, complemented by electron spin resonance measurements was examined [34]. To determine the structure of the CTD C terminus and its orientation within the membrane, the continuous-wave electron spin resonance spectroscopy on isolated CTD, residues 801–904, bound to synthetic membrane vesicles composed

of 1-palmitoyl-2-oleoyl-sn-glycero-3-phosphocholine (POPC) and 1-palmitoyl-2-oleoyl-sn-glycero-3-phosphate (POPA) was employed. Single-cysteine CTD mutants from H861C to K885C were expressed in *E. coli*, purified, and spin labeled with 3-(2-iodoacetamido)-PROXYL. Four-pulse DEER measurements at 17.3 GHz and 60 K were performed using the $\pi/2$–π–π pulse widths were 16 ns, 32 ns, and 32 ns, respectively, and the π pump pulse was 32 ns. Distance distributions for all mutants in solution were found to be broad and centered at ~40 Å but narrowed in the presence of anionic liposomes, indicating that highly dynamic regions become more ordered upon membrane binding. This concurs with the increase in helicity and decrease in proteolytic susceptibility of the CTD in the presence of anionic liposomes.

Phosphocholine spin labels on the lipid headgroup and different positions on the acyl chain (Fig. 10.11) were employed to detect the HIV gp41 fusion peptide (FP) perturbation on lipid bilayers containing different cholesterol concentrations by DEER [35]. The work findings showed that: (1) gp41 FP affects the lipid order via cooperative effect versus the peptide/lipid ratio, (2), gp41 FP induces membrane ordering in all lipid compositions, and (3) in high-cholesterol-containing lipid bilayers, gp41 FP is in the b-aggregation conformation. Schematic representation of the modes of HIV gp41 FP insertion into lipid bilayers is presented in Fig. 10.12.

A distance r between two 2,2,6,6-tetramethylpiperidine-1-oxyl-4-amino-4-carboxylic acid spin labels synthetically incorporated at positions 1 and 16 of this 19-mer peptide was measured at the nanometer scale via the electron dipole–dipole interaction between two labels [18]. Data on distance distribution functions $F(r)$ between the two spin labels for frozen Alm at 77 K are displayed in Fig. 10.13. Two data sets were collected at 77 K: (i) from aggregates of Alm in hydrated egg-yolk phosphocholine (ePC) vesicles (at peptide-to-lipid ratios of 1:200 and 1:75) and (ii) from non-aggregated Alm in pure (non-hydrated) ePC and in solvents of different polarity. The intramolecular distance between the two labels obtained in this manner was found be independent of the molecular aggregated state and the environment polarity as well.

DEER distance measurements between spectroscopically orthogonal Gd(III) and nitroxide spin labels in the nanometer range were performed on a series of membrane-incorporated orthogonally labeled WALP23 polypeptides [36]. Four WALP23 constructs were synthesized by solid-phase synthesis with cysteine at position 7, 11, 15, or 19 for labeling with MTSSL and with a DOTA–Gd(III)–lysine derivative at the N-terminus. The distance distributions (r = 3–3.5 nm) obtained in 10 GHz (X-band) and 35 GHz (Q-band) experiments exhibit a shift of the mean distance by the α-helical pitch when the nitroxide labeling site is shifted by four residues. The developed orthogonal labeling approach allowed for site-specific studies of the nitroxide environment by pulse and CW-EPR in the presence of the lanthanide label and for an independent check of the polypeptide aggregation within the lipid bilayer by nitroxide–nitroxide DEER measurements. The local environment of the nitroxide spin labels was also characterized.

Relaxation time measurements and electron spin echo envelope modulation (ESEEM) experiments using pulse EPR in combination Overhauser dynamic nuclear polarization (DNP) at X-band frequency and a magnetic field of 0.33 T were

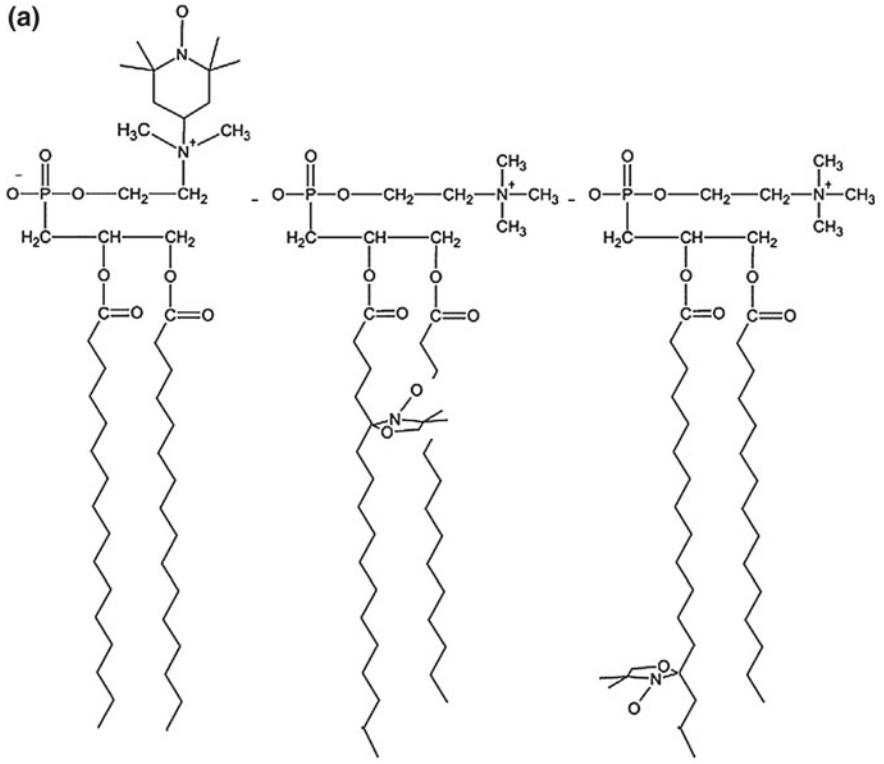

Fig. 10.11 **a** Structures of spin-labeled lipids DPPTC, 5PC, and 14PC. **b** Peptides used in this study, with mutations shown in bold letters [35]. Reprinted from [35], Copyright 2014 Elsevier

employed to investigate water accessibility in the hydrophobic α-helical peptide WALP23 inserted in unilamellar liposomes of DOPC, a membrane-inserting peptide [37]. Information on the water accessibility of the labeled site was obtained by the measurement of the change in the intensity of the ^{1}H NMR spectrum of H_2O at a Larmor frequency of 14 MHz under a continuous-wave microwave irradiation

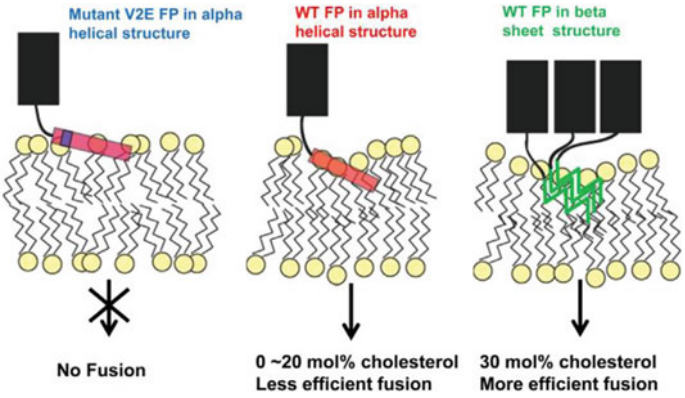

Fig. 10.12 Schematic representation of the modes of HIV gp41 FP insertion into lipid bilayers, and its effects on membrane order and fusion activities. The FP in b-sheet conformation is represented as a trimer simply because gp41 is a trimer. Its real stoichiometry during the membrane fusion process has not been confirmed. FP conformations shown are a-helical (red), b-sheet (green); the gp41 ectodomain is black [35]. Reprinted from [35], Copyright 2014 Elsevier

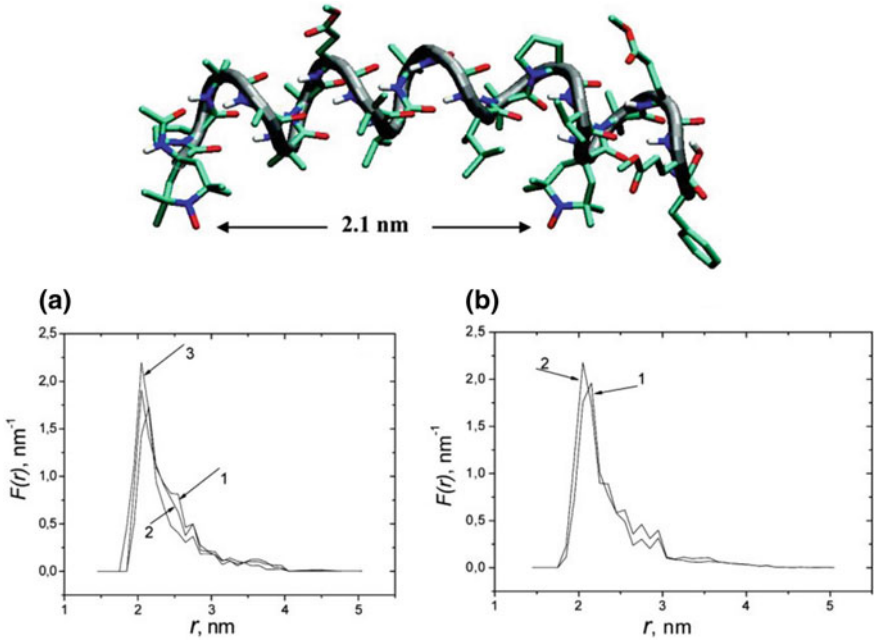

Fig. 10.13 Distance distribution functions $F(r)$ between the two spin labels for frozen Almat 77 K. (left) Curves 1, 2, and 3 are related to the PELDOR decays of Almin frozen methanol, methanol/toluene (1:4), and non-hydrated ePC. (right) Curves 1 and 2 are related to the PELDOR decays of Alm + unlabeled alamethicin (1:10) in hydrated ePC vesicles (P/L molar ratios of 1:75 and P/L = 1:200)). In the upper part of the figure, a model of Alm [1, 16], built from the crystal structure of Alm (molecule A) (27), is shown [18]. Reprinted from [18], Copyright 2008 American Chemical Society

of the nitroxide spin label. Water accessibility measurements with all techniques are conducted for eight peptides with different spin-label positions and low radical concentrations (10–20 μM). Consistently in all experiments, the water accessibility appears to be very low, even for labels positioned near the end of the helix.

10.2.2 Lipid Membranes

Spin-labeling method provides wide facilities for quantitative measurements of chemical, biochemical, and physical processes in biological and model membranes. Principles of the spin-labeling application to investigating biological membranes and recent results have been reviewed [38–45]. Location of the labels, water, and oxygen in membranes, membrane microstructure, and dynamics has been discussed in detailed. Here the recent current approaches and results in this area are illustrated by several examples.

The effectiveness of nitroxide-labeled lipids (TOTAPOL3) as polarization agents for lipids and a membrane-embedded peptide was demonstrated [43]. The chemical structure of the nitroxide lipid labels used in this work is shown in Fig. 10.14.

Rotational motion of the label was characterized by values of the ($2A_{max}$). DNP enhancements for SL-lipids in MLVs versus 20 mM TOTAPOL3 suspended with MLVs, measured via ^{13}C CP NMR spectra, are indicated in Fig. 10.15.

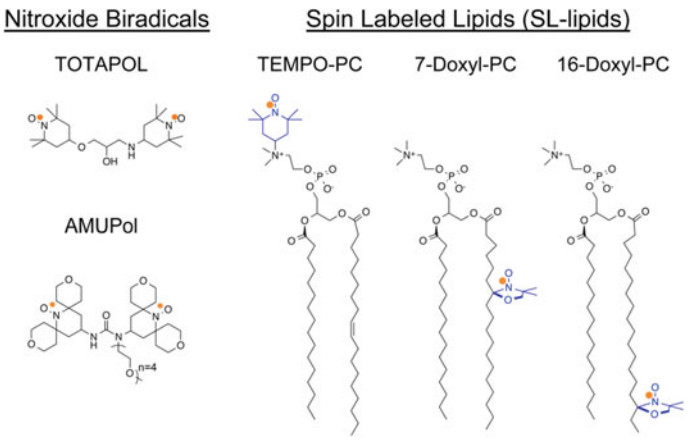

Fig. 10.14 Molecular structures of (left) common water-soluble nitroxide biradicals and (right) SL-lipids used in this study. The unpaired electron, indicated by an orange dot, is distributed over the N–O bond [43]. Reprinted from [43], Copyright 2016 American Chemical Society

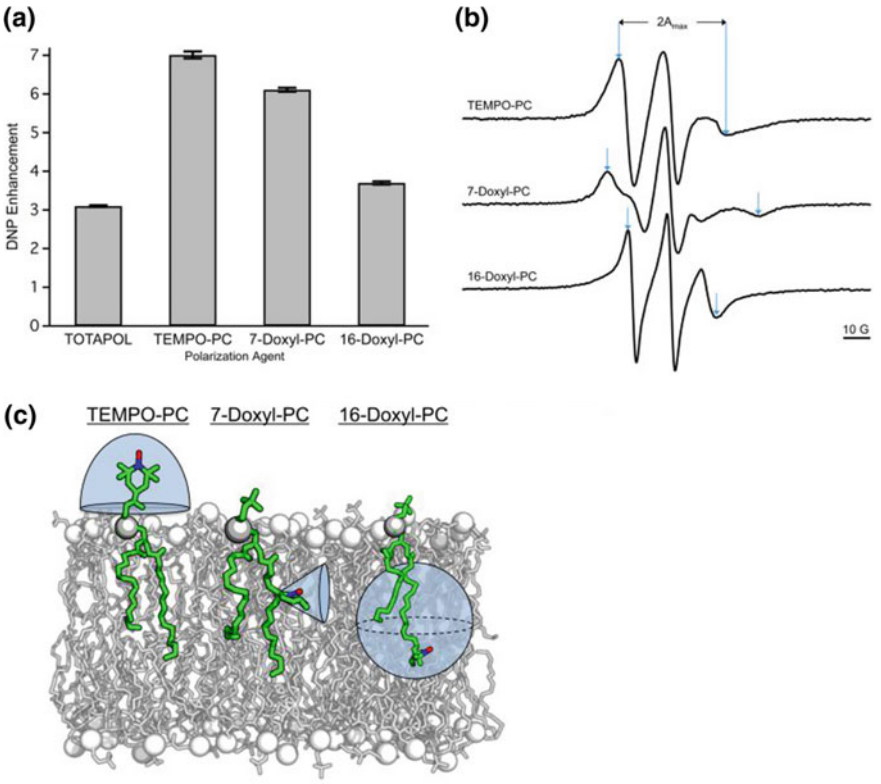

Fig. 10.15 **a** DNP enhancements for 3 mol% of indicated SL-lipids in MLVs versus 20 mM TOTAPOL3 suspended with MLVs, measured via ^{13}C CP NMR spectra. Error bars were calculated by measuring the RMS noise in the baseline of each ^{13}C CP spectrum and propagating through the DNP enhancement calculation. **b** Area normalized X-band CW EPR spectra of 3 mol% of the indicated SL-lipids reconstituted in MLVs at 282 K. Values of the super fine splitting of the label ESR spectra ($2A_{max}$) are indicated with blue arrows for each spectrum. **c** The distribution of available conformations for nitroxides in TEMPOPC, 7-Doxyl-PC, and 16-Doxyl-PC relative to the lipid bilayer normal is depicted by the shaded blue region around the respective nitroxide moiety [43]. Reprinted from [43], Copyright 2016 American Chemical Society

The relative DNP NMR sensitivity enhancement between 15-{[(7-oxyl-3,11-dioxa-7-azadispiro[5.1.5.3]hexadec-15-yl)carbamoyl][2-(2,5,8,11-tetraoxatridecan-13-ylamino)}-[3,11-dioxa-7-azadispiro[5.1.5.3]hexadec-7-yl])oxidanyl (AMUPol) and 1-[(2,2,6,6-tetramethyl-1-oxidopiperidin-4-yl)amino]-3-(2,2,6,6-tetramethyl-1-oxopiperidin-1-ium-4-yl)oxypropan-2-ol (TOTAPOL) and between deuterated and protonated lipid membranes was quantified [44]. Several lipid membranes were used in this study, namely 1,2-dimyristoyl-sn-glycero-3-phosphocholine (DMPC), d54-DMPC, 1,2-dilauroyl-sn-glycero-3-phosphoethanolamine (DLPE), 1-palmitoyl-2-oleoyl-sn-glycero-3-phosphoethanolamine (POPE), and a eukaryotic membrane mixture which

contains 1-palmitoyl-2-oleoyl-sn-glycero-3-phophocholine (POPC), POPE, egg sphingomyelin (SM), and cholesterol (Chol) at molar ratios of 25.6:25.6:25.6:23%. ^{1}H T_1 relaxation times were measured using the inversion recovery experiment. ^{1}H/^{13}C/^{15}N MAS probe 2D ^{13}C spectra and 2D ^{15}N ^{13}C correlation spectra were measured without DNP. AMUPol showed fourfold higher sensitivity enhancement than TOTAPOL. Deuterated lipid membrane does not give net higher sensitivity for the membrane peptides than protonated membrane. Overall, a 100-fold enhancement between the microwave-on and microwave-off spectra can be achieved on lipid-rich membranes containing conformationally disordered peptides. Data on measurement of the paramagnetic relaxation enhancement of lipid signals by TOTAPOL and AMUPol indicated a bimodal distribution of both radicals, a surface-bound fraction and a membrane-bound fraction where the nitroxides lie at 10 Å from the membrane surface. TOTAPOL appears to have a higher membrane-embedded fraction than AMUPol and TOTAPOL preferentially binds to the middle of the membrane, 10 from the membrane surface [46].

10.2.3 Nucleic Acids

The spin labeling in combination with classical and advance EPR and NMR methods and its pulse modification, in particular, have proved to a powerful approach to study of structure and motion/rearrangements of the nucleic acids under biologically similar conditions [47–53].

Modern synthetic chemistry developed elegant methods of tethering nitroxide and other labels to all fragments of nucleotide including the nucleobase, the sugar, and the phosphate backbone of nucleic acids (Figs. 10.16 and 10.17, as example). The spin labels can be incorporated during chemical synthesis of the oligomer (phosphoramidite approach) or post-synthetically, by reaction of a spin-labeling reagent with a reactive functional group on the oligonucleotide [47].

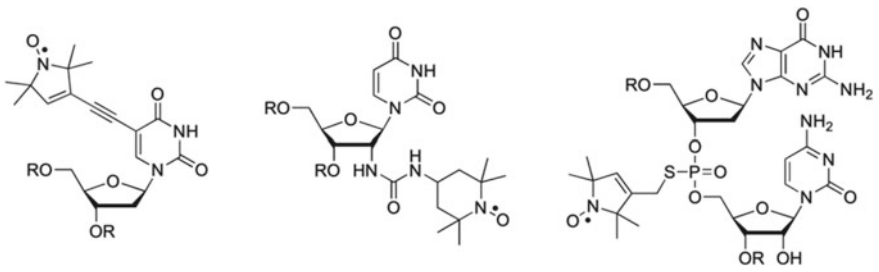

Fig. 10.16 Examples of nitroxides that have been conjugated to the nucleobase (left), the sugar (middle), and the phosphate backbone of nucleic acids (right) [47]. Reprinted from [47], Copyright 2011 De Gruyter

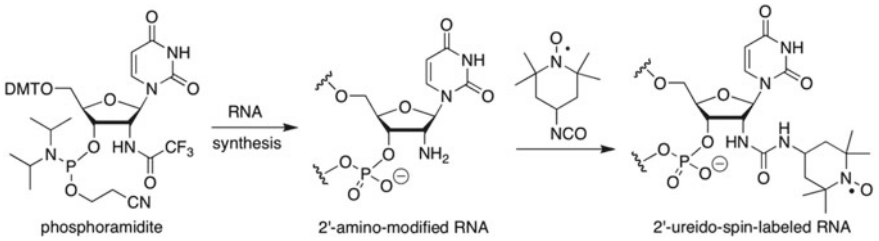

Fig. 10.17 Incorporation of 2′-amino-modification into RNA using the phosphoramidite approach (left) and post-synthetic spin labeling of 2′-amino-modified RNA with a spin-labeled isocyanate (right). DMT = 4,4′-dimethoxytrity [47]. Reprinted from [47], Copyright 2011 De Gruyter

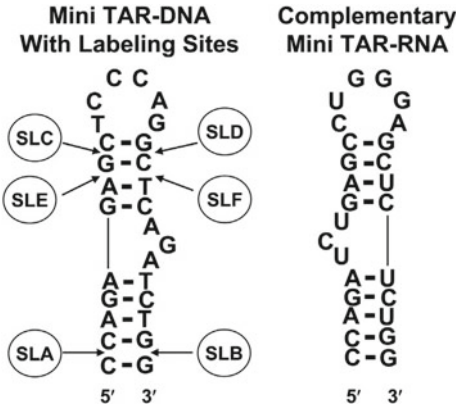

Fig. 10.18 Secondary structure of mini TAR DNA together with positions of spin labels attached via phosphorothioate linkages. The complementary mini TAR RNA is also shown. On the mini TAR DNA, the spin labels were attached in pairs, SLA-SLB, SLC-SLD, SLE-SLF, and the constructs were called SLAB, SLCD, and SLEF, respectively [48]. Reprinted from [48], Copyright Elsevier

The post-synthetical covalent modification RNA with labels was illustrated in Fig. 10.17,

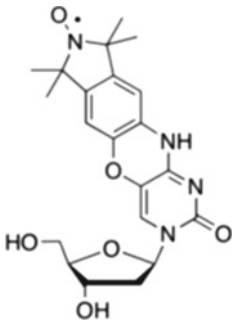

and their derivatives used for non-covalent modification were also performed.

DEER was applied to strategically placed, site-specifically attached pairs of nitroxide spin labels to monitor changes in the mini TAR DNA stem-loop structure brought on by the HIV-1 nucleocapsid protein NCp7 [48]. Spin labels (3-(2-miodoacetamide) proxyl (IPSL) for thio-amido attachment and 3-iodomethyl-(1-oxy-2,2,5,5-tetramethylpyrroline) for thio-methyl attachment) were attached at the positions SLA, SLB, SLC, SLD, SLE, and SLF of mini TAR DNA (Fig. 10.18). Measurement of distance between from several pairs of double labels (SLAB, SLCD, SLEF) within mini TAR DNA in the presence of NCp7 and complementary mini TAR RNA revealed marked changes both from the initial stem-loop structures in the absence of NCp7 to the case of duplex DNA–RNA. Specifically, when duplex TAR DNA-TAR RNA formed, double labels initially located 27.5 Å apart at the 30- and 50-termini of the 27-base mini TAR DNA and then relocated to opposite ends of a 27 bp RNA–DNA duplex with 76.5 Å between labels. Different sets of double labels initially located 26–27 Å apart in the mini TARm DNA upper stem and altered their interlabel distance to ~35 Å when 27 bp TAR DNA-TAR RNA duplex formed.

Structure of the two N-terminal dsRNA-binding domains (dsRBDs) of Dicer-binding partner TRBP in complex with a functionally asymmetric siRNA using *NOESY* NMR, DEER, and single-molecular FRET spectroscopy was solved [50]. Using suggested model a Dicer-TRBP-siRNA ternary complex, it was shown that

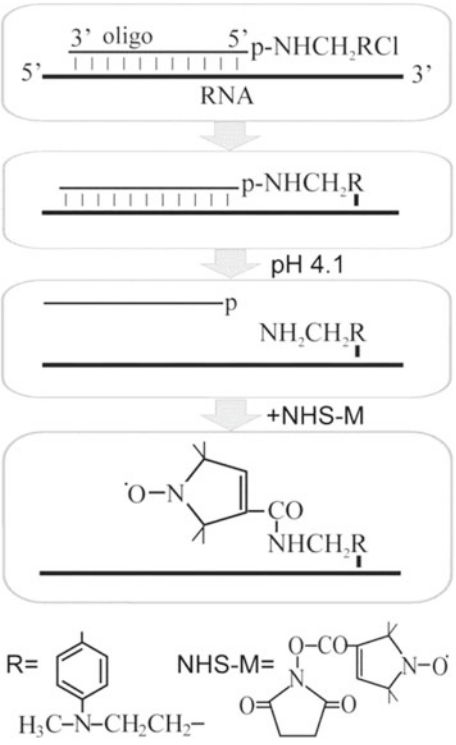

Fig. 10.19 Scheme of site-specific introduction of spin labels into definite RNA sites based on the complementary-addressed alkylation of the RNA with [4-(N-2-chloroethyl-N-methylamino)benzyl]-phosphoramides of oligodeoxyribonucleo-tides, hydrolysis of phosphoramide bond in the covalent adduct formed and selective acylation of the released aliphatic amino group by N-hydroxysuccinimidyl derivative of the spin label [51]. Reprinted from [51], Copyright 2016 Oxford International Press

TRBP's dsRBDs and Dicer's RNase III domains bind a canonical 19 base pair siRNA on opposite sides. This finding supports a mechanism whereby TRBP influences Dicer-mediated cleavage accuracy by binding the dsRNA region of the pre-miRNA during Dicer cleavage.

Hepatitis C Virus RNA internal ribosome entry site consisting of ≈330 nucleotides and having a complicated spatial structure was modified by spin labels (Fig. 10.19).

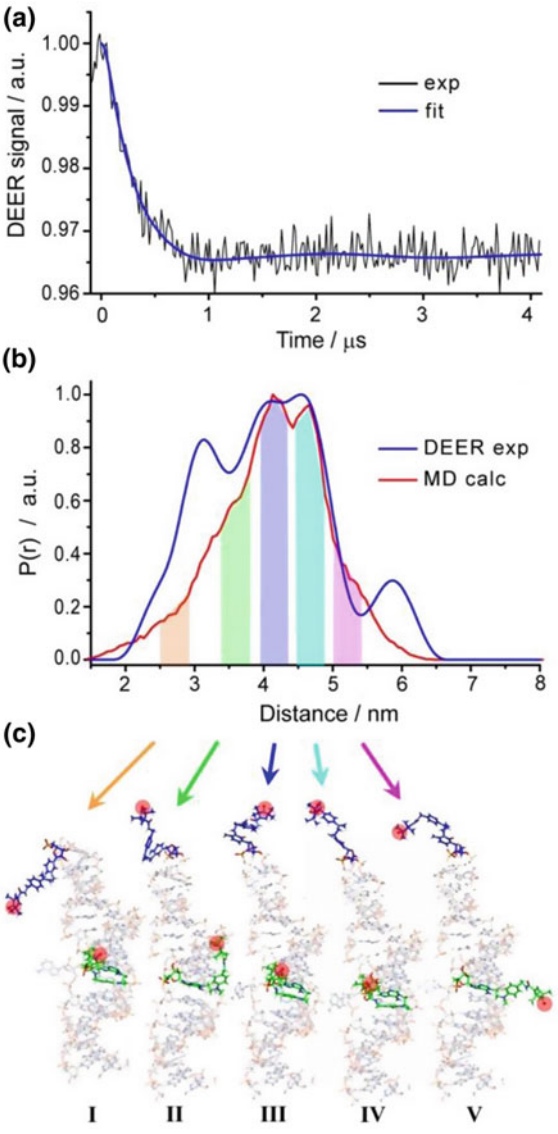

Fig. 10.20 Distance measurements on dslRNA. **a** Background-corrected Q-band DEER/PELDOR time trace (exp) and Deer analysis fitting (fit); **b** obtained distance distribution using Tikhonov regularization parameter 1000 (DEER exp) and calculated MD distribution (MD calc). **c** Typical conformations of spin labels corresponding to the selected ranges of distances (highlighted by colored bars in (**b**) and pointed out by corresponding arrows). Red circles indicate the NO group of the label, for clarity. Spin-labeled C83 (top) is shown in blue, and spin-labeled A73 (middle) is shown in green [51]. Reprinted from [51], Copyright 2016 Oxford International Press

Application of pulsed double electron–electron resonance provided spin–spin distance distribution, which agrees well with the results of molecular dynamics (MD) calculations (Fig. 10.20).

An approach that combines high-resolution NMR restraints with low-resolution long-range constraints, based on site-directed spin labeling and measurements of distance distribution restraints in the range between 15 and 80 Å by the four-pulse double electron–electron resonance (DEER), EPR technique, was developed and discussed on example of determination of structures of large RNAs and protein–RNA complexes in solution [52].

The utility and capability of EPR line shape analysis and distance measurements to monitor and describe site-specific changes in the conformational dynamics of internal loop nucleobases as well as helix–helix interactions of the kink-turn motif in the Vibrio cholerae (VC) glycine riboswitch that occur upon sequential K^+-, Mg^{2+}-, and glycine-induced folding were explored by spin labels incorporated into the 232-nucleotide sequence via splinted ligation strategy [53]. Results demonstrate the ability of SDSL to interrogate site-specific base dynamics and packing of helices in large RNAs and demonstrate ion-induced stability of the kink-turn fold of the VC riboswitch.

Data on spin labeling of nuclear acids published by 2016 were briefly reviewed in [54].

10.3 Spin Tools

10.3.1 Background

In the last decade, spin ruler method which is long-distance measurements (2–8 nm) in biomolecules obtained from pulse dipolar electron paramagnetic resonance (PD-EPR) spectroscopy in general, and double electron–electron resonance (DEER) technique in particular have been developed and widely used for solving various structural problems such as investigation of structural changes upon ligand binding, protein–protein, or protein–DNA interactions, the assembly of subunits of proteins, and for accessing the flexibility of particular regions in the biomolecule.

The recent advances of in vivo molecular EPR-based spectroscopy and imaging of tumor microenvironment (TME) and redox using functional paramagnetic probes, and applications of these approaches in various animal models of cancer magnetic resonance imaging (MRI) and low-field electron paramagnetic resonance (EPR)-based techniques were demonstrated in a series excellent works by Khramtsov group [55] and references therein. A principle key role of the important physiological components, such as acidity (pH), oxygen concentration (pO_2), intracellular glutathione (GSH) and other sulfide, redox status, and interstitial inorganic phosphate (Pi) in normal and pathological biological processes (cancer progression in tumor for example) have been established. Progress in development of functional paramagnetic probes

together with recent advances of low-field electron paramagnetic resonance (EPR)-based spectroscopy, which provided a reasonable radiofrequency penetration depth in living tissues and allows larger samples to be used, opens the way for quantitative investigation of imaging in vitro and vivo of tumor macroenvironment and redox properties.

The following chemical structures of the EPR multifunctional probes were used in [55]:

pH and redox probes, disulfide biradical probe for GSH detection, pO_2 probe.

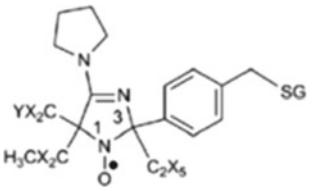

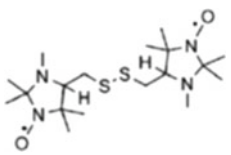

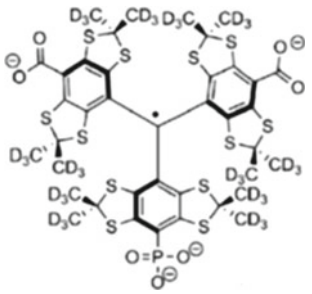

For the detection of spin probes, along with conventional versions of EPR spectroscopy, the method of field cycling proton electron double-resonance imaging (FC-PEDRI has recently been used [55, 56]. A new concept of variable field proton–electron double-resonance imaging (VF PEDRI), which allows for functional mapping using specifically designed paramagnetic probes (e.g., pH mapping) with MRI high-quality spatial resolution and short acquisition time, was proposed [57]. It was demonstrated that this method provides pH resolution of 0.1 pH units and a spatial resolution of 1.25 mm at 200 G field.

10.3.2 Spin Oximetry

Molecular oxygen plays a key role in many biochemical and physiological and pathophysiological processes such as mitochondrial respiration, synthetic and degradative reactions, oxidative damage, cell signaling, so forth. ESR oximetry is a technique that can make non-invasive sensitive and localized measurements of oxygen. Spin oximetry is a version of the method of spin label–spin probe in which molecular oxygen plays the role of a spin probe (Chap. 11). Nitroxides, stable aromatic radicals (derivatives of triarylmethyl radical, Indian ink), phthalocyanine, and micrococrystals (fusinite and carbohydrate chars) show narrow singlet ESR lines sensitive to O_2 concentration in water and cells, organs, small animals, and even parts of human body [55, 58, 59]. For example, the EPR linewidth of triarylmethyl radical can be served as spin probe for the measurement of pO_2 with accuracy 1 mm Hg and range, 1–100 mm Hg.

In pioneering work of James Hide group [60, 61] a method for measuring the oxygen diffusion-concentration product was invented. The method was based on the dependence of the spin–lattice relaxation time T_1 of the spin label on the bimolecular collision rate with oxygen [62]. Both time-domain and continuous-wave saturation methods showed strong Heisenberg exchange between spin label and oxygen which contributes directly to the T_1 of the spin label. Advantages in measurement of the oxygen transport parameter using saturation-recovery EPR have been clearly demonstrated in saturated (DMPC) and unsaturated (POPC) lipid bilayer membranes with the use of stearic acid (*n*-SASL) and phosphatidylcholine (*n*-PC) spin labels. Figure 10.21 illustrates a profile of the oxygen transport parameter across the POPC membrane obtained by X-, Q-, and W-band spectroscopy.

The effect of O_2 on the spin lattice relaxation time T_1, derived from saturation curves of the CW ESR spectra of nitroxide radicals, was examined for radicals incorporated into phosphatidylcholine (PC) liposomes and attached to lysozyme and

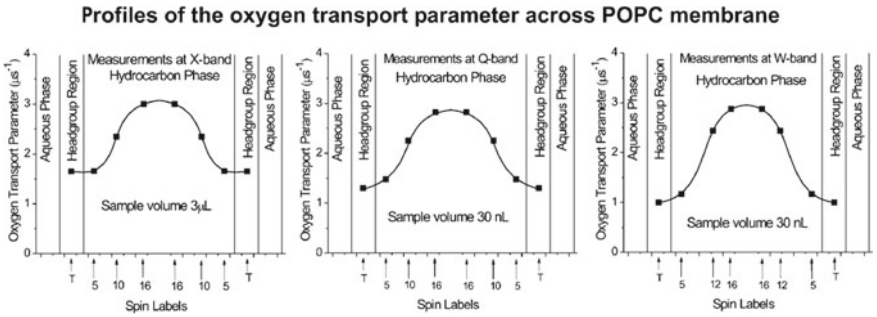

Fig. 10.21 A profile of oxygen transport (accessibility) obtained at X-, Q-, and W-band. Measurements and equilibrations with gas for X- and Q-band were performed at 29–30 °C. Measurements and equilibrations with gas for W-band were performed at room temperature [61]. Reprinted from [61], Copyright 2011 Elsevier

albumin [63]. O_2 increased the rates of spin–lattice and spin–spin relaxation by the factor $k_{ex}C$, where k_{ex} is a spin-exchange constant and C is the oxygen concentration. The experiments indicted that for the liposomes, $k_{ex}C$ increased as the spin label approached the center of the bilayer, while for the tagged proteins, $k_{ex}C$ was very close to that of the radicals in aqueous solution.

10.3.3 Spin pH Meter

A spin pH probes technique for the measurement of local acidity in biological and non-biological objects including organs and even living organisms was invented in work of Khramtsov, Weiner, Grigor'ev, and Volodarsky in 1982 and since then found wide application in biological systems, in vivo in particular [55, 64–68]. EPR spectra of stable nitroxides of the imidazoline and imidazolidine types

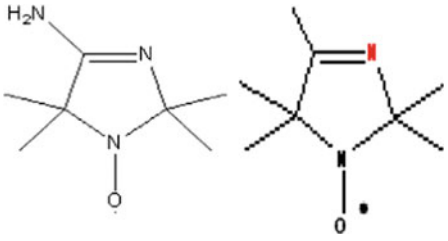

have been shown to be sensitive to pH and serve as spin pH probes.

Data on the synthesis of a wide set of pH-sensitive nitroxides is a pH spin probe (in the range from 6 to 8.0 with accuracy −0.05) of different sensitivity, stability to reduction, lipophilicity, covalent binding properties to macromolecules, and applications have been reported [65, 66, 68].

Typical pH-dependence of the observed hyperfine splitting constant, a_N, DNP spectra of the nitroxide NR1 acquired in acid, pH 4.98, and slightly alkaline, pH 7.62, and the effect of protonation of the radical heterocycle resulting in decreasing unpaired electron density at the nitrogen nucleus of the N–O fragment were presented. pH dependencies of the hyperfine splitting, a_N, for R_1 probe measured using L-band EPR spectroscopy are shown in Fig. 10.22.

10.3.4 Spin Redox Probe

Redox reactions play a key role in the fundamental chemical, photochemical, and biological processes and in the provision of energy of living organism, in particular. The spin redox probe techniques utilize ability of nitroxides and corresponding hydroxyl amines to proceed in following chemical reactions which include: (1) reduction of a

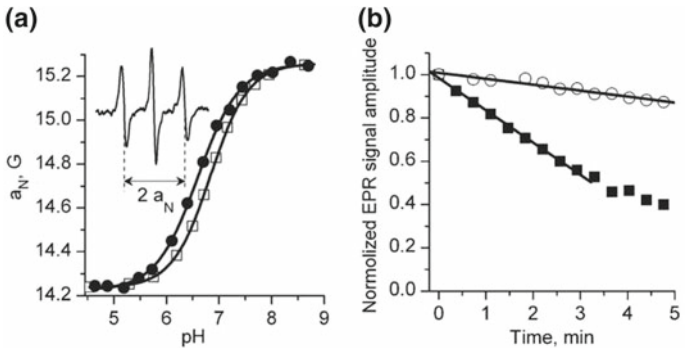

Fig. 10.22 pH dependencies of the hyperfine splitting, a_N, for R_1 probe measured using L-band EPR spectroscopy. Temperature-dependent shift of the titration curve was observed with pK_a values being equal to 6.84 (□, 23 °C) and 6.60 (●, 37 °C). Insert: L-band EPR spectrum of the R_1 probe measured in vivo after injection (10 μL, 10 mM) in mammary tumor tissue. The hyperfine splitting, a_N, was found to be equal to 14.72 G which corresponds to the value of $pH_e = 6.52$ assuming tumor tissue temperature 34 °C and p$K_a = 6.65$. **b** EPR signal decay of the probe R_1 after injection (10 μL, 10 mM) in mammary glands (○) and mammary tumors (■). The analysis of the initial part of the kinetics yields the rates of the EPR signal reduction, k_{red}, in extracellular media of the tissues being equal to 0.5×10^{-3} s^{-1} and 2.5×10^{-3} s^{-1}, respectively [65]. Reprinted from reference [65], Copyright 2012 Wiley

nitroxide with reducing agent to corresponding hydroxyl amine, (2) oxidation of a nitroxide to oxoammonium cation and (3) oxidation of hydroxyl amine with an oxidant to correspondent nitroxide. All these reactions run as the simple one-electron processes and can be readily followed by the standard and advance ESR technique [5, 68–75]. The values of the nitroxide redox potential depend on their chemical structures (Chap. 3). For example, the redox potential of piperidine derivatives nitroxide is high enough to oxidize such biological compounds as ascorbic acid, semiquinones, and superoxide radical. As long ago as 1968, reduction of nitroxides was observed in electron transport in mitochondria [75]. Later, such processes were found to be typical of various biological systems.

A typical example of determination of in vivo pH and redox assessment of TME in mouse model of breast cancer using dual-function NR1 probe is described in Fig. 10.22 [65].

Real-time assessment of extracellular pH (pH(e)), redox, and intracellular glutathione were monitored in PyMT mice-bearing breast cancer tumors during treatment with granulocyte macrophage colony-stimulating factor using L-band EPR spectroscopy and nitroxide probe and disulfide nitroxide [76]. It was observed that (1) tumor pH(e) is about 0.4 pH units lower than that in normal mammary gland tissue, (2) treatment with granulocyte macrophage colony-stimulating factor decreased the value of pH(e) by 0.3 units compared with PBS control treatment, and (3) tumor tissue reducing capacity and intracellular glutathione were elevated compared with normal mammary gland tissue, and (4) granulocyte macrophage colony-stimulating factor treatment resulted in a decrease of the tumor tissue reducing capacity and intracellular

glutathione content. In addition, pH(e) mapping was performed using recently proposed variable frequency proton–electron double-resonance imaging (VF PEDRI). The pH mapping superimposed with MRI image supports probe localization in mammary gland/tumor tissue showed high heterogeneity of tumor tissue pH(e) and a difference of about 0.4 pH units between average pH(e) values in tumor and normal mammary gland.

10.3.5 SH Moiety Assay

SH moiety assay is based on the use of RSSR probes (Fig. 10.21), in which two nitroxides are tethered with flexible bridge. The dynamic spin exchange in moment of close contact between the nitroxide leads to appearance new satellites in EPR spectra [55, 74, 77]. The reaction of thiol/disulfide exchange with a sulfide-bearing compound (glutathione, GSH for example) splits the RSSR disulfide bond resulting in formation of two monoradicals and cancelation of intramolecular spin-exchange between the monoradical fragments. Reaction of the RSSR probe with glutathione on the EPR spectra resulted in disappearance of the biradical spectral components and a corresponding increase of the intensity of the monoradical components. The rate of the increase of the amplitude of the monoradical component is proportional to the GSH concentration.

As an example, in the SH moiety assay, a set of RiSSRi biradicals (Fig. 10.23) was employed.

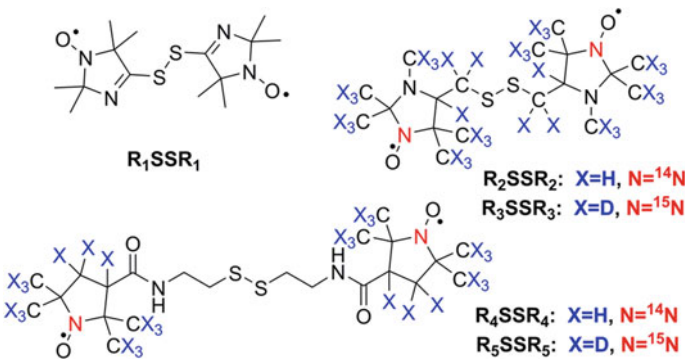

Fig. 10.23 Chemical structures of the imidazoline, R_1SSR_1, imidazolidine, R_2SSR_2 and R_3SSR_3, and pyrrolidine disulfide biradicals, R4SSR4 and R5SSR5 [77]. Reprinted from [77], Copyright 2017 American Chemical Society

10.3.6 Spin Imaging

The basic principles of using stable organic radicals involved in reversible exchange processes as functional paramagnetic probes were reviewed [77, 78]. It was demonstrated that these probes in combination with electron paramagnetic resonance (EPR)-based spectroscopy and imaging techniques provide analytical tools for quantitative mapping of critical parameters of local chemical microenvironment.

One way of field-cycled proton–electron double-resonance imaging (PEDRY) of free radicals designed in Lurie group and realized in collaboration with Khramtsov group was to use so-called phantoms [78, 79]. Images were acquired separately by changing the external magnetic field for EPR irradiation between ^{14}N and ^{15}N nuclei in FC-PEDRI. The center of the phantom consisted of several tubes of internal diameters 3–15 mm filled with a spin probe. For example, five tubes of internal diameters 15, 9, 5, 4, and 3 mm are filled with 2 mM TEMPOL solution. These were enclosed in a cylindrical container of diameter 4 cm that was filled with water doped with copper sulfate to give the same T_1 as that of the free radical solution (650 ms at 2.5 MHz). Fourteen sample tubes with internal diameters of 8 mm were attached around the outside of the cylinder, with alternate tubes being filled with 2 mM TEMPOL solution or copper sulfate-doped water. The overall diameter of the phantom was 6 cm, about the size of a small rat. The feasibility of redox imaging using nitroxyl radicals was validated by in vitro experiments showing the time-dependent redox reaction of both membrane-permeable ^{14}N/^{15}N-3-methoxycarbonyl-2,2,5,5-tetramethylpyrrolidine-1-yloxy (MC-PROXYL) and membrane-impermeable ^{14}N/^{15}N carboxy-PROXYL in the presence of ascorbic acid. Images were acquired separately by changing the external magnetic field for EPR irradiation between ^{14}N and ^{15}N nuclei in FC-PEDRI. Seven phantom tubes comprising six outer tubes with liposomes encapsulated with 100 mM ascorbic acid were shown.

Simultaneous molecular imaging of redox reactions monitored by Overhauser enhanced MRI with ^{14}N- and ^{15}N-labeled nitroxyl radicals was reported in [80]. Time-dependent PEDRI of ^{15}N/^{14}N-carboxy-PROXYL and ^{15}N/^{14}N-MC-PROXYL in liposomes encapsulating ascorbic acid (100 mM) was detected in seven phantom tubes in the presence and the absence of liposomes. The images of the decay rates for ^{14}N- and ^{15}N-enhanced PEDRI images were calculated by assuming first-order kinetics for the time-dependent decrease of the contrast, and only MC-PROXYL showed decay images in both ^{14}N- and ^{15}N-enhanced PEDRI [80].

A pH map was extracted from two PEDRI acquisitions performed at EPR frequencies of protonated and unprotonated forms of a synthesized pH-sensitive probe [81]. Probe deuteration resulted in a narrow spectral line of 1.2 G compared to a non-deuterated analog line width of 2.1 G allowing for an increase of Overhauser enhancements and reduction in rf power deposition. Binding of the probe to the cell-impermeable tripeptide, glutathione (GSH), allowed for targeting to extracellular tissue space for monitoring extracellular tumor acidosis. In vivo VRF PEDRI was performed on Met-1 tumor-bearing mice (Fig. 10.24), and broad pH distribution with acidic mean pH_e (6.8 ± 0.1) in tumor tissue was observed.

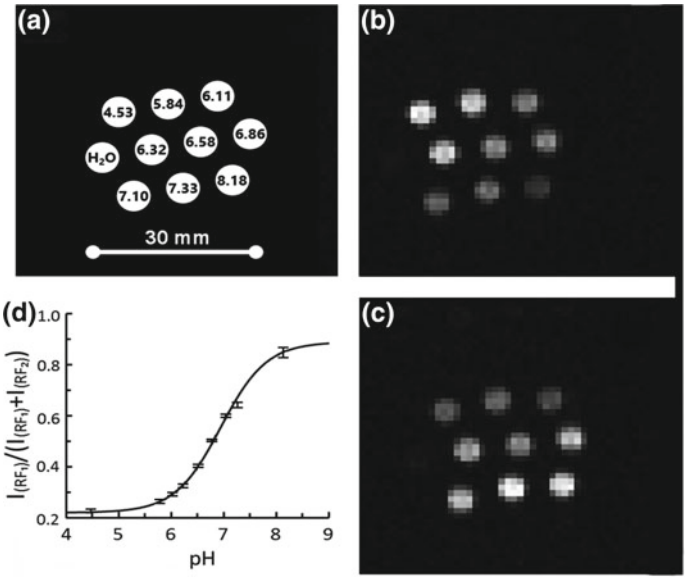

Fig. 10.24 VRF PEDRI pH calibration (**a**–**d**) and in vivo pH mapping (**e**, **f**) by using NR2 probe. Calibration has been performed by using a 10-tube phantom (**a**) at room temperature. PEDRI images were acquired at two EPR irradiations, $RF_2 = 559.3$ MHz (**b**) and $RF_1 = 562.1$ MHz (**c**), acquisition time, 8.4 s. The tube with water alone is not visible on either image due to lower intensity compared with the signal from tubes containing the paramagnetic probe. EPR off image (not shown) was subtracted from both EPR on images acquired at RF_1 and RF_2, yielding image intensities, $I_{(RF_1)}$ and $I_{(RF_2)}$. **d** pH dependence of the ratio $I_{(RF_1)}/(I_{(RF_1)}+I_{(RF_2)})$. Solid line is nonlinear least-squares fit of the data to a conventional titration equation, yielding pK_a value equal to 6.75–0.05. Error bars represent the standard deviation. In vivo PEDRI pH mapping was performed in the anesthetized breast tumor-bearing mouse (**e**, **f**). Paramagnetic NR2 probe was injected into the tumor (number 4 mammary gland, left) and normal mammary gland (number 9, right). **e** Qualitative visualization of the distribution of the NR2 probe, in vivo. The image is the average of two PEDRI images acquired at two EPR frequencies, $RF_1 = 562.1$ MHz and $RF_2 = 559.3$ MHz, NMR frequency, 784.9 kHz, matrix, 64 × 64; field of view, 80 mm. Irradiation time was 8.4 s for each acquisition. **f** pH map (in color) calculated from two PEDRI images superimposed with the MRI image (gray scale) showing the coronal view of the mouse [81]. Reprinted from [81], Copyright 2017 American Chemical Society

DNP-MRI imaging of free radical intermediates that are derived from endogenous species involved in metabolic processes was first reported [82]. Simultaneous images of free radical intermediates generated from the coenzyme Q10 (CoQ10), flavin mononucleotide (FMN), and flavin adenine dinucleotide (FAD) involved in the mitochondrial electron transport chain as well as carbamoyl-PROXYL and the radicals derived from vitamins E and K1 were visible. Each of the radical species can be distinguished in the spectroscopic images by the changing the frequency of irradiation. Figure 10.25 shows the EPR signals of the intermediate of various candidate probes.

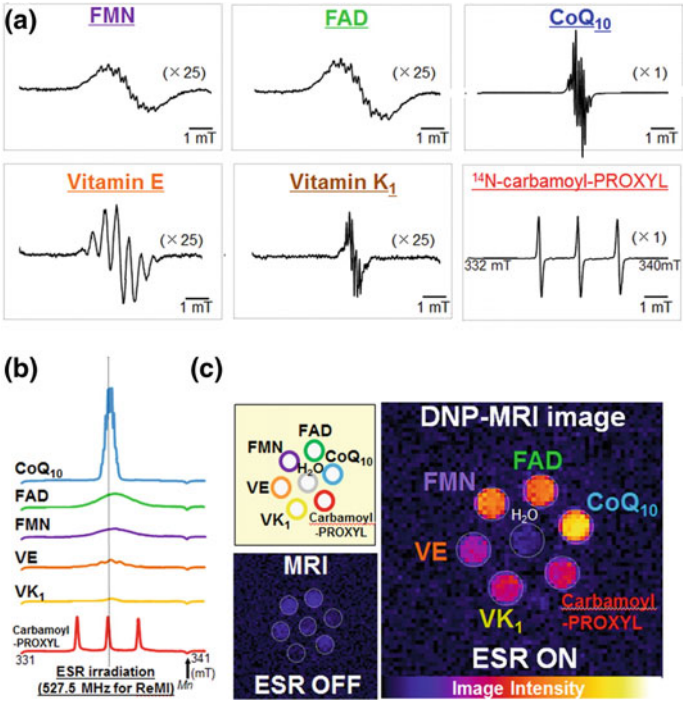

Fig. 10.25 Typical EPR spectra (**a**), the absorption EPR spectra (**b**), and simultaneous DNP-MRI image (**c**) of free radical intermediates from FMN, FAD, CoQ10, vitamin E, vitamin K1, and the synthetic stable radical ^{14}N carbamoyl-PROXYL. The vertical solid line in part **b** indicates the frequency of EPR irradiation for PEDRI (527.5 MHz), which is the resonance frequency of the central peak of carbamoyl-PROXYL. MRI spectra with and without EPR irradiation were obtained with a spin echo sequence at 850 kHz by using a homemade in vivo PEDRI system kept at room temperature [82]. Reprinted from [82], Copyright 2014 American Chemical Society

Two nitroxyl radicals, the cell membrane penetrable (carbamoyl-PROXYL) and the cell-impermeable (carboxy-PROXYL), were used in the in vivo PEDRI experiments to investigate the redox reactions which can occur in the intracellular or extracellular compartment [83]. Nitroxyl radical solution was injected to the same region of the mouse leg that had received BPVC pretreatment. In vivo DNP-MRI images and redox maps at 4 and 24 h after BPVC treatment in mice, taken after injection of 2.5 mM carbamoyl-PROXYL (50 lL) into both legs, were presented. Redox maps were calculated by using four pharmacokinetic in vivo DNP-MRI images, and decay rates were calculated for the DNP-MRI images of untreated and BPVC-treated legs. Differences between decay rates in BPVC-treated versus untreated (contralateral) legs in individual mice were shown. In vivo DNP-MRI images and redox map at 4 and 24 h after BPVC treatment in mice, taken after injection of 2.5 mM carboxy-PROXYL (50 lL) into both legs, were also indicated. Thus, the decay rate of the BPVC-treated leg was found to be faster than that of the control leg.

Real-time assessment of extracellular pH (pH(e)), redox, and intracellular glutathione was monitored in PyMT mice-bearing breast cancer tumors during treatment with granulocyte macrophage colony-stimulating factor using L-band EPR spectroscopy and nitroxide probe and disulfide nitroxide [76]. It was observed that (1) tumor pH(e) is about 0.4 pH units lower than that in normal mammary gland tissue, (2) treatment with granulocyte macrophage colony-stimulating factor decreased the value of pH(e) by 0.3 units compared with PBS control treatment, (3) tumor tissue reducing capacity and intracellular glutathione were elevated compared with normal mammary gland tissue, and (4) granulocyte macrophage colony-stimulating factor treatment resulted in a decrease of the tumor tissue reducing capacity and intracellular glutathione content. In addition, pH(e) mapping was performed using the VF PEDRI). The pH mapping superimposed with MRI image supports probe localization in mammary gland/tumor tissue shows high heterogeneity of tumor tissue pH(e) and a difference of about 0.4 pH units between average pH(e) values in tumor and normal mammary gland.

10.3.7 Molecular Dynamics. Spin Viscose Meter

The principles underlying the application of the nitroxide spin-label method as a tool for experimental investigation of protein molecular dynamics ("breathing") were formulated in the late 1960s and early 1970 by Likhtenshtein [62, 84, 85]. In parallel, complementary research on protein dynamics was performed by a proposed Moessbauer atom labeling [5, 86]. Transglobular conformational change in myoglobin and lysozyme as a consequence of a protein molecular dynamics was first demonstrated in [62].

A suggested approach for the investigation of protein dynamics relied on the well-known finding that the mobility of a molecule in a condensed phase is modulated to a great extent by the molecular dynamics of the surrounding molecules. Therefore, the particulars of nitroxide motion report on characteristics of the dynamics of the surrounding medium. An important feature of nitroxides is their structural anisotropy which causes anisotropy of magnetic interactions, such as the hyperfine splitting and the g-tensor. Radical motion leads to averaging of the hyperfine interaction and the g-tensor which causes significant changes to the ESR spectrum. Modern ESR techniques (Chap. 4) allow ones to access dynamic processes such as rotation and wobbling with a wide range of correlation time, $\tau_c = 10^2$–10^{-10} s and amplitude ending low-amplitude high-frequency vibration and the phonon processes in media. Essential knowledge about molecular dynamic state of system under investigation can be derived from the measurement of dynamic interactions between nitroxides and other paramagnetics at its encounters.

The following parameters of spin probes in liquid glasses, polymers, membranes, biomolecules, and proteins are sensitive to low-amplitude high-frequency and phonon dynamics: (1) line width of a radical pair (RP), (2) RP ESR signal splitting, (3) amplitude of RP ESR signal, (4) spin packet of a nitroxide probe $\Delta H_{1/2,}$

(5) nitroxide spin phase ($1/T_{1e} \sim \Delta H_{1/2}$) and spin–lattice relaxation rate ($1/T_{1e}$), (6) ESR spectra of nitroxides line width δ, and (7) nitroxides hyperfine splitting A_{aniso}. Atomic vibration and molecular motions of a nitroxide affect the spin relaxation parameters and line shapes of the nitroxide ESR spectra.

The first dynamic theory of the nitroxide ESR spectra for nitroxide rotation in the fast ($\tau_c = 10^{-9}$–10^{-10} s) and slow regions ($\tau_c = 10^{-7}$–10^{-8} s) was developed by Kivelson [86] and Freed [87], correspondingly. In the case of spin-labeled macromolecules (polymers, proteins, membranes, and nuclear acids), the situation appears to be more complicated when the nitroxide segment can be involved at least in two types of motions: high-amplitude low-frequency ($\tau_c \geq 10^{-8}$ s) motion or/and low-amplitude high-frequency wobbling ($\tau_c \leq 10^{-9}$ s) [87]. To distinguish from above-mentioned models, a method based on an analysis of correlation between the values of the A_{zz} shift and the line width induced by temperature and viscosity change was proposed [88]. Comparison of experimental data for a series of spin-labeled bioobjects, including biomembranes and proteins, indicated that the rotation of the nitroxyl fragments of the spin labels at an ambient temperature can be described by the model of slow anisotropic rotation with correlation time 10^{-7}–10^{-8} s under conditions where the rotation of the macromolecules and membranes is slow in the ESR time scale and can be neglected [88]. Pulsed multifrequency EPR was used to investigate orientational molecular motion of the nitroxide spin probe ([$(SO_3)_2NO^{\cdot}$], Fremy's salt) in glycerol glass near the glass transition temperature [28, 29, 89, 90]. Measuring echo-detected EPR spectra at different pulse separation times at resonance frequencies of 3, 9.5, 95 and 180 GHz of Fremy's salt, in glycerol glass near the glass transition temperature allowed for estimating parameters of transverse relaxation tensor and thus for discriminating between different relaxation mechanisms and characterize the timescale of molecular reorientations (10^{-7}–10^{-10} s).

In work [91], dynamic behavior of di-tert-butyl nitroxide in aqueous solution has been investigated by means of an integrated computational approach, including Car–Parrinello molecular dynamics and quantum mechanical calculations involving a discrete–continuum embedding. Decoupling of the structural, dynamical, and environmental contributions to the nitroxide ESR spectra allowed one to elicit the role played by different dynamic effects and stress the importance of specific vibration modes. Data on motions in a protein detected by changes in the average distance and/or the shape and width of the distribution using DEER have been reported [92]. The following findings were described: (1) DEER detection of triggered conformational changes; (2) motion of a transmembrane helix during the transition from state A to state B alters the average distance (r_{av}) between spin labels; (3) the rotameric ensemble of each label generated from a rotamer library using the program MMM; (4) A and B are distinct conformers of different energies; (5) the conformational shift manifests primarily as a change in r_{av}, and (6) altering the biochemical conditions alters the contribution of each distinct conformation (dashed curves) to the distance distribution.

An extensive set of electron spin resonance spectra of the dynamics of spin-labeled T4 lysozyme was obtained over a wide range of frequencies (9, 95, 170, and 240 GHz) and temperatures (2–32 °C) [93]. The native side chain at solvent-exposed

helical sites, 72 or 131, was labeled with nitroxide side chain (R1), or a methylated analog with hindered internal motion (R2). The spectra at all four frequencies were simultaneously fit with the slowly relaxing local structure (SRLS) model which suggests the global tumbling of the protein and the internal motion consisting of backbone fluctuations and side chain isomerizations. Quantitative spin labeling of SecB mutants containing a single cysteine per subunit or an exposed highly reactive new cysteine after removal of the nearby intrinsic cysteines was achieved with the methanethiosulfonate spin label (MTS) at positions C97 or E90C, respectively [94]. High-field (W-band) EPR measurements revealed that in labeled bovine pancreatic trypsin inhibitor (BPTI), the spin labels are exposed to a more polar/hydrophilic environment. Binding of BPTI led to a slight change in distances between labels at C97 but not at E90C.

General aspects of the dynamics of the tether linking methanethiosulfonate (MTSSL) spin probes to α-helices have been investigated with the purpose of rationalizing its effects on ESR line shapes [95]. Torsional profiles for the chain bonds have been calculated ab initio, and steric interactions with the α-helix and the neighboring residues have been introduced at the excluded-volume level. The implications for the ESR spectra of spin-labeled proteins were discussed, and suggestions for the introduction of realistic features of the spin probe dynamics into the line shape simulation were presented.

To investigate the single transmembrane (TM) domain conformational properties of integrin, β1a, 26 consecutive, single-cysteine mutants were generated for site-directed spin-labeling and continuous-wave electron paramagnetic resonance (CW-EPR) mobility and accessibility analyses [96]. The following results were presented: (1) the mobility analysis identified two integrin β1a-TM regions with different motional properties in micelles and an integrin β1a-TM helix with high immobility in liposomes; (2) the accessibility analysis verified the TM range (Val737-Lys752) of the integrin β1a-TMC in micelles; and (3) mobility and accessibility *comparisons* of the integrin β1a-TMC domains in micelles or liposomes identified a monomer embedded in detergent micelles and leucine-zipper-like homo-oligomeric clusters in liposomes were established. The phase diagram of 1,2-dipalmitoyl-*sn*-glycerophosphatidylcholin labeled (labeled at the end-chain 16-PC)–cholesterol binary mixtures versus temperature was studied using 2D-ELDOR at Ku band with the "full Sc" method [97]. The line shape changes and the homogeneous T_2's, extracted from the pure absorption spectra in the 2D-plus-mixing-time representation, allowed the characterization of the membrane phases with respect to their dynamic molecular structures and to determine the phase boundaries.

The dynamic behavior of spin labels with nitroxides located in different positions on the aliphatic chains in liposomes was first investigated with high-frequency (2-mm) ESR spectroscopy [98]. On the basis of temperature dependence of the spin probe spectra over the range temperatures, it was concluded that in the temperature range 220–260 K, the nitroxide rotation is essentially anisotropic with correlation time $\tau_c = 10^{-7}$–10^{8} s and about 10^{-9} s at physiological temperatures.

10.3.8 Spin Polarity Meter

The dependence of isotropic and anisotropic hyperfine splitting (A_{iso} and A_{aniso}) and g-factor for nitroxides on the spin density on nitrogen *atom and the energy of the* $n \rightarrow *$ *transition* in the N–O$^{\cdot}$ fragment makes this probes suitable for assessing local polarity and the availability of hydrogen bond donors to form H-bond with the N–O$^{\cdot}$ group [70, 99–102]. The physical reason for such a dependence is that the contribution of polarized resonance structure N–O$^{\cdot} \leftrightarrow$ N^{+}–O^{-} increases in a polar media, causing an increase in the spin density on nitrogen atom observed as an increase in the A_{iso} value. At the same time, the A_{aniso} values are larger for the ionic structure.

The isotropic ^{14}N-hyperfine coupling, a_0^N, of nitroxyl spin labels depends linearly on the unpaired electron spin density on the nitrogen atom (ρ_π^N) and to a lesser extent on that on the oxygen atom (ρ_π^O)v [99]:

$$a_0^N = Q_N \rho_\pi^N + Q_{NO} \rho_\pi^O,$$

where $\rho_\pi^N + \rho_\pi^O \approx 1$ and the leading term is that involving Q_N ($\gg Q_{NO}$). The spin density distribution, and hence the hyperfine coupling, is perturbed linearly by the reaction field from the polar environment [22]. The polarity dependence of the principal z-element of the hyperfine tensor is determined by both the isotropic and anisotropic terms:

$$A_{zz} = a_0^N + 2\left|T_\perp^d\right|,$$

where $-\left|T_\perp^d\right|$ is the perpendicular element of the traceless hyperfine tensor that arises from the electron–nuclear dipolar interaction.

The g-factor values are also reported to be sensitive to the medium. A correlation between a decrease of g_X and an increase in A_z has been observed for nitroxides in simple liquids and labeled proteins [101]. A polarity effect (up to $\Delta A_{iso} = 0.13$ mT) was observed for the TEMPOL radical and for the formation of H-bond with N–O group of the nitroxides $\Delta A_{iso} = 0.15$ mT). ESR spectra of a nitroxide probe in solvent of various polarities can be used for estimation of local apparent dielectric constant in the vicinity of a nitroxide incorporated in system of interest.

The dependences of electronic paramagnetic resonance properties on environmental dielectric permittivity and proticity in biomolecular assemblies were reviewed [99].

10.4 Alternative Spin Labeling

The most commonly used SLs are nitroxyl radicals, but recently SL new approaches have been shown to be an attractive alternative for PD-EPR, particularly double

electron–electron resonance (DEER). The first one, based on high-spin Gd^{3+} ($S = 7/2$) complexes, was designed and developed in Goldfarb group [103–109]. The long spin relaxation, narrow EPR signals, neutral chemical character, and stability of triarylmethyl radicals (trityls, TAMs) trityls at room temperature in liquid solutions make them a promising alternative for traditional nitroxides [15].

The following advantages of the first approach can be pointed out: (1) high sensitivity because high-field measurements at spectrometer frequencies higher than 30 GHz are associated with an increase in the absolute sensitivity; (2) Gd^{3+} complexes are stable toward oxidation or reduction, and therefore, it can be used in the reductive environment in cells; (3) neutral chemical character of this compounds, possessing neutral chemical character, does not alter the chemical properties of the parent molecule region to which they are attached; (4) and the long spin relaxation and narrow EPR signals.

The C7-Gd and C8-Gd tags, which are compact hydrophilic cyclen-based lanthanide tags for conjugation to cysteine residues in proteins, were loaded with Gd(III) on two mutants of the homodimeric ERp29 protein and investigated by EPR (Fig. 10.26) [105].

The W-band EPR spectra were found to differ between the tags in the free state and after conjugation to the protein. In addition, the spectra were sensitive to the labeling position, which may originate from an environment-dependent charge density on the Gd(III)-coordinating oxygens.

Two small and uncharged Gd(III) tags, propargyl-DO3A and C11 (Fig. 10.27), were attached to *E. coli* aspartate/glutamate-binding protein and the Zika virus NS2B–NS3 protease [106]. Distance measurements between the label on the proteins were performed by double electron–electron resonance experiments. Echo-detected EPR spectra and echo-decay spectra measurements were carried out at 10 K on a home-built pulse EPR spectrometer operating at W-band (94.9 GHz). Owning their

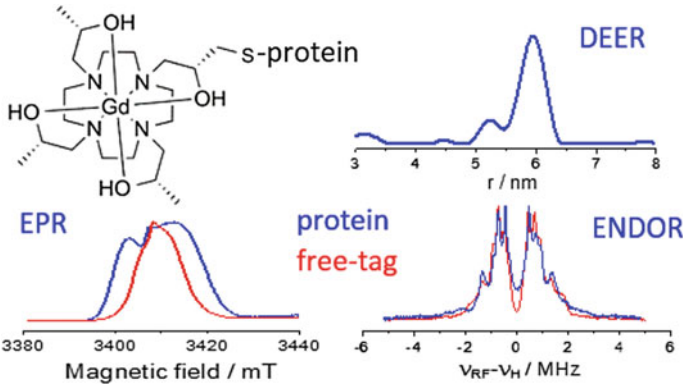

Fig. 10.26 Schematic presentation of Small Gd(III) Tags for Gd(III)−Gd(III) distance measurements in proteins by EPR spectroscopy [108]. Reprinted from [108], Copyright 2014 American Chemical Society

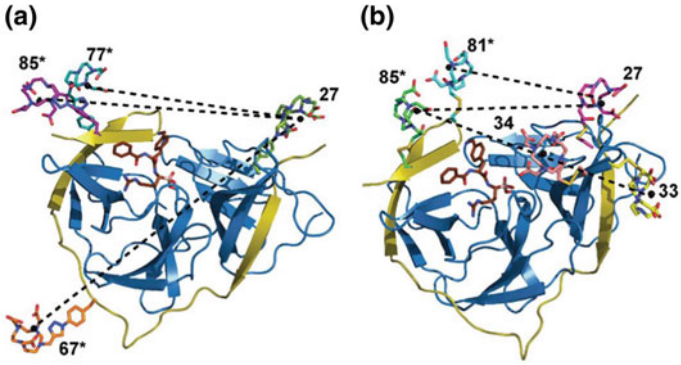

Fig. 10.27 Crystal structure of the Zika virus NS2B–NS3 protease (PDB: 5LC0) [34] with Gd(III) tags modeled at different sites. NS2B and NS3 are shown as yellow and blue ribbons, respectively. Tagged residues and the inhibitor cn-716 (indicated in orange) are shown in a line representation. Distances measured by DEER experiments are shown as dotted lines. **a** Structure with AzF residues tagged with propargyl-DO3A in positions 67*, 77*, 85* and 27. **b** Structure with cysteine residues tagged with C11 in positions 81*, 85*, 27, 33, and 34 [106]. Reprinted from [106], Copyright 2018 RCS

compact structure, the tags delivered narrower distance distributions. A closed conformation determined by X-ray crystallography in the presence of the high-affinity inhibitor cn-716 was confirmed in the EPR experiments, in which DEER measurements were performed in the presence as well as in the absence of this inhibitor. In this conformation, NS2Bc contributes to forming the substrate-binding site of the protease (Fig. 10.27).

The properties of the conformational landscape of a biomolecule, especially for proteins with disordered regions, are of capital importance to understand its function. To provide an upper bound of the statistical weight of each conformation of Ca^{2+}-bound calmodulin (CaM), Maximum Occurrence (MaxOcc) approach in combination with DEER was proposed [107]. For probing the interdomain distance distributions, three different mutants of calmodulin, N53C-T110C, N53C-A103C, and T34C-T117C, were labeled by Gd^{3+} DOTA-maleimide compound. One label was situated in the C-terminal domain and the other in the N-terminal domain. The reduction of the space that is covered by conformations with MaxOcc Z30% was appreciated with the viewpoint along the central helix, i.e., the fourth helix of the N-terminal domain. DEER data were highly complementary to NMR and small-angle X-ray scattering.

The spin labels C7-Gd

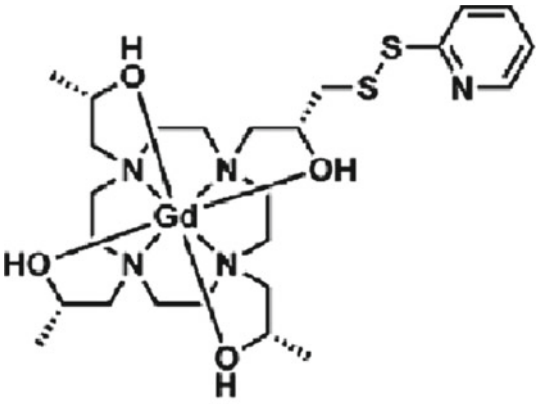

C7-Gd

and C8-Gd were loaded on two mutants of the homodimeric ERp29 protein (S114C/C157S and G147C/C157S) [108]. The labeled protein was investigated by an arsenal advance EPR techniques including the ^{1}H ENDOR, Mims ^{2}H-ENDOR, DEER, echo-detected EPR of 94.9 and 240 GHz. Due to their small size, short tether to the protein broad central EPR transition, narrow distance distribution, and sensitivity of EPR spectra to their nearby protein environment, the C7 and C8 tags were demonstrated superior for measurements of short (<4 nm) distances.

A combined method, employing NMR and EPR spectroscopies, was used to compare different types of nitroxide-based and Gd(III)-based spin labels attached to isolated RBDs of the polypyrimidine-tract-binding protein 1 (PTBP1) and to short RNA fragments (Fig. 10.28) [109]. DEER and continuous-wave EPR spectroscopy performance, resulting distance distributions, and their consistency with the predictions from the spin-label rotamers analysis were described in detail. As an example, the assumption of incomplete RBD/RNA complex formation was tested by DEER measurements in three-spin systems with two Gd(III)-based or nitroxide-based spin labels attached to the RBD2 and one IAP spin label at the U15 site of the RNA stem loop (Fig. 10.29).

In the last three decades, triarylmethyl (TAM)

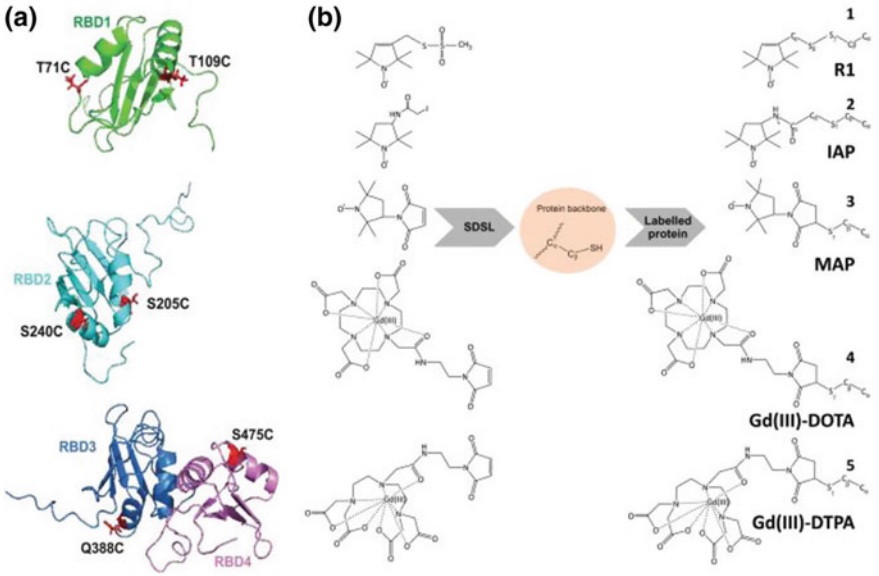

Fig. 10.28 Solution-NMR structures of the individual RBDs showing the selected mutation *EXIST* positions (red) in the a-helices of each domain (**a**). RBD34 is treated as one inter-domain construct, i.e., as a single rigid body, because of its hydrophobic interactions. SDSL with the respective spin labels, nitroxide radicals (1–3), and Gd(III)-based spin labels (4, 5), is shown in (**b**). The MTSSL-based side chain (R1) is formed by an S–S bond formation which is reversible under reducing conditions (1). Iodo-acetamido proxyl (IAP) and succinimide-containing labels (MAP, Gd(III)–DOTA, Gd(III)–DTPA) form a C–S–C thioether group (2–5), including the sulfur and the Cb atom of the cysteine residue, which makes the spin labels irreversible also under reducing conditions [109]. Reprinted from [109], Copyright 2017 RCS

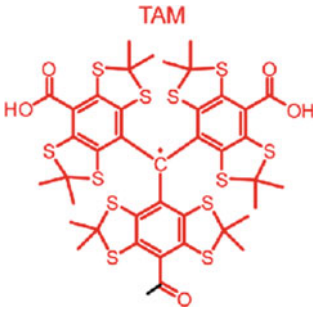

radicals have been widely employed as spin probes for oxymetry in EPR and EPR tomography owing to the narrow EPR linewidth and high stability in living systems. Nowadays, TAM successively used as spin labels for studies on the structure of proteins and nucleic acids utilizing site-directed spin labeling (SDSL) and PD-EPR spectroscopy [15, 110, 111]. The propeller-shaped structure of a TAM drawn

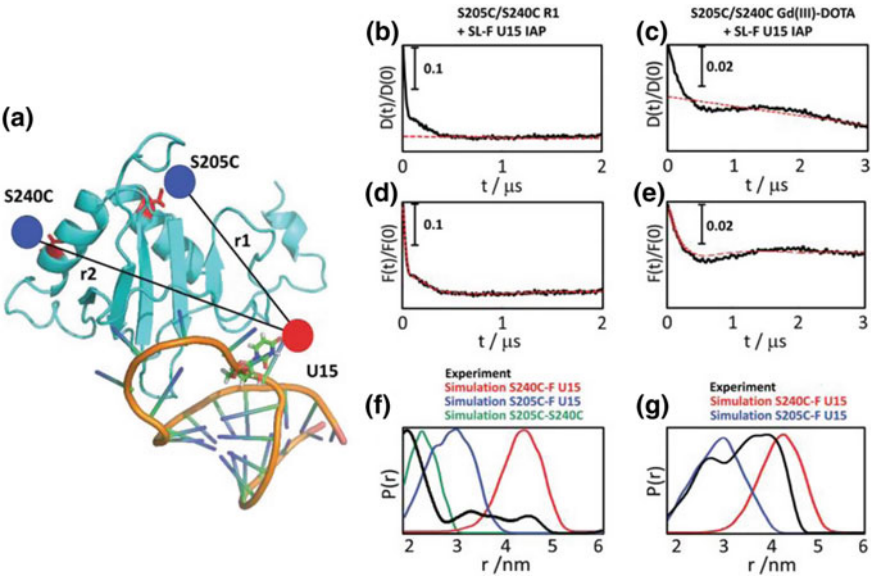

Fig. 10.29 Spectroscopically orthogonal two-label system and control with three non-orthogonal labels. **a** Representation of the RBD2–SLF complex with labeled positions on the protein and on RNA (blue and red dots). **b**, **c** Experimental data (black) and background fits (red, dashed line) for three nitroxide labels (**b**) and two Gd(III) labels combined with one nitroxide label (**c**). **d**, **e** Background-corrected DEER data (black) and form factor fit (red, dashed line) for three nitroxide labels (**d**) and two Gd(III) labels combined with one nitroxide label (**e**). **f** and **g** Experimental distance distributions (black) and simulated distance distributions (colored lines) for three nitroxide labels (**f**) and two Gd(III) labels combined with one nitroxide label (**g**) [109] Reprinted from [109], Copyright 2017 RCS

using EPR, ENDOR, and quantum-chemical analysis of two simple symmetric trityl radicals was established [110].

An idea of use of carbon-centered triarylmethyl (trityl) radicals instead of nitroxides for nanometer-distance measurements was first introduced and realized in 2012 [112].

Specifically, the tetrathiatriaryl methyl gave an EPR spectrum with one line only and has a transverse relaxation time T_m in the microsecond regime, even at room temperature in the liquid state. To evaluate the potential of trityls as spin labels for nanometer-distance measurements, two derivatives of Poly(para phenyleneethynylene)s (PolyPPEs) were prepared. Compound 1 contains one trityl and a typical nitroxide, whereas compound 2 has two trityl groups. PELDOR and double-quantum coherence (DQC), both in combination with DEER analysis showed the spin–spin distance values of about 35 and 50 Å for compounds 1 and 2, respectively, in excellent agreement with their structure. Triarylmethyl radicals were attached via disulfide linkages to substituted cysteine residues at positions 65 and 80 or 65 and 76 in T4 lysozyme immobilized on Sepharose. Interspin distances determined using double-quantum coherence (DQC) in solution were found to be close to those expected from

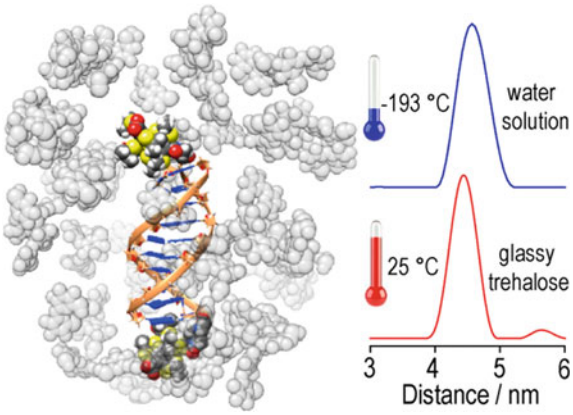

Fig. 10.30 Schematic representation of TAM-labeled DNA duplex in trehalose distance distribution studied by X-band DQC and DEER [114]. Reprinted from [114], Copyright 2014 American Chemistry Society

models [113]. The experiments revealed the narrow distance distribution in each case which indicates that the TAM-based spin label is relatively localized.

The first detailed investigation of trehalose as a prospective immobilizing agent of spin-labeled nucleic acids for pulse EPR distance measurements at room temperatures was reported [114].

Two other saccharides of close structure, sucrose and glucose, and compare their performance with trehalose were also investigated. The 10-mer DNA duplex doubly spin-labeled with TAM radical was used a model system for pulse EPR distance measurements. Schematic representation of TAM-labeled DNA duplex in trehalose distance distribution studied by X-band DQC and DEER is shown in Fig. 10.30.

In work [115], the broad range of triarylmethyl radicals (TAMs) varying polarity, number, and nature of substituents attached to carboxyl moieties located in para-positions of TA aryl rings, and structure of the TAM core were synthesized, and their relaxation times at room temperature in liquids were measured. Pulsed and low-temperature CW-EPR experiments were carried out at the X-band (9 GHz) and Q-band (34 GHz). Measurements of electron spin relaxation ($T_m \sim T_2$, T_1) were performed at the X- and Q-bands at $T = 300$ K. T_m was measured using a two-pulse electron spin echo (ESE) sequence; T_1 was measured using inversion–recovery technique with inversion π-pulse and detecting two-pulse ESE sequence. Data on Electron Spin Dephasing Time, T_m, and Electron Spin–Lattice Relaxation Time, T_1, for Investigated Radicals at 300 K at the X- and Q-Bands were tabulated and discussed in detail.

An approach that keeps structural conformation and unity of immobilized double-stranded DNA labeled with TAM (Fig. 10.31) using saccharides trehalose, sucrose, and glucose as immobilizing media, which provides conditions suitable for room-temperature EPR distance measurements, was proposed [116]. Room-temperature electron spin dephasing time of triarylmethyl-labeled DNA in trehalose was found to be noticeably longer compared to previously used immobilizers, thus providing a broader range of available distances.

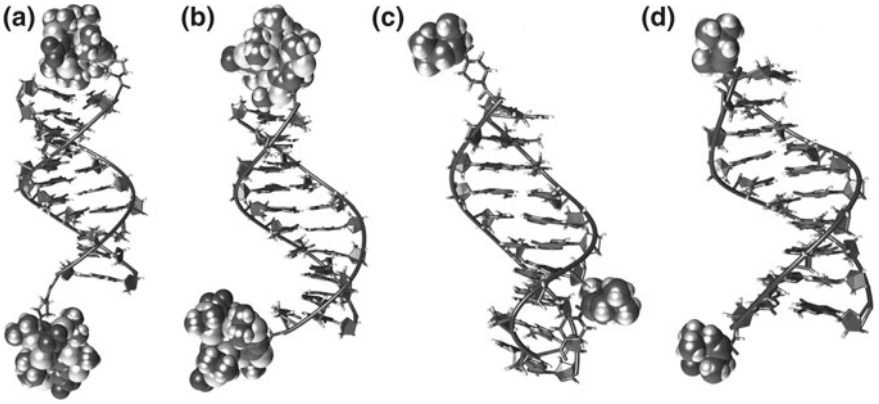

Fig. 10.31 Typical positions of spin labels relative to DNA duplexes: **a** I (D1-Pip-TAM/TAM); **b** VI (D1-NH-TAM/TAM); **c** IV (D1-Pip-NIT/NIT); **d** V (D1-NH-NIT/NIT) [116]. Reprinted from [116], Copyright 2010, American Chemical Society

The results of a nucleic acid study obtained using TAM were compared with data on nitroxyl spin labels (Fig. 10.32). In order to find structure/property relations in a series synthesized nitroxides with different substituents adjacent to NO-moiety (spirocyclohexane, spirocyclopentane, tetraethyl and tetramethyl groups), electron spin relaxation times (T_1, $T_m \approx 700$ ns) of these radicals immobilized in trehalose were measured at room temperature at X- and Q-bands (9/34 GHz) [117]. In addition, a comparison was made with the corresponding relaxation times in nitroxide-labeled DNA immobilized in trehalose. The room-temperature value of T_m in trehalose is weakly dependent on the structure of substituents adjacent to NO-moiety of nitroxide.

A new site-directed 2,5-bis(spirocyclohexane)-substituted spin label, based on the attachment of a linker containing an aliphatic amino group to the target nucleotide

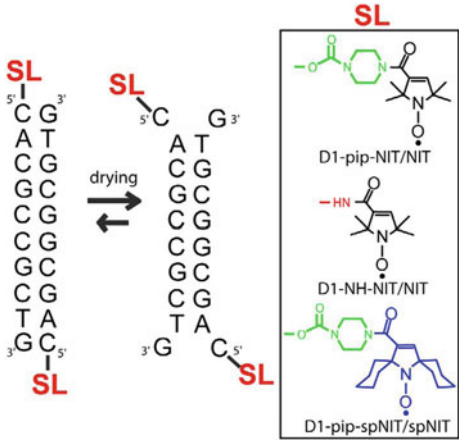

Fig. 10.32 Nitroxide-labeled DNA immobilized in trehalose [117]. Reprinted from [117], Copyright 2016 Elsevier

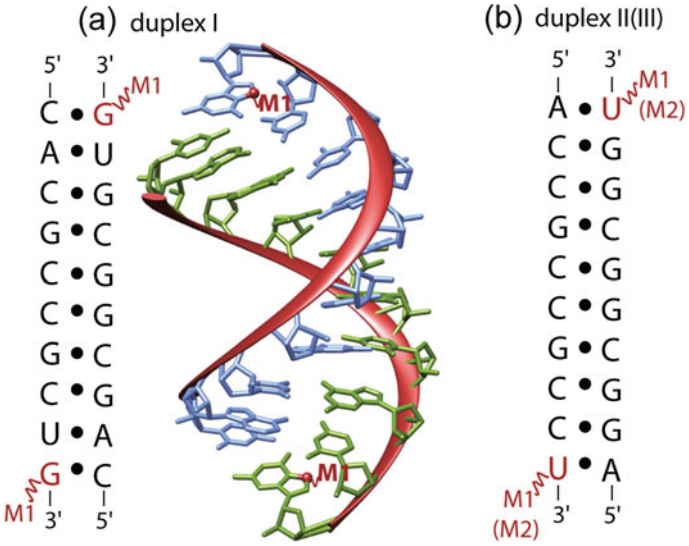

Fig. 10.33 Schematic presentation of RNA labeling by nitroxide [111]. Reprinted from [111], Copyright 2014 RCS

residue followed by selective coupling of a spin label to this amino group, was utilized [111]. This label with advanced stability and relaxation properties was tethered to the desired RNA residue via a sequence-specific reaction with the derivatives of oligodeoxyribonucleotides (Fig. 10.33). It was found that the attached label distance distribution measured employing Q-band (34 GHz) pulsed double electron–electron resonance corresponds well to values expected from model RNA duplex with known structure and distance between corresponding residues. The obtained results were validated by studying a similar RNA duplex, where the linker with the aliphatic amino group was introduced via solid-phase synthesis.

The features of PD-EPR and RE at ambient temperatures, requirements on electron spin phase memory time, ways of immobilization of biomolecules, the influence of a linker between the spin probe and biomolecule, and future opportunities were comprehensively reviewed [15]. Various aspects of spin labeling have been discussed in [119–121].

References

1. T.J. Stone, T. Buckman, P.L. Nordio, H.M. McConnell, Spin-labeled biomolecules. Proc. Natl. Acad. Sci. **54**, 1010–1017 (1965)
2. E. Fremi, Ann. Chim. Phys. Ser. 3 **15**, 408–488 (1845)
3. M.B. Neiman, É.G. Rozantzev, Y.G. Mamedova, Free radical reactions involving no unpaired electrons. Nature **196**, 472 (1962)

4. G.I. Likhtenshtein, Determination of the topography of proteins groups using specific paramagnetic labels. Mol. Biol. (Moscow) **2**, 234–240 (1968)
5. G.I. Likhtenshtein, *Spin Labeling Method in Molecular Biology* (Wiley, New York, 1976)
6. J.C. Taylor, J.S. Leigh, M. Cohn, The effect of dipole–dipole interaction between nitroxide radical and a paramagnetic ion on the line shape of the ESR spectra of radical. Proc. Natl. Acad. Sci. USA **64**, 219–206 (1969)
7. G.I. Likhtenshtein, Study on the proteins microstructure by method of spin-label paramagnetic probe. Mol. Biol. (Moscow) **4**, 782–789 (1970)
8. A.I. Kulikov, G.I. Likhtenshtein, E.G. Rozantzev, V. Suskina, A.V. Shapiro, Nitroxide bi- and polyradicals as standard models for distance estimation between the nitroxide moities. Biofizika **17**, 42–49 (1972)
9. A.I. Kokorin, K.I. Zamaraev, G.L. Grigoryan, V.P. Ivanov, E.G. Rozantsev, Distance estimation between nitroxyl radicals. Biofizika **17**, 34–41 (1972)
10. A.V. Kulikov, G.I. Likhtenstein, Application of saturation curves for evaluating distances in biological objects by the method of double spin-labels. Biofisika **19**, 420–424 (1974)
11. G.I. Likhtenshtein, Depth of immersion of paramagnetic centers, in *Magnetic Resonance in Biology*, ed. by L. Berliner, S. Eaton, G. Eaton (Kluwer Academic Publishers, Dordrecht, 2000), pp. 1–36
12. G.D. Case, J.S. Leigh Jr., Intramitochondrial position of cytochrome haem groups determined by dipolar interaction with paramagnetic cations. Biochem. J. **160**, 769–783 (1976)
13. A.V. Kulikov, G.I. Likhtenshtein, The use of spin-relaxation phenomena in the investigation of the structure of model and biological systems by method of spin labels. Adv. Mol. Relax. Interact. Process. **10**, 47–78 (1977)
14. G.I. Likhtenshtein, *Electron Spin in Chemistry and Biology: Fundamentals, Methods, Reactions Mechanisms, Magnetic Phenomena, Structure Investigation* (Springer, 1976)
15. O. Krumkacheva, E. Bagryanskaya, EPR-based distance measurements at ambient temperature. J. Magn. Reson. **280**, 117–126 (2017)
16. L.A. Syrtsova, L.A. Levchenko, E.N. Frolov, G.I. Likhtenshtein, N.N. Pisarscaya, L.V. Vorob'ev, V.A. Gromoglasova, Structure and function of the nitrogenase components from *Azotobacter vinelandii*. Mol. Biol. (Moscow) **6**, 62 (1972)
17. E.N. Frolov, G.I. Likhtenshtein, L.A. Syrtsova, Study of nonheme iron proteins. Dokl. A.N. SSSR **196**, 1149 (1971)
18. A.D. Milov, R.I. Samoilova, Y.D. Tsvetkov, M. De Zotti, C. Toniolo, J. Raap, PELDOR conformational analysis of bis-labeled Alamethicin aggregated in phospholipid vesicles. J. Phys. Chem. B **112**, 13469–13472 (2008)
19. G. Jeschke, DEER distance measurements on proteins. Annu. Rev. Phys. Chem. **63**, 419–446 (2012)
20. J.H. Freed, New technologies in electron spin resonance. Annu. Rev. Phys. Chem. **51**, 655–689 (2000)
21. G.R. Eaton, S.S. Eaton, D.P. Barr, R.T. Weber, *Quantitative EPR* (Springer, 2010)
22. A.V. Kulikov, Determination of distance between the nitroxide label and a paramagnetic center in spin-labeled proteins from the parameters of the saturation curve of the ESR spectrum of the label at 77K. Mol. Biol. (Moscow) **10**, 109–116 (1976)
23. C.L. Motion, J.E. Lovett, S. Bell, S.L. Cassidy, P.A.S. Cruickshank, D.R. Bolton, R.I. Hunter, H. El Mkami, S. Van Doorslaer, G.M. Smith, DEER sensitivity between iron centers and nitroxides in heme-containing proteins improves dramatically using broadband, high-field EPR. J. Phys. Chem. Lett. **7**, 1411–1415 (2016)
24. B. Selmke, P.P. Borbat, C. Nickolaus, R. Varadarajan, J.H. Freed, W.E. Trommer, Open and closed form of maltose binding protein in its native and molten globule state as studied by electron paramagnetic resonance spectroscopy. Biochemistry **57**(38), 5507–5512 (2018)
25. A.L. Lai, E.M. Clerico, M.E. Blackburn, N.A. Patel, C.V. Robinson, P.P. Borbat, J.H. Freed, L.V. Gierasch, Key features of an Hsp70 chaperone allosteric landscape revealed by ion-mobility native mass spectrometry and double electron-electron resonance. J. Biol. Chem. **292**(21), 8773–8785 (2017)

26. M.V. Airola, D. Huh, N. Sukomon, J. Widom, R. Sircar, P.P. Borbat, J.H. Freed, K.J. Watts, B.R. Crane, Architecture of the soluble receptor Aer2 indicates an in-line mechanism for PAS and HAMP domain signaling. J. Mol. Biol. **425**(5), 886–901 (2013)
27. G.T. Merz, P.P. Borbat, A.R. Muok, M. Srivastava, D.N. Bunck, J.H. Freed, B.R. Crane, Site-specific incorporation of a Cu^{2+} spin label into proteins for measuring distances by pulsed dipolar electron spin resonance spectroscopy. J. Phys. Chem. B **122**(41), 9443–9451 (2018)
28. B.J. Wylie, B.G. Dzikovski, S. Pawsey, M. Caporini, M. Rosay, J.H. Freed, A.E. McDermott, Dynamic nuclear polarization of membrane proteins: covalently bound spin-labels at protein-protein interfaces. J. Biomol. NMR **61**(3–4), 361–367 (2015)
29. Y. Yang, F. Yang, Y.-J. Gong, T. Bahrenberg, A. Feintuch, X.-C. Su, D. Goldfarb, High sensitivity in-cell epr distance measurements on proteins using an optimized Gd(III) spin label. J. Phys. Chem. Lett. **9**, 6119–6123 (2018)
30. S. Dunkel, L.P. Pulagam, H.-J. Steinhoff, J.P. Klare, In vivo EPR on spin labeled colicin A reveals an oligomeric assembly of the pore-forming domain in *E. coli* membranes. Phys. Chem. Chem. Phys. **17**(7), 4875–4878 (2015)
31. L.G.M. Basso, L.F.S. Mendes, A.J. Costa-Filho, The two sides of a lipid–protein story. Biophys. Rev. **8**, 179–191 (2016)
32. R.D. Nielsen, K. Che, M.H. Gelb, B.H. Robinson, A ruler for determining the position of proteins in membranes. J. Am. Chem. Soc. **127**, 6430–6442 (2005)
33. D. Snead, A.L. Lai, R.T. Wragg, D.A. Parisotto, T.F. Ramlall, J.S. Dittman, J.H. Freed, D. Eliezer, Unique structural features of membrane-bound C-terminal domain motifs modulate complexin inhibitory function. Front. Mol. Neurosci. **10**, 1–17 (2017)
34. R.S. Cooper, E.R. Georgieva, P.P. Borbat, J.H. Freed, E.E. Heldwein, Structural basis for membrane anchoring and fusion regulation of the herpes simplex virus fusogen gB. Nat. Struct. Mol. Biol. **25**, 416–424 (2018)
35. A.L. Lai, J.H. Freed, HIV gp41 fusion peptide increases membrane ordering in a cholesterol-dependent fashion. Biophys. J. **106**(1), 172–181 (2014)
36. P. Lueders, H. Jäger, M.A. Hemminga, G. Jeschke, M. Yulikov, Distance measurements on orthogonally spin-labeled membrane spanning WALP23 polypeptides. J. Phys. Chem. B **117**, 2061–2068 (2013)
37. T.F. Segawa, M. Doppelbauer, L. Garbuio, A. Doll, Y.O. Polyhach, G. Jeschke, Water accessibility in a membrane-inserting peptide comparing Overhauser DNP and pulse EPR methods. J. Chem. Phys. **144**(19), 194201/1–194201/12 (2016)
38. I.D. Sahu, G.A. Lorigan, Site-directed spin labeling EPR for studying membrane proteins. Biomed. Res. Int. **2018**, 3248289 (2018)
39. E.R. Georgieva, Nanoscale lipid membrane mimetics in spin-labeling and electron paramagnetic resonance spectroscopy studies of protein structure and function. Nanotechnol. Rev. **6**(1) (2016). https://doi.org/10.1515/ntrev-2016-0080
40. D. Marsh, T. Pali, The protein–lipid interface: perspectives from magnetic resonance and crystal structures. Biochim. Biophys. Acta: Biomembr. **1666**(1–2), 118–141 (2004)
41. M.A. Hemminga, L.J. Berliner, *ESR spectroscopy in membrane biophysics* (Springer, New York, 2007)
42. E.S. Karp, J.J. Inbaraj, M.L. Laryukhin, G.A. Lorigan, Electron paramagnetic resonance studies of an integral membrane peptide inserted into aligned phospholipid bilayer nanotube arrays. J. Am. Chem. Soc. **128**, 12070–12071 (2006)
43. A.N. Smith, U.T. Twahir, T. Dubroca, G.E. Fanucci, J.R. Long, Molecular rationale for improved dynamic nuclear polarization of biomembranes. J. Phys. Chem. B **120**, 7880–7888 (2016)
44. S.Y. Liao, M. Lee, T. Wang, I.V. Sergeyev, M. Hong, Efficient DNP NMR of membrane proteins: sample preparation protocols, sensitivity, and radical location. J. Biomol. NMR **64**, 223–237 (2016)
45. L.G. Mansor Basso, L.F. Santos Mendes, A.J. Costa-Filho, The two sides of a lipid–protein story. Biophys, Rev **8**, 179–191 (2016)

46. J.M. Franck, S. Chandrasekaran, B. Dzikovski, C.R. Dunnam, J.H. Freed, Focus: two-dimensional electron–electron double resonance and motions: the challenge of higher frequencies. J. Chem. Phys. **142**, 212302 (2015). (Review)
47. S.Th. Sigurdsson, Nitroxides and nucleic acids: chemistry and electron paramagnetic resonance (EPR) spectroscopy. Pure Appl. Chem. **83**, 677–686 (2011)
48. Y. Sun, P.P. Borbat, V.M. Grigoryants, W.K. Myers, J.H. Freed, C.P. Scholes, Pulse dipolar ESR of doubly labeled mini TAR DNA and its annealing to mini TAR RNA. Biophys. J. **108**, 893–902 (2015)
49. G.W. Reginsson, O. Schiemann, Spin labeling of DNA and RNA, in *Encyclopedia of Biophysics*, ed. by G.C.K. Roberts (Springer, Berlin, Heidelberg, 2013)
50. G. Masliah, C. Maris, L.B. König, M. Yulikov, F. Aeschimann, A.L. Malinows, J. Mabille, J. Weiler, A. Holla, J. Hunziker, N. Meisner-Kober, B. Schuler, G. Jeschk, F. H-T Allain, Structural basis of siRNA recognition by TRBP double-stranded RNA binding domains. EMBO J. **37**(6) (2018)
51. E.S. Babaylova, A.A. Malygin, A.A. Lomzov, D.V. Pyshnyi, M. Yulikov, G. Jeschke, O.A. Krumkacheva, M.V. Fedin, E.G. Bagryanskaya, Complementary-addressed site-directed spin labeling of long natural RNAs. Nucleic Acids Res. **44**(16), 7935–7943 (2016)
52. O. Duss, M. Yulikov, F.H.T. Allain, G. Jeschke, Combining NMR and EPR to determine structures of large RNAs and protein–RNA complexes in solution. Methods Enzymol. **558**(Structures of Large RNA Molecules and Their Complexes), 279–331 (2015)
53. J.M. Esquiaqui, E.M. Sherman, J.D. Ye, G.E. Fanucci, Conformational flexibility and dynamics of the internal loop and helical regions of the kink-turn motif in the glycine riboswitch by site-directed spin-labeling. Biochemistry **55**(31), 4295–305 (2016)
54. G.I. Likhtenshtein, *Electron Spin in Chemistry and Biology: Fundamentals, Methods, Reactions Mechanisms, Magnetic Phenomena, Structure Investigation* (Springer, 2016)
55. V.V. Khramtsov, In vivo molecular electron paramagnetic resonance-based spectroscopy and imaging of tumor microenvironment and redox using functional paramagnetic probes. Antioxid. Redox Signal. **28**, 1365–1377 (2018)
56. D.J. Lurie, M.A. Foster, D. Yeung, J.M.S. Hutchison, Design, construction and use of a large-sample field-cycled PEDRI imager. Phys. Med. Biol. **43**, 1877–1886 (1998)
57. V.V. Khramtsov, G.L. Caia, K. Shet, E. Kesselring, S. Petryakov, J.L. Zweier, A. Samouilov, Variable field proton–electron double-resonance imaging: application to pH mapping of aqueous samples. J. Magn. Reson. **202**, 267–273 (2010)
58. G. Ilangovan, J.L.Zweier, P. Kuppusamy, Microximetry: simultaneous determination of oxygen consumption and free radical production using electron paramagnetic resonance spectroscopy. Methods Enzymol. **381**(Oxygen Sensing), 747–762 (2004)
59. H. Swartz, Seeing is believing—visualizing drug delivery *in vitro* and in *vivo*. Adv. Drug Deliv. Rev. **57**, 1085–1086 (2005)
60. W.K. Subczynski, J.S. Hyde, The diffusion-concentration product of oxygen in lipid bilayers using the spin-label T_1 method. Biochim. Bioph. Acta **43**, 283–291 (1986)
61. W.K. Subczynski, L. Mainali, T.G. Camenisch, W. Froncisz, J.S. Hyde, Spin-label oximetry at Q- and W-band. J. Magn. Reson. **209**, 142–148 (2011)
62. G.I. Likhtenshtein, Yu.D. Akhmedov, L.V. Ivanov, L.A. Krinitskaya, Yu.V. Kokhanov, Investigation of the lysozyme macromolecule by a spin-labeling method. Mol. Biol. (Moscow) **8**, 40–48 (1974)
63. E.I. Yudanova, A.V. Kulikov, Determination of spin-exchange frequency of nitroxide radicals and oxygen by continuous saturation of ESR spectra. Biofizika **29**, 925–929 (1984)
64. V.V. Khramtsov, L.M. Weiner, I.A. Grigor'ev, L.B. Volodarsky, Proton exchange in stable nitroxyl radicals. ESR study of the pH of aqueous solutions. Chem. Phys. Lett. **91**, 69–72 (1982)
65. I.A. Grigor'ev, A. Samouilov, V.V. Khramtsov, In vivo monitoring of pH, redox status, and glutathione using L-band EPR for assessment of therapeutic effectiveness in solid tumors. Magn. Reson. Med. **67**, 1827–1836 (2012)

66. V.V. Khramtsov, In vivo spectroscopy and imaging of nitroxide probes, in *Nitroxides: Theory, Experiment and Applications*, ed. by A.I. Kokorin (2012), pp. 317–346
67. I.A. Kirilyuk, A.A. Bobko, V.V. Khramtsov, I.A. Grigor'ev, Nitroxides with two p*K* values—useful spin probes for pH monitoring within a broad range. Org. Biomol. Chem. **3**, 1269–1274 (2005)
68. L.B. Volodarsky (ed.), *Imidazolin Radicals* (CRC Press, Bosa Raton, 1988)
69. D. Meisel, G. Czapski, One-electron transfer equilibriums and redox potentials of radicals studied by pulse radiolysis. J. Phys. Chem. **79**, 1503–1509 (1975)
70. G.I. Likhtenshtein, *Biophysical Labeling Methods in Molecular Biology* (Cambridge University Press, Cambridge, New York, 1993)
71. A.P. Jagtap, I. Krstic, N.C. Kunjir, R. Hänsel, T.F. Prisner, S.T. Sigurdsson, Sterically shielded spin labels for in-cell EPR spectroscopy: analysis of stability in reducing environment. Free Radic. Res. **49**(1), 78–85 (2015)
72. N. Kocherginsky, H.M. Swarts, *Nitroxide Spin Labels. Reactions in Biology and Chemistry* (CRC Press, 1995)
73. L.B. Volodarsky, I.A. Grigor'ev, S.A. Dikanov, V.A. Reznikov, *Imidazoline Nitroxide Radicals* (Nauka (Siberian Branch), Novosibirsk, 1988), pp. 188–193)
74. V.V. Khramtsov, V.I. Yelinova (Popova), L.M. Weiner, T.A. Berezina, V.V. Martin, L.B. Volodarsky, Quantitative determination of SH groups in low- and high-molecular-weight compounds by an electron spin resonance method. Anal. Biochem. **182**, 58–63 (1989)
75. L. Ya, L. Gendel, M.A. Goldfeld, V.K. Koltover, E.G. Rozanzev, V.I. Suskina, Biofizika **13**, 1114–1115 (1968)
76. A.A. Bobko, T.D. Eubank, J.L. Voorhees, O.V. Efimova, I.A. Kirilyuk, S. Petryakov, D.G. Trofimiov, C.B. Marsh, J.L. Zweier, I.A. Grigor'ev, A. Samouilov, V.V. Khramtsov, *In vivo* monitoring of pH, redox status, and glutathione using L-band EPR for assessment of therapeutic effectiveness in solid tumors. Magn. Reson. Med. **67**, 1827–1836 (2012)
77. V.V. Khramtsov, A.A. Bobko, M. Tseytlin, B. Driesschaert, Exchange phenomena in the electron paramagnetic resonance spectra of the nitroxyl and trityl radicals: multifunctional spectroscopy and imaging of local chemical microenvironment. Anal. Chem. **89**, 4758–4771 (2017)
78. S. Kishimoto, M.C. Krishna,V.V., Khramtsov, H. Utsumi, D.J. Lurie, In Vivo Application of Proton-Electron Double-Resonance Imaging. ANTIOXIDANTS & REDOX SIGNALING 28, 1345–1363 (2018)
79. D.J. Lurie, J.M. Hutchison, L.N. Bell, I. Nicholson, D.M. Bussell, J.R. Mallard, Field-cycled proton-electron double resonance imaging of free radicals in large aqueous samples. J. Magn. Reson. **84**, 431–437 (1989)
80. H. Utsumi, K-I. Yamada, K. Ichikawa, K. Sakai, Y. Kinoshita, S. Matsumoto, M. Nagai, Simultaneous molecular imaging of redox reactions monitored by Overhauser enhanced MRI with ^{14}N- and ^{15}N-labeled nitroxyl radicals. Proc. Natl. Acad. Sci. USA **103**, 1463–1468 (2006)
81. A. Samouilov, O.V. Efimova, A.A. Bobko, Z. Sun, S. Petryakov, T.B. Eubank, D.G. Trofimov, I.A. Kirilyuk, I.A. Grigor'ev, W. Takahashi, I.L. Zweier, V.V. Khramtsov, In vivo proton–electron double-resonance imaging of extracellular tumor pH using an advanced nitroxide probe. Anal. Chem. **86**, 1045–1052 (2014)
82. F. Hyodo, S. Ito, K. Yasukawa, R. Kobayashi, H. Utsumi, Simultaneous and spectroscopic redox molecular imaging of multiple free radical intermediates using dynamic nuclear polarization-magnetic resonance imaging. Anal. Chem. **86**, 7234–7238 (2014)
83. H. Eto, F. Hyodo, N. Kosem, R. Kobayashi, K. Yasukawa, M. Nakao, M. Kiniwa, H. Utsumi, Redox imaging of skeletal muscle using in vivo DNP-MRI and its application to an animal model of local inflammation. Free Radic. Biol. Med. **89**, 1097–1104 (2015)
84. G.I. Likhtenshtein, A.P. Pivovarov, P.Kh. Bobodzhanov, E.G. Rozantsev, N.B. Smolina, Biofizika **13**, 396–400 (1968)
85. G.I. Likhtenshtein, Yu.B. Grebenshchikov, T.V. Avilova, Mol. Biol. (Moscow) **6**, 52–60 (1972)

86. D. Kivelson, Theory of EPR [electron paramagnetic resonance] line widths of free radicals. J. Chem. Phys. **33**, 1094–1106 (1960)
87. J.H. Freed, Theory of the ESR spectra of nitroxides, in *Spin Labeling. Theory and Applications*, vol. 1, ed. by L. Berliner (Academic Press, New York, 1976)
88. L.I. Antsiferova, O.V. Belonogova, V.V. Kochetkov, G.I. Likhtenshtein, Izvestiya Akademii Nauk SSSR, Seriya Biologicheskaya 494–501 (1989)
89. M.A. Voinov, D.B. Good, M.E. Ward, S. Milikisiyants, A. Marek, M.A. Caporini, M. Rosay, R.A. Munro, M. Ljumovic, L.S. Brown, V. Ladizhansky, A.I. Smirnov, Cysteine-specific labeling of proteins with a nitroxide biradical for dynamic nuclear polarization NMR. J. Phys. Chem. B **119**, 10180–10190 (2015)
90. E.P. Kirilina, I.A. Grigoriev, S.A. Dzuba, Oriental motion of nitroxide in molecular glasses. J. Chem. Phys. **121**, 12465–12471 (2004)
91. M. Pavone, P. Cimino, F. De Angelis, V. Barone, J. Am. Chem. Soc. **128**, 4338–4347 (2006)
92. H.S. Mchaourab, P.R. Steed, K. Kazmier, Toward the fourth dimension of membrane protein structure: insight into dynamics from spin-labeling EPR spectroscopy. Structure **19**, 1549–1561 (2011)
93. Z. Zhang, M.R. Fleissner, D.S. Tipikin, Z. Liang, J.K. Moscicki, K.A. Earle, W.L. Hubbell, J.H. Freed, Multifrequency electron spin resonance study of the dynamics of spin labeled T4 lysozyme. J. Phys. Chem. B **11**, 5503–5521 (2010)
94. M.M. Haimann, Y. Akdogan, R. Philipp, R. Varadarajan, D. Hinderberger, W.E. Trommer, Conformational changes of the chaperone SecB upon binding to a model substrate—bovine pancreatic trypsin inhibitor (BPTI). Biol. Chem. **392**, 849–858 (2011)
95. F. Tombolato, A. Ferrarin, J.H. Freed, Dynamics of the nitroxide side chain in spin-labeled proteins. J. Phys. Chem. B **110**, 26248–26259 (2006)
96. L. Yu, W. Wang, S. Ling, S. Liu, L. Xiao, Y. Xin, C. Lai, Y. Xiong, L. Zhang, C. Tian, CW-EPR studies revealed different motional properties and oligomeric states of the integrin β1a transmembrane domain in detergent micelles or liposomes. Sci Rep. **5**, 7848 (2015)
97. Y.-W. Chiang, A.J. Costa-Filho, J.H. Freed, Dynamic molecular structure and phase diagram of DPPC-cholesterol binary mixtures: a 2D-ELDOR study. J. Phys. Chem. B **111**, 11260–11270 (2007)
98. V.I. Krinichnyi, O.Ya. Grinberg, E.I. Judanova, M.L. Borin, Ya.S. Lebedev, G.I. Likhtenshtein, Study of molecular mobility in biological membranes by two millimeter band ESR spectroscopy. Biofizika **32**, 59–65(1988)
99. D. March, Spin-label EPR for determining polarity and proticity in biomolecular assemblies: transmembrane profiles. Appl. Magn. Reson. **37**, 435–454 (2010)
100. T.I. Smirnova, T.G. Chadwick, M.A. Voinov, O. Poluektov, J. van Tol, A. Ozarowski, G. Schaaf, M.M. Ryan, V.A. Bankaitis, Local polarity and hydrogen bonding inside the Sec14p phospholipid-binding cavity. Biophys. J. **92**, 3686–3695 (2007)
101. V.I. Krinichnyi, *2-mm Wave Band EPR Spectroscopy of Condensed Systems* (CRC Press, Boca Raton, IL, 1995)
102. G.I. Likhtenshtein, J. Yamauchi, S. Nakatsuji, R. Smirnov, *Tamura Nitroxides: Application in Chemistry, Biomedicine, and Materials Science* (Wiley, Weinhem, 2008)
103. D. Goldfarb, Gd^{3+} spin labeling for measuring. distances in biomacromolecules: why and how? Methods Enzymol. **563**, 416–457 (2015)
104. A. Feintuch, G. Otting, D. Goldfarb, Gd^{3+} spin labeling for measuring. distances in biomacromolecules: why and how? Methods Enzymol. **563**, 416–457 (2015)
105. G. Prokopiou, M.D. Lee, A. Collauto, E.H. Abdelkader, T. Bahrenberg, A. Feintuch, M. Ramirez-Cohen, J. Clayton, J.D. Swarbrick, B. Graham, G. Otting, D. Goldfarb, Measurements in proteins by EPR spectroscopy. Inorg. Chem. **57**(9), 5048–5059 (2018)
106. M.C. Mahawaththa, M.D. Lee, A. Giannoulis, A. Adams, A. Feintuch, J.D. Swarbrick, B. Graham, C. Nitsche, D. Goldfarb, G. Ottgorin, Small neutral Gd(III) tags for distance measurements in proteins by double electron–electron resonance experiments. Phys.Chem.Chem. Phys. **20**, 23535 (2018)

107. L. Gigli, W. Andrałojć, A. Dalaloyan, G. Parigi, E. Ravera, D. Goldfarb, C. Luchinat, Assessing protein conformational landscapes: integration of DEER data in maximum occurrence analysis. Phys. Chem. Chem. Phys. **20**, 27429 (2018)
108. G. Prokopiou, M.D. Lee, A. Collauto, E.H. Abdelkader, T. Bahrenberg, A. Feintuch, M. Ramirez-Cohen, J. Clayton, J.D. Swarbrick, B. Graham, G. Otting, D. Goldfarb, Small Gd(III) tags for Gd(III)–Gd(III) distance measurements in proteins by EPR spectroscopy. Inorg. Chem. **57**(9), 5048–5059 (2018)
109. C. Gmeiner, G. Dorn, F.H.T. Allain, G. Jeschke, M. Yulikov, Spin labelling for integrative structure modelling: a case study of the polypyrimidine-tract binding protein 1 domains in complexes with short RNAs. Phys. Chem. Chem. Phys. **19**, 28360 (2017)
110. M.K. Bowman, C. Mailer, H.J. Halpern, The solution conformation of triarylmethyl radicals. J. Magn. Reson. **172**, 254 (2005)
111. E.S. Babaylova, A.V. Ivanov, A.A. Malygin, M.A. Vorobjeva, A.G. Venyaminova, Yu.F. Polienko, I.A. Kirilyuk, O.A. Krumkacheva, M.V. Fedin, G.G. Karpova, E.G. Bagryanskaya, A versatile approach for site-directed spin labeling and structural EPR studies of RNAs. Org. Biomol. Chem. **12**, 3129 (2014)
112. G.W. Reginsson, N.C. Kunjir, STh Sigurdsson, O. Schiemann, Trityl radicals: spin labels for nanometer-distance measurements. Chem. Eur. J. **8**, 13580–13584 (2012)
113. Z. Yang, Y. Liu, P. Borbat, J.L. Zweier, J.H. Freed, W.L. Hubbell, Pulsed ESR dipolar spectroscopy for distance measurements in immobilized spin labeled proteins in liquid solution. J. Am. Chem. Soc. **134**, 9950–9952 (2012)
114. G.Y. Shevelev, O.A. Krumkacheva, A.A. Lomzov, A.A. Kuzhelev, O.Y. Rogozhnikova, D.V. Trukhin, T.I. Troitskaya, V.M. Tormyshev, M. Fedin, D. Pyshnyi, E.G. Bagryanskaya, Physiological-temperature distance measurement in nucleic acid using triarylmethyl-based spin labels and pulsed dipolar EPR spectroscopy. J. Am. Chem. Soc. **136**, 9874–9877 (2014)
115. A.A. Kuzhelev, D.V. Trukhin, O.A. Krumkacheva, R.K. Strizhakov, O.Y. Rogozhnikova, T.I. Troitskaya, M.V. Fedin, V.M. Tormyshev, E.G. Bagryanskaya, Room-temperature electron spin relaxation of triarylmethyl radicals at the X- and Q-bands. J. Phys. Chem. B **119**, 13630–13640 (2015)
116. A.A. Kuzhelev, G.Yu. Shevelev, O.A. Krumkacheva, V.M. Tormyshev, D.V. Pyshnyi, M.V. Fedin, E.G. Bagryanskaya, Saccharides as prospective immobilizers of nucleic acids for room-temperature structural EPR studies. J. Phys. Chem. Lett. **7**, 2544–2548 (2016)
117. A.A. Kuzhelev, R.K. Strizhakov, O.A. Krumkacheva, Y.F. Polienko, D.A. Morozov, GYu. Shevelev, D.V. Pyshnyi, I.A. Kirilyuk, M.V. Fedin, E.G. Bagryanskaya, Room-temperature electron spin relaxation of nitroxides immobilized in trehalose: Effect of substituents adjacent to NO-group. J. Magn. Reson. **266**, 1–7 (2016)
118. P. Roser, M.J. Schmidt, M. Drescher, D. Summerer, Site-directed spin labeling of proteins for distance measurements *in vitro* and in cells. Org. Biomol. Chem. **14**, 5468–5476 (2016)
119. N. Alonso-Garcia, I. Garcia-Rubio, J.A. Manso, R.M. Buey, R.H. Urien, A. Sonnenberg, G. Jeschke, J.M. de Pereda, Combination of X-ray crystallography, SAXS and DEER to obtain the structure of the FnIII-3,4 domains of integrin α6β4. Acta Crystallogr. D: Biol. Crystallogr. **71**(4), 969–985 (2015)
120. C. Gmeiner, D. Klose, E. Mileo, V. Belle, S.R.A. Marque, G. Dorn, F.H.T. Allain, B. Guigliarelli, G. Jeschke, M. Yulikov, Orthogonal tyrosine and cysteine site-directed spin labeling for dipolar pulse EPR spectroscopy on proteins. J. Phys. Chem. Lett. **8**(19), 4852–4857 (2017)
121. E.A.W. van der Cruijsen, E.J. Koers, C. Sauvee, R.E. Hulse, M. Weingarth, O. Ouari, E. Perozo, P. Tordo, M. Baldus, Biomolecular DNP-supported NMR spectroscopy using site-directed spin labeling. Chem. Eur. J. **21**, 12971–12977 (2015)

Chapter 11
Nitroxides Miscellaneous Application

11.1 Multispin Nitroxides

In the last two decades, superparamagnetic organic compounds including polymer magnets with stability at ambient temperature and/or higher magnetic ordering have been attracting attention as models of multispin systems and potential magnetic devices [1–6].

As an example, in a recent paper [6], the three-spin electron–electron–nucleus (e–e–n) cross-effect (CE) was investigated. The influence of compounds bearing nitroxides on the nuclear longitudinal relaxation time constant T_{1n}, the build-up time constants of nuclear magnetic resonance (NMR) signal, T_{DNP} and DNP-enhancement of NMR signal in a series of radicals with a systematic increase in their local electron spin concentration (mono-radical, bi-radicals, triradical, and a dendrimer with 9 nitroxide moieties (Fig. 11.1) were examined. All static DNP, NMR, and EPR

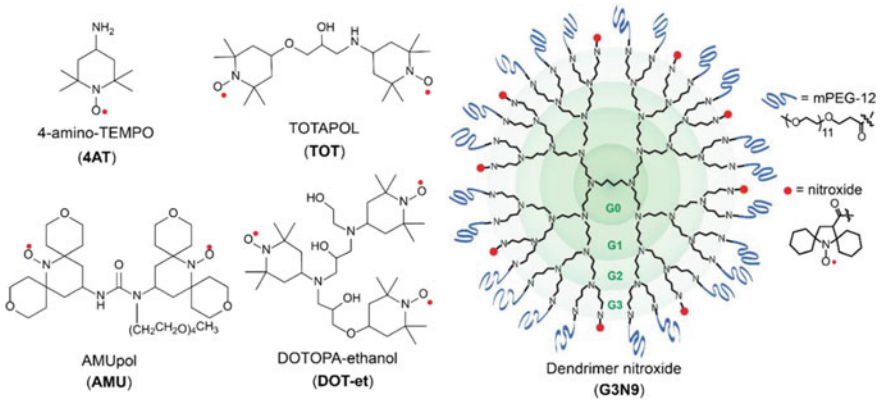

Fig. 11.1 Chemical structures of the mono-, bi-, tri-nitroxides, and dendrimer nitroxides [6]. Reprinted from [6], Copyright 2018 RCS

G. I. Likhtenshtein, *Nitroxides*, Springer Series in Materials Science 292,
https://doi.org/10.1007/978-3-030-34822-9_11

experiments were conducted at 7 T and at 4 K. Magic angle spinning MAS-DNP experiments employing a Bruker 400 MHz DNP-NMR spectrometer were performed at 92 K. The T_{1n} and T_{DNP} values for the five radicals were found to decrease significantly from mono-, bi-, triradical to the dendrimer having 37-60-fold smaller T_{1n} and T_{DNP} than the monomer, respectively, increasing e–e dipolar coupling. T_{1e} moderately increased, and T_M decreased with increasing local electron spin concentration. No correlation was found between T_M and T_{1n}.

Data on electron relaxation times and spectral diffusion rates for different radicals with 10 mM global electron spin concentration at 7 T magnetic field and 4 K temperature were tabulated. From the experimental observations and theoretical analysis made in this study, it was concluded that: (1) an increase in electron spin clustering led to an increased electron spin depolarization, (2) a dramatically shortened T_{1n} and T_{DNP} time constants under static and magic angle spinning (MAS) conditions takes place, (3) e–e–n polarization transfer rates are smaller or comparable to the nuclear spin diffusion rates, (4) polarization efficiency of nuclear spins tens to hundreds of nm away from the polarizing agent can result from a combination of direct e–e–n polarization transfer and nuclear spin diffusion processes, (5) DNP oversaturation is due to electron spin depolarization beyond optimal conditions with the dendrimer sample and attributed to the presence of strong e–e dipolar couplings, (6) strong e–e interactions, caused by electron spin clustering, increase the cross-effect rate, (7) fast cross-effect rates will benefit DNP at liquid helium temperatures, or at higher magnetic fields and pulsed DNP, and (8) slow e–e–n polarization transfer rate can be a key bottleneck to achieving maximal DNP performance.

In work [7], it was found that the cross-effect CE polarization transfer was truncated at the EPR resonant frequencies. Specifically, this effect was observed when doping Trityl-OX063 with a pyrroline nitroxide radical that possesses electron-withdrawing tetracarboxylate substituents (tetracarboxylate-ester-pyrroline or TCP) in vitrified water/glycerol at 6.9 T and at 3.3–85 occurs. The CE mechanism was replicated by quantum mechanical simulations with a mixed radical system, where the two radicals maximize the EPR spectral overlap to fulfill the cross-effect conditions, while one radical type is easily saturated but not the other due to very short T_{1e}.

The synthesis of the rigid multispin molecule based on tetrakis (4-azidophenyl) methane as a core, which is functionalized with nitroxide moieties via fourfold copper-catalyzed azide alkyne click chemistry between the azide functions of the core **1** and the alkyne moiety of an isoindoline nitroxide, was performed [8]. In order to evaluate the possibility to follow the exchange process between the isoindoline nitroxide of TPM-NO and TEMPO, the EPR spectra of the individual compounds and mixtures thereof in toluene at room temperature were recorded. The TEMPO nitroxide has a hyperfine coupling constant of about 15.5 Gauss, while TPM-NO 3 shows a hyperfine coupling constant of about 14.1 Gauss, most probably as result of spin exchange in the multispin compounds.

Diradicals 2–7 with $S = 1$ ground-state and $S = 3/2$ ground-state triradical 8 (Fig. 11.2) were described [9]. Theoretically, estimates' difference between the singlet and triplet states (ΔEST) of 2, 4, and 5 was found to be $\sim$1.8 kcal mol^{-1},

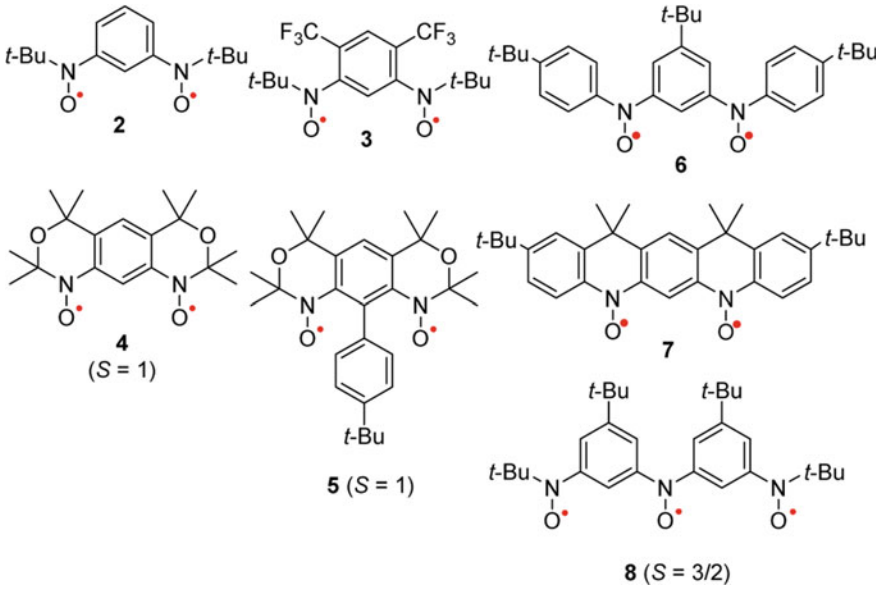

Fig. 11.2 High-spin molecules incorporating nitroxide spin centers [1]. Reprinted from [1], Copyright 2015 American Chemical Society

3.3 kcal mol^{-1}, and 2.2 kcal mol^{-1}, respectively. For triradical 8, a low energy gap between the quartet and excited doublet states, $\Delta E_{DQ} \approx 0.5$ kcal mol^{-1}, was measured by magnetic susceptibility.

11.1.1 Spin Trapping

The pioneering works, in which the principle possibility of effectiveness of the spin trapping was demonstrated, came to the light in 1968 [9]. Since then it is customary to use this technique for investigation radical processes in chemistry and biology, and many chemical, instrumental, and biochemical efforts have being undertaken to achieve "an ideal" structure [9–18].

^{1}H NMR and ESR titrations were used to determine the association constants of the complexes of R-phenyl-*N*-*tert*-butylnitrone (PBN) analogs and their superoxide spin adducts, respectively, both incorporated in methylated *â*-cyclodextrin, 2,6-di-*O*-methyl-*â*-cyclodextrin (Fig. 11.3) [13]. After the superoxide radical spin trapping reaction, EPR titrations (Fig. 11.4) afforded the association constants of the corresponding cyclodextrin-nitroxide complexes. Two-dimensional EPR simulations indicated a bimodal inclusion of the nitroxide free radical spin adducts into the cyclodextrins. For all the nitrone–cyclodextrin and nitroxide–cyclodextrin complexes, the association constants were always higher for the nitroxide complexes than

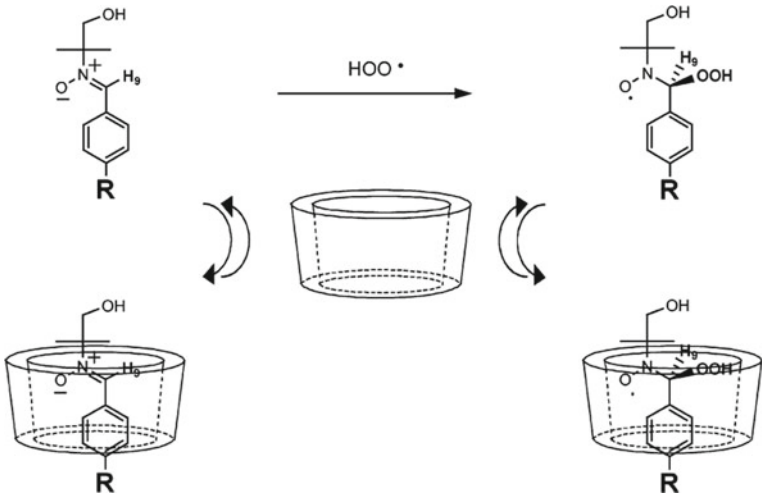

Fig. 11.3 Schematic presentation of double superoxide trapping by nitron and dextrin [13]. Reprinted from [13], Copyright 2005 American Chemical Society

for the nitrone complexes. The efficiency of the cyclodextrin inclusion technique to trap superoxide and to resist bioreduction by sodium L-ascorbate was also evaluated.

A series of new 11 hybrid 2-(diethoxyphosphoryl)-*N*-(benzylidene)propan-2-amine oxide derivatives with different aromatic substitution (PPNs) (Fig. 11.5) were synthesized, and their spin trapping potential was evaluated by EPR [14]. The experimental screening of these hydroxyphenyl- and methoxyphenyl-substituted PPNs and biocompatible nitrones 4d, 4g, and 4i deriving from caffeic, gallic, ferulic, and sinapic acids, which combined improved EPR probing of ROS formation, vasorelaxant action, and antioxidant potency was carried out. The PPNs antioxidant activity NO-donation properties in vitro, cytotoxicity and vasoprotective effect on precontracted rat aortic rings were also investigated. Figure 11.6 illustrates the author's approach to the trapping of hydroxyl and methyl radicals formatted in the supernatant of rat aortic rings stimulated by NADPH.

Data on synthesis of series of tetramethylpyrazine (TMP) derivatives and on investigation of their abilities for scavenging free radicals and preventing against oxidative stress-induced neuronal damage in vitro were presented [15]. Compounds, consisted of TMP, caffeic acid, and a nitrone group showed variety of activities: (1) radical scavenging, (2) broad neuroprotective effects, (3) rescuing iodoacetic acid-induced neuronal loss, (4) preventing from *tert*-butylhydroperoxide (*t*-BHP)-induced neuronal injury, and (5) exerting against *t*-BHP injury via activation of the phosphatidyl inositol 3-kinase (PI3K)/Akt signaling pathway. In addition, in a rat model of permanent middle cerebral artery occlusion, this compound significantly improved neurological deficits, and alleviated the infarct area and brain edema.

Two α-phenyl-*N*-tert-butylnitrone (PBN) derivatives were designed by adding a cholesterol and sugar moieties to parent nitrone to increase its lipophilicity and

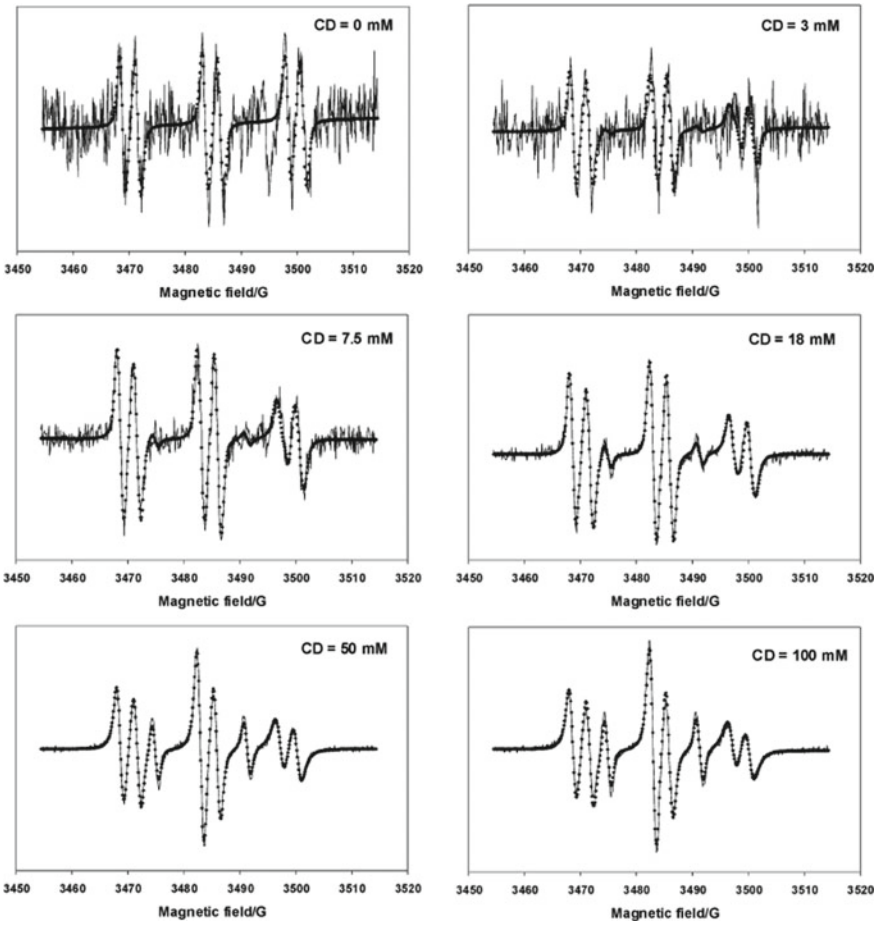

Fig. 11.4 ESR spectra after superoxide trapping by nitron and α-cyclodextrin (CD) [13]. Reprinted from [13], Copyright 2005 American Chemical Society

hydrophilic properties in the same time [16]. It was found that the new compound is able to form stable monolayers at the air/water interface and for the two derivatives bearing a sugar group, repulsive interactions with 1,2-dilinoleoyl-sn-glycero-3-phosphocholine (DLPC) in liposome occurred. The protective effect against lipid oxidation was tested using the AAPH thermolysis which generates peroxyl radicals and the Fenton reagent. The formation of conjugated dienes was quantified spectrophotometrically.

An approach using EPR and a cocktail of spin traps was designed [17]. The rationale for using this cocktail was that it would cover a wide range of biologically relevant free radicals and have a large range of hydrophilicity and lipophilicity in order to trap free radicals produced in different cellular compartments. Use of a

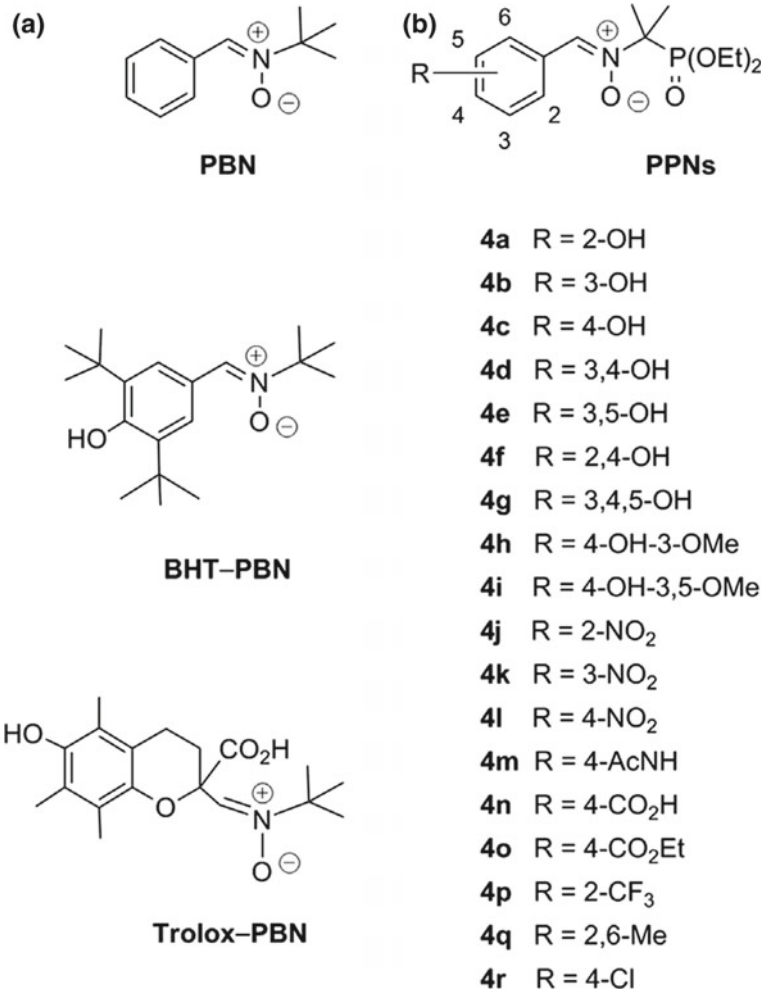

Fig. 11.5 Structures of **a** PBN and its phenol-based derivatives BHT_PBN Trolox_PBN successfully tested in in vitro and animal models of oxidative stress, and **b** phenolic (4a_4i) and non-phenolic (4j, 4q) derivatives of PPN (R ¼ H) [14]. Reprinted from [14], Copyright 2016 Elsevier

cocktail of spin traps. The ability of the technique to unambiguously detect free radical (O-, N-, C-, or S-centered) production in cells was well documented.

A novel glycine-nitronyl nitroxide (GNN) conjugate, which showed a synergetic protection against renal ischemia/reperfusion (I/R) injury, was designed, and its action mechanism was established using a hypoxia/reoxygenation (H/R) injury model of human umbilical vein endothelial cells (HUVECs) [18]. It was found that the GNN conjugate significantly elevated the cell viability via reducing the apoptosis rate in H/R-treated HUVECs and conjugate-attenuated H/R-induced mitochondrial fragmentation, mitochondrial membrane potential reduction, cytochrome *c* release,

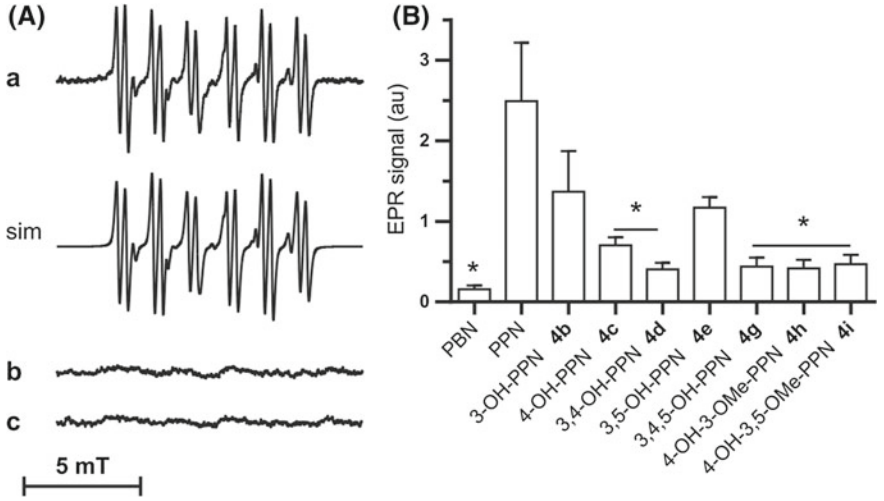

Fig. 11.6 Indirect spin trapping evidence for hydroxyl radical formation in the supernatant of rat aortic rings stimulated by NADPH (1 mM) for 80 min. After 60-min NADPH stimulation in KH buffer, the spin trap (15 mM) diluted in DMSO (1% final concentration) was added to the medium and incubated with rings for 20 min (**A**) EPR signal recorded in (**a**) the complete incubation system containing NADPH, DMSO, DTC (30 mM), and 3-OH-PPN 4b [14]. Reprinted from [14], Copyright 2016 Elsevier

and autophagy. On the example of an in vivo hind limb I/R model, the extensive applicability of GNN conjugate in different I/R models and its effect in remote organs were established.

11.2 Spin Label-Spin Probe Method

11.2.1 Fundamentals

A first version the spin label-spin probe (SLSP) approach designed and developed by Likhtenshtein group in 1970th [19–23] was based on the dynamic spin exchange interaction between a stable radical (i.e., nitroxide) attached to a molecular object of interest and chemically inert paramagnetic complex capable of diffusing freely in solution.

According to Salikhov et al. [20], the rate constant of the exchange interaction at the paramagnetic species encounters

$$k_{\mathrm{ex}} = P_{\mathrm{ex}} k_d = \frac{f_{\mathrm{g}} f_{\mathrm{ns}} k_d J^2 \tau_{\mathrm{c}}^2}{(1 + J^2 \tau_{\mathrm{c}}^2)} \tag{11.1}$$

where k_d is the rate constant of encounters in solution, P_{ex} is the probability of spin exchange in the course of lifetime (τ_c) of the encounter complex, f_g is the geometric steric factor, f_{ns} is the nuclear statistical factor, and J is the exchange integral of interaction in the encounter complex at the direct contact between the particles

If $J^2\tau_c^2 \gg 1$, k_{ex} is not dependent on J (strong exchange) and

$$k_{ex} = f_g f_{ns} k_d \tag{11.2}$$

In the case of weak exchange $J^2\tau_c^2 \ll 1$ and

$$k_{ex} = f_g f_{ns} k_d J^2 \tau_c^2 \tag{11.3}$$

For a particular pair of paramagnetic species, the value of k_{ex} depends on the microstructure, microviscosity, steric hindrances, and local charges in the region of encounters (Fig. 11.7). Hence, the methods of examining k_{ex} can be used for experimental study of these factors in biological and other objects.

A variant of the SLSP method based on direct measurement of electron spin–lattice relaxation times was developed in Hide group [21].

The principle of the SLSP was used in the following versions (1) label is a paramagnetic metal complex (e.g., iron in heme proteins) and a probe is nitroxide, (2) label

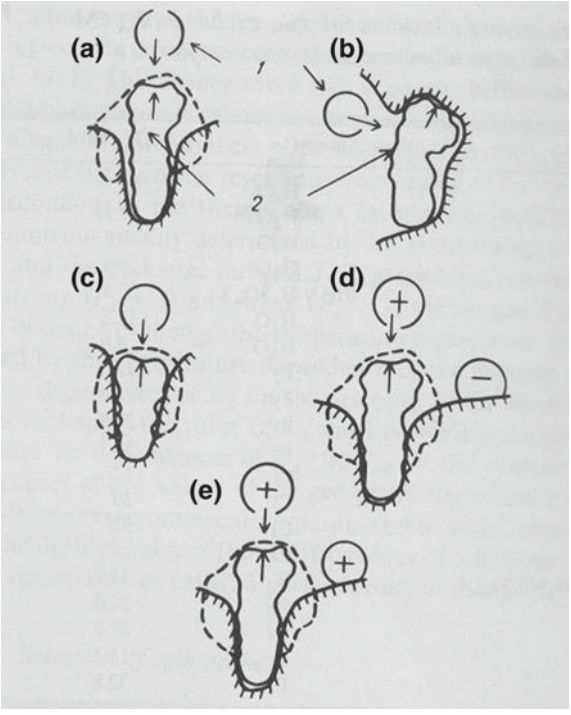

Fig. 11.7 Schematic illustration of spin label–spin probe method [19]

is a chromophore in the excited triplet state, and a probe is paramagnetic species (e.g., nitroxide), and (3) label is a molecular bearing paramagnetic nucleus (e.g., proton) and probe is a paramagnetic species (e.g., nitroxide).

11.2.2 Nitroxide in Investigation of Electrostatic Effects

11.2.2.1 Local Charges in Proteins and DNA

Electrostatic interactions are known to play one of the major roles in the myriad of cellular and molecular biology processes, ranging from enzyme catalysis, electron transfer, protein folding to insertion of proteins, toxins, and viruses into membranes as well as other more complex events.

The idea of using charged nitroxide radicals for the experimental study of local charges and electrolytic potential was first put forward and implemented in the Likhtenshtein group in 1970th as part of the spin label-spin probe method [19, 22, 23]. Subsequently, this approach was widely used to study electrostatic effects in biological molecular systems [21–30].

Methods of determination of the electrostatic potential and local charges in the vicinity of groups bearing spin are based on the sensitivity of spin relaxation rates of radicals and nuclei to encounters with charged paramagnetic species, stable radicals, or paramagnetic complexes in solution. This approach can be applied to three types of problems [26–28]. It can be used to investigate the electrostatic fields in the vicinity of an attached spin label using a second paramagnetic species with a different charge, ferricyanide anion, or diphenylchromium cation, for example [19, 22, 23]. The second approach involves monitoring the effect of a paramagnetic species, such as a complex of paramagnetic ion with a protein or the active site of a metalloenzyme, on the spin relaxation parameters of nitroxide spin probes of different charges freely diffusing in solution [28]. Measurements of the effect of paramagnetics (i.e., nitroxides) with different charges on the spin relaxation rates of the nuclei allow quantitative characterization of electrostatic effects [26–28].

Calculations of local charge Z_x in the vicinity of a paramagnetic particle (such as the active site of metalloprotein or a spin label) colliding with a nitroxide or metallocomplex with known charge Z_p can be carried out with the use of the Debye equation (11.4):

$$\frac{k^+}{k^0} \text{ or } \frac{k^-}{k^0} \frac{Z_p Z_x \alpha}{\exp(Z_p Z_x \alpha) - 1} \tag{11.4}$$

where k^+, k^-, and k^0 are the rate constants of encounters for positively charged, negatively charged, and neutral uncharged particles, respectively; and $\alpha = e^2/k_B T \varepsilon_0 r$, where e is the charge of an electron; k_B is the Boltzmann constant; temperature T = 293 K, ε_0 is the dielectric constant of water, and r is the distance between the

charges in the encounter complex. The values of (k^+/k^0) and (k^-/k^0) are determined by measurement of the rate constants of spin exchange which describes the effect of paramagnetic species on spin-phase and spin–lattice relaxation rates of the radical.

A diagram (Fig. 11.8) allows one to calculate the Z_pZ_x product using the appropriate experimentally measured $\log(k^+/k^0)$ or $\log(k^-/k^0)$ value and an r value estimated for the encounter complex. From the value of Z_xZ_p, one can ascertain the Z_x charge in the vicinity of the region of the paramagnetic complex encountered by the charged nitroxide spin probe since the Z_p charge of the nitroxide spin probe is known.

Electron-carrier horse cytochrome c and dioxygen-carrier sperm-whale myoglobin were served as models for determination of local electrostatic charges in the vicinity of paramagnetic active sites of metalloenzymes and metalloproteins, using nitroxide radicals [28]

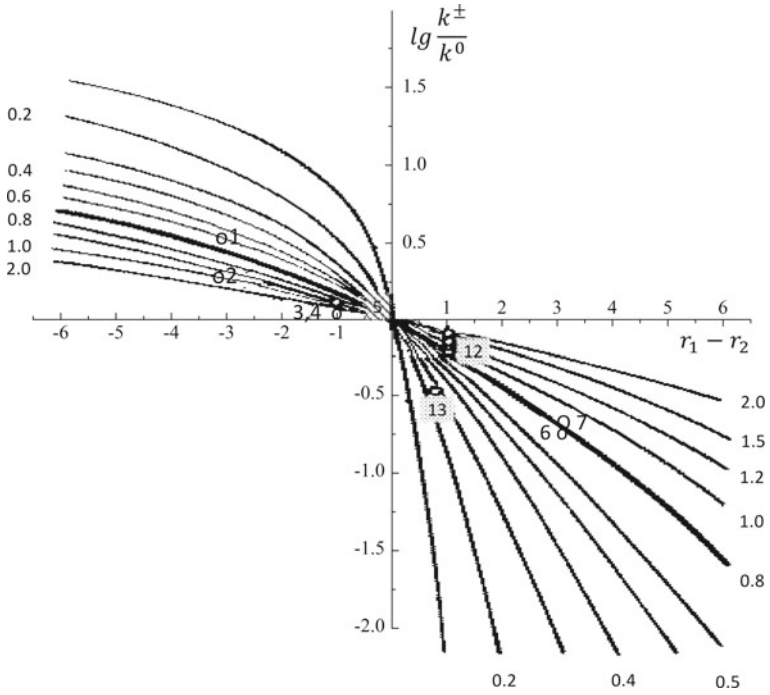

Fig. 11.8 A diagram for calculating the Z_pZ_x product [23]

Table 11.1 Apparent spin-exchange rate constants ($k+$, $k-$, and $k0$, in $M^{-1}S^{-1}$) of the positively charged (**III**), negatively charged (**II**), and neutral (**I**) nitroxide spin probes with hemin, ferricyanide anion, and heme proteins in aqueous solutions and apparent local charges (Z_H) in the vicinity of the heme groups [28]

Paramagnetic species	pH	k^+10^{-8}	$k^- \times 10^{-8}$ ($M^{-1}s^{-1}$)	$k^0 \times 10^{-8}$ ($M^{-1}s^{-1}$)	Z_H (± 0.1)
Hemin[b]		c	c	24	
$K_3Fe(CN)_6^e$	6.9	38	2	6	c
Cytochrome c (Fe^{3+})[g]	10.7	c	0.974	0.72	+0.5
Cytochrome c (Fe^{3+})[e]	6.9	c	0.841	0.71[f]	+0.3
Cytochrome c (Fe^{2+})[e]	6.9			~0	
Myoglobin[g]	7.0	c	0.561	0.77	−0.5

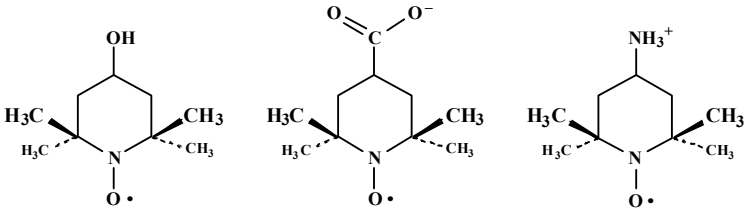

as spin probes. Calculations of local charge Z_x in the vicinity of a paramagnetic particle can be performed using the diagram based on 11.4 for encounters between two charged particles in solution (Fig. 11.8). The values of k^i and the resulting charges, Z_H calculated with 11.4, are presented in Table 11.1.

The ability to measure local charges and the potential with the help of the above-described tag probe was confirmed by several subsequent studies [24–32].

SLSP approach was employed in Hecht et al. [24] for determination of the electrostatic potential near the surface of calf thymus DNA. Spin–spin interaction between an ^{14}N-nitroxide derivative of 9-aminoacridine attached to DNA and free ^{15}N-labeled nitroxides of different charges was monitored by electron–electron double resonance (ELDOR). An approach developed in [30] also uses fast-relaxing charged and neutral paramagnetic relaxation agents (PRAs) to increase nitroxide spin-label relaxation rate solely through collisional spin exchange. With this purpose, T PRAs were calibrated in experiments on small nitroxides of known structure and charge to account for differences in their relaxation efficiency. Nitroxide longitudinal [R(1)] and transverse [R(2)] relaxation rates were measured by applying lineshape analysis to progressive saturation spectra. The ratio of measured R(1) increases for each pair of charged and neutral PRAs according to electrostatic potential. Voltage at the spin label is then calculated using the Boltzmann and Debye–Hückel equations. Voltage for spin-labeled myosin fragment S1 also agrees with calculation based on the pK shift of the reacted.

11.2.2.2 Effect of Charge on Dipolar Interactions Between Protons and a Paramagnetic Species

Proton spin–lattice relaxation is affected by paramagnetic ions and spin probes. According to theory of Hwang and Freed [31], the spin–lattice relaxation rate of proton nuclei, $1/T_{1p}$, upon encounter with a "radical" free electron, are dominated by dipolar interaction because of low electron spin density at the van der Waals distance. Slopes, $k = d(1/T_{1p})/d[R\cdot]$ of the dependence of proton spin–lattice relaxation rate on the concentration of the nitroxide probes [R·] can characterize the dipole–dipole interaction that dominates in an encounter between a proton and paramagnetic species To explore the effect of electrostatic interaction on the dipole–dipole relaxation rate, the ratios of experimental values k^+/k^0 or k^-/k^0 were used to estimate the electrostatic potential, $U(R_0)$, in the vicinity of a proton [26–28, 32].

The simple organic molecules and amino acids provide well-defined molecules to study the factors that influence electrostatic fields in more complex biologically important molecules [26–28, 32]. A molecular modeling calculation of local electrostatic potential was applied to a number of small charged (ethylamine, propionate anion, and imidazole) and uncharged (ethanol) molecules with an algorithm developed in [29]. The sign and magnitudes of the experimental and calculated parameters $U(R_0)_{exp}$ and $U(R_0)_{calc}$ (Table 11.2) correspond to expected values from simple electrostatic considerations.

Three charged hexosamines D-glucosamine·HCl, D-galactosamine·HCl, D-mannosamine·HCl, a glucuronide metabolite of paracetamol [p-acetamidophenyl-β-D-glucuronide sodium salt, and a mononucleotide [thymidine-3′-phosphate sodium salt (8)], were investigated in [32]. Ratios of these apparent relaxation rate constants

Table 11.2 Rate constants of spin–lattice relaxation of protons in small molecules under the effect of nitroxides **I-III** of different charge [27]

Molecule	Proton	$U(R_0)^{*,H}_{calcd}$ $\epsilon = 1, R = 1.2$ Å	$U(R_0)^{*}_{calcd}$ $\epsilon = 80, R = 8$ Å	$U(R_0)^{*,\#,\S}_{exptl}$
Ethanol	H(α)	15(1)	+0.03	
Ethanol	H(β)	10(1)	+0.02	
EtNH3]$^+$Cl$^-$	H(α)	126(2)	+0.25	+0.29(6)
EtHN3]$^+$Cl$^-$	H(β)	109(4)	+0.22	+0.26(8)
Imidazolium$^+$Cl$^-$	H(2)	151(3)	+0.30	+0.30(8)
Imidazolium$^+$Cl$^-$	H(4,5)	130(3)	+0.26	+0.30(4)
EtC0$_2$-Na$^+$	H(α)	−80(4)	−0.16	−0.29(3)
EtC0$_2$-Na$^+$	H(β)	−71(3)	−0.14	−0.26(4)
Aspartate-Na$^+$	H(α)			−0.30(5)
Aspartate-Na$^+$	H(β)			−0.31(6)

The k^+/k^0 and k^-/k^0 ratios (in this Table) are markedly different for protons of positively charged histidine and negatively charged aspartate

($k_+/k_- > 1$ or $k_-/k_+ > 1$.) provided a measurement of the sign and magnitude of the local electrostatic fields surrounding a particular proton in the target.

Biophysical methods to probe local electrostatic potentials of proteins and lipid bilayer systems that are based on an observation of reversible protonation of nitroxides by EPR were described in [33, 34]. The review [33] includes the following sections: (1) EPR characterization of pH-sensitive thiol-specific nitroxide labels, (2) mapping of local pH and electrostatics of peptide and protein systems with methanethiosulfonate derivatives of ionizable nitroxides, (3) pH-sensitive spin-labeled lipids for measuring surface electrostatics of lipid bilayers by EPR, (4) preparation of spin-labeled lipid vesicles, (5) EPR titration experiments with lipid bilayers, (6) analysis of EPR spectra in titration experiments, (7) interfacial pKa and the choice of an electrically neutral reference interface, and (8) surface charge and potential calculation using the Gouy–Chapman theory are outlined.

The ionizable nitroxide labels and the nitroxide-labeled phospholipids described so far cover an exceptionally wide range of ca. 2.5–7.0 pH units, making them suitable to study a broad range of biophysical phenomena, especially at the negatively charged lipid bilayer surfaces. Chemical structures of phospholipid-based nitroxide electrostatic EPR probes, IMTSL-PTE ((S)-2,3-bis(palmitoyloxy)propyl 2-(((1-oxyl-2,2,3,5,5-pentamethylimidazolidin- 4-yl)methyl)disulfanyl)ethyl phosphate) and IKMTSL-PTE ((S)-2,3-bis (palmitoyloxy)propyl 2-((4-(4-(dimethylamino)-2-ethyl-1-oxyl-5,5-dimethyl-2,5-dihydro-1H-imidazol-2-yl)benzyl)disulfanyl)ethyl phosphate) were compared with non-ionizable analog of IMTSL-PTE–MTSL-PTE ((S)-2,3-bis(palmitoyloxy)propyl 2-(((1-oxyl-2,2,5,5-tetramethyl-2,5-dihydro-1H-pyrrol-3-yl)methyl)disulfanyl)ethyl phosphate), and of the adduct of IKMTSL with 2-mercaptoethanol (IKMTSL-2me).

11.3 Immersion Depth of Nitroxide Fragment

At interpretation of data on spin-label dynamics, it is important to know the immersion death in molecular object of interest (r_{im}). A method was developed for determining the nearest distance ($r_{\min}$) between a stable radical (R·) and an ion of paramagnetic metal, an ion-relaxator (IR), which has effects on the spin–lattice relaxation time of R (T_{1e}) and is randomly distributed in the bulk of the vitrified sample [28, 35–37]. In fact, the $r_{\min}$ value is equal to the radical immersion depth. The contribution of the dipole interaction of IR to the R· spin relaxation rate is expressed by the equation:

$$\Delta(1/T_{1e}) = \frac{A_d \mu^2 \gamma^2 \tau_{1e} C}{r_{\min}^3} \quad (2) \tag{11.5}$$

where $1/T_{1e}$ is the nitroxide spin–lattice relaxation rate, which is derived by analysis of ESR spectra saturation curves, C is the IR concentration, μ and τ_{1e} are magnetic moment and the spin relaxation rate of the IR, respectively, and A_d is a factor that

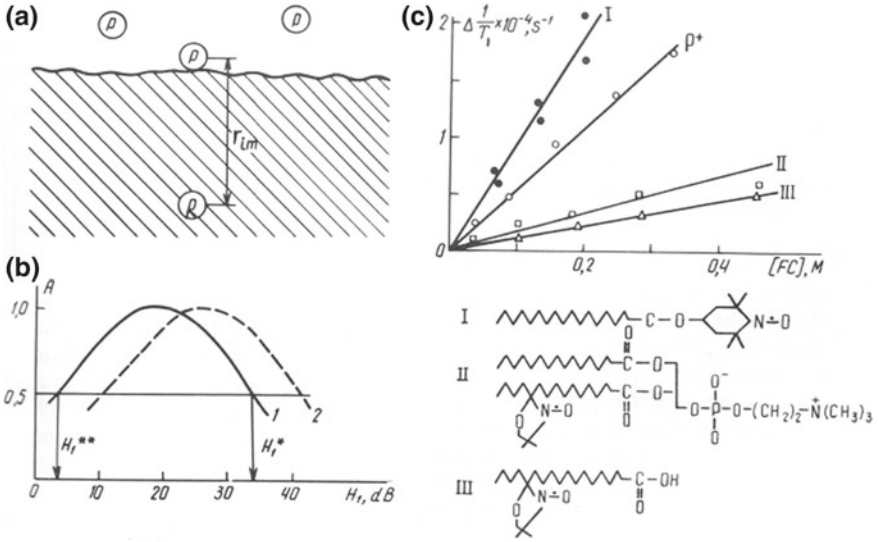

Fig. 11.9 Schematic illustration method of the immersion depth of nitroxide fragment measurement

depends on the geometry of the surface. For example, if the surface is flat, $A_d = 0.2$. The sensitivity of the ESR spectra saturation curves for spin-labeled cotton and cellulose fibers to the nature of the object and presence of ion-relaxator ferricyanide were schematically illustrated on examples of nitroxide spin probes incorporated in biomembranes, cotton fibers, and cellulose (Fig. 11.9).

A method has been developed for measuring depth of immersion of a fluorescent chromophore in biological matrices, such as biomembranes [38]. The method is based on dynamic quenching of chromophore fluorescence by a nitroxide probe freely diffused in solution. By measuring the quenching rate constant and making use of theoretical consideration and experimental data relating to exchange processes, it is possible to estimate the depth of immersion of chromophore. The ratio between the quenching rate constants for a chromophore–quencher pair in solution (diffusion limit) and after ducking in a matrix (kinetic limit) is given by:

$$k_q^k / k_q^d = \tau_c^2 10^a \exp 2[-\beta(R_0 - r_v)] \tag{11.6}$$

and the depth of immersion of the center under investigation by:

$$(R_0 - r_v) = 0.5 \times \beta^{-1}[\ln(k_q^d / k_q^k) + \ln(\tau_c^2 10^a)] \tag{11.7}$$

where k^d and k^k are the rate constant of encounters in solution, and after immersion, correspondingly; τ_c is the lifetime of the encounter complex; $\beta \nabla 2$ and 1.3 A and $a \nabla 28$ and 26 for the intersystem crossing (ICHA) and electron transfer (ET) mechanisms, respectively. Equation (11.7) can be used to estimate the depth of

immersion of a fluorescent chromophore in a "non-conductive" matrix by experimental measurement of ratio k/k with a reasonable choice of the equation parameters. A fluorescence–photochrome probe, 4.4′-dimethylaminocyanostilbene (DMACS) was incorporated in lecithin liposomes and membranes from *Bacillus subtilis* grown in the absence and presence of chloramphenicol. The quenching of the probe fluorescence by a water-soluble nitroxide radical (TEMPOL) was investigated.

To elucidate the location of a phosphorescent label (erythrosine) covalently incorporated in cotton fiber, which was a source of information about the fiber's local dynamics, a method for determining the depth of the immersion of a luminescence chromophore (r_{im}) was developed [39]. The method is based on experimental measurements of rate constants of quenching luminescence in conditions of free access between chromophore and quencher (k_{qd}) and between immersed chromophore and free quencher (k_{qk}). For the measurement of r_{im}, the 11.7 was employed. Values of immersion depth of spin label I in fibers (r_{min}, in nm) were found to be 1.0 and 1.1 nm for α-cellulose and cotton fiber cotton fiber, respectively. These values are close to the immersion depth of phosphorescence triplet label of about 0.8 nm [43]. Therefore, the labels' mobility reflects the molecular dynamics of the polymers chains in the vicinity of the label location.

11.4 Nitroxides in Cotton and Cellulose Physicochemistry and Technology

Cotton and cellulose are ones of the essential materials for the human civilization. The role of cotton fibers and cellulose in industry, medicine, and human beings' everyday life is impossible to overestimate. Since pioneering works of Marupov and Likhtenshtein groups [40, 41], nitroxides are widely used in solving a number of challenging problems of structure and functions of cotton fibers and cellulose [42–54]. This section is intended to provide the physical principles of methods based on the use of the covalently bound and adsorbed nitroxides (spin labels and spin probe, correspondingly) and its applications in the investigation of cotton fibers and cellulose microstructure and molecular dynamics and it connection with these materials durability. An arsenal of modern physical methods including electron spin resonance (ESR), Messbauer and luminescence techniques is involved in investigation of the labeled samples [43]. Involving nitroxide in chemical processes in this area is also considered.

The covalent modification of an OH group of cotton and cellulose fibers performed with correspondent nucleophilic reactions using nitroxide spin label

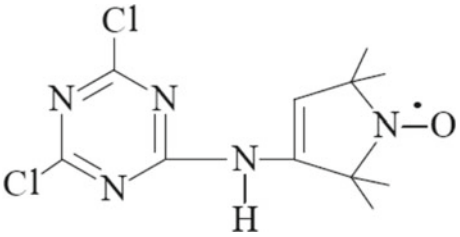

was described in detail in [40, 41]. Samples of cellulose labeled with stable nitroxyl radical

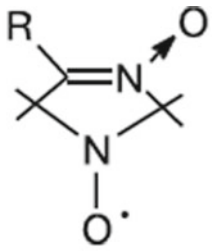

1—3

R = Me (**1**), COOH (**2**),
CH_2Br (**3**)

were prepared through mechanochemical synthesis [42]. The samples were studied by IR and EPR spectroscopy.

Modern ESR techniques allow ones to access dynamic processes that are characterized by a wide range of correlation time, $\tau_c = 10^2$–10^{-10} s (Chap. 4). Experiments show (Fig. 11.10) [43] that the investigated cotton fibers consist of two fractions: major (component h, $\tau_c \leq 10^{-8}$) and minor (component h′, $\tau_c \geq 10^{-8}$ s). Apparently, the latter is attributed to loose microscopic defects of the fibers. The contribution of these fractions in different samples is 94–98 and 6–2%, respectively. Contribution of the loose fraction enhances with increase of temperature.

The dynamic behavior of spin labels with nitroxides located in samples of cotton fiber was investigated with the use of high resolution, high-frequency (2-mm) ESR spectroscopy (Fig. 11.11) [43–45]. The studies confirmed conclusions formulated on the base of the 3-cm band (V_1) and also indicated strong anisotropic of the label nitroxide fragment

Notably, the nitroxide fragment dynamics in this microsecond temporal region and its nanosecond dynamics occur in the same temperature region (273–373 K). These findings suggest distribution of the label dynamic parameters modulated by the fibers dynamics. This conclusion was confirmed in study of molecular dynamics

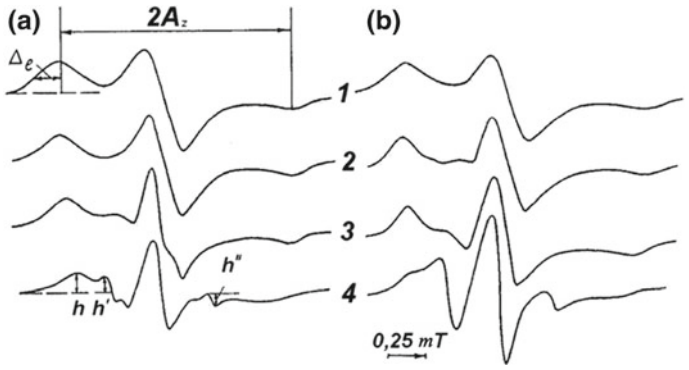

Fig. 11.10 First harmonic ESR spectra (V_1) for spin-labeled cotton fibers **a** «5595-B», **b** "Tashkent 1" Temperature (1) 123 K, (2) 213 K, (3) 323 K, (4) 373 K. Relative humidity $P/P_0 = 0.96$ [43]

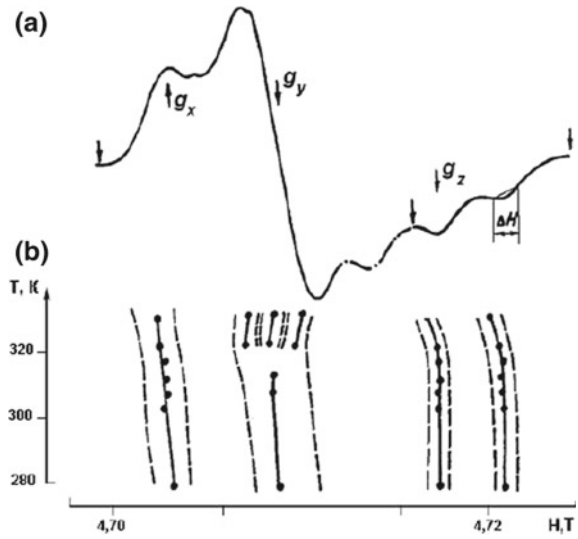

Fig. 11.11 High-resolution (2 mm) ESR spectrum of spin-labeled cotton fiber «5595-B» at relative humidity $P/P_s = 0.04$ and temperature 150 K (**a**); dependence of parameters of g and A tensors on temperature (**b**) [44]

of cotton fibers by methods of fluorescence and phosphorescence labels [43]. The free activation energy distribution of mobility of the chromophore label was found to be 10.5 kJ/mole (data on fluorescence) and 6.7 kJ/mole (data on phosphorescence).

Values of immersion depth of spin label I in fibers (r_{min}, in nm) were found to be 1.0 and 1.1 for α-cellulose and cotton fiber cotton fiber, respectively [43]. These values are close to the immersion depth of phosphorescence triplet label of about 0.8 nm.

The role of the microstructure of fibers in its stability under tensile stress is a basic challenge and applied problem. The design, fabrication, testing, or an operation stage of a polymer product's life in particular in a great extend related to its durability. A

Table 11.3 Parameters of the Zhurkov 11.8. Loose-phase (defects) fracture of cotton fibers (n) derived by the spin labeling and Zhurkov parameters for the samples at $T = 300$ K; $\xi = \mathrm{d}(h'/h)/\mathrm{d}T$ is the rate of increase of parameter $'h/h$ (Fig. 11.12), which characterizes a loosing of the polymer structure at a temperature increase above 333 K [43]

Fiber	n-defects fracture (%)	ξ (K^{-1})	σ_p (MPa)	U_0 (kJ/mole)	$\gamma.10^{-4}$ (m^3/mole)
«5595-B»	2 ± 0.5	0.009	280 ± 12	142 ± 7	2.6
«Taskent-1A»	6 ± 2	0.030	180 ± 12	141 ± 7	4.9
«*Tashkent-1B*»	2.8 ± 2	0.070	150 ± 12	141 ± 7	6.0

connection between durability of various samples of cotton fibers and its molecular properties was established using method of nitroxide spin labels (Table 11.3) [43].

A connection between durability of various samples of cotton fibers and its molecular properties was established using method of nitroxide spin labels and a Zhurkov model [46] (Table 11.3). Widely accepted Zhurkov model, assuming the kinetic nature of bond destruction through the thermo-fluctuation mechanism, enables one to obtain a simple, easy-to-use, and physically meaningful formula for the evaluation of the durability of a material after the given time in operation at the given temperature and under the given stress. According to this model, a sample durability (r) can be described with the following equation

$$r = \tau_0 \mathrm{e}^{\frac{U_0 - \sigma\gamma}{kT}} \tag{11.8}$$

where U_0 is the energy activation of mechanic destruction, τ_0 is the time of atomic vibration, σ is the applied tension, and γ is the activation volume sensitive to the sample structure. The experimental parameters of 11.8 are presented in Table 11.3.

As it is shown in Table 11.3, the energy activation of mechanic destruction is practically the same for all samples, which indicates that the process occurs as a break in chemical bonds. The difference in the samples' duration is caused by differences in fracture structural defects (n). The larger n is, the smaller ξ and σ_p are, and the higher γ is—this equates to lower sample durability. This finding opens the way to predict the durability of products made from cotton fibers or cellulose using EPR spectroscopy even in the processes of its production.

A series of microstructure studies of cotton fiber and cellulose was performed using non-covalently bound probes [47–54]. These studies confirmed the main results of earlier works on the one hand and revealed important details on the other.

Spin probe ESR method was used to study local polarity and heterogeneous viscosity of two types of unprocessed cotton fibers, *G. hirsutum* and *G. barbadense* [51]. These fibers were loaded with two nitroxide probes that differ in polarity—TEMPO and its more hydrophilic derivative TEMPOL. A series of polar and non-polar solvents was utilized. Results indicated coexistence of cellulose nanodomains with different physicochemical properties, such as polarity and microviscosity, that are affected by solvents and temperature. EPR studies of cellulose microstructure

employing the nitroxide spin-labeled albumin, as spin probe entrapped in cellulose triacetate fibers, were carried out [52]. The experiments show that within the fiber, two phases are present: medium viscosity inside microcavities and more rigid phase.

The effect of water content on the physicochemical properties of the amorphous regions in cotton was studied by measuring the electron paramagnetic resonance of TEMPOL [47]. Mobility of nitroxide radicals, deposited in cotton at different loadings, as a function of the relative humidity (RH) and temperature, was investigated. The method of nitroxide spin labels of different charges developed earlier in [22, 23] was employed to investigate the effect of charge on spin probe interactions and dynamics in the nanopores of cotton, using 4-amino-TEMPO (T–NH_2) and 4-carboxy-TEMPO (T–COOH) deposited on dry cotton [48].

Forty samples of cotton filaments from naturel and mutant plants spin-labeled by a nitroxide 2,2,5,5-tetramethyl-3-aminopyrrolidine-(3,5-dichlorotriazine)-1-oxyl (I), chemically bound by the cellulose hydroxyl group, were prepared [49]. Experiments revealed different conformational changes of cotton cellulose grown from seeds exposed to different doses of gamma-irradiation. The spin-label investigation of flax shive cellulose structural and molecular dynamics properties in the process of its nitration using the spin label I revealed that the macromolecules' packing density in the less ordered nitrate fields is higher than that of natural flax cellulose. A correlation between the "order" and "disorder" relation in natural cellulose and in finite nitrogen products was established. The plasticizing capacity of the solvents at 0° decreases through the EtOH, H_2O, and $CHCl_3$ series. A facile grafting to protocol based on the generation of radicals at the surface of cellulose by mild UV irradiation ($\lambda_{max} \sim 311$ nm) of an immobilized photoinitiator was conducted [50]. The radicals photoinduced generated in cellulose were trapped with a nitroxide-functionalized polymer. Spin capturing was reported, using nitrones that after a first radical reaction generate a nitroxide which are able to undergo a second radical coupling. A nitroxide amphiphilic block copolymer of poly(ethylene glycol)-b-poly(2,2,6,6-tetramethylpiperidinyloxy-4-yl-methacrylate) was used as a recoverable catalyst for selective catalytic oxidation of cellulose [53].

In conclusion, covalent modification cotton fibers and cellulose by the labels and the use electron spin resonance are allowed to establish the label location and molecular motion the labeled samples which in turn is modulated by the polymers local molecular dynamics and its distribution within 10^{-4}–10^{-9} s range of correlation times. Data on dependencies of the fibers' molecular dynamics on origin, temperature, water, and other plasticizing agents, nutrition, period of maturing, virus infection, and radiation of seeds have been presented. Combination of ESR experiments and Zhurkov technique have revealed a strong dependence of fibers' resistance to stress (durability) on microscopic structural defects. Employing non-covalently bound nitroxides as spin probes provided a way for studies of effect of humidity on the supramolecular structure of cotton, local polarity, and heterogeneous viscosity of two types of unprocessed cotton fibers, cellulose modification by nitroxide-mediated graft polymerization, composites of poly(lactic) acid reinforced with TEMPO-oxidized fibrillated cellulose, and photoinduced macromolecular functionalization of cellulose vianitroxide spin trapping.

11.5 Spin Cascade

Measurements of active encounters between molecules in native membranes containing ingredients, including proteins, are of prime importance. To estimate rare encounters in a high range of rate constants (rate coefficients) in membranes, a spin cascade method (SCM) was invented and developed in Likhtenshtein group [54–57]. The SCM is based on four well-known fundamental physical phenomena: (1) singlet triplet transition in an excited chromophore with the formation of a paramagnetic state with a relative long lifetime (triplet probe, TP), (2) quenching of excited triplet state of TP by a paramagnetic species (spin probe, SP), (3) *cis-trans*-isomerization of a photochrome compound (fluorescence–photochrome probe, FPP), and (4) triplet–triplet energy transfer between TP and FPP.

As was shown in the Likhtenshtein group, paramagnetism and the relative long lifetime of chromophores in the excited triplet state provide the possibility for these compounds to be used as phosphorescence (triplet) labels for solving a number of structural and dynamics problems [57, 58]. Dexter triplet–triplet TT energy transfer is a process of exchanging both spin and energy between a pair of molecules or molecular fragments [59]. Nitroxides are effective quenchers of excited states by the exchange mechanisms [57].

Within the spin cascade method, specifically, a spin probe is nitroxide (5-doxyl stearic acid), triplet probe is erythrosin B in exited state, and fluorescence–photochrome probe (FPP) is (4-dimethylamino-4-aminostilbene) [56].

Stilbenes exhibit a diverse photochemical behavior in solution such as reversible *cis/trans*-isomerization cyclization of cis-stilbene which involves rearrangement along a double bond [54, 60, 61]. Due to the fact that *trans*-stilbene exhibits fluorescence and *cis*-stilbene is fluorescence silent, the photoisomerization process can be readily monitored by the highly sensitive fluorescent techniques. The *trans–cis* photoisomerization of stilbenes can proceed by two in-principle mechanisms: (i) the direct process involving exited single state and (ii) the triplet-sensitized photoreaction of stilbenes that caused *trans–cis* photoisomerization.

The spin cascade method was employed to estimate rare encounters in a high range of rate constants (rate coefficients) in multilamellar liposomes (Fig. 11.12) [55].

Experimental rate constant of the triplet probe phosphorescence quenching by nitroxide (k_q) and the rate constant of the triplet–triplet energy transfer (k_T) evaluated in 2D terms were obtained as $k_q = 1.05 \times 10^{15}$ cm^2/(mol s) and $k_T = 1.26 \times 10^{12}$ cm^2/(mol s), respectively. The values of diffusion rate constants in model lipid membranes together with similar data obtained from other methods, that cover characteristic times over eight orders of magnitude, were found to be in good agreement with the advanced theory of diffusion-controlled reactions in two dimensions (Fig. 11.13) [62]. In addition, using the spin cascade method, the following dynamic parameters of the cascade system components can be experimentally measured: (1) the spin-label rotation correlation time and spin relaxation parameters, (2) the fluorescence and phosphorescence polarization correlation times, (3) the rate constants

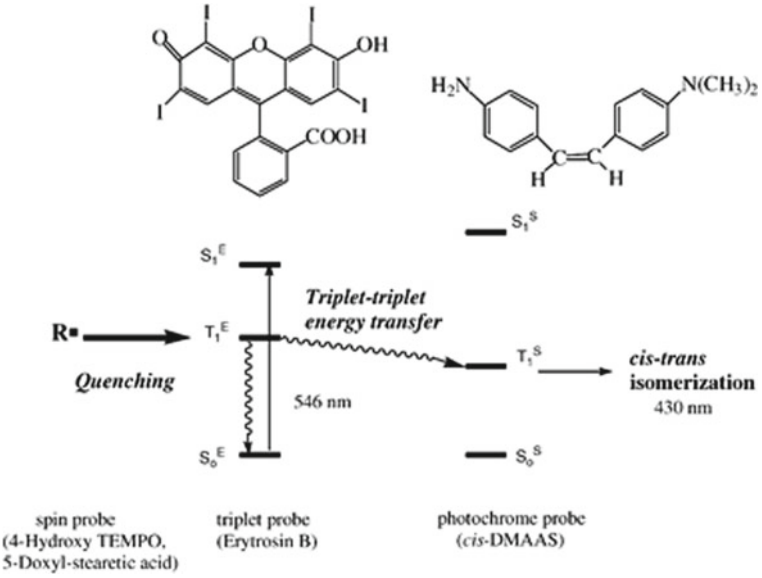

Fig. 11.12 Representation of energy levels of cascade reactants and competition between the $T_1^E \rightarrow T_1^S$ and $T_1^E \rightarrow S_o^S$ processes [56]

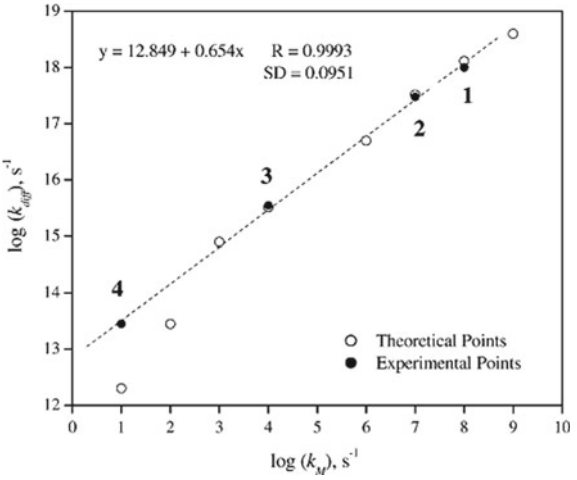

Fig. 11.13 Values of experimental and theoretical diffusion rate constants in model lipid membranes versus corresponding characteristic rate coefficient [56]

of the chromophore singlet- and triplet-state quenching by nitroxides, and (4) the rate constant of photoisomerization. This set of parameters is a cumulative characteristic of the dynamic state of biomembranes in the wide range of the probes amplitude and characteristic time. Proficiency of the method can be expanded by a choice of the cascade components with the higher efficiency of triplet–triplet energy transfer, higher

sensitizer lifetime, and by an increase of the time of integration of experimental data on a photochrome photoisomerization.

11.6 Nitroxides in Matrices

Multifrequency continuous wave (CW) and echo-detected (ED) electron paramagnetic resonance (EPR) were employed to study the mobility of 4-methoxy-2,2,6,6-tetramethylpiperidine-*N*-oxyl (MT) and *N*-(2-methylpropyl)-*N*-(1-diethylphosphono-2,2-dimethylpropyl)-aminoxyl (DEPN) confined in nanocapsules of *p*-hexanoyl calix[4]arene, using W-band and 360 GHz cw [63]. Experiments indicated that between 90 and 200 K, the caged nitroxide undergoes isotropic small-angle fluctuations (librations), whereas at higher temperatures restricted rotations of the radical with correlation times of 0.75×10^{-10} s and 1.2×10^{-10} s dominate at 325 and 300 K, respectively. The activation energy of the rotational motion of encapsulated MT radicals was evaluated as $E_a = 1.0$ kcal mol^{-1}.

New covalently linked spin-labeled cyclodextrin (CD) was prepared via the attachment of nitronyl nitroxide 2-(4-hydroxyphenyl)-4,4,5,5-tetramethyl-4,5-dihydro-1H-imidazole-3-oxide-1-oxyl to permethylated β-cyclodextrin I, and its molecular dynamics were investigated employing ESEEM/CW EPR approaches [64].

The experiments indicated that: (1) nitronyl nitroxide exhibits dynamic equilibrium between conformations with radical fragment outside the cavity and radical capping the cavity of CD, (2) covalent attachment of nitronyl nitroxide to CD leads to a corresponding increase of the rotational correlation time by an order of magnitude; (3) nitronyl nitroxide covalently attached to CD retains its sensitivity to nitric oxide, and (4) the reduction rate constant of nitroxide fragment in I is close to that of corresponding free radical.

Rotation of methyl groups which present in spin labels including MTSL contributes in spin echo dephasing [65]. These effects were removed in iodoacetamide azaadamantyl spin label in fluid solution and in 9:1 trehalose/sucrose glass. For example, in 9:1 toluene/CH_2Cl_2 solution at 293 K, the isotropic nitrogen hyperfine coupling is 19.2G, T_1 is 0.37 ms, and T_m is 0.30–0.35 ms. Although complexation of the azaadamantyl spin label with β-cyclodextrin slows tumbling in aqueous solution by about a factor of 10, it does not affect significantly on $1/T_1$ or $1/T_m$ in 9:1 trehalose:sucrose between 80 and 293 K. It was suggested that relaxation is dominated by Raman and local mode processes.

Interfacial electrostatic properties of hydrated mesoporous and nanostructured alumina powders are determining factors for the use of these materials in heterogeneous catalysis and as a sorption media for filtration and chromatographic applications. The purpose of work [66] was to measure Stern potential in cylindrical nanosized hydrated channels of the mesoporous molecular sieves (MMS) MCM-41 and SBA-15 with channel of different diameters (2.3–8.1 nm) utilizing pH-sensitive nitroxide radicals (NR).

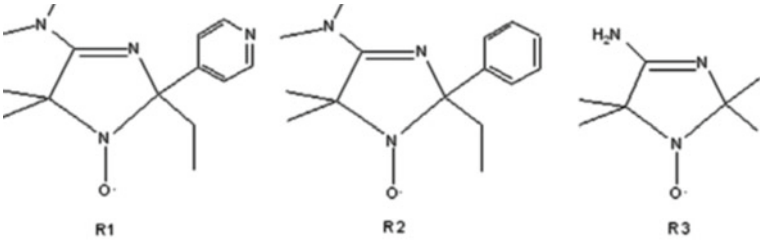

Stern potential is an electric potential on the external boundary of the Stern layer versus the bulk electrolyte. The Stern layer accounts for ions' finite size and consequently an ion's closest approach to the electrode. The layer is on the order of the ionic radius. EPR spectroscopy was employed to study rotational dynamics of pH-sensitive NRs adsorbed in the water-filled nanochannels. The following experimental findings were reported: (1) Two populations of the probe molecules in the sieve channels, one undergoing a fast rotational diffusion and the other one being significantly slower motion of the probe, were observed; (2) the solution acidity (pKel) inside the channels and near-surface electrical potential was estimated using the pH spin probes; (3) negative and positive values of Stern potential for the positively and negatively charged surfaces of MMS channels were found; and (4) the ranges of pH of external solution for the near-zero charge, boost-charging of the channel surface, and for dissociation of functional groups in the MMS studied were determined. Values of near-surface potential of the positively (4–19 mv) and negatively (from −110 to −179 mv) charged MMS were shown in a table.

EPR spectroscopy [X-band (9 GHz)] of new pH-sensitive nitroxides (4-dimethylamino-5,5-dimethyl-2-(4-(chloromethyl) phenyl)-2-ethyl-2,5-dihydro-1H-imidazol-1-oxyl hydrochloride semihydrate (nitroxide R1) was employed to evaluate the surface charge and interfacial acid–base equilibria at the pore surface of mesoporous powders of α-Al_2O_3, γ-Al_2O_3, $Al_2\ O_3 \times nH_2O$, and basic γ-Al_2O_3 and nanostructured γ-Al_2O_3 [67]. Mesoporous γ-Al_2O_3 was synthesized by heating aluminum hydroxide. The materials in the form of pristine were modified with aluminum-tri-sec-butoxide, hydroxyaluminum glycerate, phospholipids, soy phosphatidylcholine, cholesterol, negative composition of soy lecithin Epikuron 200, phosphatidylcholine, and cetyl pyridinium chloride. It was found that for basic γ-Al_2O_3 and $Al_2O_3 \times nH_2O$, the values of nitroxide R1 pKa were shifted by ΔpKa $\approx +0.6$ and up to $\approx$+1.2 pH units, respectively, while the shift for γ-Al_2O_3 was found as $\Delta pKa = +3.5$. The order of descending magnitude of the effective surface electrostatic potential Ψ is mesoporous γ-Al_2O_3 > Al_2O_3 × basic γ-Al_2O_3 > α-Al_2O_3.

EPR spectroscopy of two pH-sensitive NRs of the imidazoline type, 4-dimethylamine-2-ethyl-5,5-dimethyl-2-pyridine- 4-yl-2,5-dihydro-1H-imidazole-1-oxyl (R1) and 4-dimethylamine- 2-ethyl-5,5-dimethyl-2-phenyl-4-yl-2,5-dihydro-1H-imidazole-1-oxyl (R2), and of the imidazole type, 4-amino-2,2,5,5-tetramethyl-2,5-dihydro-1H- imidazole- 1-oxyl (R3) was employed to examine the conditions for

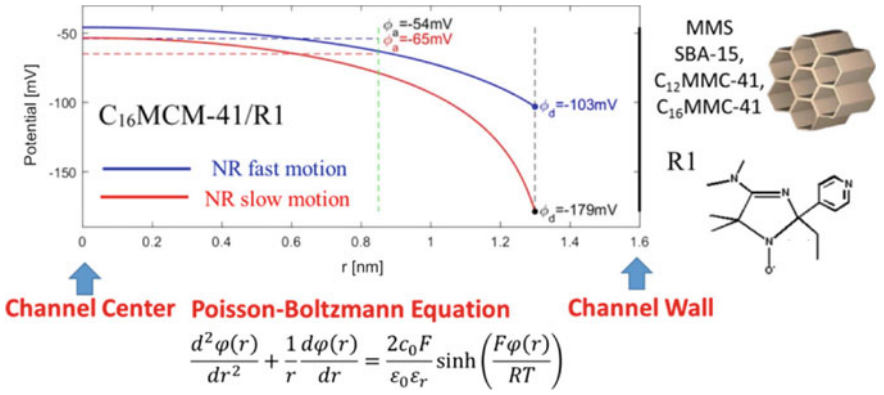

Fig. 11.14 Radial profiles of electrostatic potential $\varphi(r)$ obtained from numerical solutions of the PB equation using different boundary conditions, channel center Poisson–Boltzmann equation and the nanochannels of silica-based mesoporous molecular sieves mode [68]. Reprinted from [68], Copyright 2018 American Chemical Society

the efficient electrostatic surface potential screening inside the nanochannels of silica-based mesoporous molecular sieves (MMS) filled with water at ambient conditions and a ionic strength of 0.1 M [68]. All-silica MCM-41 materials were synthesized using dodecyltrimethylammonium bromide (C12MCM-41) and hexadecyl trimethylammonium bromide (C16MCM-41) and exhibited average channel diameters of 2.3 and 3.2 nm, respectively. CW X-band (9 GHz) CW EPR spectra of NRs in bulk aqueous solution and upon incorporation into the channels of solid MMS samples were recorded at temperature 293 K. EPR experiments with water-soluble ionizable pH-sensitive nitroxides provided the means to determine an average effective local pH_{loc}. The experiments, using water-soluble ionizable pH-sensitive nitroxides, showed that the nitroxide molecules can diffuse in aqueous volume inside the nanopores of the MMS. In SBA-15 channels filled with aqueous solutions, when the pore radius is about fourfold larger than the Debye radius, pH_{loc} averaged over the central section of the nanochannel was found to be higher by 0.2–0.3 pH units than pH_{ext}. Data on the average electrostatic potential over the central volume of the nanochannels measured by "mobile" EPR probes and the surface potential at the channel surface determined from EPR titrations of immobilized nitroxides were in a good agreement with results of the classical Poisson–Boltzmann theory for the channels down to 3.2 $\pm$ 0.1 nm in diameter. The main results of the work are schematically illustrated in Fig. 11.14.

References

1. N.M. Gallagher, A. Olankitwanit, A. Rajca, High-spin organic molecules. J. Org. Chem. **80**(3), 1291–1298 (2015)

2. X. Meng, W. Shi, P. Cheng, Magnetism in one-dimensional metal nitronyl nitroxide radical system. Coord. Chem. Rev. **378**, 134–150 (2018). https://doi.org/10.1016/j.ccr.2018.02.002
3. S. Kumar, Y. Kumar, S.K. Keshri, P. Mukhopadhyay, Recent advances in organic radicals and their magnetism. Magnetochemistry **2**, 42 (2016). https://doi.org/10.3390/magnetochemistry2040042
4. K.-A. Hansen, J.P. Blinco, Nitroxide radical polymers a versatile material class for high-tech applications. Polym. Chem. **9**, 1479–1516 (2018)
5. Y. Xie, K. Zhang, M.J. Monteiro, Z. Jia, Conjugated nitroxide radical polymers: synthesis and application in flexible energy storage devices. ACS Appl. Mater. Interfaces. **11**(7), 7096–7103 (2019). https://doi.org/10.1021/acsami
6. A. Leavesley, S. Jain, I. Kamniker, H.H. Zhang, S. Rajca, A. Rajca, S. Han, Maximizing NMR signal per unit time by facilitating the e-e-n cross effect DNP rate. Phys. Chem. Chem. Phys. **20**(43), 27646–27657 (2018)
7. A. Equbal, Y. Li, A. Leavesley, S. Huang, S. Rajca, A. Rajca, S. Han, Truncated cross effect dynamic nuclear polarization: an overhauser effect doppelganger. J. Phys. Chem. Lett. **9**(9), 2175–2180 (2018)
8. A. Bihlmeier, G. Jeschke, S. Bräse, M. Tsotsalas, Radical exchange reaction of multi-spin isoindoline nitroxides followed by EPR spectroscopy. RSC Adv. **6**, 55715–55719 (2016)
9. E.G. Janzen, B.J. Blackburn, Detection and identification of short-lived free radicals by an electron spin resonance trapping technique. J. Am. Chem. Soc. **90**, 5909–5910 (1968)
10. A. Nawab, A. Nichols, R. Klug, J.I. Shapiro, K. Sodhi, Spin trapping: a review for the study of obesity related oxidative stress and Na +/K + -ATPase. J. Clin. Cell Immunol. **8**(3), 505 (2017)
11. M. Heinenberg, B. Menges, S. Mittler, H. Ritter, Polymeric nitrons. 2. Synthesis, irradiation and waveguide mode spectroscopy of polymeric nitrons derived from polymeric Benzaldehydes and N Isopropylhydroxylamine. Macromolecules **35**(9), 3448–3455 (2002)
12. P.L. Zamora, F.A. Villamena, Theoretical and experimental studies of the spin trapping of inorganic radicals by 5,5-Dimethyl-1-pyrroline *N*-Oxide (DMPO). J. Phys. Chem. A **116**(26), 7210–7218 (2012)
13. D. Bardelang, A. Rockenbauer, H. Karoui, J.P. Finet, P. Tordo, Inclusion complexes of PBN-type nitrone spin traps and their superoxide spin adducts with cyclodextrin derivatives: parallel determination of the association constants by NMR titrations and 2D-EPR simulations. J. Phys. Chem B **109**, 10521–10530 (2005)
14. M. Cassien, C. Petrocchi, S. Tetiot-Laurent, M. Robin, E. Ricquebourg, C. Kandouli, A. Asteian, A. Rockenbauer, A. Mercier, M. Culcasi, S. Pietri, On the vasoprotective mechanisms underlying novel phosphorylated nitrones: focus on free radical characterization, scavenging and NO-donation in a biological model of oxidative stress. Eur. J. Med. Chem. **119**, 197–217 (2016)
15. H. Chen, G. Tan, J. Cao, G. Zhang, P. Yi, Y. Pei, Y. Sun, Z. Zhang, Y. Wang, Design, synthesis, and biological evaluation of novel tetramethylpyrazine derivatives as potential neuroprotective agents. Chem. Pharm. Bull. **65**, 56–65 (2017)
16. L. Socrier, M. Rosselin, F. Choteau, G. Durand, S. Morandat, Cholesterol-nitrone conjugates as protective agents against lipid oxidation: A model membrane study. Biochim. Biophys. Acta Biomembr. **1859**(12), 2495–2504 (2017)
17. V. Marchand, N. Charlier, J. Verrax, P.P. Buc-Calderon, P. Levêque, B. Gallez, Use of a cocktail of spin traps for fingerprinting large range of free radicals in biological systems. PLoS ONE **12**(3), e0172998 (2017)
18. X. Gao, Y. Bi, K. Chi, Y. Liu, T. Yuan, X. Li, W. Bi, Glycine-nitronyl nitroxide conjugate protects human umbilical vein endothelial cells againsthypoxia/reoxygenation injury via multiple mechanisms and ameliorates hind limb ischemia/reperfusion injury in rats. Biochem. Biophys. Res. Commun. **488**(1), 239–246 (2017)
19. G.I. Liktenshtein, Y.B. Grebenshcikov, P.K. Bobodzhanov, Y.V. Kokhanov, Investigation of the macrostructure of proteins the paramagnetic label-paramagnetic probe technique. Moleculyarnaya Biologiya **4**, 682–691 (1970)

20. K.M. Salikhov, A.B. Doctorov, Y.N. Molin, K.I. Zamaraev, Spin relaxation of radicals and complexes upon encounters in solution. J. Magn. Reson. **5**, 189–196 (1971)
21. J.S. Hyde, H.M. Swartz, W.E. Antholine, The spin probe-spin label methods, in *Spin Labeling. Theory and Application*, vol. 2, ed. by L. Berliner (Academic Press, New York, 1976), pp. 72–113
22. G.I. Likhtenstein, Y.B. Grebentchikov, P.K. Bobodzhanov, Y.V. Kokhanov, Study on the proteins microstructure by method of spin-label paramagnetic probe. Mol. Biol. (Moscow) **4**, 782–789 (1970)
23. G.I. Likhtenstein, Y.B. Grebentchikov, E.G. Rosantev, V.P. Ivanov, Study on the electrostatic charges in proteins by method of paramagnetic probes. Mol. Biol. (Moscow) **6**, 498–507 (1972)
24. J.L. Hecht, B. Honig, Y.K. Shin, W.L. Hubbell, Electrostatic potentials nearthe- surface of DNA—Comparing theory and experiment. J. Phys. Chem. **99**(19), 7782–7786 (1995)
25. Y.K. Shin, W.L. Hubbell, Determination of electrostatic potentials at biological interfaces using electron electron double resonance [Article]. Biophys. J. **61**(6), 1443–1453 (1992)
26. G.I. Likhtenshtein, I. Vaisbuch, I. Adin, A. Shames, R. Glaser, Distribution of electrostatic-field around biological molecules studied by methods of spin-probes and NMR. Biophys. J. **72**, A129 (1997)
27. G.I. Likhtenshtein, I. Adin, A. Krasnoselsky, I. Vaisbuch, A. Shames, Glaser, NMR and ESR studies of electric field distribution around biologically important molecules. Biophys. J. **77**, 443–454 (1999)
28. G.I. Likhtenshtein, Depth of immersion of paramagnatic centers, in *Magnetic Resonance in Biology*, ed. by L. Berliner, S. Eaton, G. Eaton (Kluwer Academic Publishers, Dordrecht, 2000), pp. 1–36
29. B.J. Depmeier, A.J. Driessen, W.J. Hehre, J. Johnson, A.C. Peng, L. Lou, J. Yu, *MacSpartan version 1.0.2* (Wavefunction, Irvine, CA, 1996)
30. J.T. Surek, D.D. Thomas, A paramagnetic molecular voltmeter. J. Magn. Reson. **190**(1), 7–25 (2008)
31. L.P. Hwang, J.H. Freed, Dynamics effect of pair correlation function on spin-relaxation by translational diffusion in liquids. J. Chem. Phys. **63**, 4017–4025 (1975)
32. R. Glaser, A. Novoselsky, A. Shames, G.I. Likhtenshtein, NMR studies of electrostatic fields around charged monosaccharides and related molecules. Isr. J. Chem. Special Lemieux Issue **40**, 263–269 (2000)
33. M.A. Voinov, A.I. Smirnov, Ionizable nitroxides for studying local electrostatic properties of lipid bilayers and protein systems by EPR, in *Methods in Enzymology*, vol. 564 (Electron Paramagnetic Resonance Investigations of Biological Systems by Using Spin Labels, Spin Probes, and Intrinsic Metal Ions, Part B) (2015), pp. 191–192
34. M.A. Voinov, A. Ruuge, V.A. Reznikov, I.A. Grigor'ev, A.I. Smirnov, Mapping local protein electrostatics by EPR of pH-sensitive thiol-specific nitroxide. Biochemistry **47**(20), 5626–5637 (2008)
35. A.V. Kulikov, Determination of distance between the nitroxide label and a paramagnetic center in spin-labeled proteins from the parameters of the saturation curve of the ESR spectrum of the label at 77K. Mol. Biol. (Moscow) **10**, 109–116 (1976)
36. A.V. Kulikov, G.I. Likhtenstein, Application of saturation curves for evaluating distances in biological objects by the method of double spin-labels. Biofisika **19**, 420–424 (1974)
37. A.V. Kulikov, G.I. Likhtenshtein, The use of spin-relaxation phenomena in the investigation of the structure of model and biological systems by method of spin labels. Adv. Molecul. Relax. Proc. **10**, 47–78 (1977)
38. N.V. Strashnikova, N. Medvedeva, G.I. Likhtenshtein, Depth of immersion of fluorescent chromophores in biomembranes studied by quenching with nitroxide radical. J. Biochem. Biophys. Methods **48**, 43–60 (2001)
39. I.K. Yusupov, G.I. Likhtenshtein, Phosphorescence quenching as an approach for estimating localization of triplet label in cotton fibers. Biofizika **57**(2), 286–291 (2012)
40. R.M. Marupov, P.K. Bobodzhanov, N.V. Kostina, A.B. Shapiro, Spin label study of the structure and conformational properties of cotton filament grown from γ-irradiated seeds. Biofizika **21**, 825–828 (1976)

41. R.M. Marupov, P.K. Bobodzhanov, I.K. Usupov, E.N. Frolov, G.I. Likhtenshtein, Study of temperature stability of cotton fibers by spin labeling. Biofizika **24**, 519–523 (1979)
42. A.V. Dushkin, I.B. Troitskaya, V.V. Boldyrev, I.A. Grigor'ev, Mechanochemical method for introduction of a spin marker in cellulose. Russ. Chem. Bull. **54**, 1155–1159 (2005)
43. I.K. Ysupov, G.I. Likhtenshtein, Study of microstructure and molecular dynamics of cotton and cellulose fibers by methods of physical labels. Int. Res. J. Pure Appl. Chem. **6**(3), 105–119 (2015)
44. V.I. Krinichnyi, O.Y. Grinberg, I.K. Yusupov, R.M. Marupov, P.K. Bobodzhanov, G.I. Likhtenshtein, Y.S. Lebedev, Two-millimeter band ESR study of spin-labeled cotton fiber. Biofizika **31**, 482–485 (1986)
45. V.I. Krinichnyi, *2-mm Wave Band EPR Spectroscopy of Condensed Systems* (CRC Press, Boca Raton, Florida, 1995)
46. S.N. Zhurkov, E.A. Egorov, Effect of tensile stress on the molecular mobility in oriented polymers. Dokl. Akad. Nauk SSSR **152**, 1155–1158 (1963)
47. S. Frantz, G.A. Hübner, O. Wendland, E. Roduner, C. Mariani, M.F. Ottaviani, S.N. Batchelor, Effect of humidity on the supramolecular structure of cotton, studied by quantitative spin probing. J. Phys. Chem. B. **109**(23), 11572–11579 (2005)
48. S. Frantz, O. Wendland, E. Roduner, C.J. Whiteoak, S.N. Batchelor, Effect of charge on spin probe interaction and dynamics in the nanopores of cotton. J. Phys. Chem. C **111**(39), 14514–14520 (2007)
49. S. Islomov, R. Marupov, R.G. Zhbankov, PKh Bobodzhanov, L.V. Zabelin, G.N. Marchenko, Spin-label study of structural properties of nitrates based on flax shive cellulose. Zh. Prikl. Spektrosk. **45**, 633–638 (1986)
50. G. Dietrich, M.J.P. Blinco, A. Hirschbiel, M. Bruns, L. Barner, C. Barner-Kowollik, Photo-induced macromolecular functionalization of cellulose via nitroxide spin trapping. Biomacromol **13**(5), 1700–1705 (2012)
51. A. Marek, M.A. Voinov, A.I. Smirnov, Spin probe multi-frequency EPR study of unprocessed cotton fibers. Cell Biochem. Biophys. **75**(2), 211–226 (2017)
52. S. Gulinelli, E. Mantovani, A. Zanobi, EPR characterization of cellulose triacetate fibers used for enzyme immobilization. Appl. Biochem. Biotechnol. **6**, 129–141 (1981)
53. S. Liu, Y. Xing, J. Han, E. Tang, Catalytic oxidation of cellulose with a novel amphiphilic nitroxide block copolymer as a recoverable catalyst. Cellulose (Dordrecht, Netherlands) **24**(9), 3635–3644 (2017)
54. G.I. Likhtenshtein, *Stilbenes: Application in Chemistry, Life Science and Material Science* (WILEY-VCH, Weinhem, 2009)
55. V. Papper, N. Medvedeva, I. Fishov, G.I. Likhtenshein, Quenching of cascade reaction between triplet and photochrome probes with nitroxide radicals: a novel labeling method in study of membranes and surface systems. Appl. Biochem. Biotechnol. **89**, 231–248 (2000)
56. N. Medvedeva, V. Papper, G.I. Likhtenshten, Study of rare encounters in a membrane using quenching of cascade reaction between triplet and photochrome probes with nitroxide radicals. Phys. Chem. Chem. Phys. **7**, 3368–3374 (2005)
57. G.I. Likhtenshtein, *Electron Spin in Chemistry and Biology: Fundamentals, Methods, Reactions Mechanisms, Magnetic Phenomena, Structure Investigation* (Springer, Berlin, 2016)
58. V.M. Mekler, A.I. Kotel'nikov, G.I. Likhtenstein, Study of model and biological membranes by probes emitting annihilated delayed fluorescence. Biofizika **28**, 503–504 (1983)
59. D.L. Dexter, A theory of sensitized luminescence in solids. J. Chem. Phys. **21**, 836–850 (1953)
60. G.S. Hammond, J. Saltiel, Photosensitized *Cis-Trans* Isomerization of the Stilbenes. J. Am. Chem. Soc. **84**, 4983–4984 (1962)
61. D.H. Waldeck, Photoisomerization dynamics of stilbenes. Chem. Rev. **91**, 415–436 (1991)
62. K.R. Naqvi, J. Martins, E. Melo, Recipes For analyzing diffusion-controlled reactions in two dimensions: time-resolved and steady-state measurements. J. Phys. Chem. B **104**, 12035–12038 (2000)
63. E.G. Bagryanskaya, D.N. Polovyanenko, M.V. Fedin, L. Kulik, A. Schnegg, A. Savitsky, K. Mobius, A.W. Coleman, G.S. Ananchenko, J.A. Ripmeester, Multifrequency EPR study of the

mobility of nitroxides in solid-state calixarene nanocapsules. Phys. Chem. Chem. Phys. **11**(31), 6700–6707 (2009)
64. R.K. Strizhakov, E.V. Tretyakov, A.S. Medvedeva, V.V. Novokshonov, V.G. Vasiliev, V.I. Ovcharenko, O.A. Krumkacheva, M.V. Fedin, E.G. Bagryanskaya, Permethyl-b-cyclodextrin spin-labeled with nitronyl nitroxide: synthesis and EPR study. Appl. Magn. Reson. **45**, 1087–1098 (2014)
65. S.S. Eaton, A. Rajca, Z. Yang, G.R. Eaton, Azaadamantyl nitroxide spin label: complexation with β-cyclodextrin and electron spin relaxation. Free Radical Res. **52**(3), 319–326 (2018)
66. E.G. Kovaleva, L.S. Molochnikov, E.L. Golovkina, M. Hartmann, I.A. Kirilyuk, I.A. Grigoriev, Electrical potential near hydrated surface of ordered mesoporous molecular sieves assessed by EPR of molecular pH-probes. Microporous Mesoporous Mater. **203**, 1–7 (2015)
67. E.G. Kovaleva, L.S. Molochnikov, D.P. Stepanova, A.V. Pestov, D.G. Trofimov, I.A. Kirilyuk, A.I. Smirnov, Interfacial electrostatic properties of hydrated mesoporous and nanostructured alumina powders by spin labeling EPR. Cell Biochem. Biophys. **75**, 159–170 (2017)
68. E.G. Kovaleva, L.S. Molochnikov, D.O. Antonov, D.P. Tambasova Stepanova, M. Hartmann, A.N. Tsmokalyuk, A. Marek, A.I. Smirnov, Proton activity in nanochannels revealed by electron paramagnetic resonance of ionizable nitroxides: a test of the Poisson-Boltzmann double layer theory. J. Phys. Chem. C **122**, 20527–20538 (2018)

Index

G. I. Likhtenshtein, *Nitroxides*, Springer Series in Materials Science 292,
https://doi.org/10.1007/978-3-030-34822-9